ESA-QCA00178T-C

Call-Off-Order Title: Study of Radiation Effects in Cryogenic Electronics and Advanced Semiconductor Materials

Report Title: **Literature Study on Radiation Effects in Advanced Semiconductor Devices**

Report Specification: Deliverable D4

Authors : C. Claeys and E. Simoen

Contractor : Interuniversity Microelectronics Centre (IMEC)

Work Order : 1938/96/NL/LB

ESTEC Technical management: A. Mohammadzadeh

Document No : P35284-IM-RP-0013

Status : Final version

Date : March 30, 2000

European Space Agency

Contract Report

The work described in this report was done under ESA contract. Responsibility for the contents resides in the author or organisation that prepared it.

Work Order 1938/96/NL/LB :

Study of Radiation Effects in Cryogenic Electronics and Advanced Semiconductor Materials

Literature Study on Radiation Effects in Advanced Semiconductor Devices

Deliverable D4

C. Claeys and E. Simoen

Distribution List :

C. Claeys	IMEC
G. Declerck	IMEC
E. Simoen	IMEC
H. Maes	IMEC
J. Roggen	IMEC
A. Mohammadzadeh	ESTEC/QCA
N. Boisard	ESTEC/ECT
4 copies unnamed	ESTEC (att. A. Mohammadzadeh)

Table of Contents

Introduction 1

1. Radiation Damage in Ge and Ge-Based Devices 3

1.1 Space Applications 3
1.2 Displacement Damage in Ge 4
1.2.1 Room Temperature Particle Irradiation 6
1.2.2 Low Temperature Particle Irradiation 13
1.3 Ionization Damage in Ge 15
1.4 Conclusions 15
References 17

2. Radiation in SiGe Materials and Devices 19

2.1 SiGe Properties and Applications 19
2.1.1 Material Properties 19
2.1.2 Applications 21
2.1.3 IMEC Activities 24
2.2 Radiation Damage in SiGe 24
2.2.1 Radiation Damage in Ge Doped Si and in Bulk SiGe 24
2.2.2 Radiation Damage in Relaxed SiGe Layers 25
2.2.3 Radiation Damage in Strained SiGe Layers 30
2.3 Processing-Induced Radiation Damage in SiGe 42
2.3.1 Dry Etching and Electron Beam Sputtering Damage 42
2.3.2 Ion Implantation Damage in SiGe 45
2.3.3 Ion Implantation Damage Model 49
2.4 Radiation Damage in SiGe Devices 50
2.4.1 Diodes 50
2.4.2 HBTs 55
2.5 Conclusions 64
References 65

3. Space Radiation Aspects of Silicon Bipolar Technologies 70

3.1 Device Structures and Basic Radiation Effects 70
3.1.1 Device Structures and Definitions 72
3.1.2 Radiation Damage Mechanisms 72
3.2 Degradation in Vertical (n-p-n) BJTs 74
3.2.1 Phenomenology of Total Dose Damage 74
3.2.2 Basic Low Dose-Rate Degradation Mechanisms 77
3.2.3 Charge Separation in BJTs 81
3.2.4 Hardening Guidelines for Vertical BJTs 87
3.2.5 Hardening Assurance and Testing 88
3.2.6 Bulk Damage in Vertical Transistors 89
3.3 Lateral Transistors 90
3.1 Phenomenology 90
3.2 Physical Mechanisms and Modeling 94
3.4 Conclusions 97
References 99

4. Radiation Effects in Scaled CMOS 100

4.1 Impact of Scaling on the Radiation Response 101
4.1.1 Gate Length Dependence 101
4.1.2 Non-Homogeneous Damaging 104
4.1.3 Gate-Induced Drain Leakage (GIDL) 108
4.2 Processing Induced Radiation Damage Effects 110
4.2.1 Plasma Damage 110
4.2.2 Rapid Thermal Annealing (RTA) 112
4.2.3 Gate Material and Contacting 114
4.3 Alternative Gate Dielectrics 116
4.3.1 Doped Oxides 116
4.3.2 Nitrided (NO) and Reoxidised Nitrided Oxides (RNO) 117
4.3.3. N_2O or Nitrous Oxides 131
4.4. Ultra-Thin Oxides 133
4.4.1 Radiation Induced Leakage Current (RILC) 133
4.4.2 Single Event Gate Rapture 136

4.5 Device Isolation 136
4.5.1 LOCOS Isolation 137
4.5.2 Shallow Trench Isolation 140
4.6. Conclusions 142
References 143

5. GaAs Based Field Effect Transistors for Rad-Hard Applications 148

5.1 GaAs Material Properties and Device Structures 148
5.1.1 III-V Substrates and Native Defects 148
5.1.2 MESFET Structure and Operation 154
5.1.3 HEMT Structure and Operation 157
5.2 Macroscopic and Microscopic Displacement Damage Effects in GaAs 159
5.2.1 Macroscopic Displacement Damage in GaAs 159
5.2.2 Microscopic Displacement Damage Modeling 164
5.2.3 Correlation with Radiation Defects 166
5.3 Radiation Damage and Hardening in GaAs MESFETs 168
5.3.1 Displacement and Ionization Damage in FETs 168
5.3.2 HEMTs 183
5.4 Conclusions 195
References 196

6. Opto-Electronic Components for Space 200

6.1 Opto-Electronic Components 200
6.1.1 Light Emitting Diodes (LEDs) and Laser Diodes (LDs) 200
6.1.2 Photodetectors 206
6.1.3 Optocouplers 208
6.1.4 IMEC activities 208
6.2 Basic Radiation Effects and Material Issues 209
6.2.1 Damage Factors and NIEL 209
6.2.2 Radiation Defects and Material Aspects in Ternary Compounds 211

6.3 Radiation Effects in Opto-Electronic Components 217
6.3.1 LEDs and LDs 217
6.3.2 Photodetectors 225
6.3.3 Optocouplers 232
6.4 Conclusions 235
References 236

7. Ferroelectric Materials and Devices 239

7.1 IMECs Activities on Ferroelectrics 239
7.1.1 Material Aspects 239
7.1.2 Device Research 240
7.2 Radiation Hardness of Ferroelectric Materials and Devices 241
7.2.1 Purpose of the Testing 241
7.2.2 Experimental Test Conditions 242
7.2.3 Experimental Results on Ferroelectric Capacitors 242
7.3 Conclusions 248
References 249

8. Conclusions and Future Activities 250

Acknowledgment 251

Abstract

This report constitutes the Deliverable D4 of Work Order 1938/96/NL/NB on "Study of Radiation Effects in Cryogenic Electronics and Advanced Semiconductor Materials". It gives a critical literature review of the published information on the radiation performance of advanced materials and devices. Different technologies such as Ge, SiGe, bipolar, submicron CMOS, and GaAs are discussed. Attention is also given to optoelectronic and ferroelectric materials and components. The most important conclusions resulting from the literature study are summarized and used to define a proposal for future radiation activities.

INTRODUCTION

This report contains Deliverable D4 associated with Work Order 1938/96/NL/LB on 'Study of Radiation Effects in Cryogenic Electronics and Advanced Semiconductor Materials", Activity 2 dealing with "Radiation Effects in Advanced Semiconductor Materials". It gives a critical literature review of the expected radiation performance of advanced materials and devices that may be envisaged by ESA to be used for future missions. Both silicon and non-silicon based technologies have been studied. The Deliverable contains 7 chapters each outlining a particular technology, while a final chapter eight summarizes the most important conclusions and also defines a proposal for future irradiation rounds. For each of the different technologies, the impact of irradiation on both fundamental material properties (i.e. ionization and displacement damage) and on the performance characteristics of different components are critically reviewed. Special attention is also given to the relevant IMEC activities in these technological fields. Each chapter also contains an extensive reference list, as this will form the basis for the justification of the future activities within this contract.

The first chapter discusses radiation damage in Ge and Ge based devices. Although for most ULSI applications Si has taken over from Ge, Ge and its compounds are still used in a large variety of space related applications. Typical examples are infrared detectors, Ge-based thermistors for bolometers, nuclear-radiation detector diodes operating at cryogenic temperatures and epitaxial GaAs/Ge tandem solar cells. Especially the latter components are gaining much interest in recent years.

The second chapter reviews radiation effects in Si-Ge alloys, allowing band-gap engineering between 1.12 eV (Si) and 0.74 eV (Ge). This unique feature, together with the compatibility with silicon processing offers very promising perspectives for a wide-scale application of $Si_{1-x}Ge_x$ hetero-epitaxy in next generation ULSI technologies. Especially in the field of rf telecommunication large efforts are ongoing for the moment. Depending on the envisaged applications both strained and relaxed SiGe layers are used. In addition to these heterojunction structures, there is also interest in the use of bulk SiGe crystals for the fabrication of solar cells.

Silicon Bipolar Junction Transistors (BJT) have since the early days been studied for analog or mixed signal applications. Therefore BJTs are frequently used in space systems, including operational amplifiers, comparators and voltage regulators. In the last decade BiCMOS (Bipolar Complementary Metal-Oxide-Semiconductor) circuits gained a lot of attention because of their current-drive capability, linearity, and excellent matching characteristics. Especially, the microwave performance of bipolar technologies compares favorably with respect to CMOS for use in GHz telecommunications applications. The implementation of a SiGe heterojunction base will further trigger the breakthrough of BiCMOS in the near future. The radiation performance of different bipolar technologies is studied in Chapter 3.

The dominant technology on the market place is still CMOS and this will also remain so in the future. This has a direct influence on the COTS approach used for space missions. However, the main driving force is to reduce the feature size in order to increase

the packing density and to enhance the device performance. Therefore Chapter 4 studies the impact of CMOS scaling on the expected radiation performance. Special attention is given to the different options for gate dielectrics (e.g. nitrided and reoxidised nitrided oxides), the process improvement to enhance the device reliability, advanced dry etching techniques, and the envisaged isolation schemes such as e.g. shallow trench isolation.

Chapter 5 reviews the GaAs and related III-V compound technologies, which are mainly used for high-speed digital and microwave/millimeter wave applications. In general, these materials are radiation hard to total dose radiation tolerance levels up to 1 Grad(GaAs), which is at least two orders of magnitude better than for hardened Si-based technologies. However, the semi-insulating substrate may cause some specific phenomena. The relevant material properties and the structure of the Metal-Semiconductor Field-Effect Transistor (MESFET) and the High Electron Mobility Transistor (HEMT), also called Modulation Doped FET (MODFET) are described. Special attention is given to InP based MMIC (Monolithic Microwave Integrated Circuit) technologies.

Some space applications are making use of so-called photonics systems. Because of the direct band gap, yielding a high quantum efficiency, and the superior radiation tolerance of GaAs and related compounds, III-V opto-electronic components are the preferred technology for applications in a broad wavelength range, going from 700 to 1600 nm, whereby operation at 1300 nm is particularly suitable for fiber optics. Chapter 6 describes the behavior of modern III-V opto-electronic components, with emphasis on Light Emitting Diodes (LED), Laser Diodes (LD), and Photodiodes or Photodetectors (PD).

For the sake of completeness, Chapter 7 briefly discusses some aspects of ferroelectrics materials and devices. Applications of direct interest are infrared sensors and non-volatile memories. The potential radiation performance of a sol-gel based PZT material, developed at IMEC, is highlighted.

The last Chapter summarizes the most important conclusions resulting from the critical literature review of the different technologies with a good potential for future space applications. This will allow to draw some conclusions concerning the requirements of additional radiation testing of these advanced materials and devices.

1. RADIATION DAMAGE IN Ge and Ge-BASED DEVICES

In this chapter, the radiation properties of germanium will be discussed in view of space applications. In a first section a round up of the potential space applications is given. Since in most cases, the bulk of the material is used for particle or photon detection, the primary degradation effect due to the exposure to space radiation will be displacement damage. This will be reviewed in a second section. Finally, the impact of ionization damage will be briefly addressed.

1.1 Space Applications

Although the first bipolar transistors have been developed on Ge, during the last three decades silicon has become the dominant semiconductor material, surely for Ultra and Very Large Scale Integration (ULSI-VLSI) technologies. This is due to the favorable oxidation properties of Si, which enabled the development of the planar technology, while it is very difficult to form a stable oxide on the germanium (or $Si_{1-x}Ge_x$) surface. Nevertheless, for some niche markets, Ge is an important material and finds its way to space applications as well.

A first class of applications is infrared and far-infrared spectroscopy using a cooled Ge detector. For example, stressed Ge:Ga detectors will be used for the FIRST mission [1], for the spectral range 85 to 210 μm. They operate in the liquid helium temperature (LHT) range, i.e. between 1.5 and 2 K. For the wavelength range beyond 200 μm, stressed Ge:Ga detectors provide a unique combination of sensitivity and long-wavelength response. The sensitivity is quoted to be two to three orders of magnitude better than that of a bolometer operated in the same temperature range [2]. In the meantime, also unstressed Ge:Ga and Ge:Sb detectors for astrophysical investigations are under development [3].

A second related group of devices are the Ge-based thermistors for bolometer applications [4]. Operational temperatures lie in the sub 1 K range. A basic requirement for a semiconductor thermistor is a uniform resistivity and hence doping. This can be achieved by the Neutron Transmutation Doping (NTD) process. In contrast to the case of silicon, where NTD technologies can only produce n-type Si, p-type Ge is generally obtained in NTD Ge, starting from high-purity n-type material. There are three Ge isotopes, which transmute to dopants after having captured a thermal neutron in their nucleus, according to the reactions:

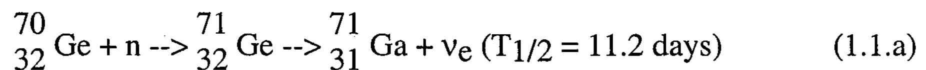

$${}^{70}_{32}Ge + n \dashrightarrow {}^{71}_{32}Ge \dashrightarrow {}^{71}_{31}Ga + \nu_e \ (T_{1/2} = 11.2 \text{ days}) \quad (1.1.a)$$

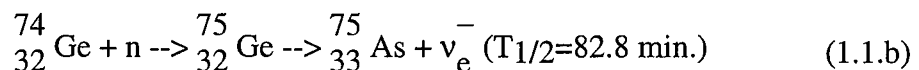

$${}^{74}_{32}Ge + n \dashrightarrow {}^{75}_{32}Ge \dashrightarrow {}^{75}_{33}As + \bar{\nu}_e \ (T_{1/2}=82.8 \text{ min.}) \quad (1.1.b)$$

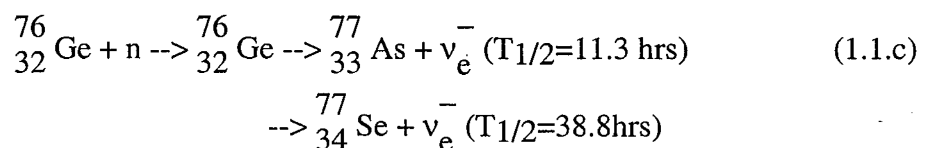

$${}^{76}_{32}Ge + n \dashrightarrow {}^{76}_{32}Ge \dashrightarrow {}^{77}_{33}As + \bar{\nu}_e \ (T_{1/2}=11.3 \text{ hrs}) \quad (1.1.c)$$

$$\dashrightarrow {}^{77}_{34}Se + \bar{\nu}_e \ (T_{1/2}=38.8\text{hrs})$$

The first reaction leads to the creation of acceptors; the two others generate a single (As) and a double donor. Since the abundance of the 70 isotope is more than 95 %, the first reaction will be dominant, leading to the homogeneous p-type doping of the material. Of course, as for the NTD of silicon, radiation defects will be created during the neutron exposure and have to be annealed out by a proper heat treatment.

High-purity and ultra-high purity germanium is a material suitable for the fabrication of nuclear-radiation detector diodes, which operate typically at 77 K under full depletion conditions [5-7]. They are frequently used in γ-ray spectroscopy. Although in the past mostly p-type material was used [5,7], efforts are being devoted to the development of n-type detectors, which are claimed to be more radiation hard [6]. The reason is that irradiation introduces predominantly hole traps in the material, while in n-type detectors the electrons have to travel the largest distance before being collected at the positively biased cathode.

The interest in epitaxial GaAs/Ge solar cells for space applications has drastically increased in recent years [8-9]. In that case, an III-V active solar cell is deposited epitaxially by, for example, Metal Organic Chemical Vapor Deposition (MOCVD) techniques on highly doped n^+ Ge wafers (range 10^{16} to 10^{17} cm^{-3}). The advantages are that it is easier to grow III-V compounds pseudomorphically on Ge than on Si substrates, because of the lower lattice mismatch. Another benefit of Ge is its larger mechanical strength compared with Si. The wafers can, therefore, be made thinner, e.g. 200-300 μm for a 100 mm diameter. This offers a weight advantage, which is of primary importance for space. Next, if a highly doped p^+ wafer is used, an active tandem cell can be fabricated, whereby the Ge absorbs in the longer wavelength region of the solar spectrum. On top of that, there are a number of economical reasons to prefer Ge wafers in stead of GaAs substrates (price, availability, larger diameter, better crystal perfection). Finally, it has been observed that GaAs/Ge solar cells have a larger radiation tolerance than their GaAs/GaAs counterparts [8-9].

Given this wide range of potential space applications, it is important to study and understand the space radiation damage in the Ge lattice. It should be remarked in this respect that the world's largest supplier of Ge wafers is Union Minière (UM) in Olen (Belgium) and that IMEC has a long-term collaboration with UM in the field of Ge wafers for solar cell and opto-electronic applications.

1.2 Displacement Damage in Ge

Similar as for Si, one can calculate the so-called Non-Ionizing Energy Loss (NIEL) for Ge [10]. The NIEL concept is very useful if one wants to normalize the displacement damage to some reference energy, which is usually 10 MeV for protons and 1 MeV for electrons or neutrons. It is also extremely useful for the space environment where a whole spectrum of energies impinges on the components, so that one can use the integrated NIEL to estimate the damage for the whole particle spectrum. The non-ionizing energy deposition S_d, expressed in keV-cm^2/g is obtained by summing the product of the cross section σ_i and

the recoil energy $E_i(E)$ for each incident particle energy E, of interest, and for each kind of nuclear interaction, i, of interest. This results in a NIEL given by [10]:

$$S_d = (N/A) \sum_i \sigma_i(E)\, E_i(E) \tag{1.2}$$

Here, N is Avogadro's number and A is the gram atomic mass of the target. In principle, the NIEL contains Coulombic interactions, prevailing at low particle energies and elastic and inelastic nuclear interactions, progressively becoming more important for higher proton (ion) energies. The resulting NIEL for germanium is represented in Fig. 1.1, for protons and electrons.

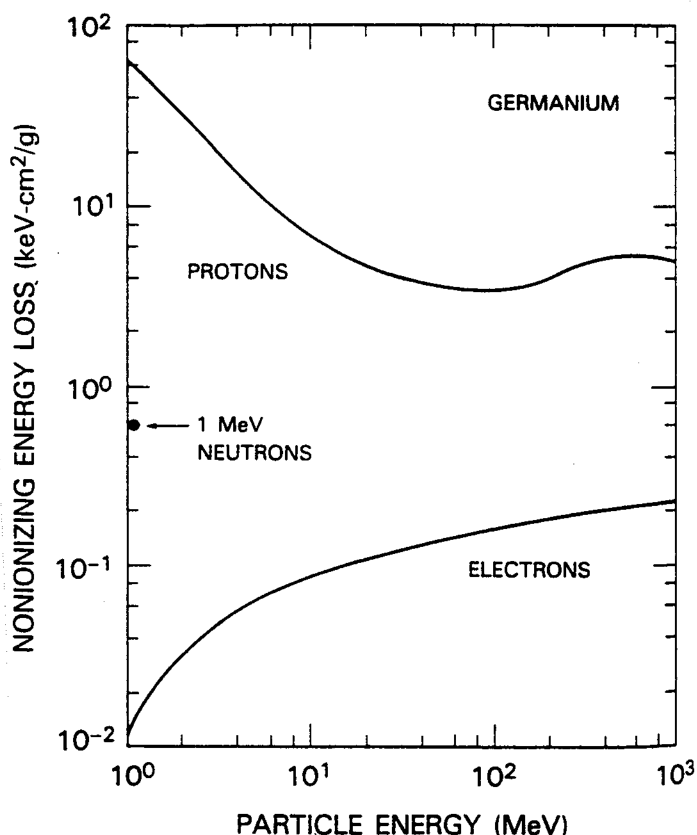

Fig.1.1. Calculations of the NIEL in Ge due to incident protons and electrons. (After Marshall et al. [10]).

An analytical expression for the displacement cross section is given by [11]:

$$\sigma = \pi \left[\frac{Zq^2\gamma}{mc^2(\gamma^2-1)}\right]^2 \left(\frac{E_m}{E_d} - 1\right] \tag{1.3}$$

with $\gamma=\sqrt{1-v^2/c^2}$ with v the incident particle velocity and c the velocity of light, m the particle mass, Z the target atomic number and T_m the maximum energy transmitted to the

nuclei. E_d is the threshold energy for displacement. It turns out to be 27.5 eV in Ge [11] compared with 21 eV in Si. Under a constant energy of irradiation E, the concentration of primary defects N_T is given by:

$$\frac{dN_T}{dt} = \sigma(E)\, N_{at}\, \phi \qquad (1.4.a)$$

resulting in:

$$N_T = \sigma\, N_{at}\, (\phi t) \qquad (1.4.b)$$

with ϕ the particle flux (assumed constant), t the irradiation time and N_{at} the atomic density of the crystalline target (cm^{-3}). The particle fluence $\Phi = \phi t$, if the flux is constant. This leads to an average primary defect introduction rate $r_T = \partial N_T / \partial \Phi$ at room temperature of 0.14 cm^{-1} for n-type Si and 0.03 cm^{-1} for n-type Ge, for a 1.5 MeV electron irradiation. This implies that about 5 times more primary vacancy-interstitial pairs are formed in Si compared with Ge, by electron irradiation. It should be remarked here that the maximum energy that can be channeled into displacements in Ge is about 2 MeV compared with 0.2 MeV in silicon [10].

1.2.1 Room Temperature Particle Irradiation

While the stable radiation defects in silicon are pretty well established (see e.g. [12]), the results on Ge are rather scattered and much less documented. This is partially due to the difficulties in analyzing the defects. It is for example very difficult if not impossible to apply Electron Paramagnetic Resonance (EPR) to study radiation defects in Ge, a technique that was very successful for the defect identification in irradiated Si [13]. It is only with the introduction of the Deep Level Transient Spectroscopy (DLTS) technique (see for example [5-7]) that systematic studies of the radiation defects in Ge became amenable. In the meantime, investigations have been performed on high-energy electron [14-19], low energy proton [16,19] and high-energy ion [20-21] irradiations. In addition, the impact of neutron irradiation on high purity germanium (doping density in the range 10^{10} cm^{-3}) has been studied for NTD purposes [19,22-23].

Typical spectra after room temperature ion irradiation of n-type Ge are represented in Fig. 1.2 [20], showing the presence of 5 stable radiation-induced electron traps (ET) in the upper half of the band-gap. Based amongst others on the thermal stability (annealing behavior) to be discussed below, the assignment schematically represented in Fig. 1.3 has been established. The corresponding signatures, derived from an Arrhenius plot are summarized in Table I and compared with the position of the activation energy (enthalpy) E_T and the effective capture cross section σ_∞ [14,24]. The defect signature is found from the measured emission rate for electrons (n-type) or holes (p-type) as follows:

$$e_{n,p}(T) = N_{c,v}\, v_{th}\, \sigma_\infty \exp(-E_T/kT) \qquad (1.5)$$

with v_{th} the thermal velocity of the respective carriers, k Boltzmann's constant and T the absolute temperature. $N_{c,v}$ is the effective density of states in the conduction or valence band, respectively.

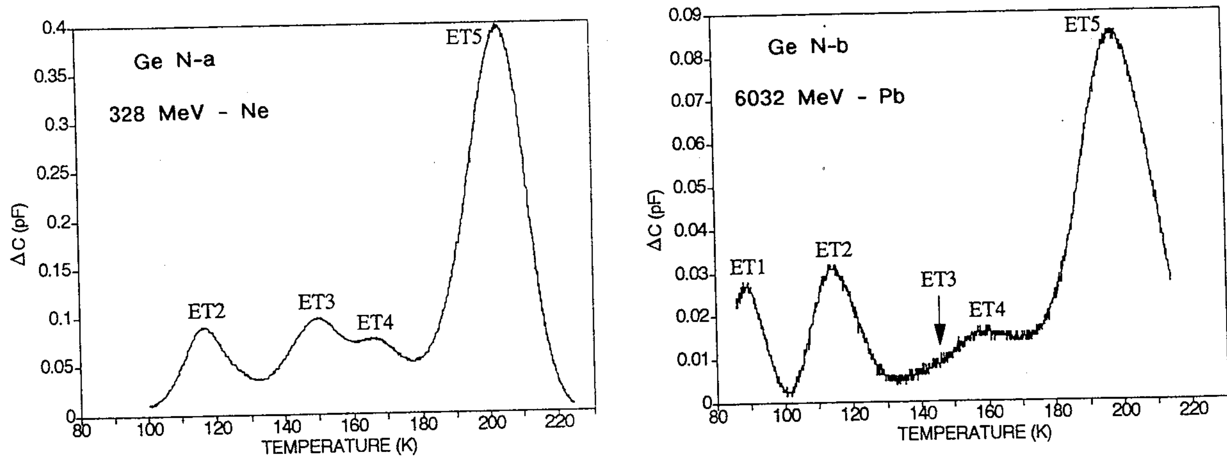

Fig. 1.2. Typical DLTS spectrum obtained in n-type germanium after a 1.8×10^{10} cm^{-2} Ne irradiation (a) and a 1.5×10^{9} cm^{-2} Pb irradiation (b). (After Marie et al. [20]).

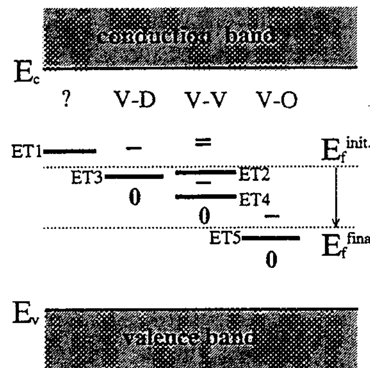

Fig. 1.3. Charge state levels associated with the defects present at room temperature in heavy ion irradiated germanium. V-D, V-V and V-O are related to the vacancy-doping impurity (E-center), divacancy and vacancy-oxygen complexes (A-center), respectively. The Fermi levels before E_f^{init} and at the end E_f^{final} of the irradiation are also reported. (After Marie et al.[21]).

Hole traps (HT) in electron irradiated Ge have been studied extensively by Fukuoka and Saito [17], for Ga, In, As and Sb doped material. A typical spectrum for p-Ge is shown

in Fig. 1.4, where three levels appear at E_V+0.21 eV, +0.24 eV and +0.31 eV. The 0.24 eV level is only found in In-doped Ge and anneals with an activation energy of 1.52 eV. For irradiated n-type Ge, a minority carrier (hole) trap is observed at E_V+0.29 eV approximately, which is thought to correspond with H(0.31) [17]. Typical introduction rates for 1.5 or 10 MeV electrons are in the range 0.02 - 0.05 cm^{-1}, both in n- and p-type material. Furthermore, a larger introduction rate is found for lowly doped material. From this, it is concluded that the dominant hole trap is a complex defect, with no dopant atom incorporated and based on its thermal stability, consisting of a complex of primary point defects, possibly a divacany or a vacancy cluster [17].

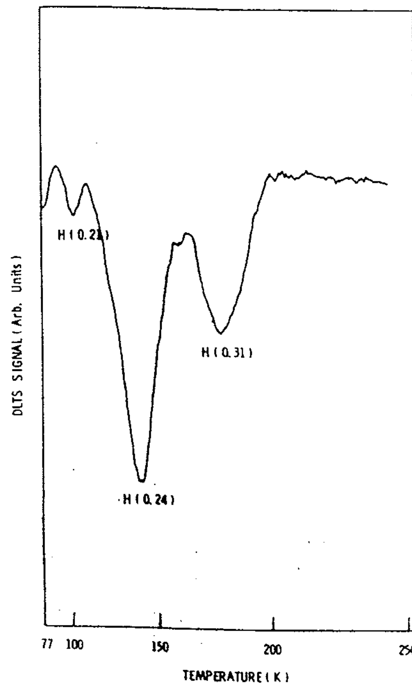

Fig. 1.4. DLTS spectrum after irradiation of In-doped p-type Ge. (After Fukuoka and Saito [17]).

As can be seen, the same type of radiation defects introduces a similar type of energy level, occurring in the same band-half, for both Si and Ge. In some cases, however, the level is clearly shifted, like e.g. for the A-center or for the E-center(s). As a result, little overlap occurs in Ge between the E-center and the $V\text{-}V^{-/o}$ level, for example. Another striking difference is the broader range of apparent cross sections found in Ge, while the range is much tighter in Si, centered on a value of 10^{-15} cm^2. It should be emphasized, however, that there is much less consensus on the identifications of Table 1.1 - the number of studies is too limited to firmly establish the nature of some of the radiation-induced defects. It has for example been reported in electron irradiated p-Ge that a level at E_v+0.42 eV belongs to the divacancy [16]. Additionally, there is quite some difference between the energy levels reported in [14-15] (see Table 1.1) and in [21], even for the peaks assumed to belong to the same defect complexes. There is also evidence that higher order vacancy/interstitial clusters can be formed in particle irradiated high-purity Ge [19,23].

Finally, two V_2-H related defects have been assigned at E_V+0.3 eV and E_V+0.42 eV in low-energy proton irradiated p-type Ge [16].

One way to further study the nature of the radiation-induced defects is by investigating their thermal stability upon isochronal or isothermal annealing [15-17,19]. The annealing temperature T_A for room temperature induced radiation defects is summarized in Table 1.2 [24]. T_A is defined as the temperature where after isochronal annealing for a certain time only 10 % of the original trap concentration survives. Comparing with the T_A's for Si, it appears that the dominant radiation defects are less stable in Ge. Fig. 1.5a and 1.5b show the annealing behavior of the divacancy related levels in electron-irradiated p- and n-type Ge, respectively [15]. There appears to be a dependence of the annealing on the electron energy. For the 1 MeV irradiation, the V-V center decomposes slightly above 100 ^{o}C. For the 2 MeV electron exposure, on the other hand, first an increase of the V-V concentration is found, for the three levels, probably following the decomposition of E-centers, which anneal at the same or slightly lower temperatures, according to Table II. This is better illustrated in Fig. 1.6 [21].

Table 1.1. Defect parameters of the dominant radiation induced defects in Ge (subscript Ge) and in Si (subscript Si) obtained from the Arrhenius plot of DLTS. Data of Refs 14, 24 and 25 have been combined. ET is an electron trap whereby the activation energy (enthalpy) is related to the bottom of the conduction band, while HT denotes a hole trap related to the top of the valence band. The nature of the traps is indicated by A (acceptor) or D (donor).

Defect Charge State	ET_{Ge} (eV)	σ_∞Ge (cm^2)	ET_{Si} (eV)	σ_∞Si (cm^2)
$V\text{-}V^{-/o}$ (A)	ET(0.46)	$5x10^{-15}$	ET(0.39)	$4x10^{-15}$
$V^{=/-}$ (A)	ET(0.42)	$(1\text{-}5)x10^{-16}$	ET(0.23)	$(0.5\text{-}2)x10^{-15}$
$V\text{-}V^{o/+}$ (D)	HT(0.17)	?	HT(0.19)	$2x10^{-15}$
V-P (A)	ET(0.32)	$(5\text{-}10)x10^{-12}$	ET(0.44)	$3x10^{-15}$
V-O (A)	ET(0.53)	$10^{-13}\text{-}10^{-14}$	ET(0.17)	10^{-14}

Table 1.2. Annealing temperature of the dominant radiation-induced defects in Ge and Si. (After Goubet and Stievenard [24]).

Defect Center	T_AGe (K)	T_ASi (K)
V-V	450	570
V-P	400	400-550
V-O	450	620

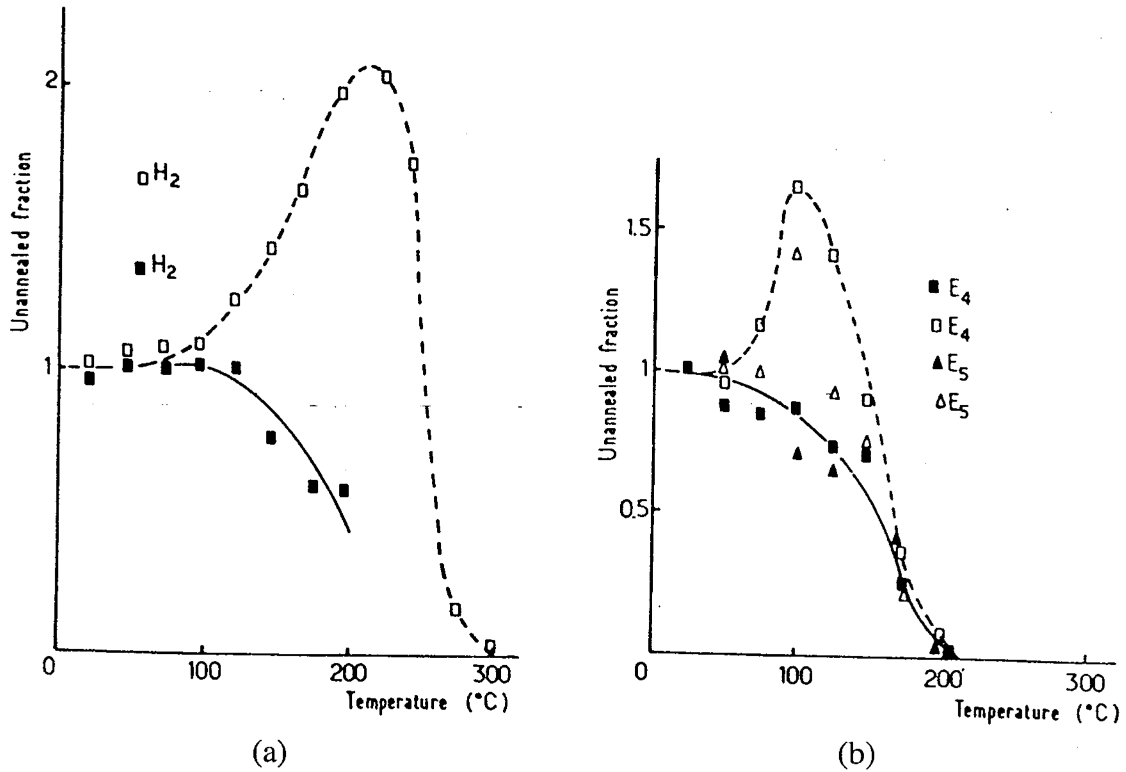

Fig. 1.5. (a) Unannealed fraction of traps H2 versus isochronal annealing temperature. The solid line corresponds to a 1 MeV electron irradiation, the dashed line with 2 MeV e^-. (b) Unannealed fraction of traps E4 and E5 versus isochronal annealing temperature. The solid line corresponds to a 1 MeV electron irradiation, the dashed line with 2 MeV e^-. (After Mooney et al. [15]).

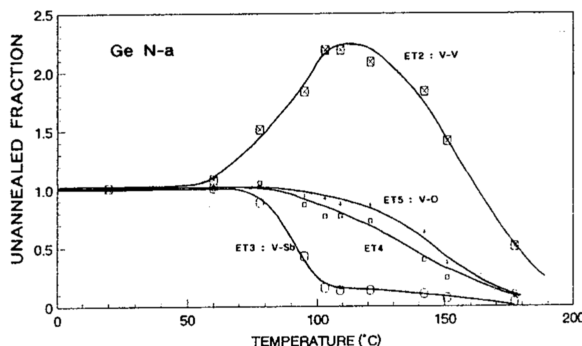

Fig. 1.6. Annealing behaviour of electron traps produced by Ne ion irradiation in an n-type Ge sampe (isochronal annealing, 30 min, argon atmosphere). (After Marie et al. [20]).

With respect to the defect introduction rate $r_T=\partial N_T/\partial\Phi$ in room temperature irradiated Ge, some detailed studies have been performed [21-23]. In many instances, a linear increase of the trap concentration with increasing fluence Φ has been observed. When monitoring the conductivity of irradiated Ge as a function of ion fluence, first a reduction is observed until a minimum occurs, which corresponds with type inversion e.g. from n- to p-type, and subsequently the conductivity increases again [21]. An example is shown in Fig. 1.7 [21]. The change in resistivity is definitively due to the creation of stable radiation centers, on the one hand, and to the deactivation of dopants, incorporated in V-Donor complexes, on the other. From such conductivity measurements, the introduction rates can be extracted, yielding the result of Fig. 1.8 [21].

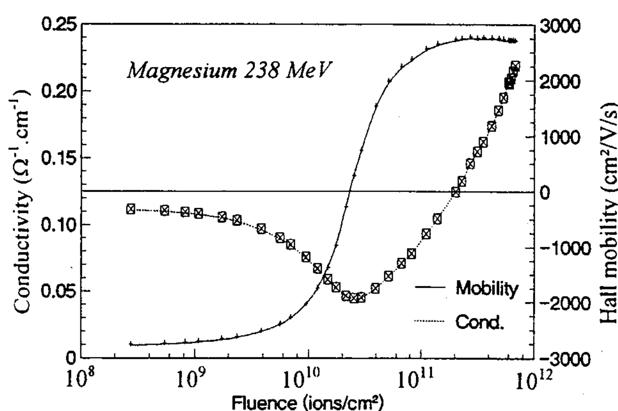

Fig. 1.7. Conductivity-fluence and Hall mobility-fluence experimental curves for n-type Ge (starting concentration 2.4×10^{14} cm^{-3}). (After Marie et al. [21]).

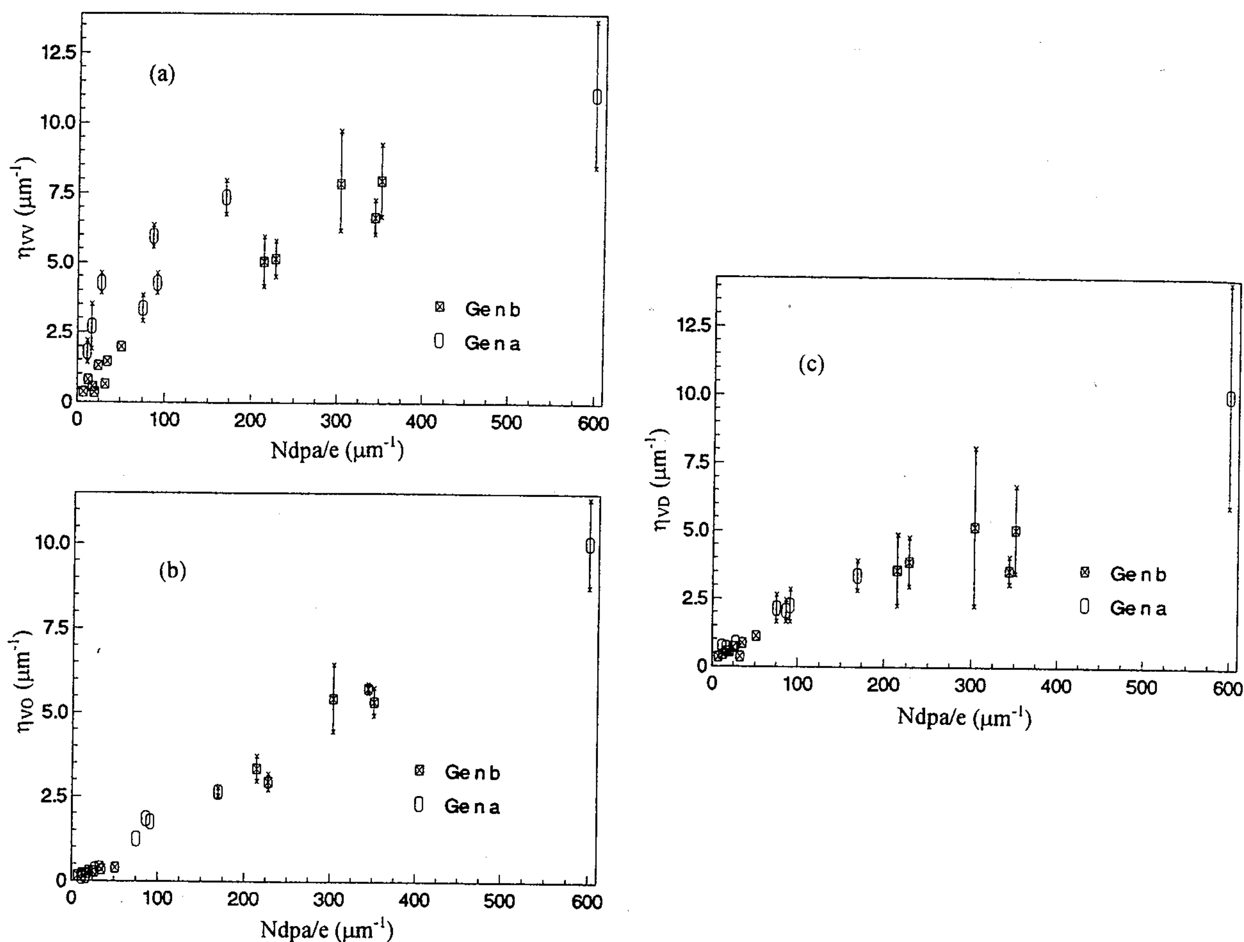

Fig. 1.8. Individual introduction rate of each defect versus Ndpa/q for the two kinds of n-type Ge material: (a) divacancy, (b) vacancy-oxygen complex, (c) vacancy-doping impurity complex. a=4.15×10^{14} cm^{-3} and b=2.4×10^{14} cm^{-3}.(After Marie et al. [21]).

It is evident from Fig. 1.8 that the divacancy has the largest introduction rate, saturating at a level of around 0.75×10^{-3} cm^{-1}. This observation has been confirmed by neutron irradiation of n- and p-type high purity Ge as well [23]. Horizontally, the theoretical number of primary defects created per incident ion and per unit length is represented. It is clear that the introduction rates depend on the doping density of the material [15,21-23]. The type inversion is thought to be mainly due to the V-O complex, while the decreasing fraction of the observed defects with respect to the initially created defects (Fig. 1.9) is due to the behavior of the divacancy (see Fig. 1.8a).

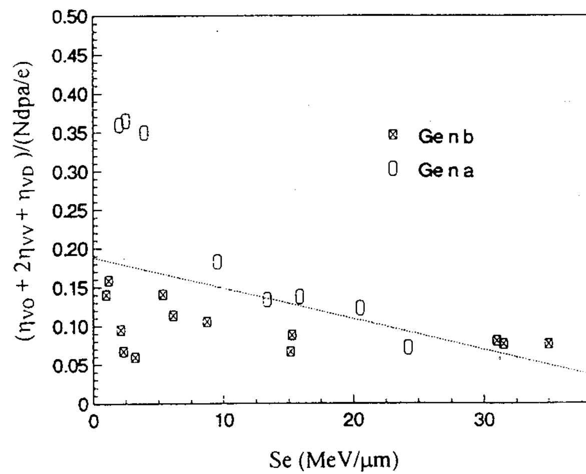

Fig. 1.9. Fraction of observed to created defects versus electronic stopping power S_e. (After Marie et al. [21]).

1.2.2 Low Temperature Particle Irradiation

Since many of the envisaged applications of Ge and Ge-devices are at low temperatures, it is important to have an idea about the cryogenic radiation damage. Originally, 4.2 K [26-29] and 77 K [30-31] irradiations were performed to investigate the stability of the primary displacement damage (vacancies and interstitials). Different annealing stages have been identified: stages at ≈35 K and 65 K are ascribed to the mobility of the interstitial [20], while the vacancy becomes unstable at about 90 K in n-type Ge and around 170 K in p-type Ge [20]. The mobility of vacancies and interstitials thus depends on the position of the Fermi level (charge state of the vacancy) and will reduce going from heavily doped n-type, over high purity material to p-type Ge.

More recent experiments at low temperature are based on DLTS measurements and have been performed on 4.2 K electron irradiated Ge [15] and on neutron irradiated high-purity Ge [22-23]. It has been found that the induced defects are totally different from the room temperature ones [15,23]. The introduction rate strongly depends on the doping level: while values in the range 10^{-3} to 10^{-2} cm^{-1} are found for ≈10^{15} cm^{-3} doped n-type material, lower values (10^{-5} to 10^{-4} cm^{-1}) have been obtained for 10^{13} cm^{-3} n-Ge [15]. In other words, the lower the doping density, the smaller the introduction rate. This could point to a higher mobility of the primary defects in the lowly doped material. Additionally, the chance of getting trapped by a dopant atom also reduces in high resistivity Ge. It has also been noted that 90 % of the created damage, which is derived from the deactivated dopant concentration, is not found by DLTS. It is believed that this missing damage could be primary vacancy-interstitial pairs, which recombine at 65 K [15]. Furthermore, two levels occurring at E_C-0.12 eV are associated with the Ge interstitial or complexes involving an interstitial. Another vacancy related level in the range E_C-0.1 to -0.2 eV anneals at ≈100 K [15].

The annealing stages in n- and p-type high-purity Ge after 10 K fast neutron irradiation are shown in Fig. 1.10a and 1.10b, respectively. Annealing stages at ≈40 K and 100 K in n-type Ge are clearly visible and in agreement with the earlier results by Swanson [32]. They correspond to the interstitial mobility (35 K) and the vacancy mobility (95 K) region. In p-type material, on the other hand, no significant annealing was found below ≈175 K. Therefore, it is concluded that the primary defects in n-type Ge are stable up to ≈35 K and up to ≈160 K in p-type material [23]. Furthermore, it has been observed that the total introduction rate of primary defects upon 10 K neutron exposure is a factor 2 lower than the theoretical estimates (50 cm^{-1}). This is explained by the fact that even at low temperatures, the interstitials are mobile and part of them escape and recombine. For room temperature irradiations, the measured total introduction rate is in the range 1.2 cm^{-1} (p-Ge) to 1.9 cm^{-1} (n-Ge), suggesting p-type material to be more radiation tolerant. It should also be remarked that for p-Ge, the introduction rate after low temperature irradiation and anneal up to 320 K is slightly larger than the room temperature rate. This means that warming up a Ge detector operating in a radiation environment at cryogenic temperatures can have adverse effects on the performance. In many cases, it is better to keep the system cold.

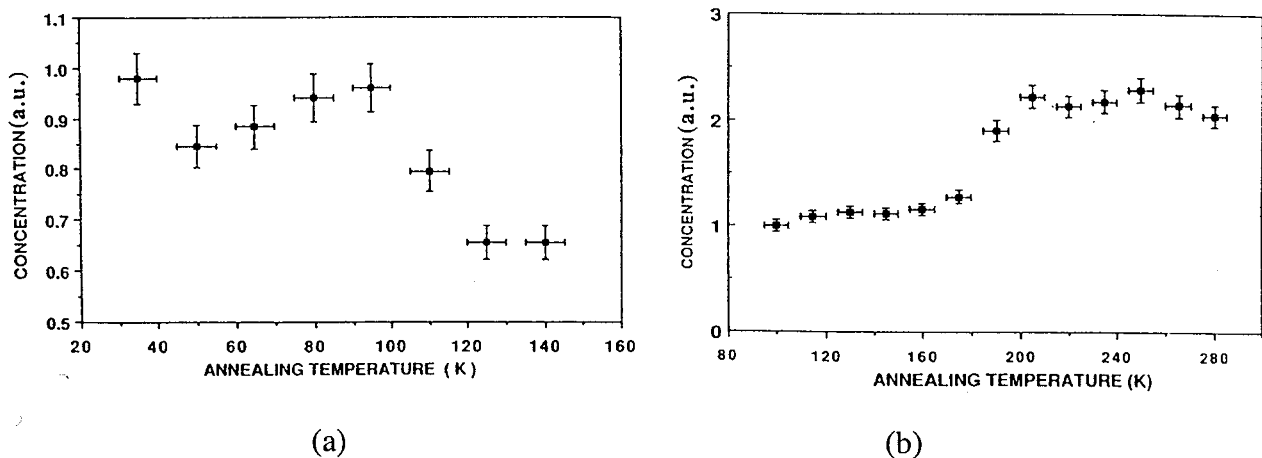

Fig 1.10. (a) Net shallow donor concentration vs. annealing temperature in n-type material irradiated at 10 K (10 min at each temperature). The reference value is the one taken just after irradiation (initial carrier concentration 10^{10} cm^{-3}) for a neutron fluence of 10^{10} cm^{-2}. (b) Net shallow acceptor concentration vs. annealing temperature in p-type material sample showing the presence of the 200 K annealing stage. The reference value is the one taken just after annealing at 80 K. The neutron fluence is 1.1×10^{10} cm^{-2}.(After Fourches et al. [23]).

It has finally been observed that the dominant stable radiation defect at room temperature is the divacancy, as illustrated by Fig. 1.11 [23]. It also shows the linear increase of the concentration with neutron fluence. For higher fluences, however, overlap of the damage clusters occurs, giving rise to disordered regions with a very high density of

defects. This causes the DLTS peaks to broaden and to take the shape of a continuum of states, which are not homogeneous distributed in the volume of the material.

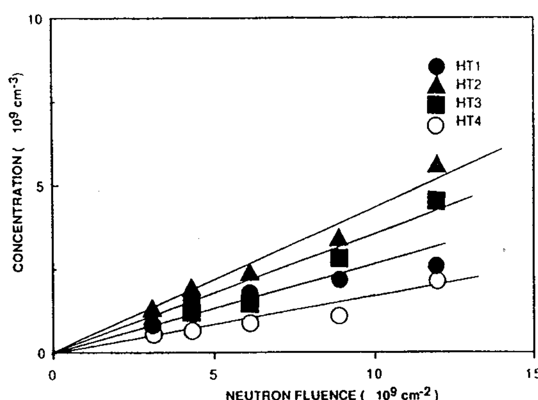

Fig. 1.11. Concentration of hole traps created by irradiation at room temperature in p-type material vs. neutron fluence. (After Fourches et al.[23]).

1.3 Ionization Damage in Ge

So far, only one type of Ge-based devices has shown evidence to suffer from ionization damage [2,33]. It has namely been observed that stressed Ge:Ga photoconductors degrade even for a very low back-ground dose of high-energy γ-quanta (< 4 rad). This results in an increase in the conductivity (Fig 1.12a) and a reduction of the breakdown voltage (Fig. 1.12b). Hits by a few high-energy photons or particles can change the responsivity of the detector, operating in the 1 - 4.2 K regime, by decades. It is believed that the induced changes are related to the creation of electron-hole pairs in the material, which can not escape the detector and, therefore, get trapped in the donor and acceptor sites, respectively. This changes the compensation ratio and the conductivity. An alternative contact configuration has been proposed, to eliminate the barriers at the p^+ contacts, in order to remove the created minority carriers from the volume of the detector [33].

1.4 Conclusions

It is clear from the above that the nature of the radiation-induced defects in Ge is far less well-established than in silicon. The reasons are the lower technological relevance and interest and the difficulty to apply analytical techniques which have proven succesful for silicon (EPR,...). From a fundamental viewpoint, a lot of questions remain open regarding for example the divacancy: is the same difference in peak height observed for the two acceptor levels in n-Ge in the damage peak region after high-energy proton, ion or neutron irradiation? Does the concentration roll-off to the surface occur as in silicon? Furthermore, although there are some indications of its role, no real systematic study of the impact of the substrate parameters (crystal growth, doping density and type, O, C and H content,...) on the radiation damage has been performed so far. From a viewpoint of space applications, it would be good to have some data on high-energy proton irradiations, which are lacking for

the moment. Also a systematic study of the damage profile, using for example high purity starting material would allow to compare the defects in the flat tail region with the damage peak region.

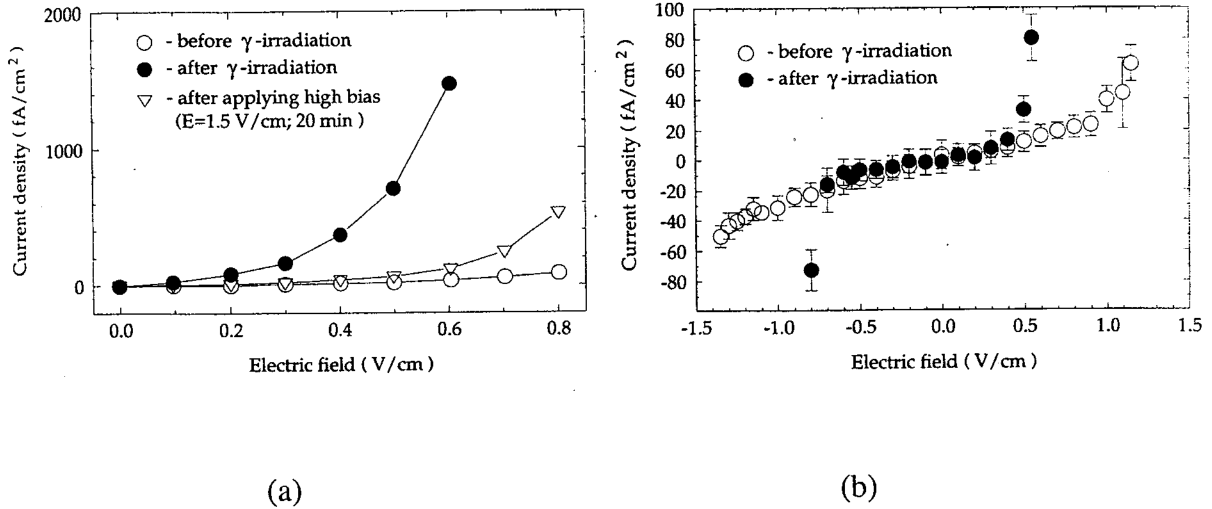

(a) (b)

Fig. 1.12. (a) Effect of low-dose γ-irradiation on the current-voltage characteristics of stressed Ge:Ga detectors at the temperature of 1.65 K and photon background of 10^8 cm^{-2} s^{-1}. A temperature increase to 4.2 K entirely suppresses the radiation-induced changes, and the detectors exhibit the same current-voltage characteristics as before irradiation. Increasing the electric field above the breakthrough does not completely suppress the effects. (b) Effect of γ-irradiation on the value of the breakdown field in the stressed Ge:Ga detector at T=1.65 K and the photon background <10^6 cm^{-2}s^{-1}. The radiation-induced shift is associated with the decrease in the effective compensation ratio of the samples after γ-irradiation. (After Patrashin et al. [2]).

References

[1] J. Wolf, R. Katterloher, D. Lemke, U. Grözinger, L. Hermans, O. Frenzl, D. Engemann, J. Beeman and M. Fabbricotti, "Far-infrared stressed Ge:Ga array for FIRST", in: *Proc. 30th ESLAB Symposium on Submillimetre and Far-Infrared Space Instrumentation*, ESA **SP-388**, pp. 25-28 (1996).

[2] M. Patrashin, B. Fouks, U. Grözinger, D. Lemke and J. Wolf, "Residual conductivity of stressed Ge:Ga photoconductors after low-dose gamma irradiation", J. Appl. Phys. **82**, 1450 (1997).

[3] J.W. Beeman, W.L. Hansen and E.E. Haller, "Extrinsic germanium photoconductors for far-IR astronomy: Research results and works in progress", in: *Proc. 30th ESLAB Symposium on Submillimetre and Far-Infrared Space Instrumentation*, ESA **SP-388**, pp. 21-24 (1996).

[4] E.E. Haller, K.M. Itoh and J.W. Beeman, "Neutron transmutation doped (NTD) germanium thermistors for sub-mm bolometer applications", in: *Proc. 30th ESLAB Symposium on Submillimetre and Far-Infrared Space Instrumentation*, ESA **SP-388**, pp. 115-118 (1996).

[5] E. Simoen, P. Clauws, J. Broeckx, J. Vennik, M. Van Sande and L. De Laet, "Correlation between DLTS-measurements and the performance of high purity germanium detectors", IEEE Trans. Nucl. Sci. **NS-29**, 789 (1982).

[6] A. Blondeel, PhD Thesis, Universiteit Gent (1998).

[7] E. Simoen, PhD Thesis, Universiteit Gent (1985).

[8] M.A. Chung, D.L. Meier, J.R. Szedon and J. Bartko, "Electron radiation and annealing of MOCVD GaAs and GaAs/Ge solar cells", in: Proc. 20st Photovoltaic Specialists Conference, The IEEE (New York), pp. 924-929 (1988).

[9] B.E. Anspaugh, "Proton and electron damage coefficients for GaAs/Ge solar cells", ", in: Proc. 22nd Photovoltaic Specialists Conference The IEEE (New York), pp. 1593-1598 (1991).

[10] P.W. Marshall, C.J. Dale, G.P. Summers, E.A. Wolicki and E.A. Burke, "Proton, neutron and electron-induced displacement damage in germaniun", IEEE Trans. Nucl. Sci. **36**, 1882 (1988).

[11] J.J. Goubet, D. Stievenard, D. Mathiot and M. Zazoui, "Electron-irradiation-induced defects in Si-Ge alloys", Phys. Rev. B **46**, 10113 (1992).

[12] C. Claeys and E. Simoen, "Literature study on radiation effects in cryogenic electronics", Deliverable D1, WO 1938/96/NL/LB, Document no P35284-IM-RP-0003 (1997).

[13] G.D. Watkins, "Electron paramagnetic resonance of point defects in solids, with emphasis on semiconductor", in Point Defects in Solids, Eds J.H. Crawford Jr. and L.M. Slifkin, Plenium Press, Chapter 4 (1975).

[14] F. Poulin and J.C. Bourgoin, "Characteristics of the electron traps by electron irradiation in n-type germanium", Phys. Rev. B **26**, 6788 (1982).

[15] P.M. Mooney, F. Poulin and J.C. Bourgoin, "Annealing of electron-induced defects in n-type germanium", Phys. Rev. B **28**, 3372 (1983).

[16] K. Itoh and J.W. Corbett, "Interaction of point defects with hydrogen in germanium", Jpn J. Appl. Phys. **22**, L724 (1983).

[17] N. Fukuoka and H. Saito, "The hole trapping defects in irradiated germanium as studied by DLTS", Physica **116B**, 343 (1982).

[18] S.S. Li, C.G. Choi and R.Y. Loo, "Studies of radiation-induced defects in one-MeV electron and low-energy proton irradiated germanium and $Al_xGa_{1-x}As$ p-n junction solar cells", in: Proc. 18th Photovoltaic Specialists Conference, The IEEE (New York), pp. 640-645 (1985).
[19] N. Fukuoka, M. Honda, Y. Nishioka, K. Atobe and T. Matsukawa, "Property of radiation-induced defects in germanium single crystals", Jpn J. Appl. Phys. **34**, 3204 (1995).
[20] P. Marie, M. Levalois and P. Bogdanski, "Irradiation-induced defects in n-type germanium", J. Appl. Phys. **74**, 868 (1993).
[21] P. Marie, M. Levalois and E. Paumier, "Swift-heavy-ion induced damage in germanium: An evaluation of defect introduction rates", J. Appl. Phys. **79**, 7555 (1996).
[22] N. Fourches, A. Huck, G. Walter and J.C. Bourgoin, "Fast neutron irradiation induced defects in high purity germanium", Materials Science Forum **38-41**, pp. 1233-1238 (1989).
[23] N. Fourches, G. Walter and J.C. Bourgoin, "Neutron-induced defects in high-purity germanium", J. Appl. Phys. **69**, 2033 (1991).
[24] J.J. Goubet and D. Stievenard, "Annealing study of electron irradiation-induced defects in SiGe alloys", Appl. Phys. Lett. **66**, 1409 (1995).
[25] M.-A. Trauwaert, "Radiation and impurity related deep levels in Si: A deep level transient spectroscopy study correlated with other spectroscopic techniques", PhD Thesis, Katholieke Universiteit Leuven, Appendix C (1995).
[26] G.W. Gobeli, "Alpha-particle irradiation of Ge at 4.2 K", Phys. Rev. **112**, 732 (1958).
[27] J.W. Mackay and E.E. Klontz, J. Appl. Phys. **30**, 1269 (1959).
[28] T.A. Callcot and J.W. Mackay, Phys. Rev. **161**, 692 (1967).
[29] J. Bourgoin and F. Mollot, "Behaviour of primary defects in electron-irradiated germanium", Phys. Stat. Sol. B **43**, 343 (1971).
[30] N. Fukuoka and H. Saito, Jpn. J. Appl. Phys. **13**, 1524 (1974).
[31] N. Fukuoka and H. Saito, Jpn. J. Appl. Phys. **15**, 237 (1976).
[32] M.L. Swanson, Can. J. Phys. **44**, 2181 (1960).
[33] M. Patrashin, H. Shibai, H. Okuda, N. Hiromoto, M. Fujiwara and B. Fouks, "Suppression of the radiation-induced effects in Ge:Ga detectors", *Proc. 30th ESLAB Symposium on Submillimetre and Far-Infrared Space Instrumentation*, ESA **SP-388**, pp. 29-32 (1996).

2. RADIATION DAMAGE IN SiGe MATERIAL AND DEVICES

The Si-Ge alloys form a complete series of solid solution and, therefore, allow performing band-gap engineering between 1.12 eV (Si) and 0.74 eV (Ge). This unique feature, together with the compatibility with silicon processing offers very promising perspectives for a wide-scale application of $Si_{1-x}Ge_x$ hetero-epitaxy (x: the Ge fraction) in next generation ULSI technologies. Therefore, in a first section, the material properties and SiGe based devices will be briefly outlined. Next, a summary is given on the radiation damage studies in strained and relaxed SiGe layers and in bulk SiGe. Additional information can be retrieved from the study of processing induced radiation damage, for example caused by plasma etching, metal deposition or ion implantation. Finally, the radiation tolerance of some recent devices and technologies will be discussed.

2.1 SiGe Properties and Applications

2.1.1 Material Properties

As already mentioned, Si-Ge alloys can be formed continuously between x=0 and x=1. However, due to the larger atomic radius of Ge (1.23 Å versus 1.17 Å for Si), some strain is introduced in the lattice when more and more Ge atoms are incorporated. The lattice mismatch can amount to 4.2%. This results in a reduction of the alloy band-gap E_g, as shown in Fig. 2.1 [1]. Most of the band-gap shift occurs for the valence band maximum, while the conduction band minimum shows only a minor shift (Fig. 2.2a) [2]. However, above 15 atomic % Si (x=0.85), the position of the band-gap minimum shifts from the Ge-like L points (<111>), to the Si-like X points (bottom along <100> directions), which has consequences for the bulk material properties [3-4]. The addition of a fraction *y* of C to form ternary $Si_{1-x-y}Ge_xC_y$ alloys yields an additional degree of freedom for band-gap engineering in this sense that the band-gap change is now divided between the valence and conduction band [5]. This might be of interest for the fabrication of n-channel heterostructure Field Effect Transistors, or pnp heterojunction bipolar transistor (HBT).

Recently, interest has developed for the crystal growth of bulk SiGe by the Czochralski (Cz) technique [3,6], whereby potential applications could be solar cells [7-8], or substrates for the deposition of epitaxial layers. However, most efforts are devoted to the incorporation of strained or relaxed SiGe layers in silicon processing. An epitaxial layer is obtained either by Molecular Beam Epitaxy (MBE) or by Ultra High Vacuum (UHV) or Low-Pressure Chemical Vapor Deposition (LPCVD). For most ULSI applications, thin (100 nm range) strained layers on silicon are necessary. The strain comes from the lattice mismatch between the Si-Ge alloy and the silicon substrate, which increases for increasing x. For a thickness below a certain critical thickness h_c, the layer grows pseudomorphically; above h_c, the strain relaxes, giving rise to the formation of dislocations, which may cross the layer (threading dislocations). Figure 3 shows the critical thickness versus the mismatch. The presence of these dislocations degrades not only the structural but also the electrical and optical integrity of the layer. Furthermore, as can be seen from Fig. 2.3, h_c reduces with temperature T, implying that a strained layer deposited at a certain temperature will relax when heated up sufficiently long at a higher temperature. This is one of the important

limitations for the use of Si-Ge in ULSI technologies, requiring a reduced thermal budget after epitaxy. Fortunately, this goes along with the on-going effort for technology scaling to deep submicron dimensions. Another handicap is the difficulty in forming a good stable oxide on Si-Ge. In most cases, this is solved by the deposition of a thin Si cap layer, which is then thermally oxidized. In some cases, a relaxed buffer layer is introduced in between the silicon substrate and the strained layer, confining the dislocations to the buffer layer.

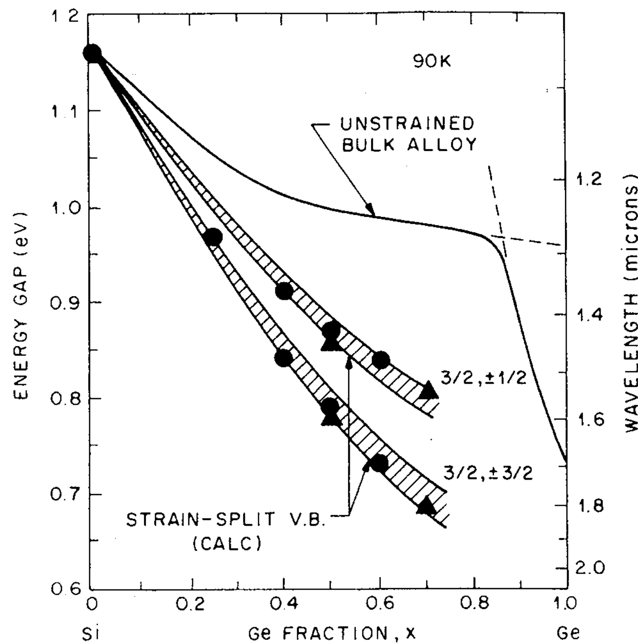

Fig. 2.1. Summary of energy-gap values at 90 K. The double points at the same value of x correspond to a splitting of the valence band. The calculations showing the strain-split valence band are indicated by the cross-hatched bands. (After Lang et al. [1]).

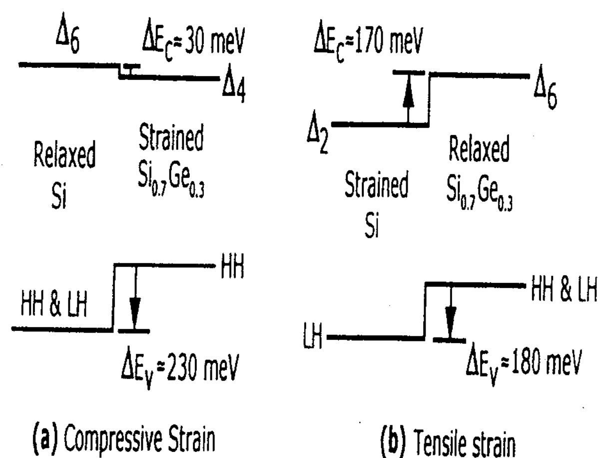

Fig. 2.2. Band alignments between Si and $Si_{0.70}Ge_{0.30}$ on two substrates: (a) Si and (b) $Si_{0.70}Ge_{0.30}$. (After Maiti et al [2]).

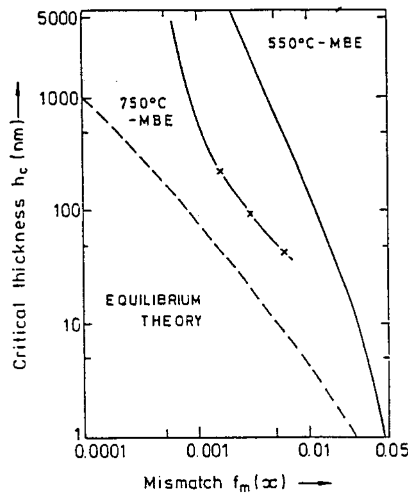

Fig. 2.3. Critical layer thickness h_C for misfit dislocation generation against mismatch parameter $f_m(x)$. (After Jain and Hayes [4]).

For other applications (solar cells, relaxed buffer layer, detectors, sensors,...) or for materials' characterization related purposes thicker, relaxed epi-layers may be useful. However, in order to limit the formation of threading dislocations and to preserve a good quality layer, adapted growth techniques have to be applied. In that case, the final layer is deposited on an intermediate one, whereby the Ge content is gradually (i.e. step-wise) changed from 0 at the silicon interface, towards the desired value, allowing for a gradual strain relaxation. This limits the threading dislocation density to reasonable values ($\leq 10^5$ cm^{-2} for x=0.3) [9], compared with early material grown without graded buffer (range 10^8 to $10^{12} cm^{-2}$). The latter densities are too high to make the material appropriate for ULSI applications. The combination of the graded (stepped *x*) and relaxed layer (constant *x*) is often called a virtual substrate.

Due to the continuous improvement in the SiGe epitaxial layer quality, one should be careful in comparing early results with more recent reports, with respect to irradiation-induced defects and radiation hardness. Some of the inconsistencies and contradictions could be explained by the presence of grown-in extended defects.

2.1.2 Applications.

The most successful application so far, where SiGe heterostructures realized a breakthrough to commercial products is in the field of HBTs (for an overview see e.g. [10]). Replacing the epitaxial silicon base by a SiGe heterojunction, as schematically illustrated in Fig. 2.4, offers several important advantages. First of all, due to the band offset, higher current gain $\beta = I_C/I_B$ values can be reached, with I_C the collector and I_B the base current. This is because the flow of holes from base to emitter is reduced owing to the barrier in the valence band. Second, the hole mobility in the SiGe layer is significantly higher than in a p-Si base, increasing thus the base transit time and hence, the maximum oscillation frequency

f_{max} and the cutoff frequency f_T of the devices. This renders HBTs particularly attractive for high-frequency (microwave) applications, where they become a serious competitor for the III-V based technologies, pushing continuously the limits upwards. This could be of importance for future satellite communications systems. Implementing SiGe in BiCMOS opens up the market for mixed mode analog-digital applications, like for example the huge portable telecommunications market. Finally, the HBT can be optimized for cryogenic operation down to 77 K or even 4.2 K, a region where the classical silicon BJT is no longer operational [10]. It has in fact been shown that for a cryogenic SiGe HBT the performance at 77 K supersedes the one at room temperature in many aspects, similar as for a cooled MOSFET. In order to benefit fully from its potential, it is mandatory to use a graded Ge strained epitaxial layer, as shown in Fig. 2.5, for example, whereby the Ge fraction lies typically in the range 8 to 16 %.

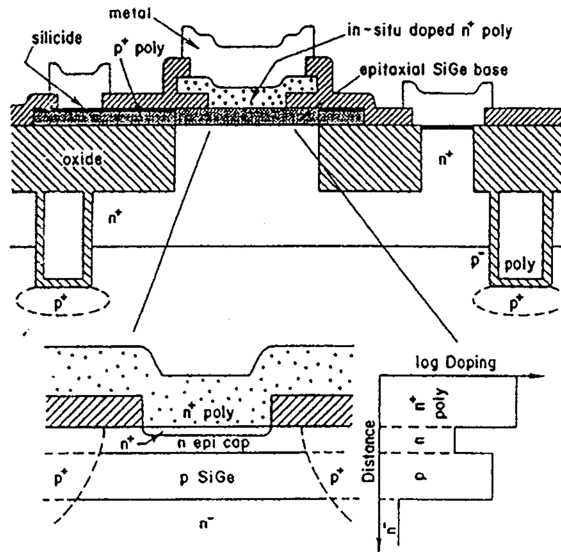

Fig. 2.4. Schematic cross section of the self-aligned epitaxial emitter-cap SiGe technology which has been optimized for 77 K operation. (After Cressler [10]).

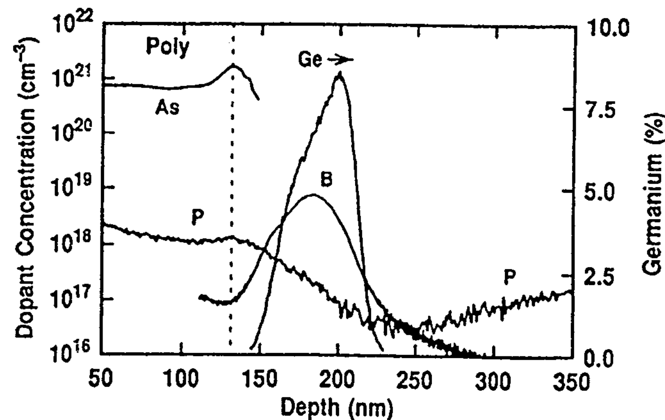

Fig. 2.5. Measured SIMS impurity profile for the epitaxial emitter-cap SiGe technology. (After Cressler [10]).

The enhancement of the hole mobility in p-SiGe can also be exploited for the development of high-mobility p-channel heterostructure (or quantum well) MOSFETs [11-12], rendering them attractive for high-speed applications and making the deep submicron p-channel device more compatible with its n-channel counterpart. A next step could be the development of SiGe based CMOS, using the layer scheme of Fig 2.6a [12] or Fig. 2.6b [13], corresponding to a strained silicon layer buried or surface channel, respectively. In recent years even more exotic concepts have been proposed and demonstrated, which could lead to future deep submicron (sub 100 nm) technologies, like MODFETs [2], vertical MOSFETs [14] or strained p-Si p-MOSFETs [2]. However, most of these devices and technologies should be considered as exploratory and products are expected to see the market somewhere during the next decade or so. The same applies for many of the so-called quantum devices [15] like resonant tunneling structures and hot-carrier transistors.

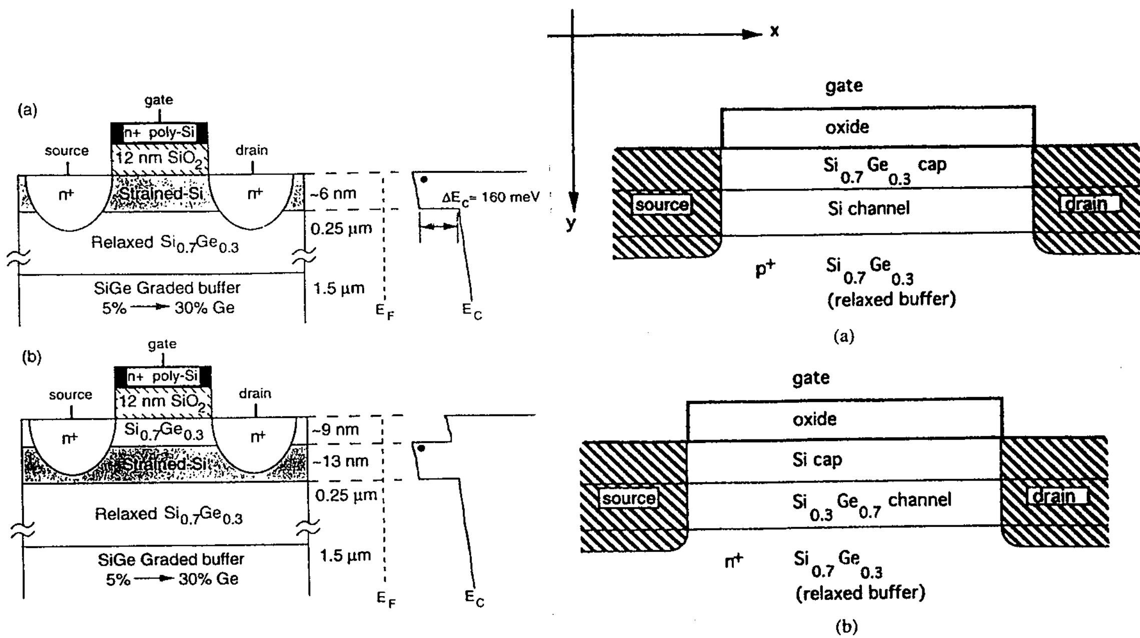

Fig. 2.6. Schematic representation of a strained-Si n-channel (a) and a strained SiGe p-channel (b) MOSFET (left) (After O'Neill et al. [12]). The structures on the left correspond to a strained-Si surface channel (a) and a buried-channel (b) n-MOSFET. (After Welser et al. [13]).

SiGe has also large potential as photosensitive material, enabling the development of infrared Schottky barrier photodetectors [16-17] and photodiodes [18-19]. Less successful are the attempts to develop SiGe based Light Emitting Diodes, although some progress has been made using Er-doped material (see e.g. Ref. 20).

2.1.3 IMEC Activities

Since the mid-80ties IMEC has been involved in the development and study of the epitaxial deposition of SiGe layers. Nowadays, this expertise is being used for the development of a 0.35 μm BiCMOS technology, implementing a graded SiGe base. First devices are expected to become available this year. In addition, a new device concept is being developed at IMEC, based on the vertical MOSFET depicted in Fig. 2.7 [14]. The advantage of this device is that scaling below 100 nm becomes relatively easy, without the use of complex and expensive lithography tools. In addition, simulations point out that short-channel effects like the drain-induced barrier lowering, the threshold voltage V_T roll-off, etc. are reduced. This has recently been confirmed by experimental results [14], so that vertical devices should be a viable candidate for sub-0.1 μm CMOS. Efforts are also being spent to produce Si-Ge based integrated sensors and detectors, like a room temperature bolometer [21]. Finally, research is being devoted to study the potential of bulk and epitaxial SiGe solar cells. It has for example been demonstrated that a 14 % efficiency solar cell can be fabricated from bulk SiGe wafers, grown by Union Minière in Olen [8].

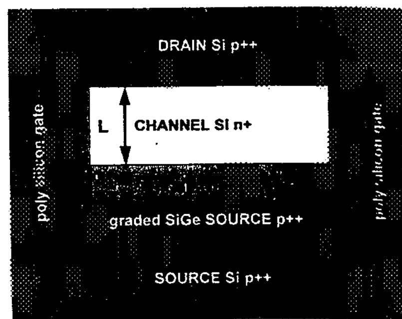

Fig. 2.7. Schematical representation of the vertical MOSFET. (After De Meyer et al. [14]).

2.2 Radiation Damage in SiGe

2.2.1 Radiation Damage in Ge Doped Si and in Bulk SiGe

There has been a suspicion that the presence of the isoelectronic substitutional impurities Ge and Sn in silicon might yield a radiation hardening effect. This is related to the fact that the larger foreign atom introduces a compressive strain in the lattice and therefore will attract vacancies when created, to form Sn-V or Ge-V pairs for example. This process immobilizes the latter, so that they are not available for defect reactions with other impurities and thus creating stable secondary irradiation damage. Another consequence may be that the recombination with interstitials during the irradiation will be enhanced. The fact that no stable isolated Ge-vacancy complexes can be formed in silicon at room temperature may be in support of this idea [22-23].

It has for example been demonstrated that in Sn-doped Si the introduction rate of the divacancy V-V center is at least a factor 10 lower, compared with undoped Si [24]. Similar

evidence exists for Ge: it has for example been observed that the formation of the A center in γ-irradiated Si:Ge, with a Ge concentration in the range 10^{18}-10^{20} cm^{-3} is retarded [23]. Nevertheless, the issue of Ge-doping radiation-hardening is controversial and conflicting results have been reported [25]. Careful analysis of the available evidence learns that there exists a threshold Ge concentration above which a hardening effect does exist [25]; the same applies for Sn-doping [24]. Depending on the electrical parameter considered, this [Ge] threshold may be around $7.5x10^{19}$ cm^{-3} (β of BJT) or at •10^{20} cm^{-3} (recombination lifetime) [25]. Below that, no effect is seen or even a softening of the devices occurs. This could be due to the fact that the large Ge atom not only attracts vacancies but can have a cluster ('cloud') of other small impurities like oxygen or carbon, which interact with V to form stable defects. For low Ge concentration, this adverse effect may dominate the enhanced primary point defect annihilation ascribed to the presence of Ge atoms [25].

The formation and thermal stability of the vacancy and vacancy-related defects has been studied in bulk Cz SiGe by the positron annihilation technique [26-27]. It has been observed that an abrupt change in the bulk positron lifetime occurs for a Ge fraction of 0.8 to 0.83, in agreement with the shift in the conduction band minimum from the L (Si) to the X point (Ge). After 10^{18} cm^{-2} 3 MeV electron exposure no stable vacancy clusters were observed for Ge rich alloys. The absence of vacancy clusters for x>0.8 can be explained by assuming that both the monovacancy and maybe the divacancy are unstable in "Ge" and disappear from the crystal before agglomeration to quadrivacancies. In other words, the mobility of the vacancy depends on the electronic structure of the crystal and is higher in Ge-rich crystals compared with Si-rich alloys. The lower stability of vacancy-related defects in Ge compared with Si can also be derived from the lower annealing temperatures reported in Table 1.2 of the previous chapter.

For Si-rich alloys, on the other hand (x•0.37), it is expected that the V-Impurity and divacancies will be the major defect species. For the intermediate Ge range (0.6•x•0.8), the higher positron lifetimes suggest the presence of larger vacancy clusters. Furthermore, from thermal annealing experiments, it is concluded that the formation of larger vacancy clusters due to the agglomeration of single vacancies is inhibited due to the presence of Ge. This effect is similar as for heavily doped Si compared with undoped material, where vacancy-dopant complexes retard the vacancy clustering. This role is overtaken here by the Ge, which is assumed to pair with the vacancy for reasons of strain compensation. This is also in line with the retarded A-center formation found in Ge doped silicon [23], whereby the created vacancies are trapped at specific sites, so that they are not available for pairing with interstitial oxygen. In addition, these trapped vacancies are not necessarily electrically active, so that it may not be possible to detect them by DLTS, for example.

2.2.2 Radiation Damage in Relaxed SiGe Layers

Radiation-induced defects in relaxed SiGe layers have been studied by a number of groups, after both high-energy electron [28-29] and proton irradiation [30-32]. Early results obtained on low-quality n-type material are somewhat inconsistent, allowing no clear identification of the observed trap levels [28-29]. More recent experiments on better quality material deposited on a graded buffer layer have enabled a more firm identification of the most prominent radiation-induced defects [30-32]. For the case of n-type material spectra for

different Ge fractions are summarized in Fig. 2.8 [30-31]. Some clear trends are evident from Fig. 2.8: first, the concentration of defects for the same irradiation conditions (2 MeV protons at a fluence of $1.5x10^{12}$ cm^{-2}) reduces strongly for increasing x. The introduction rate of trap T4 reduces by a factor 4 in going from a Ge content from 5 % (r_T=90 cm^{-1}) to 25 % (r_T=20 cm^{-1}). This strongly suggests a hardening effect due to the presence of Ge, in line with the above observations.

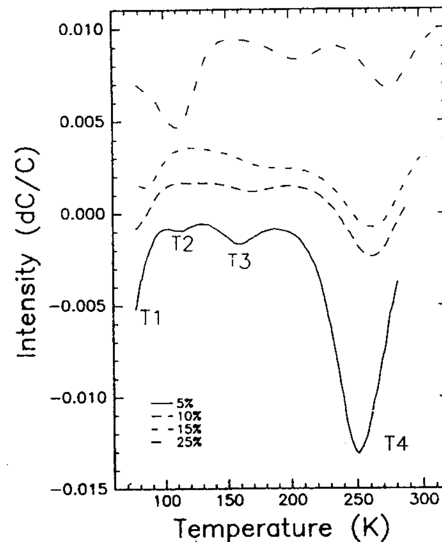

Fig. 2.8. DLTS spectra of $Si_{1-x}Ge_x$ epitaxial layers of the mentioned compositions after irradiation with identical fluences of 2 MeV protons. The spectra were all recorded using a repetition rate of 1 kHz. (After Kringhoj and Nylandsted Larsen [30]).

A second conclusion to be drawn from Fig. 2.8 is that the same basic radiation defects are present, whereby the level position is composition dependent. This is derived from the shift of the DLTS peak maximum with x to higher temperatures for T1 to T4. However, when analyzing in more detail the Gibbs free energy of the defects, it is concluded that the energy position is not changing with respect to the conduction band (Fig. 2.9) [30]. Also the electron capture cross section σ_n for T4 is independent of alloy composition, yielding an average value of $6\text{-}8x10^{-16}$ cm^2. This order of magnitude suggests an acceptor nature of the trap T4, which is, therefore pinned to the conduction band. Finally, from the constant full width at half maximum of the DLTS peaks, it is concluded that no alloy broadening occurs in the case of T4. Based on the above evidence, peak T4 has been identified as the Sb-V pair (Sb doped n-type material). It is speculated that T3 may be the V-$V^{=/-}$ charge state of the divacancy, while the origin of the other trap levels is unclear.

The level T4 corresponds most likely with the P2 peak of Goubet and Stievenard [29], observed after 10^{15} cm^{-2} 1.5 MeV electron irradiation of 30 % Ge relaxed films, albeit that the material is here phosphorous doped n-type SiGe (P-V centers). Their P1 level is

assigned to the doubly negative charge state of V-V. The corresponding defect parameters have been summarized in Table 2.1. In addition, the authors have investigated the isochronal (10 min) annealing behavior of these traps, in order to more firmly establish the identity. The result is shown in Fig. 2.10, whereby P1 anneals at 560 K and P2 at 470 K. Note also the increase of P1 occurring at the annealing stage of P2. Like for pure silicon, it is believed to correspond to the clustering of two vacancies, released from the P-V centers (P-doped n-type material).

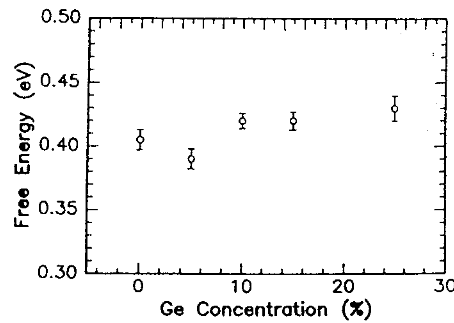

Fig. 2.9. Gibbs free energy of the T4 defect as a function of composition. The uncertainties are statistical uncertainties only; the systematic uncertainties are estimated to be of the order of 5 %. (After Kringhoj and Nylandsted Larsen [30]).

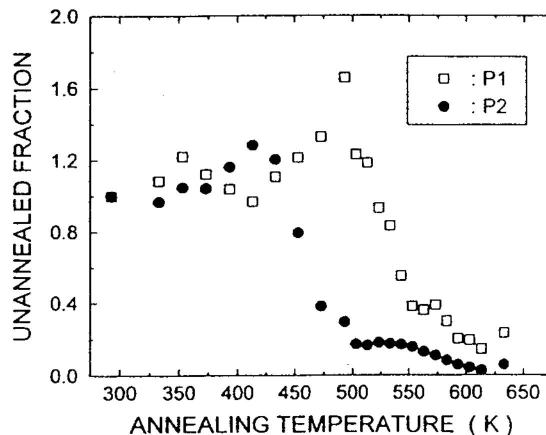

Fig. 2.10. Unannealed fraction of the defects P1 and P2 vs. the temperature of isochronal annealing for 10 min under He atmosphere. (After Goubet and Stievenard [29]).

The situation in proton irradiated relaxed p-type SiGe layers is somewhat more complex [32], as illustrated by Fig. 2.11. Beside two hole traps H1 and H2 found for all x, an additional near mid-gap center is found for x•5%. In this case, the level positions tend to shift towards lower temperature for increasing x, which is opposite to the shift observed in Fig. 2.8. It should be remarked, however, that in Fig. 2.11 hole emission towards the valence

band is monitored, while in Fig. 2.8, electron emission towards the conduction band is observed. From the shift of the activation enthalpy with composition, shown in Fig. 2.12 for the levels H1, H2 and H3, it is concluded that the trap levels are also pinned to the conduction band, i.e. their relative energy position with respect to the conduction band minimum remains fixed. The corresponding defect parameters can be found in Table 2.1.

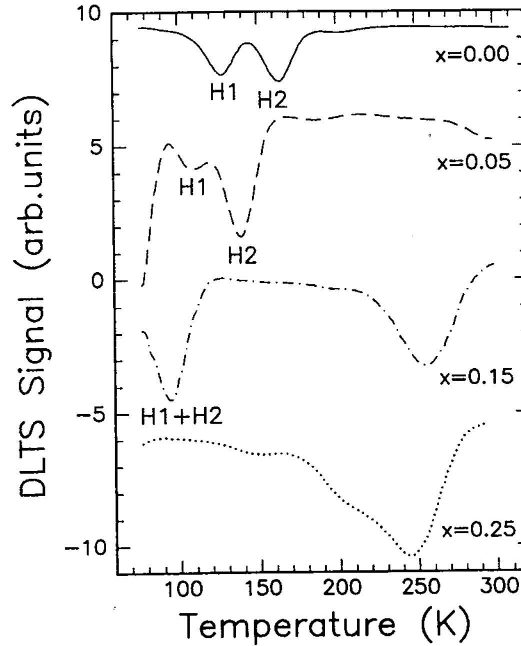

Fig. 2.11. DLTS spectra from 2 MeV proton irradiated p-$Si_{1-x}Ge_x$ diodes of the mentioned compositions. (After Monakhov et al. [32]).

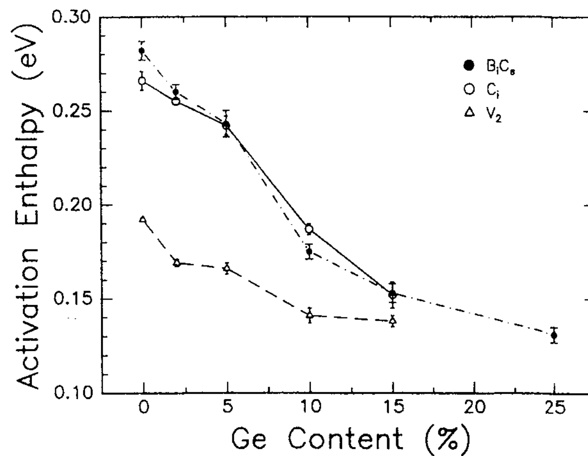

Fig. 2.12. The extracted activation enthalpies relative to the valence band for the three identified levels as a function of Ge content. The error bars represent one igma values from the Arrhenius fit. (After Monakhov et al. [32]).

A new level H3 develops for all x, after annealing at 150 ^{o}C, whereby there is a clear link between the annihilation of level H2 and the creation of H3. Another interesting observation is that the stability of the levels H1, H2 and H3 increases for increasing *x*, as evidenced e.g. by Fig. 2.13 [32]. A similar conclusion is reached for the stability of vacancy related radiation defects in bulk SiGe, derived from positron annihilation lifetime [26-27].

Table 2.1. Defect parameters for the main radiation defects in relaxed $Si_{1-x}Ge_x$ epi-layers.
*Activation enthalpy, according to Fig. 2.12.
**Apparent capture cross section derived for x=0 from the intercept.

Fraction Ge &type	Apparent Activation Energy (eV)	σ_∞ (cm^2)	Annealing temperature T_A (K)	Identity	Reference
30 % (n-P)	E_c-0.32	10^{-15}	560	$V\text{-}V^{=/-}$	29
30% (n-P)	E_c-0.49	$2x10^{-15}$	470	P-V	29
25% (n-Sb)	E_c-0.51	$6\text{-}8x10^{-16}$	--	Sb-V	30
15% (p-B)	E_v+0.14*	$4x10^{-16}$**	550	$V\text{-}V^{+/o}$	32
25% (p-B)	E_v+0.13*	$5x10^{-15}$**	400	C_i	32
15% (p-B)	E_v+0.15*	--	650-700	B_iC_s	32

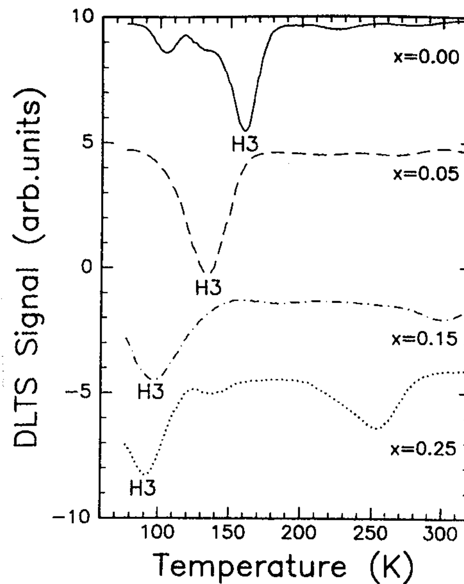

Fig. 2.13. DLTS spectra from 2 MeV proton irradiated p-$Si_{1-x}Ge_x$ diodes of the mentioned compositions after annealing at 300 ^{o}C for 30 min. (After Monakhov et al. [32]).

In analogy with the case of pure silicon [33], the levels H1 to H3 are to be related and have been tentatively assigned to the V-V$^{+/o}$ donor, the interstitial carbon C_i and the B_iC_s complex. The increased stability of the H2 peak is likely due to a reduced mobility of C_i in SiGe compared with pure Si. Here, a similar 'retarded' formation is observed as for the A center in Ge doped Si, whereby C_i is trapped at a site, which is not electrically active

2.2.3 Radiation Damage in Strained SiGe Layers

So far, only few reports are available on the radiation damage in thin strained layer n-SiGe [34-35]. Results of 5.4 MeV alpha particle irradiations on 4% n-type SiGe are in line with the results obtained on relaxed n-SiGe: compare for example the spectra of Fig. 2.14 with the ones displayed in Fig. 2.8. The same trend is observed: a reduction of the trap concentration for the same fluence ($3x10^{11}$ cm^{-2}) going from x=0 to 0.04, while the apparent trap position (DLTS peak maximum temperature) shifts to higher values for the same emission rate window. Level EA2 (P-V) has an apparent activation energy of E_c-0.44 eV and a capture cross section (from the intercept of the Arrhenius plot) of $7.6x10^{-16}$ cm^2, in reasonable agreement with the data of Table 2.1. The V-V$^{=/-}$ EA1 level in α irradiated 4 % n-SiGe has a signature of E_c-0.24 eV and σ_n=$2.3x10^{-16}$ cm^2, in fair agreement with the data in Table 2.1. Defect level EA3 is only detected in material containing Ge, after the alpha particle exposure.

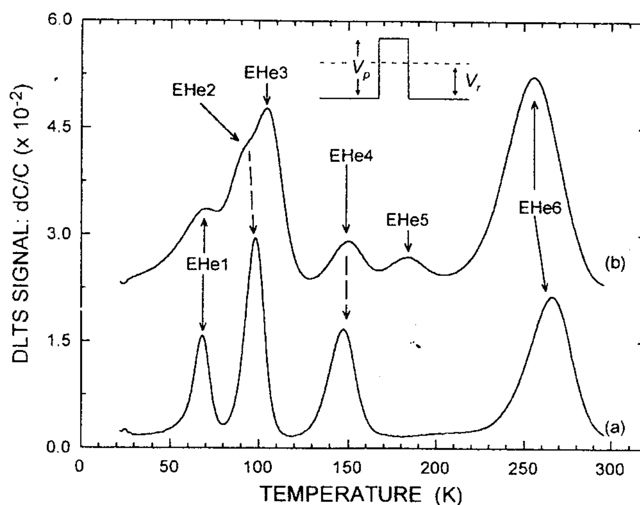

Fig. 2.14. DLTS spectra of 5.4 MeV alpha particle irradiated $Si_{1-x}Ge_x$. Curve (a) is for x=0.04, curve (b) is for x=0. Spectra were recorded at a quiescent reverse bias of 0.5 V, and at a frequency of 46 Hz. (After Goodman et al. [34]).

Far more efforts have been spent on strained-layer p-SiGe by Vanhellemont [36-37] and Ohyama and co-workers on exploratory (first-generation) heterojunction bipolar devices (diodes and BJTs) fabricated at IMEC [38-47]. Irradiations were performed for a wide range of particles, energies and fluences, summarised in Table 2.2. No bias was applied during the

exposures. The devices studied are schematically depicted in Fig. 2.15 and contain a 100 nm highly B-doped p-$Si_{1-x}Ge_x$ base layer with a density of $6x10^{17}$ cm^{-3} (diodes) and $2x10^{18}$ cm^{-3} (BJTs), derived from high-frequency Capacitance-Voltage (C-V) measurements on a reverse biased junction. Beside a x=0 reference device, three Ge contents were studied (x=0.08, 0.12 and 0.16).

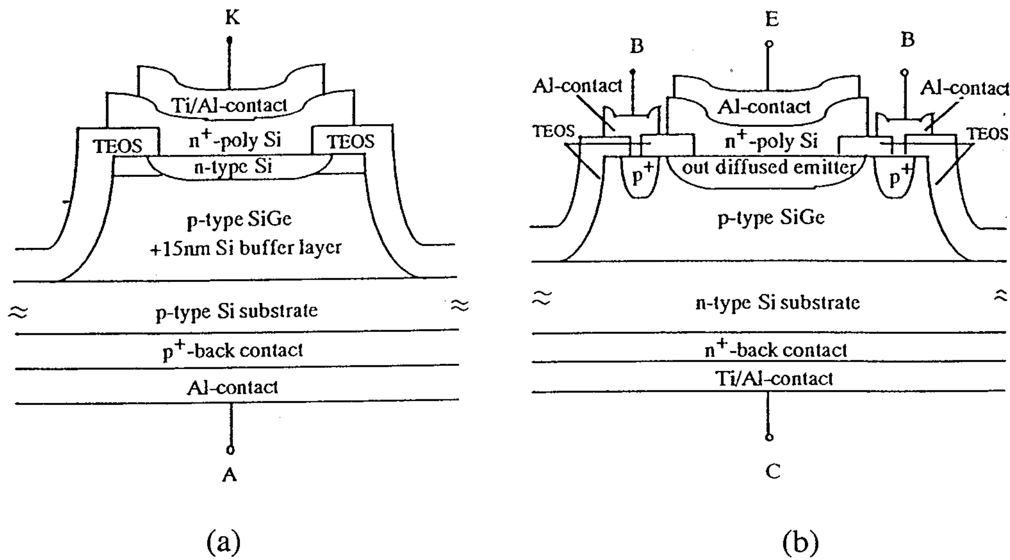

Fig. 2.15. Cross section of the strained layer epitaxial diodes (a) and HBTs (b) fabricated at IMEC.

Table 2.2. Summary of the irradiation conditions used to study the radiation damage in p-type SiGe strained-layer epitaxial devices.

Particle	Energy (MeV)	Fluence range (particles/cm^2)	Devices irradiated	Refs
e-	1	$4x10^{13}$ $2.6x10^{16}$	diode	36-38
e-	2	$1-10x10^{16}$	HBT	39
n	1	$10^{11}-10^{15}$	diode & HBT	39-41
H+	20	10^9-10^{14} 10^9-10^{14}	diode HBT	42-45
H+ α	86 20	$10^{10}-5x10^{13}$	diode	46-47

The degradation of both the material properties (B doping density, deep levels traps by means of DLTS) and of the device performance (reverse I_R and forward I_F current, capacitance C, current gain β or h_{FE}) have been studied and the correlation between microscopic and macroscopic damage has been investigated. The device degradation results will be reported in a following section. In addition, calculations of the number of knock-on atoms have been performed for each particle and energy, in order to understand more fundamentally the impact of the nuclear particles on the material and device degradation. In order to identify the irradiation-induced deep levels, isochronal (15 min) annealings were performed typically between 75°C up to 300°C. This was compared with the recovery of the device performance upon annealing and enabled to derive an activation energy for the damage removal.

Electron irradiation causes severe device and material degradation above a certain threshold fluence [36-39], to be discussed in more detail later. At the same time, the creation of radiation induced deep levels is evidenced by DLTS spectroscopy on exposed heterojunction diodes. However, the amount and nature of the stable defects depend markedly on the Ge content. This follows for example from a comparison of Fig. 2.16a and 2.16b [38] and is even more clearly illustrated by the electron trap concentrations versus fluence shown in Fig. 2.17.

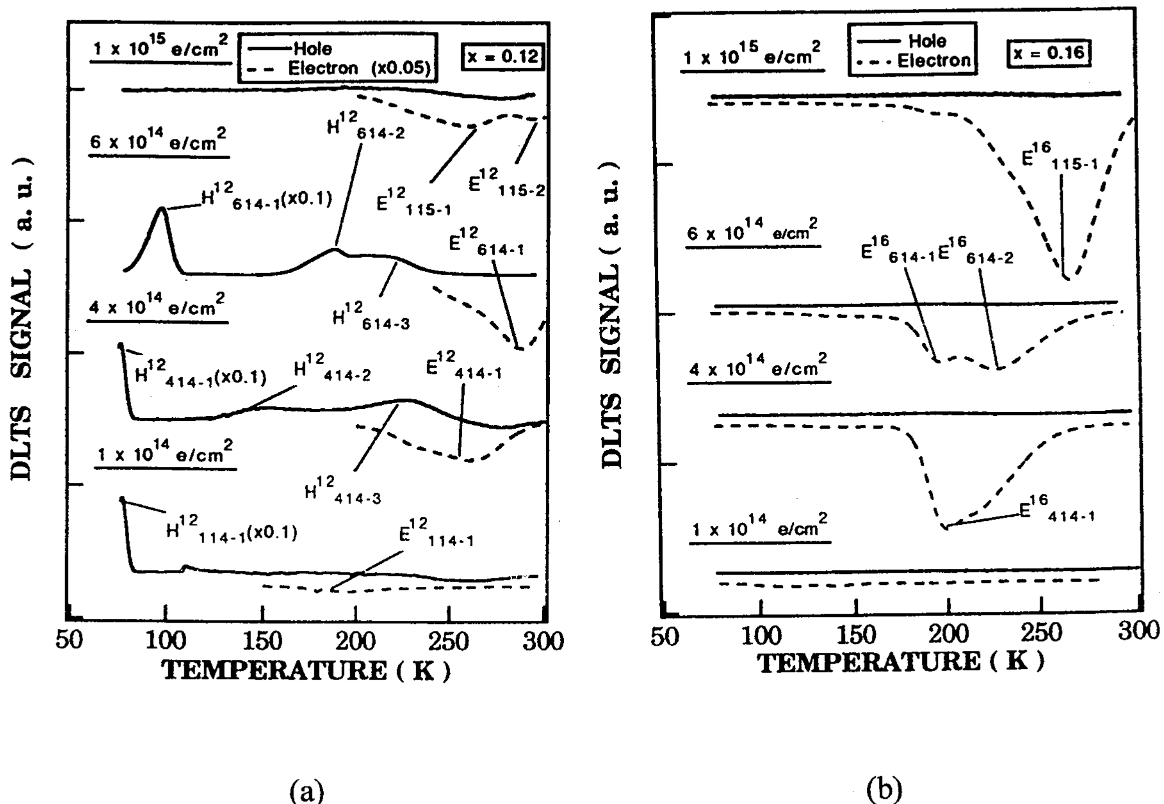

(a) (b)

Fig. 2.16. DLTS spectra in a 1 MeV electron irradiated p-type $Si_{0.88}Ge_{0.12}$ (a) and $Si_{0.84}Ge_{0.16}$ (b) epitaxial layer revealing both hole and electron traps, for different fluences. (After Ohyama et al. [38]).

In the spectra of the x=0.12 layers, both majority (hole) and minority (electron) traps are found after an injection pulse (Fig. 2.16a). The activation energy for the hole traps derived from an Arrhenius plot is [38]: E_V+0.11 eV; E_V+0.28 eV and E_V+0.46 eV and this for a fluence of $4x10^{14}$ cm^{-2}. This could tentatively correspond to the V-V donor level; and either C_i or B_iC_s (compare with Table 2.1). The deeper hole trap could be similar as the one observed in proton irradiated strained p-type layers, occurring for x>0.05 [32].

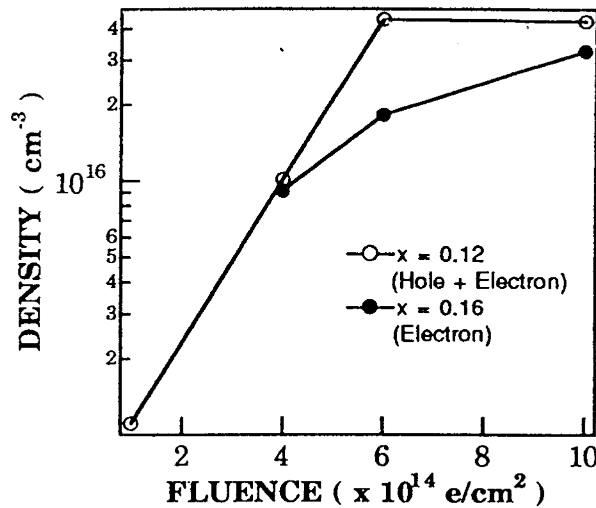

Fig. 2.17. 1 MeV electron fluence dependence of the deep level trap density for two Ge compositions. The B doping density in the SiGe layer is $6x10^{17}$ cm^{-3}. (After Ohyama et al. [38]).

However, it is to be noted from Fig. 2.16a or 2.16b that the temperature position of the hole traps (if they belong to the same defect centre !) is not constant. It should furthermore be remarked that the back-ground capacitance of the reverse biased diode shows a strong variation with temperature after irradiation (see Fig. 2.18), indicative of carrier freeze-out on a deep level and of reduction of the active shallow dopant (B) concentration. In other words: the irradiation removes active B from its substitutional site to create interstitial B, which may form higher order stable defects. The strong capacitance freeze-out in Fig. 2.18 has some further consequences: it indicates that the density of radiation-induced deep defects is no longer negligible (or even larger) compared to the background doping density (see also the data in Fig. 2.17, which have been calculated from the simple low-concentration DLTS formula and, therefore, may underestimate actual concentrations for large fluences). This renders the correct determination of the radiation-induced deep-level parameters difficult if not impossible [38], if standard capacitance DLTS is used. In addition, due to the reduction of the active B concentration, the depletion width where the traps are located, shifts further away from the junction, for a fixed reverse bias of -0.8 V. For a sufficiently large de-activation, the depletion region penetrates the underlying silicon substrate, so that some of the deep level signals are actually coming from the silicon substrate or from the SiGe/Si interface [36,38-39]. This is, however, not the case for the fluence range below $\approx 10^{15}$ cm^{-2} [38] (see also Fig. 2.19). On the other hand, for higher

fluences and, therefore, stronger de-activation of B, the depletion region will extend into the silicon substrate region. This is the case when the measured capacitance drops more than 25 % below its pre-rad value, corresponding to a B de-activation of 40 % [37]. The lowering of the active B concentration in the epitaxial layer also lowers the electric field in the depletion region and could for Coulomb attractive traps cause a change in the Poole-Frenkel barrier lowering and hence in the activation energy of such traps.

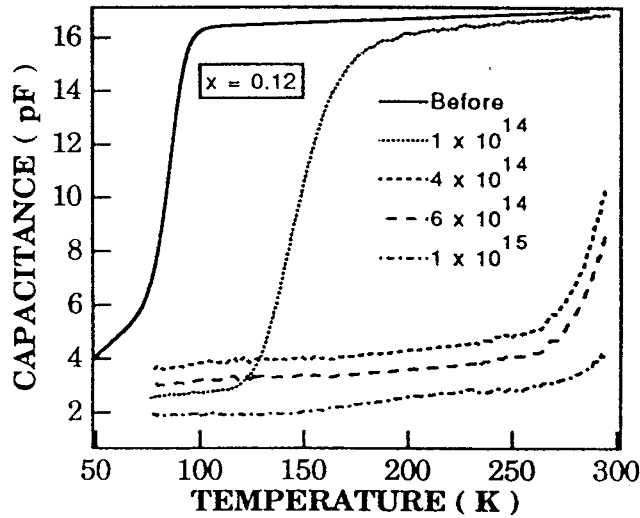

Fig. 2.18. Capacitance-Temperature (C-T) plot for a 1 MeV electron irradiated strained-layer epitaxial diode with x=0.12. (After Ohyama et al. [38]).

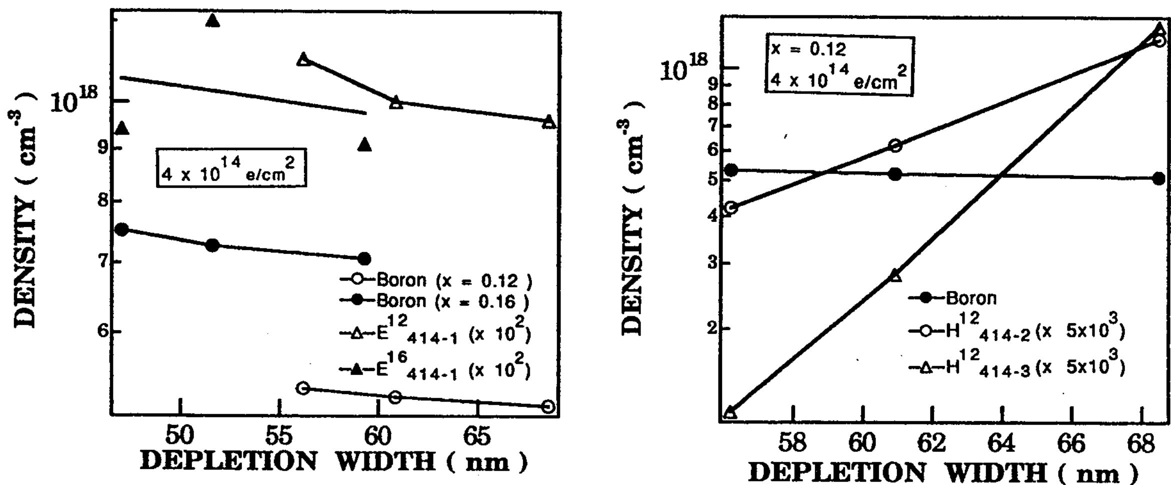

(a) (b)

Fig. 2.19. Depth profile of boron and deep level concentration for 1 MeV irradiated SiGe heterojunction diodes. (a) hole traps and (b) electron traps. (After Ohyama et al. [38]).

In addition to the hole traps, also electron traps are observed in Fig. 2.16. For x=0.16 these are the only radiation-induced levels observed above the DLTS detection limit. Activation energies are in the range E_C-0.56 eV (x=0.12) and E_C-0.66 eV (x=0.16). The trap level profile has also been studied for different reverse biases, yielding the results of Fig. 2.19a for the hole traps and of Fig. 2.19b for the electron trap(s), respectively. From these figures, it is derived that the hole traps show a profile which reduces towards the surface. It is known from studies of irradiated silicon that vacancy related levels (A-center and V-V) show a lower concentration towards the surface [48], which is a perfect sink for vacancies. It is therefore speculated that some of the unknown hole traps may be V-related, e.g. V-B complexes [49]. The electron trap, which is close to mid-gap and hence an effective generation center shows a similar profile as the active B, with a concentration which reduces with depth. In analogy with the case of silicon, it is assumed that these levels are related to interstitial B [49], possibly a complex with B_S: B_i-B_S. It is furthermore well-known that interstitial B is the dominant radiation defect in highly B doped silicon, irradiated at low temperatures [50-52], giving rise to an electron trap at E_C-0.45 eV. However, this level anneals at 240 K and is not expected to be stable at room temperature, even for SiGe, with rather high x. Due to its mid gap position this electron trap(s) will have a strong impact on the electrical characteristics of irradiated heterojunction diodes [38].

With respect to the introduction rates $r_T=\partial_{N_T}/\partial\Phi$, the following can be remarked. From the linear part of Fig. 2.17, a slope of 25 (x=12%) and 22 (x=16%) 1/cm is derived [38]. This is, however, significantly lower than the B de-activation rate K_B in the range 100 to 200 cm^{-1} [36-38], obtained from C-V measurements. This parameter is derived as follows, assuming a linear reduction of the boron concentration N_B with fluence Φ:

$$N_B(\Phi) = N_B(0) + K_B\,\Phi \qquad (2.1)$$

with $N_B(0)$,$N_B(\Phi)$ the boron concentration before and after irradiation. K_B can be considered as a damage coefficient for the B de-activation and is expressed in units of 1/cm. Equation (2.1) is in first instance valid for not too large fluences (<10^{15} cm^{-2}) because for higher Φ, the p-SiGe base layer will be fully depleted even for zero reverse bias and the doping density in the substrate will be probed then. The data for high-energy electrons and other particles are summarized in Table 2.3.

Also shown in Table 2.3 is the number of knock-on atoms per particle N_d, which should be a measure for the deposited energy, similar as the NIEL parameter. It is calculated as follows [40-41]. First, the average energy of primary knock-on atoms is calculated from [41]

$$\langle E_P \rangle = E_d \ln\left(\frac{E_{Pmax}}{E_d}\right) \qquad (2.2)$$

with E_{Pmax} and E_d the maximum energy for knock-on atoms and the displacement threshold energy, respectively. For E_d, a value of 25 eV is used for both Si and Ge [40]. The fractional displacement concentration is given by:

$$C_d = \sigma_d(E)\, \nu(\langle E_P \rangle) \tag{2.3}$$

while the NIEL E_I is given by [41]:

$$E_I = \frac{N}{A} \langle E_P \rangle\, \sigma_d(E) \tag{2.4}$$

N is Avogadro's number, A the atomic mass of the target, $\sigma_d(E)$ is the primary knock-on cross section and $\nu(\langle E_P \rangle)$ is the number of displacement atoms per one primary knock-on atom. Finally, N_d is obtained by multiplying C_d by the number of target atoms. It is derived from Table 2.3, that N_d decreases for increasing Ge fraction, which is in line with the lower de-activation or trap introduction rates. This suggests that the alloy hardening effect can at least partially be explained by the lower energy density deposited by the impinging high-energy particles [38]. This is further supported by the calculated absorbed energy profiles shown in Fig. 2.20 [38]).

Table 2.3. Calculated number of knock-on atoms (Eq. (2.3)), B damage coefficient (Eq. (2.1)) and trap introduction rate from DLTS, derived for irradiated strained layer p-SiGe heterojunction diodes.

Irradiation	N_d			K_B (cm^{-1})			r_T (cm^{-1})		
	Ge %: 8	12	16	Ge %: 8	12	16	Ge %: 8	12	16
1 MeV e-				--	-195	-149	--	25	22
2 MeV e-	2.49	2.48	2.47	--	-215	-173			
1 MeV n	301	295	288	--	-1584	-1287			
20 MeV H+	992	895	883						
86 MeV H+	272	265	259						
20 MeV α				-8.5	-4.2	-2.4	240	150	80
					($x10^4$)				

Another important issue with respect to radiation damage is its stability upon thermal annealing and possible recovery of the degraded device performance. This has been studied extensively for the 1 MeV electron irradiated diodes [38]. For example, the electron traps discernable in Fig. 16b for x=0.16 are stable up to ≈300°C (Figs 2.21a and 2.21b), if the stability limit is defined at 10 % unannealed fraction (Fig. 2.21b). From Fig. 2.21b also follows that the defect annealing is in first order composition independent. The high annealing temperature in fact rules out an assignment to B_i, since this level disappears at

much lower temperatures ([50-52]). It is more likely a higher order complex involving B and some other impurity or point defect. From the annealing rates of Fig. 2.22 for x=0.12 and x=0.16, respectively, an activation energy of 0.23 eV and 0.2 eV has been derived, which also agrees with the recovery behavior of the reverse diode current. It again emphasizes the important role played by the near mid-gap electron traps in the device performance degradation of irradiated SiGe heterojunction devices.

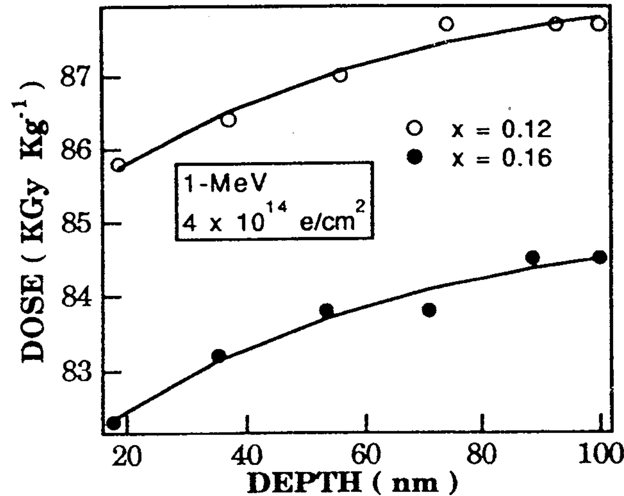

Fig. 2.20. Absorbed energy in a $Si_{1-x}Ge_x$ epitaxial layer. The calculation is performed using the multi-layer depth dose code [EDMULT]. (After Ohyama et al. [38]).

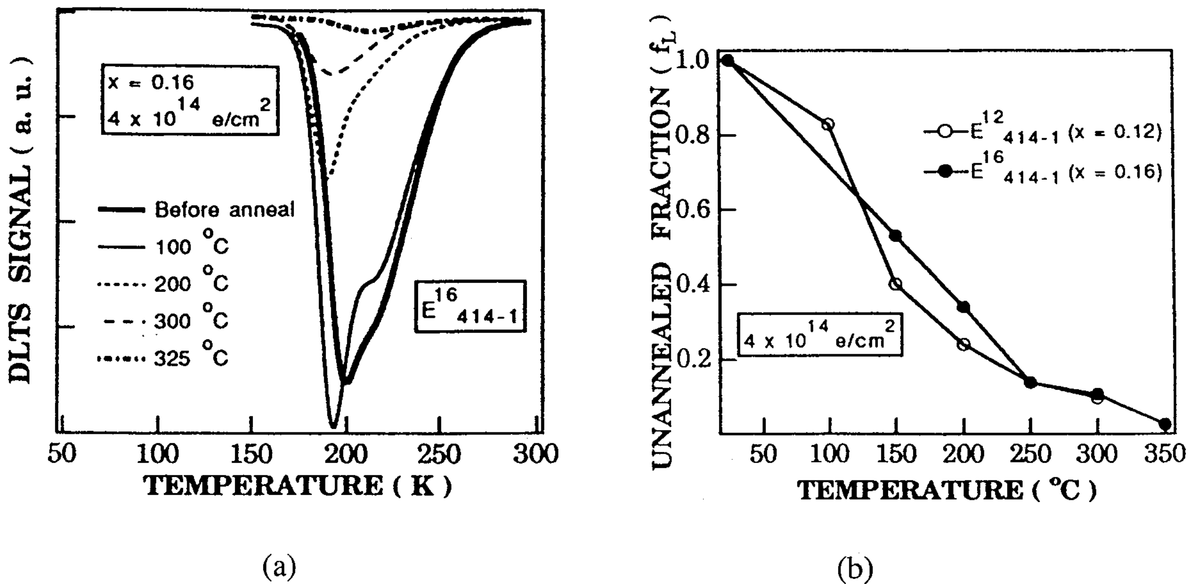

Fig. 2.21. Isochronal annealing of the electron trap level for diodes with x=0.16, after $4x10^{14}$ cm^{-2} 1 MeV electron irradiation (a) and unannealed fraction of the electron traps for x=0.12 and 0.16 as a function of annealing temperature (b). The anneals were for 15 min. (After Ohyama et al. [38]).

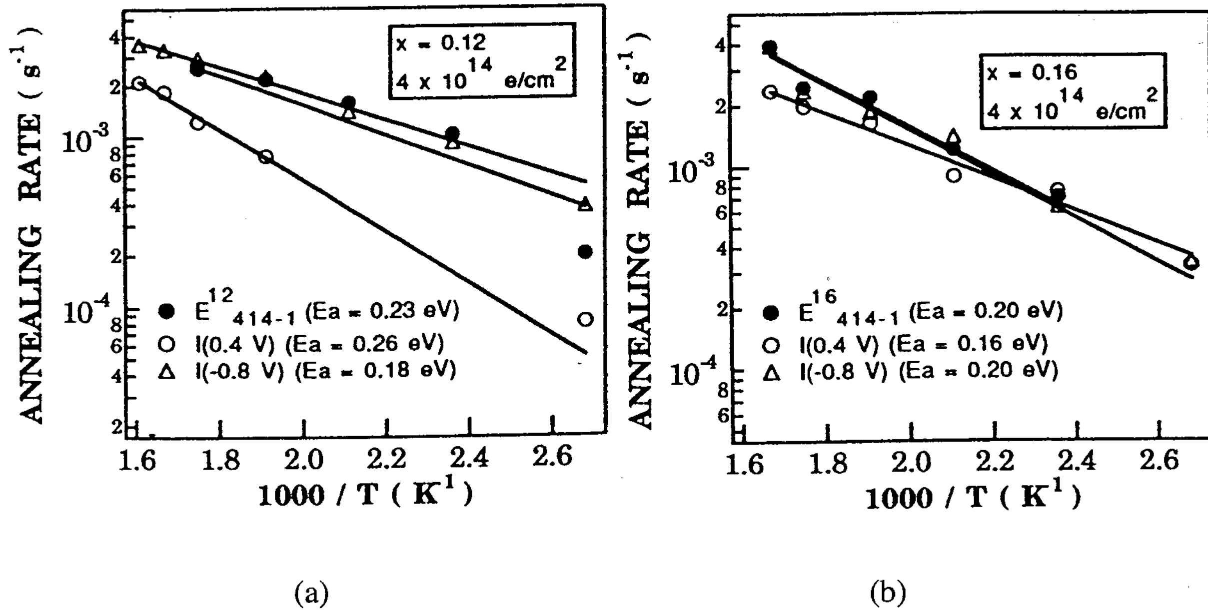

Fig. 2.22. The relationship between the annealing rate and the reciprocal annealing temperature for the electron trap level and for the diode current at a bias of -0.8 V and 0.4 V for (a) x=0.12 and x=0.16 (b). (After Ohyama et al. [38]).

Roughly the same qualitative results have been obtained for irradiations with fast neutrons or high-energy ions. For example, similar electron traps and freeze-out behavior (B de-activation) have been found for 1 MeV neutron and 20 MeV proton irradiations, as evidenced by Fig. 2.23 [41] and 2.24 [43], respectively. Only for the α-irradiations, a different type of spectra is observed in Fig. 2.25. However, as found systematically for all irradiations, the trap concentrations and B de-activation reduce with Ge fraction x, confirming the alloy hardening effect. Furthermore, a similar defect and device recovery is found, for example after 20 MeV proton exposure (Fig. 2.26) [43]. A slightly higher activation energy for annealing of the electron traps is found in that case (0.27 eV).

Finally, deep levels have also been studied in the emitter-base and base-collector junctions of the irradiated heterojunction BJTs [39-40,43-45]. In the case of 1 MeV neutron exposure, the same type of electron traps was observed, in addition to a deep hole trap (Fig. 2.27a) [40]. However, in most cases, it was only possible to detect electron traps in the n-type silicon collector region, showing the "classical" silicon radiation defects (V-O, V-V, P-V) (Fig. 2.27b).

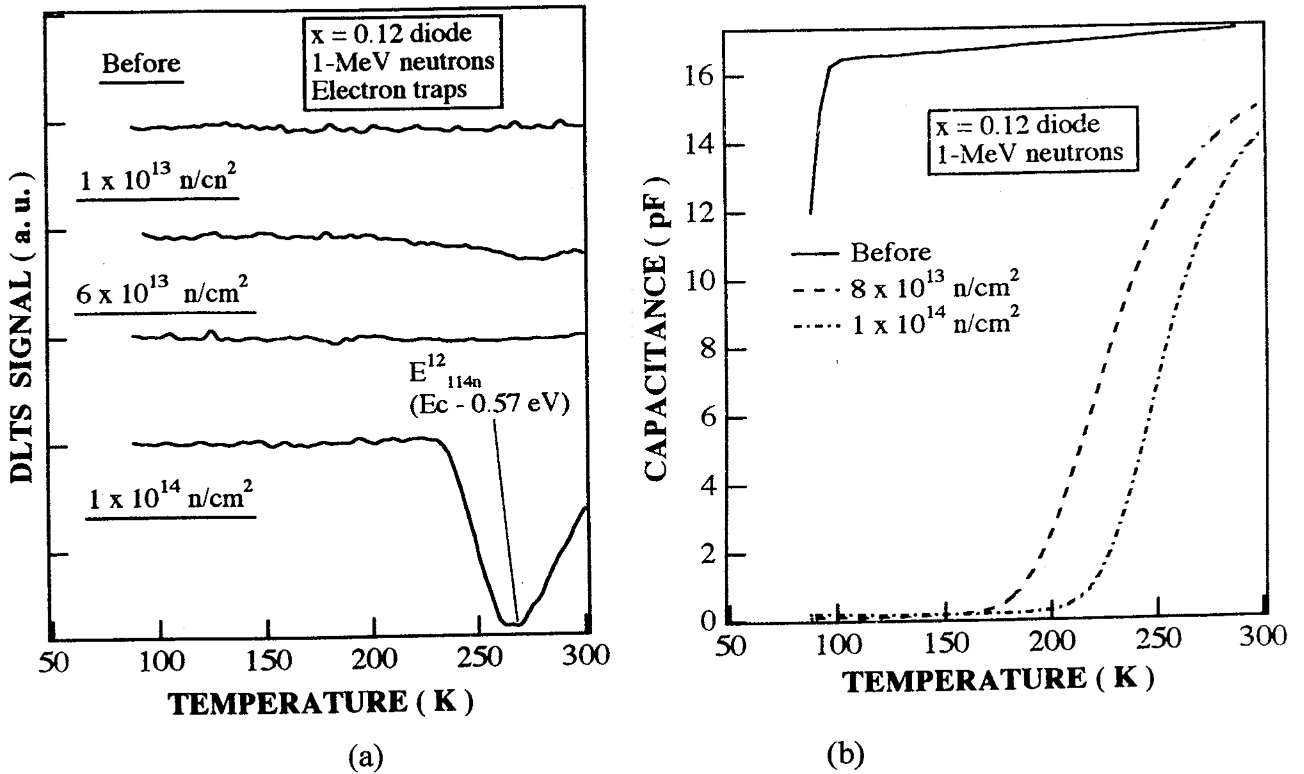

(a) (b)

Fig. 2.23. DLTS spectra (a) and corresponding C-T plot (b) for x=0.12 p-SiGe diodes irradiated by 1 MeV neutrons. (After Ohyama et al. [41]).

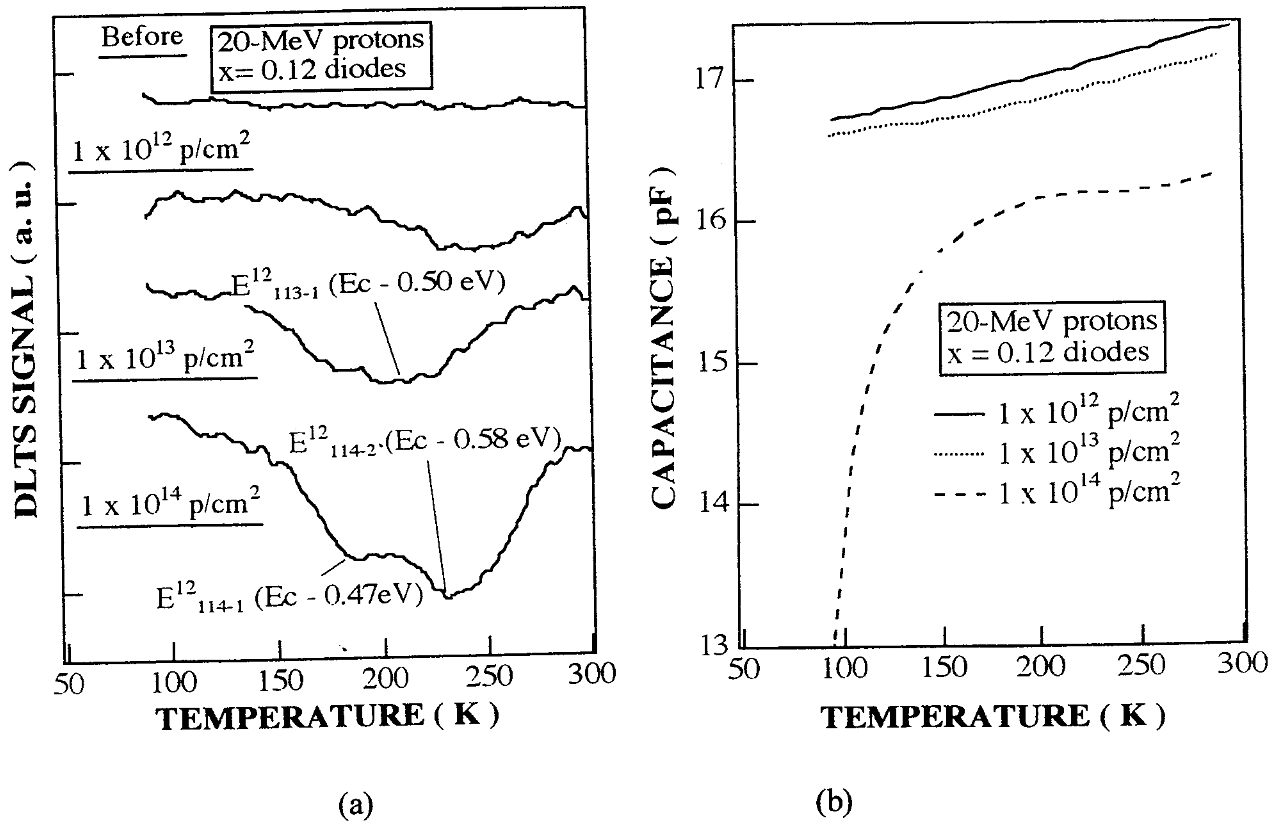

(a) (b)

Fig. 2.24. DLTS spectra (a) and corresponding C-T plot (b) for x=0.12 p-SiGe diodes irradiated by 20 MeV protons. (After Ohyama et al. [43]).

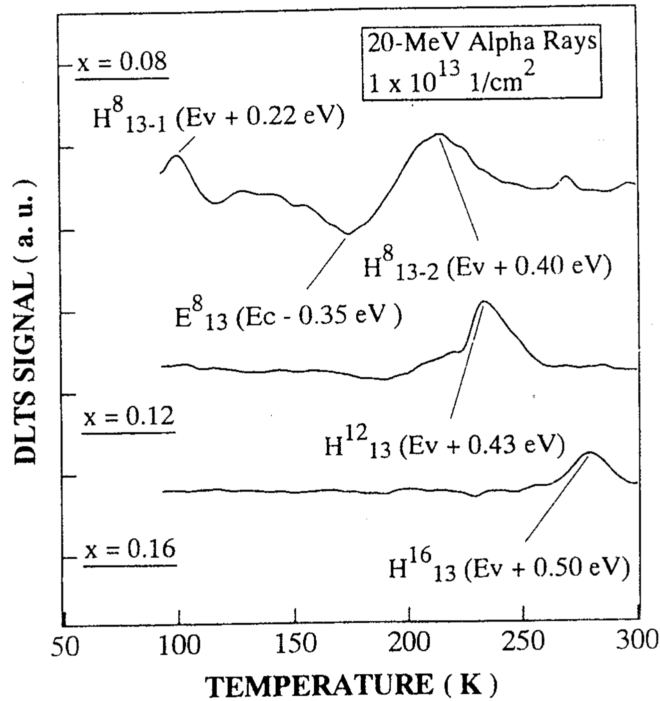

Fig. 2.25. DLTS spectra for $Si_{1-x}Ge_x$ diodes with different germanium content, subjected to 20 MeV alpha particles with a fluence of 10^{13} cm^{-2}. (After Ohyama et al. [47]).

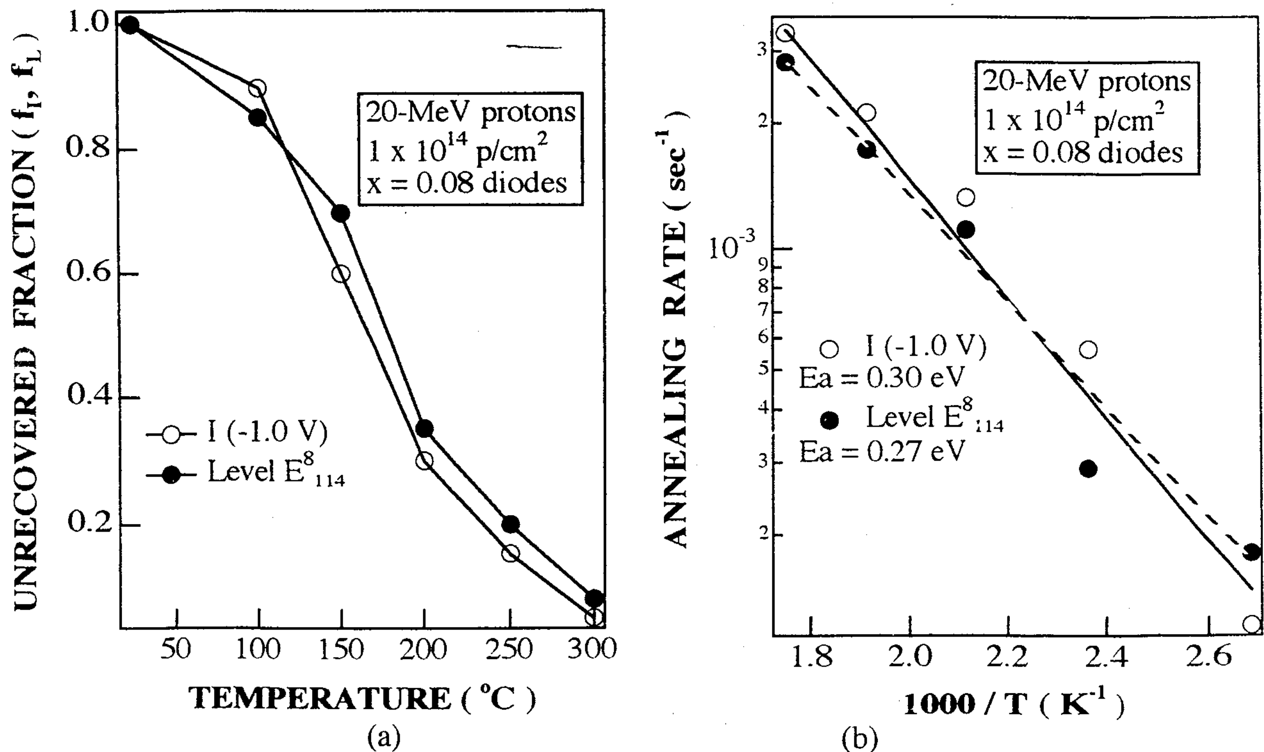

Fig. 2.26. Unrecovered fraction versus annealing temperature (15 min) for the reverse diode current at -1 V (f_I) and for the electron trap levels (f_L) obtained for $Si_{1-x}Ge_x$ diodes with x=0.08, after 20 MeV proton exposure (a). Relationship between the annealing rate and the inverse temperature for the same parameters (b). (after Ohyama et al. [43]).

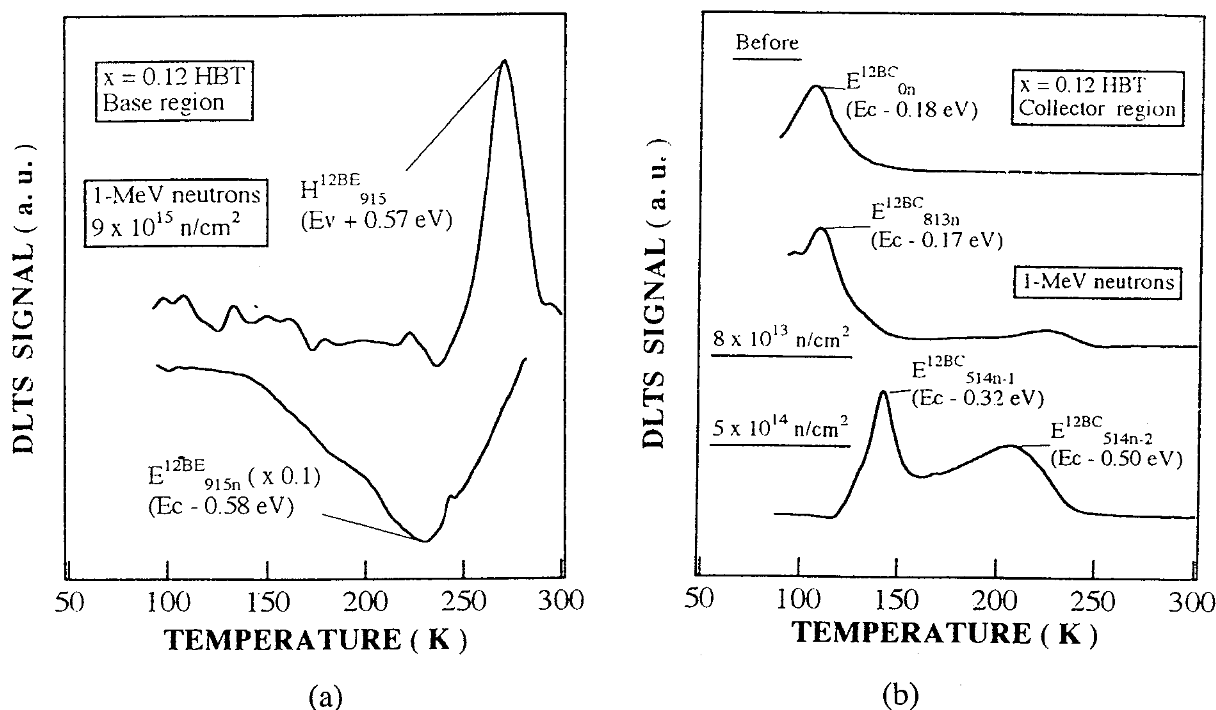

Fig. 2.27. DLTS spectra for x=0.12 HBTs (a) base and (b) collector region. The introduction rate of the electron trap in (a) is 10 cm^{-1}, which is about one decade larger than for the hole trap H_{915}^{12BE}. (After Ohyama et al. [40].

Summarizing the results obtained for the p-type SiGe strained layers, the following trends have become obvious. First, the microscopic device degradation, i.e. the boron deactivation and the trap level introduction rate, reduce significantly for higher x. In some cases, a factor 3 improvement can be observed, for x going from 0.08 to 0.16. This can be partially explained by the lower number of knock-on atoms created, although there is not a linear correlation between the calculated damage parameters and the measured damage coefficients.

From Table 2.3 it is also evident that the boron de-activation is significantly larger than the total density of radiation induced traps. Although it is possible that not all traps have been revealed by DLTS, as the measurement range was limited to the region above 77 K, it strongly suggests that the displaced B atoms are partially in a clustered form (pairs or higher order complexes). One should, however, keep in mind that for higher fluences, the calculation of the trap concentration from DLTS must be handled with care, because of the freeze-out phenomenon occurring. At the same time, it is strongly suspected that some of the introduced hole and electron traps are B related.

One of the most harmful radiation induced defects in strained p-type SiGe layers is the near mid-gap electron trap(s), which should be an efficient leakage current generation center. It is a rather stable defect, showing an annealing stage around 500 600 K, which is too high to correspond to B_i for example. A higher order complex involving B is therefore put forward. The fact that the same annealing activation energy is found for both the trap

level concentration and the reverse current supports this idea. The activation energy lies typically in the range 0.2 to 0.3 eV..

2.3 Processing-Induced Radiation Damage in SiGe

Modern processing uses fabrication steps whereby often radiation damage by low energy electrons (metal sputtering), ions (ion implantation, dry etching,...) or photons (X-rays mainly) can occur. Since this degrades the electrical and structural material properties, it is important to understand and control their formation. Quite some information has been gathered in recent decades, showing some overlap with the high energy radiation behavior. Recently, these investigations have been extended to the case of SiGe layers, in view of their application in ULSI technologies.

2.3.1 Dry Etching and Electrom Beam Sputtering Damage

The impact of low-energy 1 keV He ion etching on n-type SiGe layers with different compositions and degrees of relaxation has been studied by Goodman et al. [34-35] and compared with high-energy α-irradiation and radio-frequency sputter-deposition of Au Schottky barrier diodes. In total 6 electron traps have been observed after He ion etching, four of them are similar to the case of silicon (Fig. 2.28). Most of the deep levels have a uniform profile for the depth range studied. An important remark is that the trap level concentration for the 4 % Ge containing material is one decade *larger* than for the pure silicon. This is in strong contrast to what has been reported above for high-energy particle irradiations. Two traps EHe5 and EHe3 have only been observed for the Ge containing layers and increase in concentration with x, suggesting that the damage in the SiGe layers is more severe than in silicon. Similar spectra and identical defect levels were obtained for the rf deposited Au Schottky barrier diodes without He ion etching [34]. The role of the Ge content on the He etching induced damage is shown in Fig. 2.29. Both the trap concentration and position behave strangely as a function of x. Opposite shifts have been found for EHe3 and EHe6 as a function of x. The activation energy of EHe6 for x=0.04 is E_C-0.52 eV and for EHe3 E_C-0.19 eV. Finally, it has been demonstrated by comparison with the results for 5.4 MeV alpha particles that a totally different defect spectrum is found (compare with Fig. 2.14). This may partly explain the contrasting observation of increasing trap densities with increasing Ge fraction x.

Similar studies have been undertaken for p-SiGe [35,53-54], whereby Ar-ion etching was compared with 5.4 MeV α–exposures and e-beam damage. A whole range of deep levels has been found (Fig. 2.30a). However, the main defect level He2 is the same for all types of irradiations and has an activation energy of E_V+0.529 eV (x=0) and a hole capture cross section of 9.4×10^{-14} cm^2. From the shift of the energy position (activation energy for hole emission) it is derived that the trap is pinned to the conduction band (Fig. 2.30b). The activation energy can be described by the empirical relationship [50]:

$$E_T(x) = 1.3\ E_g(x) - 0.94\ \text{(eV)} \qquad (2.5)$$

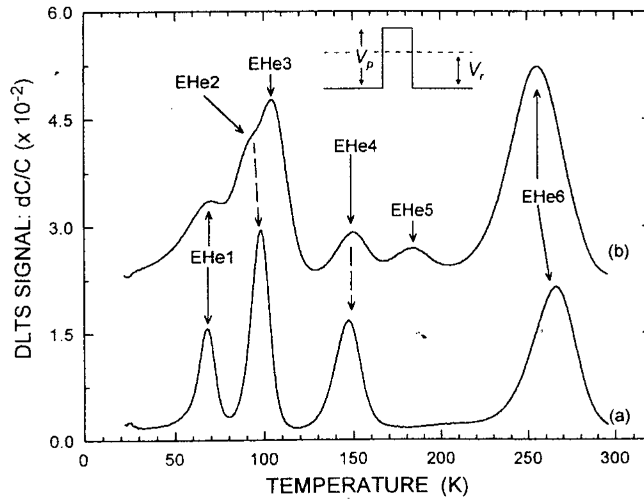

Fig. 2.28. DLTS spectra of 1 keV He-ion sputter-etched $Si_{1-x}Ge_x$ at a fluence of 10^{12} cm^{-2}. Curve (a) is for x=0, curve (b) is for x=0.04. Spectra are recorded at a quiescent bias of 0.5 V. The measurement frequency was 46 Hz. (After Goodman et al. [34]).

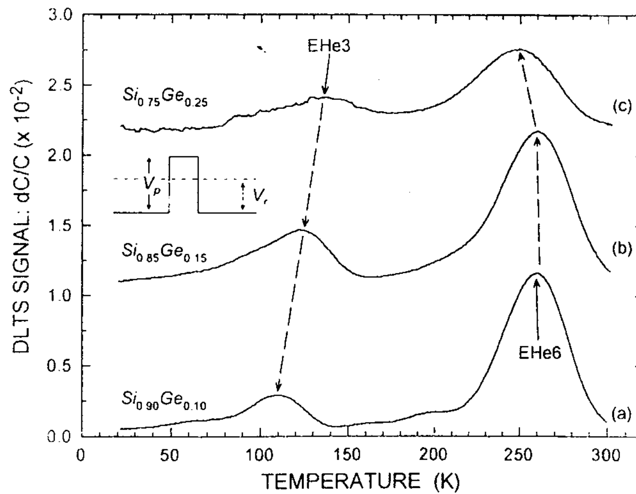

Fig. 2.29. DLTS spectra of 1 keV He-ion sputter-etched $Si_{1-x}Ge_x$ at a fluence of 10^{12} cm^{-2}. Curves (a), (b) and (c) are for x=0.10, 0.15 and 0.25, respectively. Spectra are recorded at a quiescent bias of 0.5 V. The measurement frequency was 46 Hz. (After Goodman et al. [34]).

with $E_g(x)$ the band gap energy corresponding to a Ge fraction x. Trap He2 furthermore shows a pronounced profile (Fig. 2.31) [35], which is in fact believed to be exponentially increasing towards the surface, with a characteristic length λ=0.23 nm. From the observation that the height of the Sc Schottky barrier increase for SiGe exposed to electron beam damage, it is concluded that most of the created traps should be of a donor nature [53]. This

is, however, in contrast to the observed Poole-Frenkel shift for increased reverse diode bias [53], which rather suggests traps which are attractive to holes. Given the large hole capture cross section for the dominant trap He2, it is concluded that this centre is atttractive to holes and, therefore, more likely a deep acceptor.

Note finally the peculiar behaviour of level He1, which does not shift with the Ge fraction [35,53-54], indicating that it is pinned to the valence band. This means that the shift of a trap center with x depends on whether it is pinned to the valence or the conduction band and hence on the nature of the trap: donor or acceptor character and hole or electron trap.

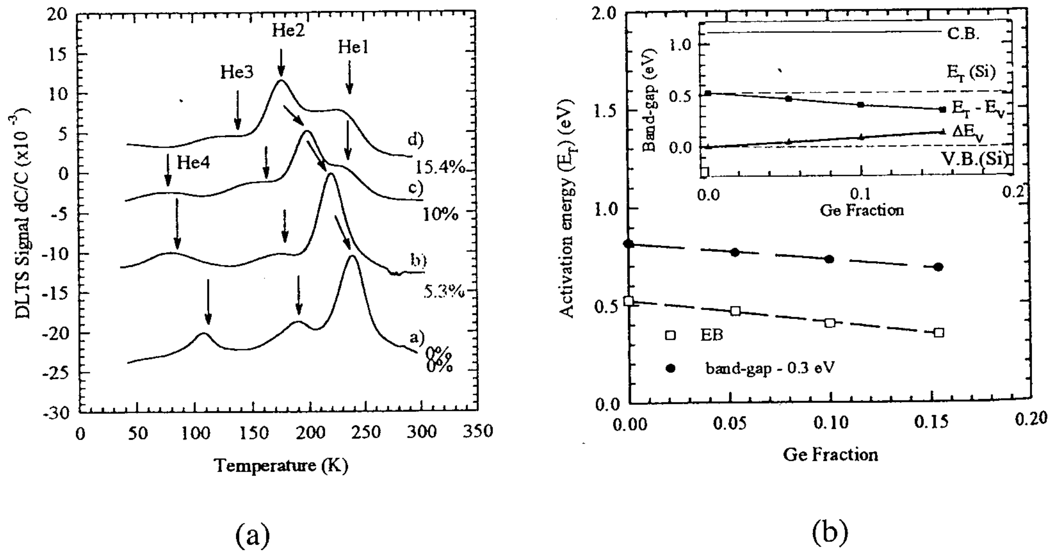

Fig. 2.30. DLTS spectra of electron beam deposited Sc Schottky barrier diodes on p-$Si_{1-x}Ge_x$ with different Ge content. (a) Variation of $Si_{1-x}Ge_x$ band-gap (solid circles) and the activation energy of the most prominent defect (open squares) as a function of Ge-content. (b) Correlation of the change in activation energy and valence band relative to silicon with Ge-content is shown in the insert. (After Mamor et al. [54]).

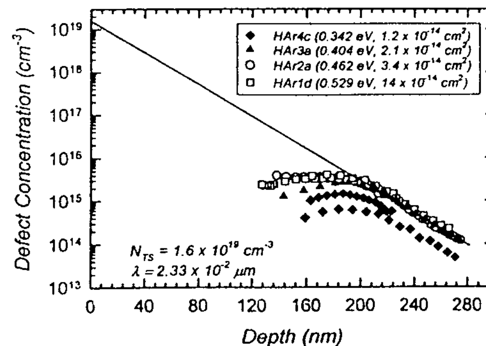

Fig. 2.31. Depth profile of the major defect in 0.75 keV Ar-ion etched p-SiGe. The characteristic length and the surface concentration have been derived. (After Goodman et al. [35]).

2.3.2 Ion Implantation Damage in SiGe

Ion implantation is still the technique of choice in order to selectively dope silicon in ULSI technologies. However, for deep submicon technologies, the doping profiles should be tightly restricted to narrow sub 0.1 μm junction regions. This not only requires a good thermal budget management but at the same time a severe ion-implantation defect control. In spite of decades of research, the understanding of defect formation during ion implantation is still not sufficiently deep for that purpose. This is one of the reasons for the current interest in MeV self- and ion implantations in silicon, producing a damage layer which is sufficiently far from the surface and thus enabling a full characterization of the damage peak by techniques like Transmission Electron Microscopy (TEM) or Rutherford Back-Scattering (RBS). This can then be compared with a Monte Carlo simulation of the damage peak using for example numerical codes like TRIM. Such studies have been undertaken for epitaxial SiGe as well, since the early 90ties [55-59]. Generally, rather thick relaxed layers have been used for that purpose. It has been noted, however, that ion implantation not only gives rise to defects, but can also cause a strain relaxation in the SiGe layers [55].

Extensive studies have first of all pointed out that the ion implantation damage can not simply be extrapolated from the behavior of the elemental semiconductors Si or Ge [55-56]. It appears that the fundamental damage mechanisms in alloys behave differently than in Si, even for unstrained layers. In practice, the ion-implantation induced damage produced in a SiGe layer is much higher than in silicon and is furthermore highly non-linear with Ge fraction (and dose). This is illustrated in Fig. 2.32 [55]. Furthermore, it has been observed that for x≥0.5 the damage behavior follows closely the behavior of Ge (x=1) [55-56]; this is also shown in Fig. 2.33. Figures 2.32 and 2.33 represent the maximum damage (peak) as a function of ion dose or ion implantation temperature. When the relative damage becomes 1, a buried amorphous layer is formed, due to the overlap of the damage cascades.

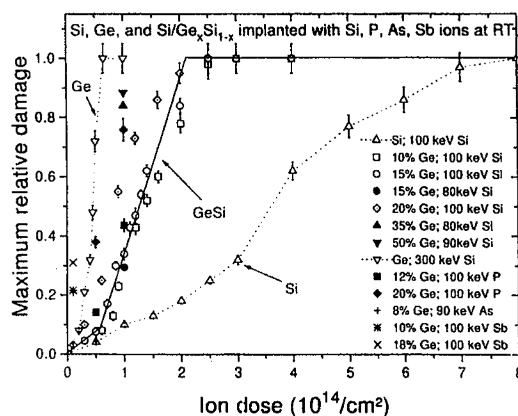

Fig. 2.32. The values of maximum relative damage obtained from ^{4}He ion channeling spectra for Si, P, As and Sn implanted Si(100), Ge(100) and pseudomorphic Si(100)Ge$_x$Si$_{1-x}$ (0.08•x•0.5) plotted versus the ion dose. A unity value in the maximum relative damage means that a continuous amorphous layer is formed in the ion implanted sample. A solid line is added as a guide to the eye to indicate the highly non-linear nature of damage buildup as a function of incrementing ion dose in the Ge-Si system. (After Lie [55]).

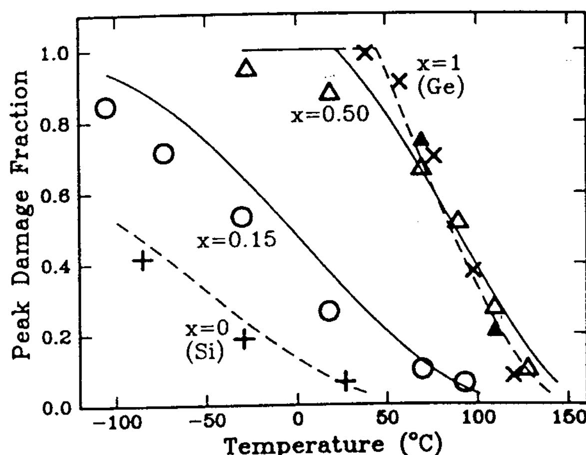

Fig. 2.33. Temperature dependence of the Ge peak damage fraction (the atomic fraction of displaced Ge at the peak of the damage profile) for a dose of 10^{14} $^{30}Si/cm^2$ (J=0.05 μA/cm^2) in $Si_{1-x}Ge_x$ layers with x=0 (+), 0.15 (o), 0.8 (closed triangles) and 1 (x) at energies of 70, 80, 90, 90 and 100 keV, respectively, in order to have the same depth of the peak. (After Haynes and Holland [56]).

Comparison with TRIM simulations leads to the conclusion that while the damage peak position is well described, this is not the case for the peak height (Fig. 2.34) [56].The discrepancy increases even for increaing x. Such an effect could be explained by assuming an increase in the deposited energy or a reduction of the mobility of the primary defects produced or both [55-56].

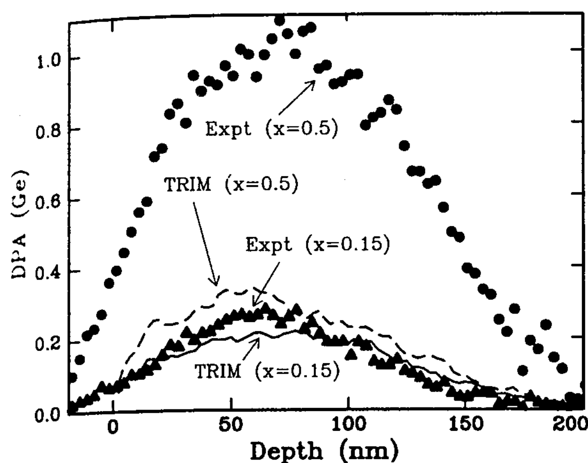

Fig. 2.34. Measured damage profiles extracted from the Ge portion of the 19° channeling spectra are compared to the Ge recoil distributions calculated by TRIM using a displacement energy of 15 eV. (After Haynes and Holland [56]).

It has been shown extensively that the ion-implantation created damage is a strong function of the substrate temperature (Fig. 2.33) [55-56]. Above a certain temperature T_O no damage is formed due to a more efficient defect annealing, caused by a larger intrinsic point defect mobility. This threshold temperature increases monotonically with Ge fraction for $0<x<0.5$, while for x•0.5, T_O is approximately constant. Note also that for the same Si ion dose (10^{14} cm^{-3}) a larger fractional peak damage is reached in Fig. 2.33, for higher *x*. In other words, the critical dose for amorphisation reduces with *x*, as evidenced by Fig. 2.35 [58], for 2 MeV Si-implanted $Si_{1-x}Ge_x$ at room temperature. The corresponding critical dose can be empirically modeled by [58]:

$$D^* = a^* x^{-0.93} \tag{2.6}$$

with $a^*=1.5 \times 10^{14}$ cm^{-2} and for 0.04•x•0.36.

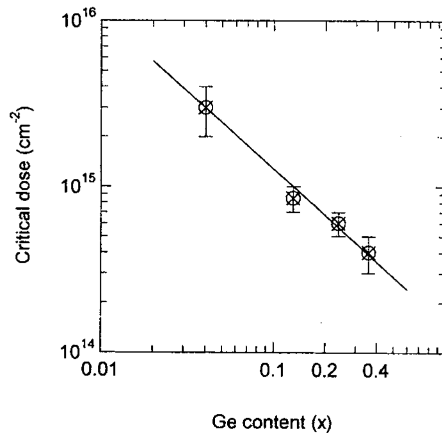

Fig. 2.35. Critical dose as a function of Ge content for the formation of a buried amorphous layer in 2 MeV Si-implanted $Si_{1-x}Ge_x$ alloys estimated by TEM (o) and ORDP (x). (After Nylandsted-Larsen et al. [58]).

A final relevant observation is that the resulting damage shows a dose rate effect, as illustrated by Fig. 2.36 [56]. For each alloy, the damage produced increases strongly with the dose rate near T_O, while it is much less sensitive around room temperature. The onset of such dose rate effects indicates that a fundamental change in the mode of damage growth occurs near T_O. From the data presented above, it becomes clear that the addition of Ge in the alloy inhibits the dynamic damage annealing during ion implantation and, therefore, Ge retards the short-range mobility of the primary point defects, i.e. within the damaged volume. For implantations well below T_O, it is assumed that all the damage is formed within the cascades, while near T_O, other damage mechanisms may become competitive [56]. The cascade mechanism is then considered as prompt, with a homogeneous nucleation of the damage, while a second dose rate dependent mechanism near T_O has a heterogeneous

nucleation and occurs retarded (delayed) because it requires diffusion of primary defect species [57]. This second mechanism is, therefore, strongly temperature and dose rate dependent. Finally, DLTS studies have revealed the presence of three electron traps in ion implanted n-type SiGe, which have been assigned to the A-center (T_1), the V-V (T_2) and the Sb-V complex (T_3) (Fig. 2.37) [58].

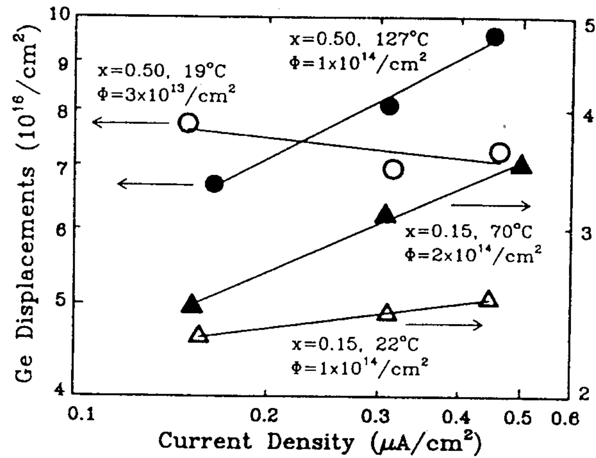

Fig. 2.36. Dose-rate dependence of the depth-integrated Ge damage yield near RT and at elevated temperatures. The fluence was selected for each alloy and temperature to give a damage fraction ≈30 %. (After Haynes and Holland [56]).

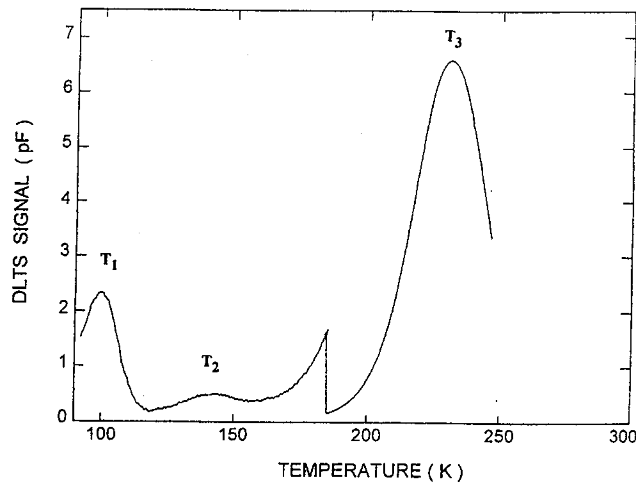

Fig. 2.37. DLTS spectrum of a Schottky diode made on the $Si_{0.96}Ge_{0.04}$ alloy. The gain was multiplied by 10 for data obtained at temperatures below 190 K. Implantation was for 10^{10} Si^+ cm^{-2} at a dose rate of 10^9 $cm^{-2}s^{-1}$. (After Nylandsted Larsen et al. 58]).

2.3.3 Ion Implantation Damage Model

Comparing the defect behavior in irradiated with implanted SiGe alloys, a strongly contrasting behavior is found. While the stable (and electrically active) point defect (PD) concentration reduces with the Ge fraction, the opposite is true for the peak damage in ion implantations, where besides PDs more extended clusters are formed, resulting in a local amorphous region. In fact, also for ion-etched or e-beam exposed epitaxial layers, a tendency has been observed where the PD concentration is higher for higher x, although the nature of the point defects has been shown to be different than in high energy irradiated material [34-35,53-54]. In summary, the stable radiation damage in the peak region seems to behave differently than the one in the tail, where low damage levels are reached.

In order to understand these trends, it is helpful to study in more detail the peak ion implantation damage as a function of dose (Fig. 2.38a and b). These figures first of all confirm the higher damage for higher x and consist of three distinctive regions, before continuous amorphisation sets in for s=1. For low doses, the damage yield s increases linearly with D. In this region, it is assumed that no overlap occurs between the individual damage cascades [59]. For intermediate doses a sublinear increase is found. In this case, collision cascades develop in already damaged regions, which enhances the chance for recombination of the point defects. However, for even higher doses, clustering of the point defects in the highly damaged region will compete with recombination and stabilizes the PDs. At the same time the formation and stimulated increase of the amorphous regions is responsible for the superlinear damage increase, until complete amorphisation occurs.

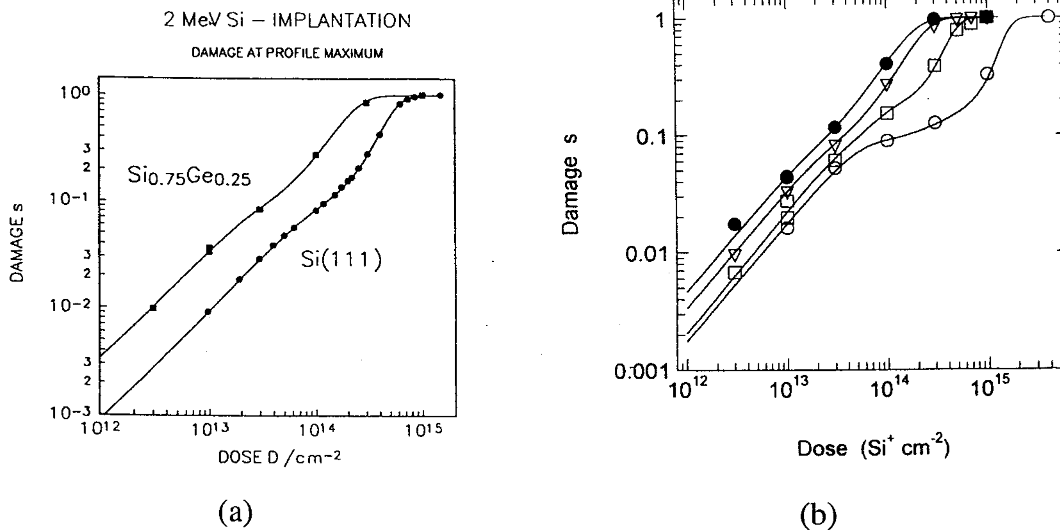

Fig. 2.38. (a) Dose dependence of the optically determined damage at the depth of the profile maximum for 2 MeV Si^+ implantations into $Si_{0.75}Ge_{0.25}$ and pure Si at room temperature. (After Lindner [59]). (b) Dose dependence of the optically determined damage at profile maximum for 2 MeV Si^+ implantation of the SiGe alloys with x=0.04 (o), 0.13 (squares), 0.24 (triangles) and 0.36 (closed circles). (After Nylandsted-Larsen et al. [58]).

Based on the results of Fig. 2.38 for example, a model has been proposed, which includes a number of important material parameters, represented in Fig. 2.39 [59]. First, the point defect production parameter P_p for $Si_{0.75}Ge_{0.25}$ appears to be a factor 2.8 larger, while the amorphous volume generation rate P_a is even a factor 8.3 larger than in Si. Since the stopping power in both materials is almost the same, these differences have to be attributed to a reduced stability of the chemical bonds and/or to a less effective intra-cascade annealing process. On the other hand, the recombination of PDs from different cascades described by the parameter R is 4 times stronger in the SiGe alloy than in Si (Fig. 2.39). The inter-cascade recombination increases with target temperature, which is due to the elevated PD mobility and increase with ion mass, which is attributed to the larger collision cascades of heavier ions. The increased inter-cascade PD recombination could be partially explained by the tendency of Ge to capture a V, which is then immobilized for recombination with an interstitial.

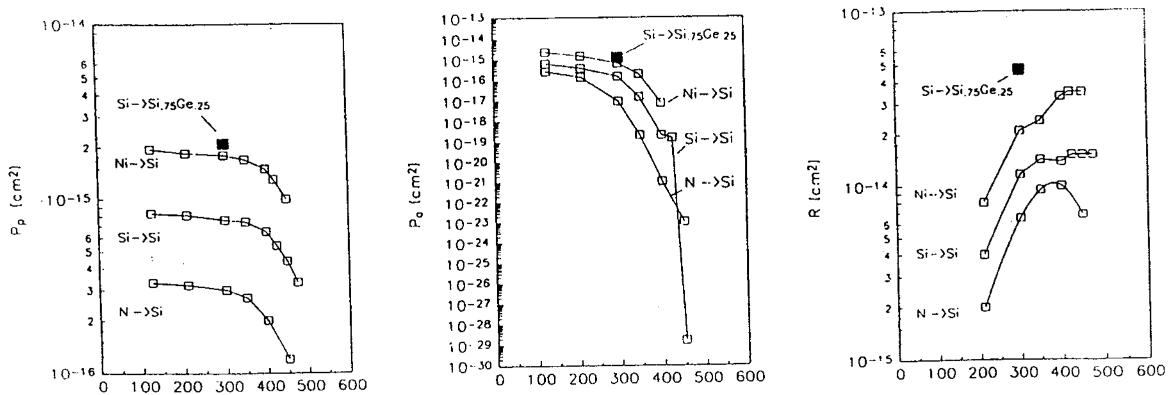

Fig. 2.39. Temperature dependence of defect production and interaction parameters, used to describe the dose dependence of damage generated by Si→$Si_{0.75}Ge_{0.25}$ and Si→Si. (After Lindner [59]).

2.4 Radiation Damage in Silicon Devices

Most radiation studies so far have been focussing on SiGe heterojunction devices (diodes or BJTs); little or no results are related to SiGe based field effect transistors. For the bipolar type of devices, the device degradation is in first instance related to displacement damage. However, as will be seen, also ionization damage plays a role for high speed BiCMOS technologies.

2.4.1 Diodes

Initial studies on heterojunction [60-61] and homojunction diodes [62] concentrated on the degradation of the forward and reverse current-voltage (I-V) characteristics. It was observed that qualitatively, the degradation of the forward I-V was similar as for a silicon diode [60]. In homojunctions irradiated by 1 Mrad of 1 or 8.5 MeV protons, a reduction of the reverse current was observed, which could be ascribed to an increase of the barrier height

for thermionic emission. At the same time, the corresponding Richardson constant of the Schottky barrier increased after the irradiation, which indicates the creation of traps at the p^+-$Si_{1-x}Ge_x$/p^--Si interface [62].

As mentioned before, a systematic study of strained layer diodes and BJTs has been undertaken by Vanhellemont, Ohyama and co-workers, using the matrix of Table 2.2. The results of these studies on diodes can be summarized as follows. Exposure to high-energy particles causes a marked degradation of the I-V characteristics, like in Fig. 2.40a [37]. Both the forward and the reverse current increase after irradiation, whereby the increase of the reverse current is linear with fluence, for not too high fluences (Fig. 2.40b). This allows to define a damage coefficient for the reverse current I_R:

$$I_R(\Phi) = I_R(0) + K_I\,\Phi \qquad (2.7)$$

with $I_R(\Phi)$,$I_R(0)$ the post and pre-rad leakage current at a certain reverse bias. Generally, V_R=-0.8 V was taken [37]. Similarly, the forward current also increases for low V_F, while in the series resistance dominated region, the current drops gradually with fluence (Fig. 2.40a). Both the increase of the forward and the reverse current indicate the creation of traps: recombination centers in the neutral part of the SiGe layer and generation centers in the depletion region, respectively. This is supported by the area dependence of the leakage current increase after irradiation (Fig. 2.41): the scaling of the reverse current with the area demonstrates the dominance of the volume generation current component over peripheral (surface) or other mechanisms.

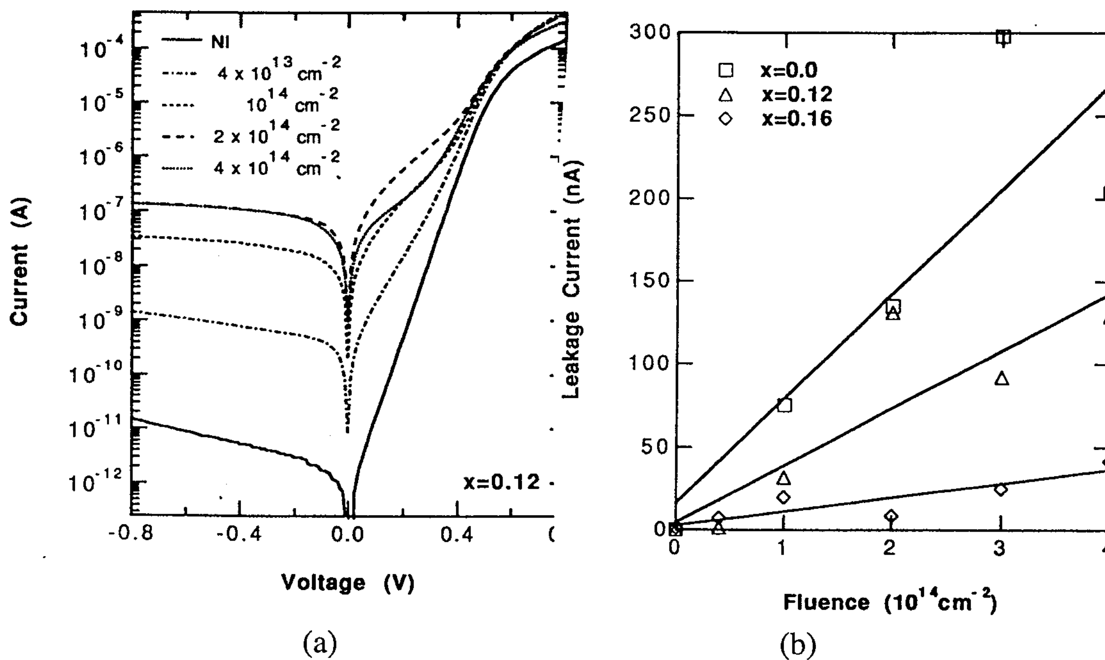

Fig. 2.40. (a) I-V characteristics recorded before (NI: not irradiated) and after irradiation with different fluences of 1 MeV electrons for x=0.12. (b) Variation of the leakage current at -0.8 V reverse bias for the three types of diodes with 1 MeV electron fluence. (After Vanhellemont et al. [37]).

The reduction of the forward current for V_F>0.5 V is in line with the reported B de-activation. The latter is derived from the C-V measurements, which show a gradual reduction of capacitance with fluence (Fig. 2.42). This reduction is more pronounced for lower x (Fig. 2.42b).

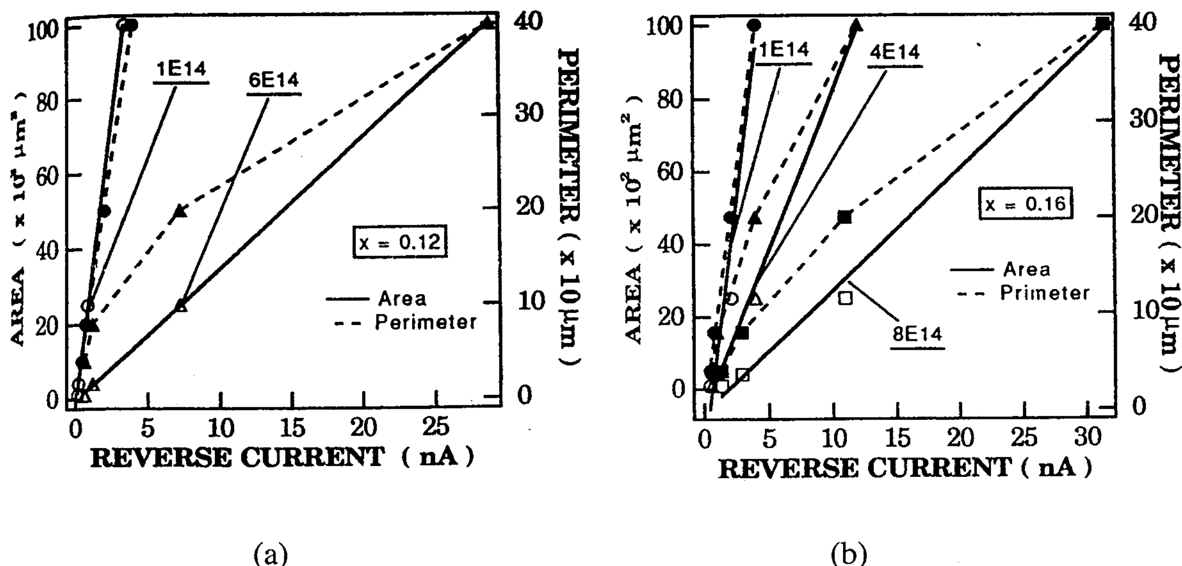

(a) (b)

Fig. 2.41. Reverse current at -0.8 V as a function of the diode area and perimeter for (a) x=0.12 and (b) x=0.16 diodes. (After Ohyama et al. [38]).

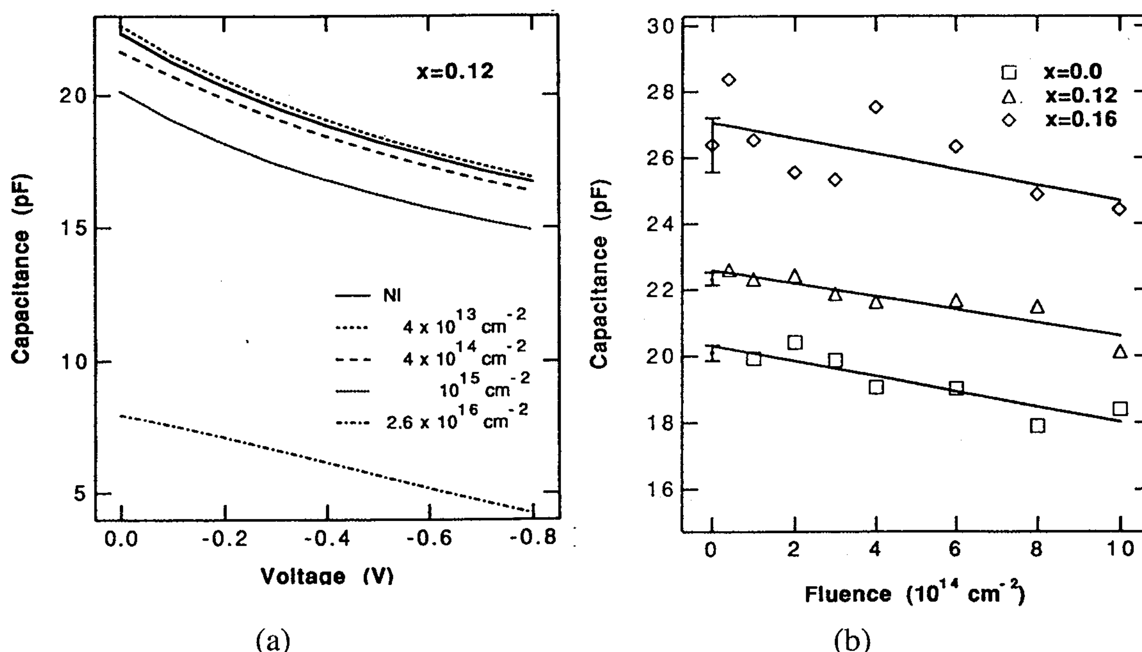

(a) (b)

Fig. 2.42. C-V characteristics recorded before (NI) and after irradiation with different fluences of 1 MeV electrons for x=0.12. (b) Variation of the capacitance with V=0 for the three types of diodes with 1 MeV electron fluence. (After Vanhellemont et al. [37]).

Annealing studies combined with DLTS have revealed a close correlation between the reverse current and the near mid gap-electron traps around E_C-0.5 eV. The annealing behavior of the diode I-V is depicted in Fig. 2.43a for an x=0.16 device; the temperature dependence is shown in more detail in Fig 2.43b for V_F=0.4 V and V_R=-0.8 V. An activation energy of ≈0.2 eV was derived for the recovery of the reverse diode current.

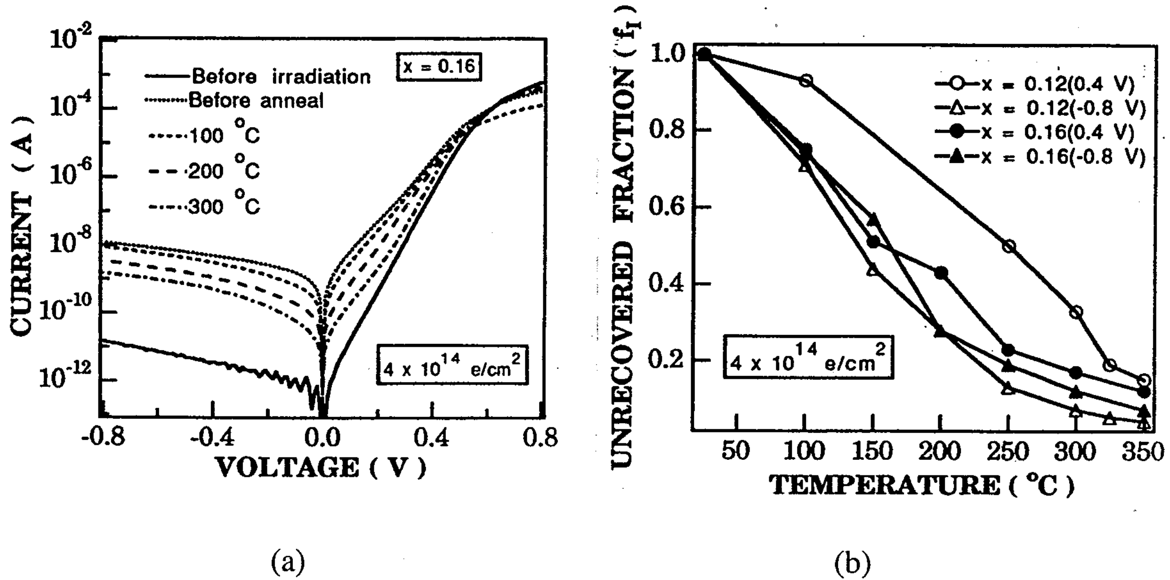

Fig. 2.43. (a) The recovery of the I-V dependence for the $4x10^{14}$ e/cm^2 irradiated x=0.16 diode, (b) The temperature dependence of the unrecovered fraction for -0.8 V and 0.4 V. (after Oyama et al. [38]).

Finally, a clear correlation has been observed between the damage coefficient for the reverse current at -0.8 V (Fig. 2.44a) and for the B de-activation (Fig. 2.44b), for the case of 20 MeV α-irradiations [46-47]. This correlation is more explicitly shown in Fig. 2.45 and can be fitted by the following empirical model:

$$K_I = 1.58x10^{-24} K_B^{0.49} \tag{2.8}$$

This again emphasizes the relationship between the displacement of B atoms into interstitial position and the leakage current generation centers in the depletion region.

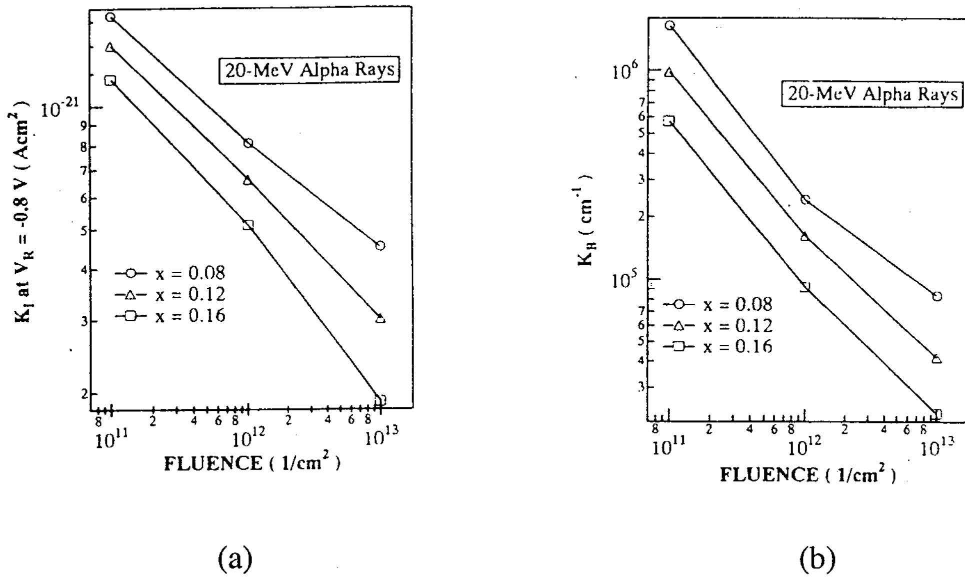

Fig. 2.44. (a) Reverse current damage coefficient at -0.8 V and (b) boron de-activation coefficient as a function of 20 MeV α-fluence, for different Ge content. (After Ohyama et al. [47]).

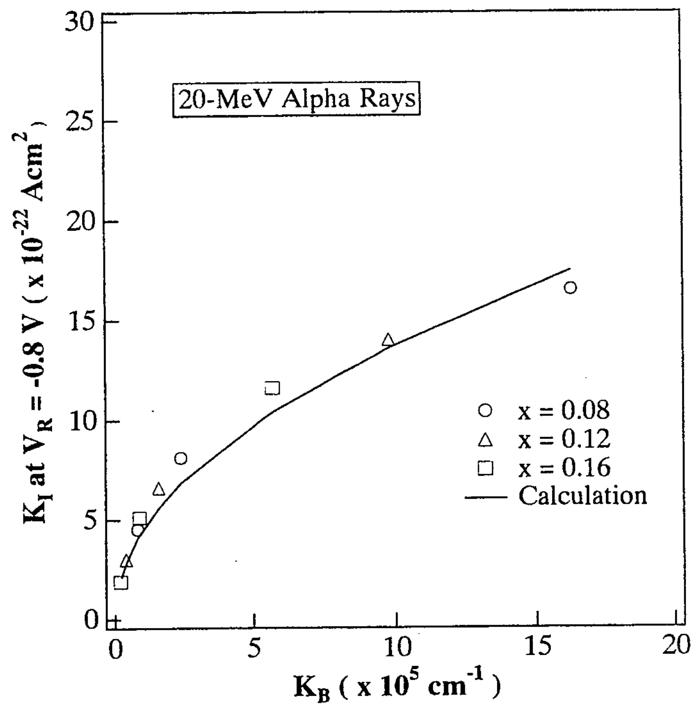

Fig. 2.45. Effective reverse current damage coefficient versus the effective B de-activation coefficient for the 20 MeV alpha fluence and Ge contents studied. (After Ohyama et al. [47]).

Finally, the damage coefficient K_I defined in Eq. (2.7) is summarized in Table 2.4, for the different irradiations and Ge contents studied. It is clear that the increase of the leakage current increases with particle mass and reduces with energy for the same particle. Furthermore, the degradation becomes larger for larger *x*, in line with previous results for K_B and for r_T (Table 2.3).

Table 2.4. Reverse current damage coefficient at 25 ^oC and V_R=-0.8 V for the different particles and Ge contents studied.

Irradiation	$K_{I0.08}$ (Acm^2)	$K_{I0.12}$ (Acm^2)	$K_{I0.16}$ (Acm^2)	Reference
1 MeV e-	--	$6.5x10^{-23}$	$5.1x10^{-23}$	S38
2 MeV e-	--	$6.0x10^{-24}$	$2.6x10^{-24}$	S41
1 MeV n	--	$6.2x10^{-21}$	$5.5x10^{-21}$	S41
20 MeV H^+	10^{-20}	$8.0x10^{-21}$	$4.2x10^{-21}$	S42
20 MeV α	$4.5x10^{-22}$	$3.0x10^{-22}$	$1.8x10^{-22}$	S47

2.4.2 HBTs

The displacement damage in IMEC's exploratory HBTs has been studied extensively. The degradation of the base (I_B) and collector (I_C) current with 1 MeV neutron fluence is illustrated by Figs 2.46a and b, respectively [40]. The base current shows a clear increase with Φ, whereby a non-ideal recombination current develops (Fig. 2.46a). For high base-emitter voltage V_{BE}, both the base and collector currents decrease, due to the increased series resistance. The latter is probably related to the B de-activation in the epitaxial SiGe base layer. The B de-activation can be derived from the C-V measurements shown in Fig. 2.47a and 2.47b, for the emitter-base and the base-collector junction.

Similarly as for the diode reverse current, one can define a damage coefficient for the DC current gain $h_{FE}(\Phi)=I_C(\Phi)/I_B(\Phi)$, yielding [40]:

$$\frac{1}{h_{FE}(\Phi)} = \frac{1}{h_{FE}(0)} + K_h \Phi \quad (2.9)$$

The resulting K_h values for a V_{BE} =0.8 V are summarized in Table 2.5. In general, the degradation behavior of the BJTs is qualitatively the same for the different particles studied. The same global trends are derived from Table 2.5 as for the diodes: more radiation tolerance for larger x and higher damage for higher particle mass, for the same energy, in line with the number of knock-on atoms of Table 2.2.

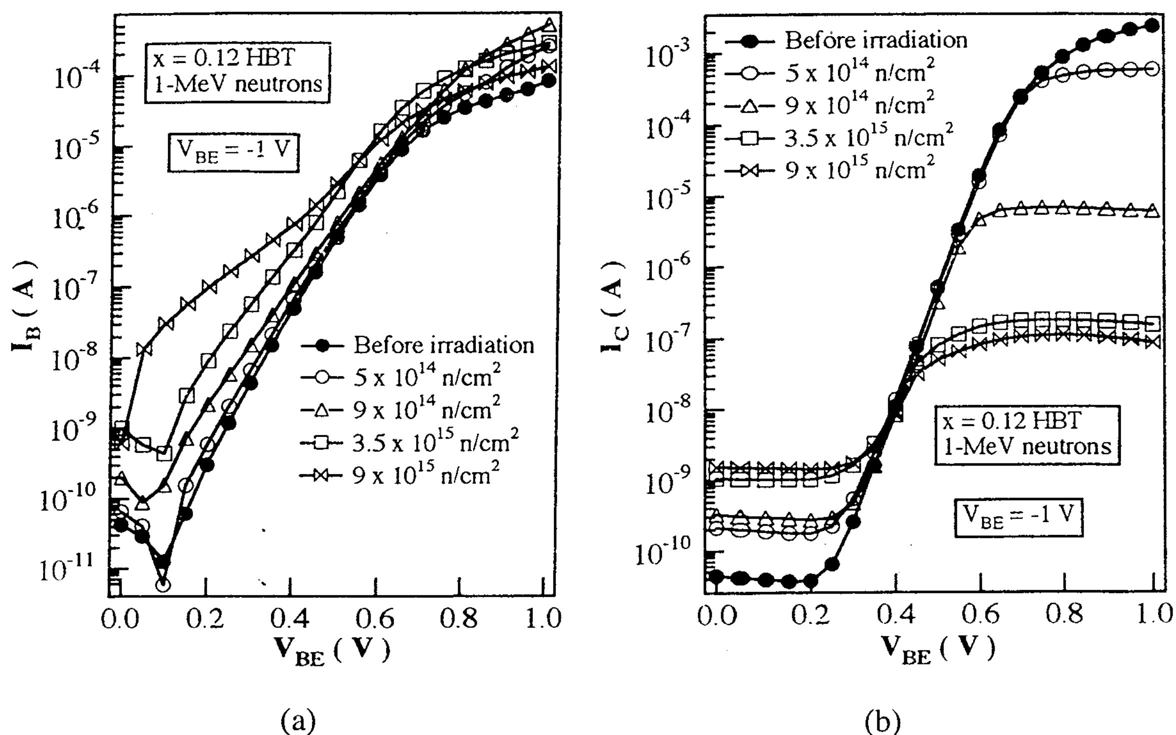

Fig. 2.46. Change of the base (a) and the collector current (b) with 1 MeV neutron fluence for an x=0.12 HBT . (After Ohyama et al. [40]).

Annealing in the temperature range 75 to 300 °C causes a considerable recovery of the base (Fig. 2.48a) and collector current (Fig. 2.48b). It is for example clear from Fig. 2.48 that B becomes activated again by annealing, yielding a lower effect of the series resistance on the forward base current. The corresponding annealing rate versus temperature is shown in Fig. 2.49, from which an average activation energy of ≈0.55 eV is derived. This is somewhat larger than the values derived for the diodes or the DLTS traps. This suggests that different traps (a different mechanism) may be responsible.

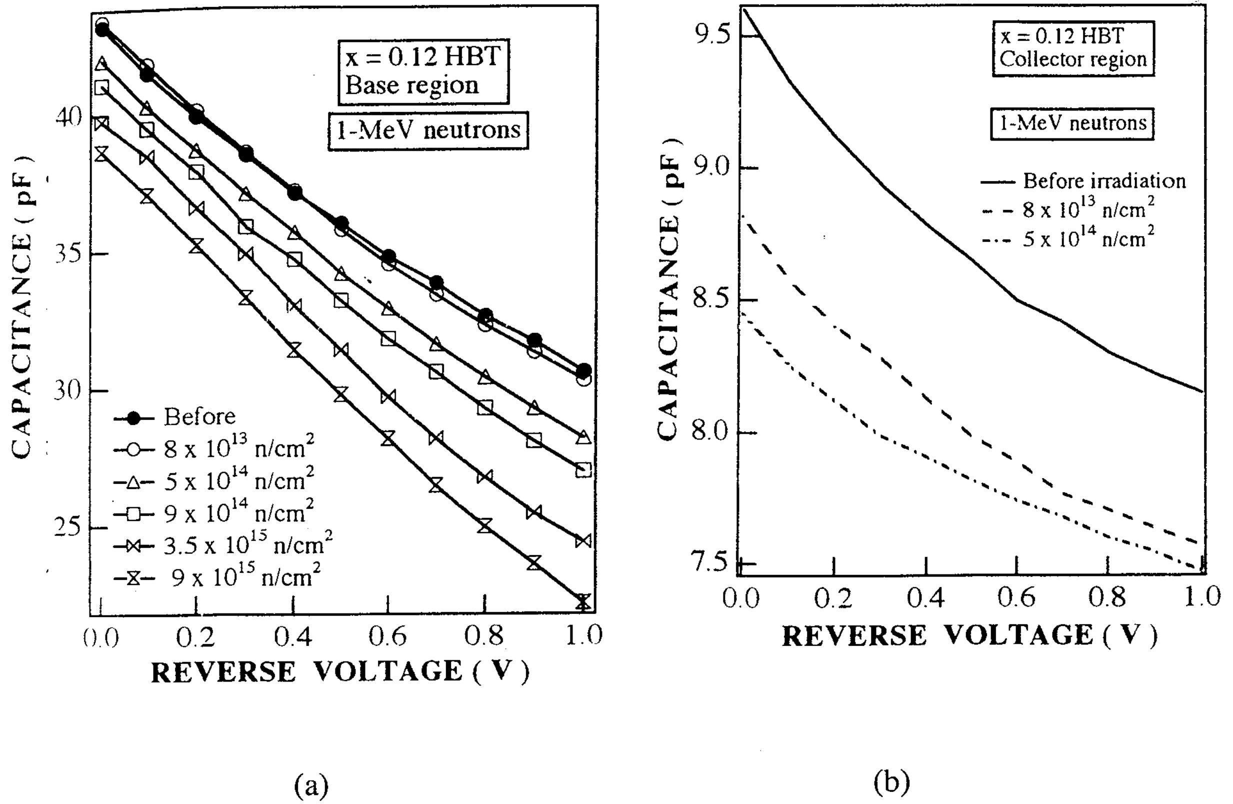

Fig. 2.47. Capacitance as a function of reverse voltage for x=0.12 HBTs for the emitter-base (a) and base-collector (b) junction. (After Ohyama et al. [40]).

Table 2.5. Damage coefficient for the current gain at V_{BE}=0.8 V for the SiGe heterojunction bipolar transistors, with different x.

Irradiation	$K_{h0.08}$ (cm^2)	$K_{h0.12}$ (cm^2)	$K_{h0.16}$ (cm^2)	Reference
2 MeV e-	$3.5x10^{-16}$	$2.7x10^{-16}$	$2.1x10^{-16}$	40
1 MeV n	$2.9x10^{-13}$	$1.8x10^{-13}$	$1.1x10^{-13}$	40
20 MeV H^+	$9.5x10^{-13}$	$5.7x10^{-13}$	$3.3x10^{-13}$	42
86 MeV H^+	$6.2x10^{-13}$	$2.3x10^{-13}$	$1.1x10^{-13}$	42

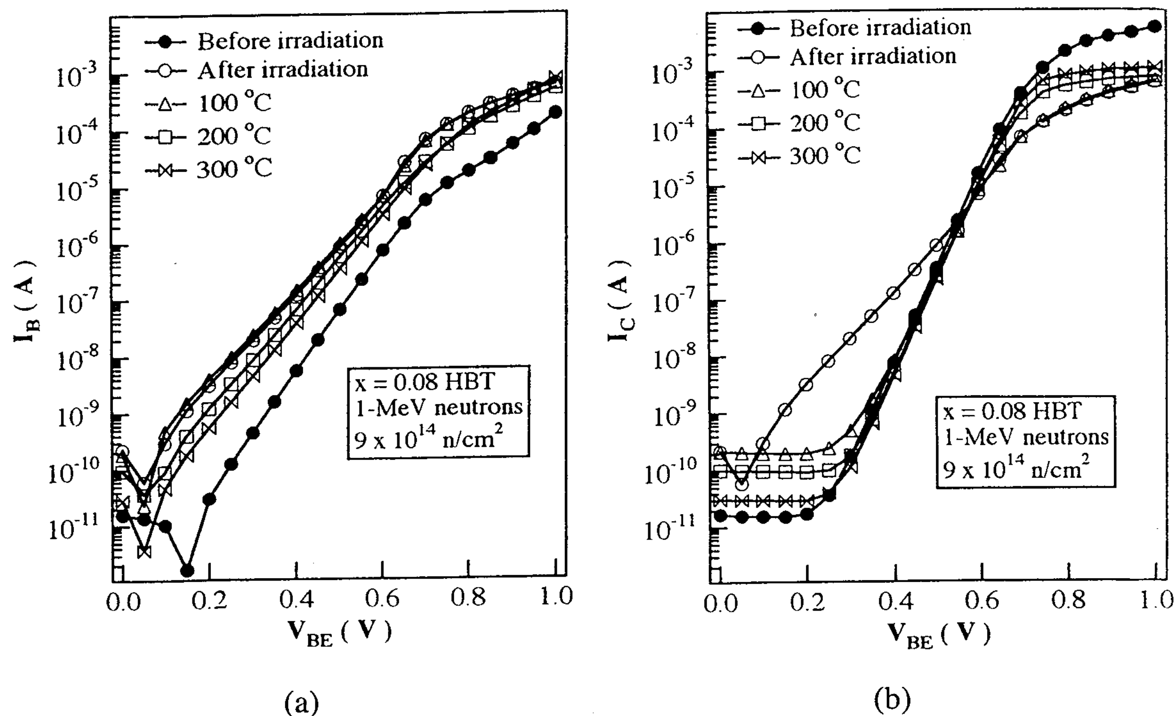

Fig. 2.48. The recovery of the base (a) and collector (b) current of the x=0.08 HBTs irradiated by 1 MeV neutrons to a fluence of $9x10^{14}$ cm^{-2}, upon 15 min isochronal annealing. (After Ohyama et al. [40]).

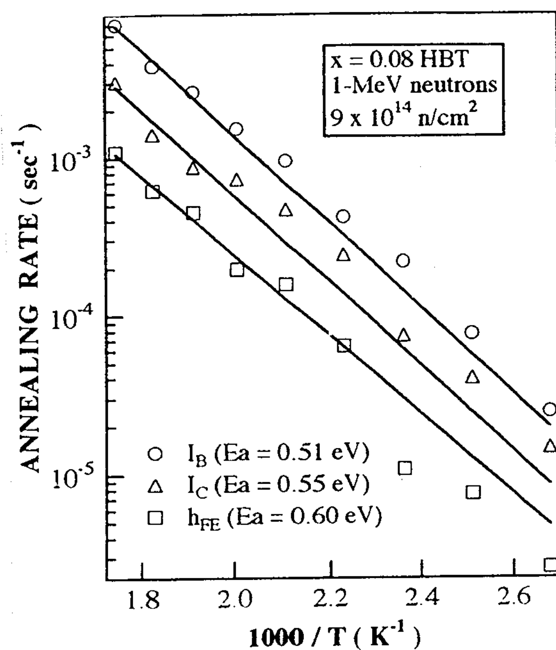

Fig. 2.49. Relationship between annealing rate and the reciprocal temperature for the x=0.08 HBTs irradiated by $9x10^{14}$ cm^{-2} 1 MeV neutrons. (After Ohyama et al. [40]).

The study of ionization damage tolerance in an advanced, fully developed 0.5 μm BiCMOS technology, with SiGe HBTs has been performed by the group of Cressler, employing room temperature [63-64] and 77 K γ-irradiations [64] and also neutron exposures [65]. The structure of the HBTs is represented in Fig. 2.4, whereby both Si and SiGe epitaxial transistors have been fabricated on the same wafers. This technology is expected to be intrinsically radiation hard, because of the use of trench isolation, of the thin oxide/nitride emitter-base spacer and of a high doping density at the surface of the epi base region.

The total dose degradation of the SiGe HBTs is summarized in Figs 2.50 to 2.52, for RT exposures up to 10 Mrad(Si). As expected, an increase of the non-ideal recombination base current is found for low I_C in Fig. 2.50, resulting in a lowering of the current gain for low collector current (Fig. 2.51). However, the shift of the peak β is only 20 % after 10 Mrad(Si) total dose, which is much more tolerant than many so-called radiation-hardened bipolar technologies. This confirms the intrinsic hardness of the structure of Fig. 2.49.

The response of the current gain as a function of total γ-dose shows three regions in Fig. 2.52: below 20 krad no degradation whatsoever is observed. For intermediate doses (≤1 Mrad(Si)), β increases ! This is believed to correspond to an increase of the collector current, shown for example in Fig. 2.53 [64]. It is demonstrated there that the increase in I_C is not due to a radiation-induced inversion of the base-emitter surface or a radiation-induced heating, but rather related to a change of the lifetime properties of the emitter-base junction. Beyond 2 Mrad(Si), β decreases.

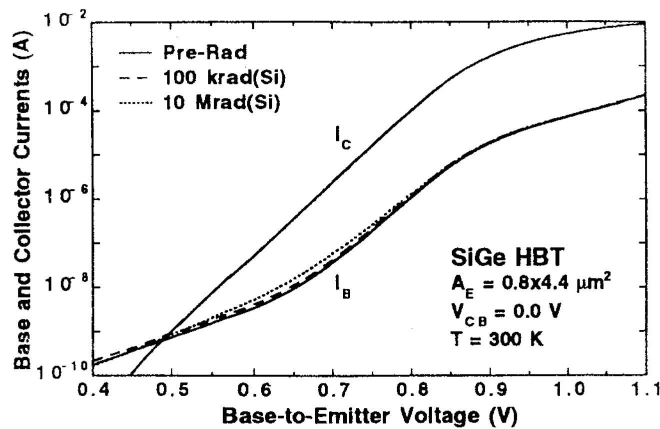

Fig. 2.50. Typical Gummel characteristics for a SiGe HBT (emitter area A_E=0.8x4.4 μm^2) both before and after radiation exposure at RT. (After Babcock et al. [64]).

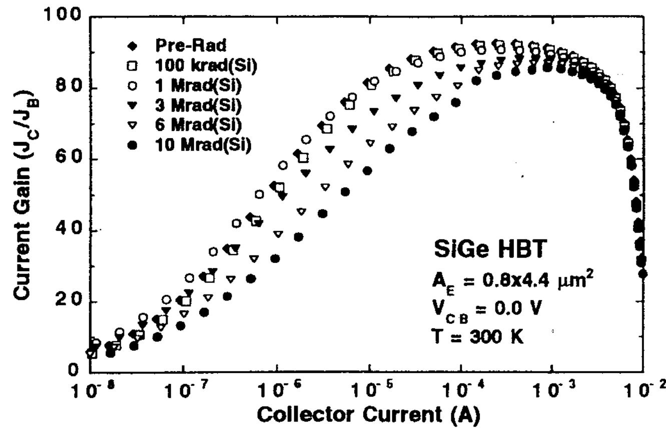

Fig. 2.51. Pre- and post-radiation current gain (b) versus the collector current at 300 K for the SiGe HBT (A_E=0.8x4.4 μm^2) shown in Fig. 50. (After Babcock et al. [64]).

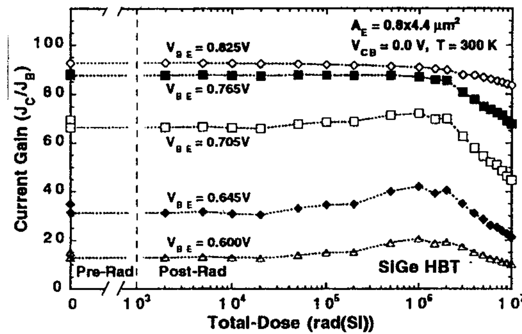

Fig. 2.52. Current gain at 300 K of the SiGe shown in Fig. 50 as a function of total dose at constant base-to-emitter voltage V_{BE}. (After Babcock et al. [64]).

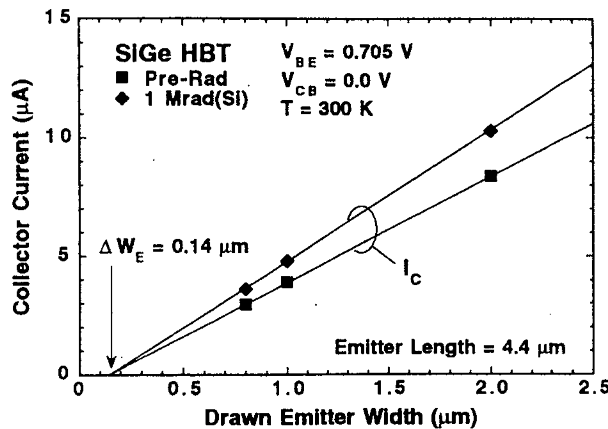

Fig. 2.53. Technique used to extract the electrical area of the SiGe HBT by plotting the measured collector and base current of the SiGe HBTs as a function of the drawn emitter width. For extraction of ΔW_E the emitter length is held constant and the V_{BE}=0.705 V; also shown is the measured collector currents after 1.0 Mrad(Si) (After Babcock et al. [64]).

From the area/perimeter dependence of the current gain degradation it is concluded that for doses below 2 Mrad(Si) the changes are governed by changes in the emitter-base bulk properties. For higher doses, perimeter effects start to be discernable, pointing towards a positive charging of the spacer oxides [64]. There is also evidence that charging of the trench oxides occurs for high doses, which affects the Miller capacitance [64].

The radiation response after 77 K exposure (important for certain space applications) is shown in Fig. 2.54. In this case, the current gain initially decreases slightly, but recovers for doses >1Mrad(Si). This is related to a slight improvement of the post-radiation I_B characteristics and a slight increase in I_C [65]. It has finally been observed that after irradiation, the low frequency 1/f noise increases and GR noise components can be introduced (Fig. 2.55). The latter are related to the occurrence of Random Telegraph Signals (RTSs) in the base current of the transistor [63-64]. The noise increase can be a problem for analog or mixed mode applications in BiCMOS.

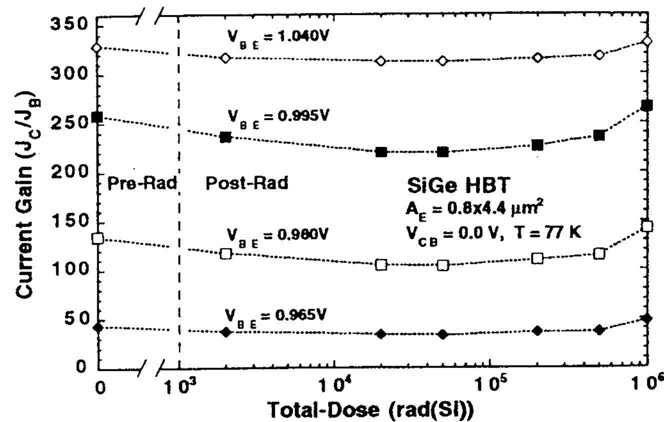

Fig. 2.54. Current gain at 77 K of the SiGe HBT as a function of total dose radiation at constant V_{BE}. Note that β is larger at 77 K than at 300 K (Fig. 50) for this device, which has been optimized for cryogenic operation. (After Babcock et al. [64]).

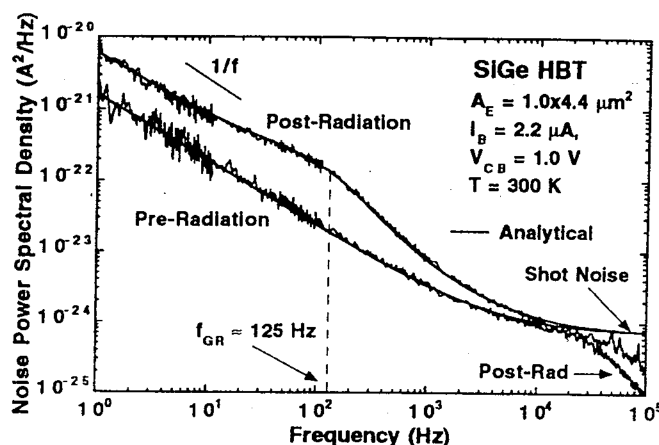

Fig. 2.55. Equivalent input referred base noise power spectral density S_{IB} measured pre- and post-radiation at 300 K for a SiGe HBT (A_E=1.0x4.4 μm^2) showing a radiation induced GR center. (After Babcock et al. [64]).

Qualitatively similar results have been obtained after neutron exposure [65]. From Fig. 2.56 it is derived that there is no marked difference in hardness between a Si or a SiGe base transistor. Additionally, the Ge doping profile used has little impact on the response. The damage factor in Fig. 2.56 is defined as β_{post}/β_{pre}. The technological details do have, however, a strong impact: compare for example the damage factor for a hardened technology, with the corresponding value for non-hardened exploratory devices (Fig. 2.57), [65]. Finally, also the dynamic radiation response has been evaluated after neutron exposure. While hardly no change was found in the cutoff frequency f_T, a stronger degradation was found for the maximum oscillation frequency f_{max}, which was more pronounced for the HBTs (compare Fig. 2.58 a and b). According to the expression:

$$f_{max} = \sqrt{\frac{f_T}{8\pi R_b C_{cb}}} \qquad (2.10)$$

this degradation is either due to a change in the total base resistance R_b or in the total base-collector capacitance C_{cb}, for constant cutoff frequency. Analyzing the S parameters in more detail shows that R_b increases after irradiation, although this is not related to an increase in the sheet resistance of the SiGe base layer. The constancy of f_T, on the other hand, points to the fact that the lifetime and transit (transport) parameters in the intrinsic transistor are not affected by the irradiation. This is confirmed by Early voltage measurements, which do not indicate the creation of bulk traps in the base-emitter depletion region after neutron exposure [65]. This is in contrast with the results obtained on the IMEC devices, which have a much larger 'target' volume.

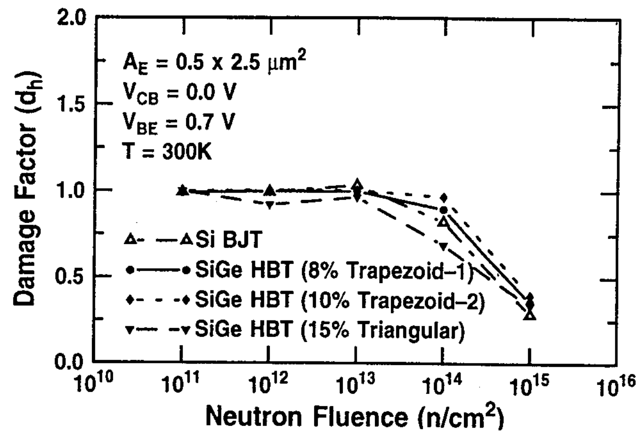

Fig.2.56. Normalised current gain as a function of neutron fluence for SiGe and Si transistors. (After Babcock et al. [65]).

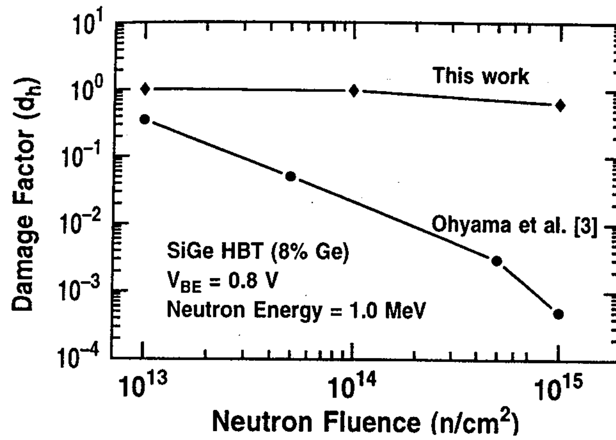

Fig. 2.57. Damage factor as a function of neutron fluence for a SiGe HBT with 8 % Ge content. (After babcock et al. [65]).

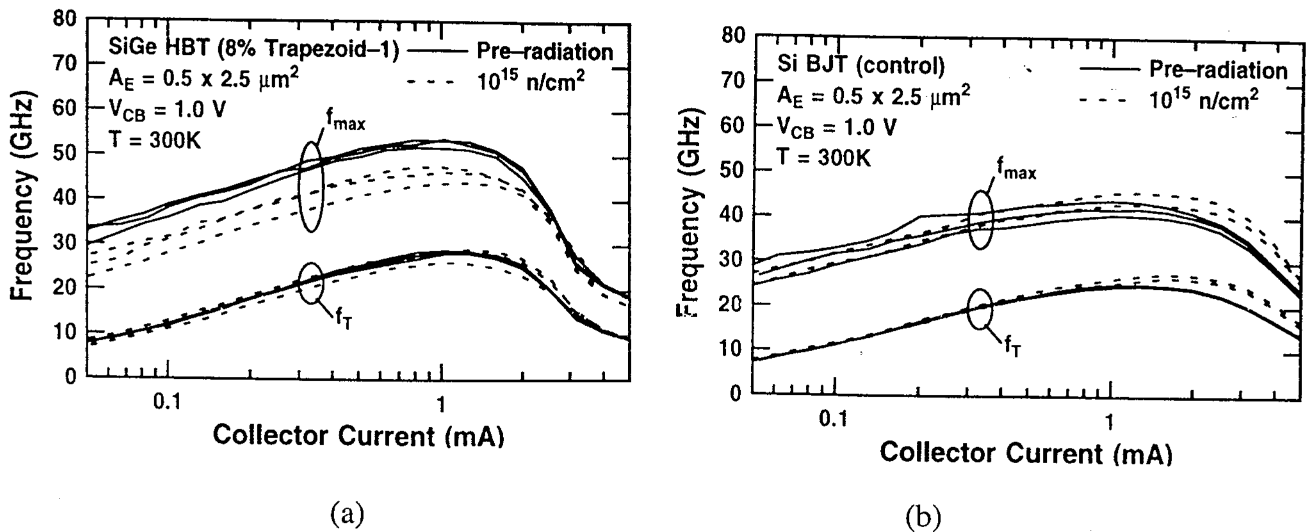

Fig. 2.58. Maximum oscillation frequency and cutoff frequency as a function of collector current for the SiGe HBT (a) and the Si BJT (b), before and after irradiation. (After Babcock et al. [65]).

It has finally been demonstrated that radiation hard bipolar transistor and thyristors can be fabricated in n-Si material doped with $7.5x10^{19}$ cm^{-3} Ge [25].

2.5 Conclusions

In recent years, a considerable amount of information has been gathered concerning the radiation response of SiGe material and devices. However, much work remains to be done both at the fundamental side and at the more practical end. The nature of the dominant radiation defects is becoming clear, although the identification is more difficult due to the Ge fraction dependence of the trap level parameters. Some deep levels are pinned to the conduction band, other to the valence band. This fact should also be taken into consideration when modeling the impact of a specific GR center on the electrical properties of the epilayer (generation-recombination lifetime, leakage current, etc...). Furthermore, other unknown mechanisms may play a role in determining the electrical properties of trap levels, like alloy broadening and local valence band fluctuations owing to the fluctuations in the Ge content.

It was also demonstrated that adding Ge to the lattice in many cases causes a hardening of the alloy. However, for several applications, the range of useful Ge fraction is rather narrow (8 to 16 % for HBTs); 25-30 % for field-effect transistors... Furthermore, when the peak damage is considered the opposite trend is often found, especially after implantation or for near surface damage produced by dry etching, sputtering, etc... Further studies are needed to fully understand the interaction of radiation with SiGe epilayers.

While the radiation response of SiGe diodes and BJTs is fairly well documented, so far nothing is known about the field-effect devices (vertical MOSFETs, MODFETs, SiGe channel MOSFETs,...). Considerable work needs to be done in this field, in order to quantify and model the ionization damage and to compare these advanced devices with more standard MOSFETs.

References

[1] D.V. Lang, R. People, J.C. Bean and A.M. Sergent, "Measurement of the band gap of Ge_xSi_{1-x}/Si strained-layer heterostructures", Appl. Phys. Lett. **47**, 1333 (1985).

[2] C.K. Maiti, L.K. Bera and S. Chattopadhyay, "Strained-Si heterostructure field effect transistors", Semicond. Sci. Technol. **13**, 1225 (1998).

[3] T. Honda, M. Suezawa and K. Sumino, "Growth and characterization of bulk Si-Ge single crystals", Jpn. J. Appl. Phys. **35**, 5980 (1996).

[4] S.C. Jain and W. Hayes, "Structure, properties and applications of Ge_xSi_{1-x} strained layers and superlattices", Semicond. Sci. Technol. **6**, 547 (1991).

[5] H.J. Osten, "Band-gap changes and band offsets for ternary $Si_{1-x-y}Ge_xC_y$ alloys on Si(001)", J. Appl. Phys. **84**, 2716 (1998).

[6] M. Franz, K. Pressel and P. Gaworzewski, "Alloy effects in boron doped Si-rich and SiGe bulk crystals", J. Appl. Phys. **84**, 709 (1998).

[7] M. Wolf, R. Brendel, J.H. Werner and H.J. Queisser, "Solar cell efficiency and carrier multiplication in $Si_{1-x}Ge_x$ alloys", J. Appl. Phys. **83**, 4213 (1998).

[8] K. Said, J. Poortmans, M. Libezny, J. Nijs, R. Mertens, C. Vinckier, D. Vyncke, W. Seifert, M. Kittler, I. Silier, A. Gutjahr and M. Konuma, "Low-temperature passivation for SiGe-alloy solar cells", in: Proc. 14th European Photovoltaic Solar Eenergy Conference", Barcelona (Spain), 30 June - 4 July 1997, pp. 986-992 (1997).

[9] F.L. LeGoues, B.S. Meyerson, J.F. Morar and P.D. Kirchner, "Mechanism and conditions for anomalous strain relaxation in graded thin films and superlattices", J. Appl. Phys. **71**, 4230 (1992).

[10] J.D. Cressler, "Status and trends in the cryogenic operation of SiGe bipolar technology", In: The Proc. of the Symposium on Low Temperature Electronics and High Temperature Superconductivity, Eds. C.L. Claeys, S.I. Raider, R. Kirschman and W.D. Brown, The Electrochem. Soc. Proc. Vol. **95-9**, The Electrochem. Soc. (Pennington, NJ), pp. 159-177 (1995).

[11] D.K. Nayak, J.C.S. Woo, J.S. Park, K.L. Wang and K.P. MacWilliams, "Enhancement-mode quantum-well Ge_xSi_{1-x} PMOS", IEEE Electron Device Lett. **12**, 154 (1991).

[12] A.G. O'Neill and D.A. Antoniadis, "Deep submicron CMOS based on silicon germanium technology", IEEE Trans. Electron Devices **43**, 911 (1996).

[13] J. Welser, J.L. Hoyt and J.F. Gibbons, "Electron mobility enhancement in strained-Si n-type metal-oxide-semiconductor field-effect transistor", IEEE Electron Device Lett. **15**, 100 (1994).

[14] K. De Meyer, S. Biesemans, N. Collaert, S. Kubicek and P. Verheyen, "New architectures for deep submicron MOSFETs", In: Proc. ESSDERC '98, Eds. A. Touboul, Y. Danto, J.-P. Klein and H. Grünbacher, Editions Frontières (Paris, France), pp. 63-68 (1998).

[15] R.P.G. Karunasiri and K.L. Wang, "Quantum devices using SiGe/Si heterostructures", J. Vac. Sci. Technol. **B9**, 2064 (1991).

[16] O. Nur, M. Willander, R. Turan, M.R. Sardela, Jr. and G.V. Hansson, "Metal-semiconductor junctions on p-type strained $Si_{1-x}Ge_x$ layers", Appl. Phys. Lett. **68**, 1084 (1996).

[17] D. Dentel, L. Kubler, J.L Bischoff, S. Chattopadhyay, L.K. Bera, S.K. Ray and C.K. Maiti, "Molecular beam epitaxial growth of strained $Si_{1-x}Ge_x$ layers on graded $Si_{1-y}Ge_y$ for Pt silicide diodes", Semicond. Sci. Technol. **13**, 214 (1998).

[18] T.G. Jung, C.Y. Chang, C.S. Liu, T.C. Chang, H.C. Lin, W.C. Tsai, G.W. Huang and L.P. Chen, "Characterization of the Si/SiGe heterojunction diode grown by ultrahigh vacuum chemical vapor deposition", Appl. Phys. Lett. **76**, 4921 (1994).

[19] A. Vonsovici, L. Vescan, R. Apetz, A. Koster and K. Schmidt, "Room temperature photocurrent spectroscopy of SiGe/Si p-i-n photodiodes grown by selective epitaxy", IEEE Trans. Electron Devices **45**, 538 (1998).

[20] S.-J. Chang, D.K. Nayak and Y. Shiraki, "1.54 μm electroluminescence from erbium-doped SiGe light emitting diodes", J. Appl. Phys. **83**, 1426 (1998).

[21] S. Sedky, P. Fiorini, M. Caymax, C. Baert, L. Hermans and R. Mertens, "Characterization of bolometers based on polycrystalline silicon germanium alloys", IEEE Electron Device Lett. **19**, 376 (1998).

[22] G.D. Watkins, "Defects in irradiated silicon: EPR of the tin-vacancy pair", Phys. Rev. B **12**, 4383 (1975).

[23] K. Schmalz and V.V. Emtsev, "Radiation-induced defects in Czochralski-grown silicon doped with germanium", Appl. Phys. Lett. **65**, 1575 (1994).

[24] B.G. Svensson, J. Svensson, J.L. Lindström, G. Davies and J.W. Corbett, "Generation of divacancies in tin-doped silicon", Appl. Phys. Lett. **51**, 2257 (1987).

[25] S.V. Bytkin, "Use of germanium doped silicon (n-Si<Ge>) for manufacturing radiation hardened devices and integrated circuits", In: Proc. RADECS '97, Eds. G. Barbottin and P. Dressendorfer, The IEEE (New York), pp. 141-146 (1998).

[26] A. Kawasuso, S. Okada, I. Yonenaga, T. Honda and M. Suezawa, "Positron annihilation study of electron-irradiated silicon-germanium bulk alloys", Materials Science Forum, Vols **258-263**, pp. 127-132 (1997).

[27] A. Kawasuso, S. Okada, M. Suezawa, T. Honda and I. Yonenaga, "Positron annihilation in electron-irradiated Si_xGe_{1-x} bulk crystal ", J. Appl. Phys., 81, pp. 2916-2918 (1997)

[28] J.J. Goubet, D. Stievenard, D. Mathiot and M. Zazoui, "Electron-irradiation-induced defects in Si-Ge alloys", Phys. Rev. B **46**, 10113 (1992).

[29] J.J. Goubet and D. Stievenard, "Annealing study of electron irradiation-induced defects in SiGe alloys", Appl. Phys. Lett. **66**, 1409 (1995).

[30] P. Kringhoj and A. Nylandsted Larsen, "Irradiation-induced defect states in epitaxial n-type $Si_{1-x}Ge_x$ alloy layers", Phys. Rev. B **52**, 16333 (1995).

[31] A. Nylandsted Larsen, "Defects in SiGe", Materials Science Forum, Vols. **258-263**, pp. 83-90 (1997).

[32] E.V. Monakhov, A. Nylandsted Larsen and P. Kringhoj, "Electronic defect levels in relaxed, epitaxial p-type $Si_{1-x}Ge_x$ layers produced by MeV proton irradiation", J. Appl. Phys. **81**, 1180 (1997).

[33] P.J. Drevinsky, C.E. Caefer, S.P. Tobin, J.C. Mikkelsen, Jr. and L.C. Kimerling, "Influence of oxygen and boron on defect production in irradiated silicon", Mat. Res. Soc. Symp. Proc., Vol. **104**, pp. 167-172 (1988).

[34] S.A. Goodman, F.D. Auret, K. Nauka and J.B. Malherbe, "Defect characterization in n-type $Si_{1-x}Ge_x$ after 1.0 keV helium-ion etching", J. Electron. Mater. **26**, 463 (1997).

[35] S.A. Goodman, F.D. Auret, M. Mamor, P.N.K. Deenapanray and W.E. Meyer, "Electronic properties of defects introduced in n- and p-type $Si_{1-x}Ge_x$ during ion etching", Materials Science Forum, Vols **258-263**, pp. 133-138 (1997).
[36] J. Vanhellemont, M.-A. Trauwaert, J. Poortmans, M. Caymax and P. Clauws, "1 MeV electron irradiation induced degradation of boron doped strained $Si_{1-x}Ge_x$ layers", Thin Solid Films **222**, 166 (1992).
[37] J. Vanhellemont, M.-A. Trauwaert, J. Poortmans, M. Caymax and P. Clauws, "Fast degradation of boron-doped strained $Si_{1-x}Ge_x$ layers by 1-MeV electron irradiation", Appl. Phys. Lett. **62**, 309 (1993).
[38] H. Ohyama, J. Vanhellemont, H. Sunaga, J. Poortmans, M. Caymax and P. Clauws, "On the degradation of 1-MeV electron irradiated $Si_{1-x}Ge_x$ diodes", IEEE Trans. Nucl. Sci. **41**, 487 (1994).
[39] H. Ohyama, J. Vanhellemont, Y. Takami, K. Hayama, H. Sunaga, J. Poortmans, M. Caymax and P. Clauws, "Germanium content dependence of radiation damage in strained $Si_{1-x}Ge_x$ epitaxial devices", IEEE Trans. Nucl. Sci. **41**, 2437 (1994).
[40] H. Ohyama, J. Vanhellemont, Y. Takami, K. Hayama, H. Sunaga, J. Poortmans and M. Caymax, "Degradation of $Si_{1-x}Ge_x$ epitaxial heterojunction bipolar transistors by 1-MeV fast neutrons", IEEE Trans. Nucl. Sci. **42**, 1550 (1995).
[41] H. Ohyama, J. Vanhellemont, Y. Takami, K. Hayama, H. Sunaga, J. Poortmans and M. Caymax, "Radiation source dependence of degradation and recovery of irradiated $Si_{1-x}Ge_x$ epitaxial devices", In: Proc. RADECS '95, The IEEE (New York), pp. 66-71 (1996).
[42] H. Ohyama, K. Hayama, J. Vanhellemont, J. Poortmans, M. Caymax, Y. Takami, H. Sunaga, I. Nashiyama and Y. Uwatoko, "Degradation of $Si_{1-x}Ge_x$ epitaxial devices by proton irradiation", Appl. Phys. Lett. **69**, 2429 (1996).
[43] H. Ohyama, J. Vanhellemont, Y. Takami, K. Hayama, H. Sunaga, I. Nashiyama, Y. Uwatoko, J. Poortmans and M. Caymax, "Degradation and recovery of proton irradiated $Si_{1-x}Ge_x$ epitaxial devices", IEEE Trans. Nucl. Sci. **43**, 3089 (1996).
[44] H. Ohyama, J. Vanhellemont, Y. Takami, H. Sunaga, I. Nashiyama, Y. Uwatoko, J. Poortmans and M. Caymax, "Degradation of SiGe devices by proton irradiation", Radiat. Phys. Chem. **50**, 341 (1997).
[45] H. Ohyama, E. Simoen, C. Claeys, J. Vanhellemont, Y. Takami, H. Sunaga, J. Poortmans and M. Caymax, "Lattice defects in $Si_{1-x}Ge_x$ devices by proton irradiation and their effect on device performance", Solid State Phenomena, Vols. **57-58**, pp. 239-244 (1997).
[46] H. Ohyama, E. Simoen, C. Claeys, Y. Takami, K. Hayama, T. Hakata, K. Kobayashi, H. Sunaga, J. Poortmans and M. Caymax, "The impact of the Ge content on the characteristics of strained $Si_{1-x}Ge_x$ epitaxial diodes before and after degradation by high energy particles", In: Proc. ESSDERC '98, Eds. A. Touboul, Y. Danto, J.P. Klein and H. Grünbacher, Les Editions Frontières (Paris, France), pp. 548-551 (1998).
[47] H. Ohyama, E. Simoen, C. Claeys, Y. Takami, K. Hayama, T. Hakata, H. Sunaga, J. Poortmans and M. Caymax, "Impact of high energy particle irradiation on the electrical

performance of $Si_{1-x}Ge_x$ epitaxial diodes", In: Proc. 2nd Int. Conf. on Materials for Microelectronics, The Institute of Materials (London, UK), pp. 11-18 (1998).
[48] K.L. Wang, Y.H. Lee and J.W. Corbett, "Defect distribution near the surface of electron-irradiated silicon", Appl. Phys. Lett. **33**, 547 (1978).
[49] L.C. Kimerling, M.T. Asom, J.L. Benton, P.J. Drevinsky and C.E. Caefer, "Interstitial defect reactions in silicon", Materials Science Forum, Vols. **38-41**, pp. 141-150 (1989).
[50] G.D. Watkins and J.R. Troxell, "Negative-U properties for point defects in silicon", Phys. Rev. Lett. **9**, 593 (1980).
[51] J.R. Troxell and G.D. Watkins, "Interstitial boron: A negative-U system", Phys. Rev. B 22, 921 (1980).
[52] G.D. Watkins, "Negative-U properties for point defects in silicon", In: Defects in Semiconductors", Eds Nayaran and Tan, North-Holland, Inc, pp. 21-30 (1981).
[53] M. Mamor, F.D. Auret, S.A. Goodman and G. Myburg, "Electrical characterization of defects introduced in p- $Si_{1-x}Ge_x$ during electron-beam deposition of Sc Schottky barrier diodes", Appl. Phys. Lett. **72**, 1069 (1998).
[54] M. Mamor, F.D. Auret, S.A. Goodman, G. Myburg, P.N.K. Deenapanray and W.E. Meyer, "Electrical characterization of electron beam induced defects in epitaxially grown $Si_{1-x}Ge_x$ ", Materials Science Forum, Vols. **258-263**, pp. 115-120 (1997).
[55] D.Y.C. Lie, "Doping and processing epitaxial $Si_{1-x}Ge_x$ films on Si(100) by ion implantation for Si-based heterojunction devices applications", J. Electron Mater. **27**, 377 (1998).
[56] T.E. Haynes and O.W. Holland, "Damage accumulation during ion implantation of unstrained $Si_{1-x}Ge_x$ alloy layers", Appl. Phys. Lett. **61**, 61 (1992).
[57] O.W. Holland and T.E. Haynes, "Damage saturation during high-energy ion implantation of $Si_{1-x}Ge_x$ ", Appl. Phys. Lett. **61**, 3148 (1992).
[58] A. Nylandsted Larsen, C.O. Raifeartaigh, R.C. Barklie, B. Holm, F. Priolo, G. Franzo, G. Lulli, M. Bianconi, R. Nipoti, J.K.N. Lindner, A. Mesli, J.J. Grob, F. Cristiano and P.L.F. Hemment, "MeV ion implantation induced damage in relaxed $Si_{1-x}Ge_x$", J. Appl. Phys. **81**, 2208 (1997).
[59] J.K.N. Lindner, "Radiation damage of 2 MeV Si ions in $Si_{0.75}Ge_{0.25}$: optical measurements and damage modelling", Nucl. Instrum. Methods Phys. Research B **112**, 316 (1996).
[60] M. Willander, G.-D. Shen, D.-X. Xu and W.-X. Ni, "Current transport in strained n-$Si_{1-x}Ge_x$ /p-Si heterojunction diodes", J. Appl. Phys. **63**, 5036 (1988).
[61] D.X. Xu, G.D. Shen, M. Willander, J. Knall, M.-A. Hasan and G.V. Hansson, "The influence of defects on device performance of MBE-grown Si homojunction and strained $Si_{1-x}Ge_x$ /Si heterostructures", J. Electron Materials **19**, 1033 (1990).
[62] J.S. Park, T.L. Lin, E.W. Jones, S.D. Gunapala, G.A. Soli and B.A. Wilson, "Proton irradiation effects on strained $Si_{1-x}Ge_x$ /Si heterostructures", Appl. Phys. Lett. **63**, 3497 (1993).
[63] J.A. Babcock, J.D. Cressler, L.S. Vempati, S.D. Clark, R.C. Jaeger and D.L. Harame, "Ionizing radiation tolerance and low-frequency noise degradation in UHV/CVD SiGe HBTs", IEEE Electron Device Lett. **16**, 351 (1995).

[64] J.A. Babcock, J.D. Cressler, L.S. Vempati, S.D. Clark, R.C. Jaeger and D.L. Harame, "Ionizing radiation tolerance of high-performance SiGe HBTs grown by UHV/CVD", IEEE Trans. Nucl. Sci. **42**, 1558 (1995).

[65] J.M. Roldan, W.E. Ansley, J.D. Cressler, S.D. Clark and D. Nguyen-Ngoc, "Neutron radiation tolerance of advanced UHV/CVD SiGe HBT BiCMOS technology", IEEE Trans. Nucl. Sci. **44**, 1965 (1997).

3. SPACE RADIATION ASPECTS OF SILICON BIPOLAR TECHNOLOGIES

Bipolar Junction Transistors (BJT) have important applications in analog or mixed signal ICs and BiCMOS (Bipolar Complementary Metal-Oxide-Semiconductor) circuits because of their current-drive capability, linearity, and excellent matching characteristics. Furthermore, their microwave performance compares favorably with respect to CMOS, explaining the use in GHz telecommunications applications. The implementation of a SiGe heterojunction base will further push the penetration of BiCMOS in the microwave applications field. In addition, BJTs are frequently used in space systems, including operational amplifiers, comparators and voltage regulators, in order to accomplish analog functions. Early generations of BJT based circuits mainly suffered from radiation-induced leakage currents associated with the degraded field-oxide isolation regions. However, solutions for these problems have been implemented in present-day technologies, so that other degradation mechanisms are more important now. In this chapter, a review will be given related to radiation damage in modern BJTs. In a first part, the different type of device architectures (vertical, substrate, lateral BJT) will be briefly defined and the basic degradation mechanisms described. In a second part, focus is on the radiation effects in vertical NPN BJTs. Part three covers the radiation degradation in lateral and substrate BJTs. In the last part, some conclusions will be drawn. It should finally be mentioned that IMEC has been actively involved in the development of BiCMOS technologies. Presently, a 0.35 μm technology is available, while the development of the next generation (0.25 μm) is underway. Both epitaxial silicon and SiGe versions of these technologies are being developed in parallel.

3.1 Device Structures and basic Radiation Effects

3.1.1 Device Structuress and Definitions

Different types of BJT architectures can be used for specific applications. They are illustrated in Fig. 3.1, for p-n-p devices [1]; complementary structures exist for the n-p-n counterparts. One can distinguish between vertical (V), lateral (L) and substrate (S) transistors. In the case of vertical and substrate devices, the current flow is mainly in the vertical direction. Lateral devices are characterized by a current flow parallel to the surface. A schematic top view of a vertical device is given in Fig. 3.2, defining the emitter and intrinsic base. The extrinsic base is adjacent to the intrinsic one and is more highly doped to reduce the contact and base series resistance. Originally, a crystalline silicon emitter was used, contacted by aluminum metallization. More recently, a polycrystalline (poly) emitter is replacing the crystalline emitter, which is more amenable for scaling to the submicron regime. Both single and double polysilicon technologies have been developed. In the latter case, a polysilicon base and emitter contact of opposite doping type is implemented. An important part of the structure is the oxide covering the surface of the base-emitter junction region, often called sacrificial, screening or spacer oxide. In commercial technologies, the oxide is grown before the implantation of the base and, therefore, suffers from ion implantation damage. In addition, it is generally exposed to a high temperature annealing, necessary for the dopant activation in the base and in the (poly) silicon emitter. The

resulting oxide quality is less than in ordinary MOS gates, leading to a higher than normal native density of interface traps (range 10^{11} cm^{-3}). As we will see, this has serious consequences for the radiation hardness of modern BJTs.

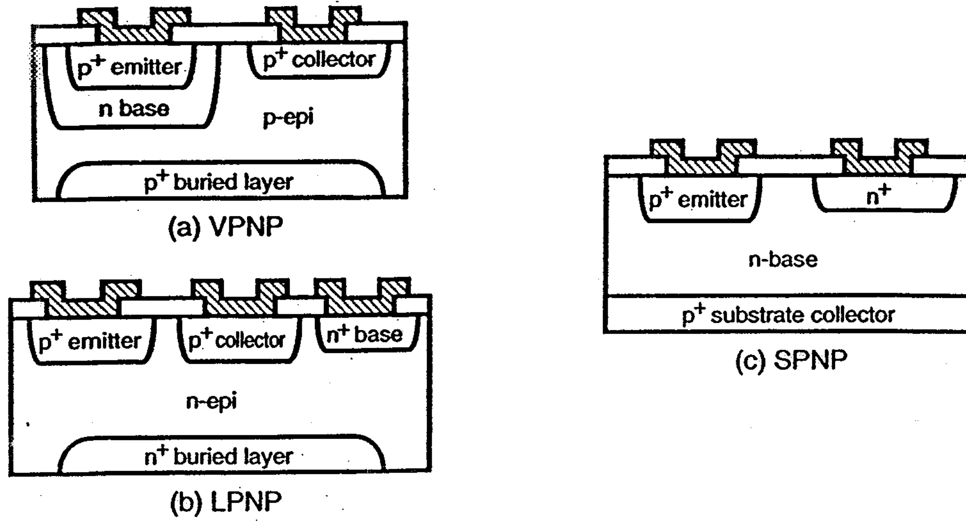

Fig. 3.1. Qualitative cross sections of (a) vertical (VPNP), (b) lateral (LPNP) and (c) substrate (SPNP) transistors. (After Schrimpf [1]).

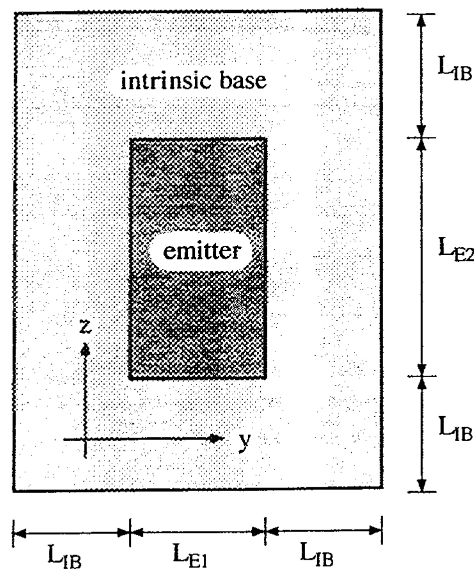

Fig. 3.2. Schematic top view of a BJT.

3.1.1 Radiation Damage Mechanisms

In bipolar devices, three main damage mechanisms can be distinguished [2]. First, there is the positive oxide trapped charge, which modifies the surface potential at the Si-SiO_2 interface. As a result, p-type doped silicon will become depleted, or even inverted, depending on the doping density and the amount of trapped hole charge, while n-doped regions become accumulated. Depletion of the p-type base (n-p-n) or emitter (p-n-p) will increase the (surface) recombination current and, hence, the non-ideal base current I_B. This in turn leads to a reduction of the static current gain $\beta=I_C/I_B$, with I_C the collector current. Inversion of the p-type surface layer can lead to increased leakage current along the field oxide isolation regions. At the same time, the breakdown voltage of the transistor can be reduced, as summarized in Table 3.1 [2]. Similar as for a MOS device, the charge yield strongly depends on the quality (hardness) of the oxide and of the bias (field) across it. For modern BJTs, a low oxide field is generally present in normal operation, while at the same time high charge yields, typical for soft oxides have been observed (see part 4).

Table 3.1. Summary of total dose mechanisms for bipolar devices. (After Johmston and Plaag [2]).

Mechanism	Energy dependence Particle/radiation	Bias dependence (low fields) during irradiation	Effect on devices
Surface recombination velocity	slight	weak	gain reduction
Oxide trapped charge	slight	strong	inversion gain reduction increased leakage decreased breakdown
Bulk damage	strong	none	gain reduction

A second degradation source is surface recombination in the base-emitter depletion region. It can be related to the density of interface traps D_{it} through the equation:

$$s_o = \frac{1}{2} v_t \sqrt{\sigma_n \sigma_p \pi k T D_{it}} \qquad (3.1)$$

with s_o the surface recombination velocity, v_t the thermal velocity, kT the thermal energy and σ_n, σ_p the capture cross section for electrons and holes, respectively. As can be noted from Eq. (3.1), a radiation-induced increase of D_{it} will generate a proportional increase in the surface recombination velocity and in the corresponding recombination base current. It should be noted, however, that in contrast to MOS devices, the relevant D_{it} is the one corresponding to mid gap energy (if σ_n=σ_p) and, hence, to a maximum recombination rate. For MOS devices, it is the whole energy range from mid gap up to the relevant band edge that plays a role in the device performance.

A third degradation mechanism is bulk (displacement) damage which is particularly pronounced for high energy particle irradiation and to a lesser extent for ^{60}Co γ's. In the latter case, it are secondary energetic Compton electrons, which produce the displacement damage in the silicon lattice. It is not relevant for X-ray exposures. The main effect is the reduction of the minority carrier lifetime, resulting in a linear degradation of the reciprocal current gain with particle fluence Φ [3-5], given by:

$$\frac{1}{\beta} = \frac{1}{\beta_o} + K\,\Phi \qquad (3.2)$$

K is the damage factor and β_o is the initial static current gain. The experimental damage factor normalized to 1 MeV equivalent (Si) neutron damage for silicon BJTs is represented in Fig. 3.3 and compared with the calculated non ionizing energy loss (NIEL), showing an excellent agreement.

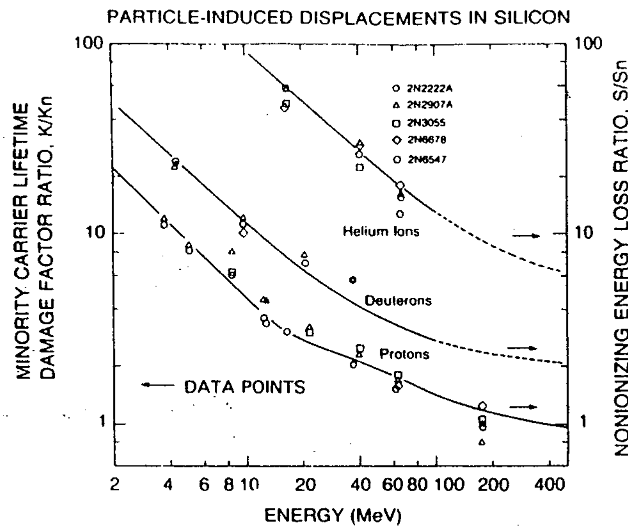

Fig. 3.3 Damage factors for bipolar transistors for protons, deuterons and helium ions normalized to 1 MeV equivalent (Si) neutron damage factors as a function of energy. The solid lines (right hand ordinate) are calculations of the corresponding ratios of the non-ionizing energy loss (NIEL) in silicon. (After Dale et al. [5]).

The main degradation mechanisms and their impact on the BJT characteristics are summarized in Table 3.1 [2]. At the same time, the qualitative dependence on the energy of the impinging particle/photon and on the oxide field is indicated.

3.2 Degradation in vertical (n-p-n) BJTs

In this part, the different degradation mechanisms for vertical n-p-n BJTs will be discussed. Similar effects are expected for VPNP, although these devices are much harder than their n-p-n counterparts. The basic reason is that the oxide trapped charge induced depletion of the p-type region is in the "lowly" doped base in the first case, while it occurs in the heavily doped p^+ emitter in the second case. As will be seen, total dose (oxide trapped charge) effects are the main source of damage in modern scaled BJTs. Due to the narrow base widths and high base doping densities used, displacement damage is in many cases negligible or of second order

3.2.1 Phenomenology of Total Dose Damage

The primary effect of total dose degradation of vertical n-p-n transistors is the increase of the base current with dose (Fig. 3.4a) and a corresponding reduction of the current gain (Fig. 3.4b) [6-8]. The base current increase ΔI_B is particularly pronounced for small base-emitter voltage V_{BE}, causing a shift of the peak β to higher V_{BE}. In addition, a total dose induced increase of the collector current ΔI_C has also been noted [8-9], as shown in Fig. 3.5. It is, however, strongly technology dependent [8] and only observed for certain types of poly emitter BJTs, under reverse V_{BE} irradiations.

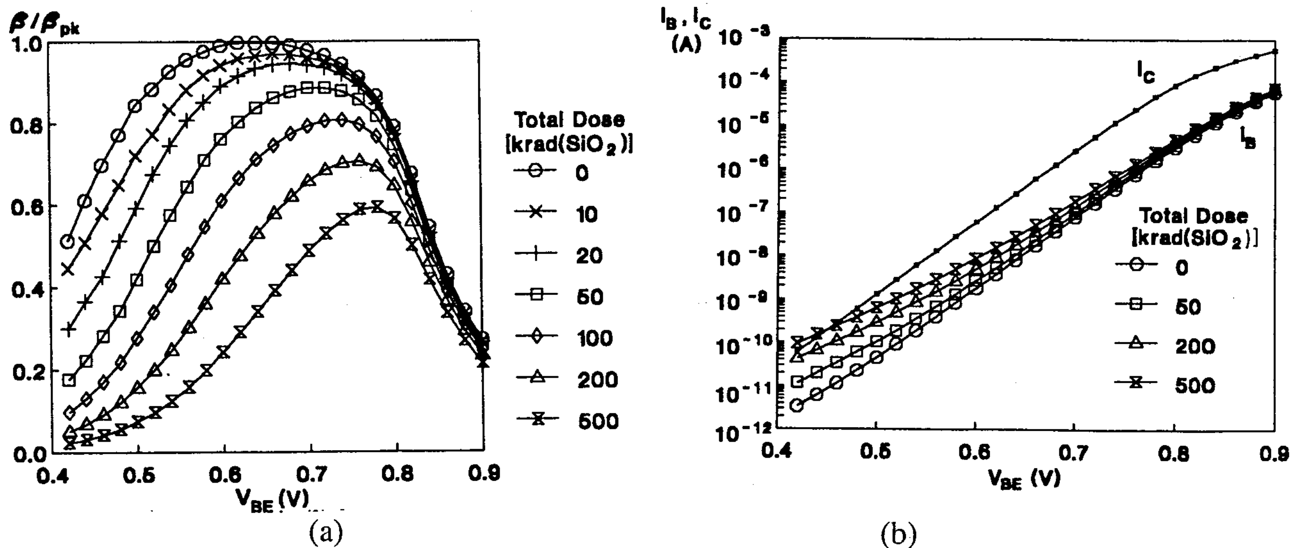

Fig. 3.4. (a) Typical Gummel curves for a bipolar transistor exposed to ionizing radiation. (b) Typical dc current gain (β) degradation in a bipolar transistor exposed to ionizing radiation. β_{pk} is the peak pre-irradiation current gain. (After Nowlin et al. [8]).

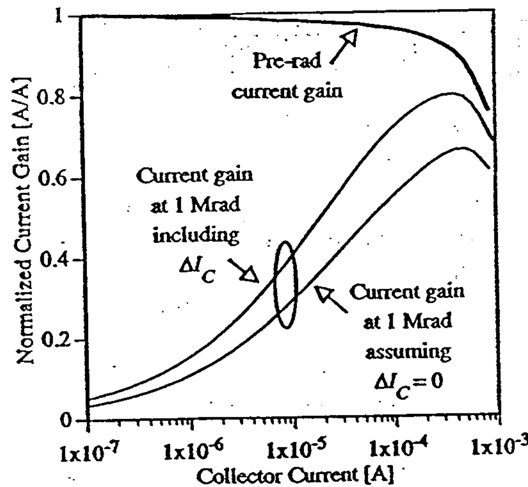

Fig. 3.5. Measured common-emitter current gain, normalized to the peak pre-irradiated value, versus the collector current. Shown are the pre-irradiated current gain plotted against the pre-irradiated collector current, current gain at a total dose of 1 Mrad(SiO_2) plotted against the actual measured collector current at that dose, and current gain at a total dose of 1 Mrad(SiO_2) plotted against the pre-irradiated collector current. (After Wei at al.[9]).

It has furthermore been demonstrated that the excess base current increases superlinearly with dose D, for not too large D (Fig. 3.6) and becomes higher for larger perimeter/area (P/A) ratios [8]. However, for sufficiently large dose, the excess base current saturates (Fig. 3.7) [10]. This saturation value of ΔI_B is independent of the dose rate during the exposure, or of the irradiation bias. It is only a function of the measurement V_{BE} [10]. Implanted or polysilicon emitter n-p-n BJTs show qualitatively similar degradation [8].

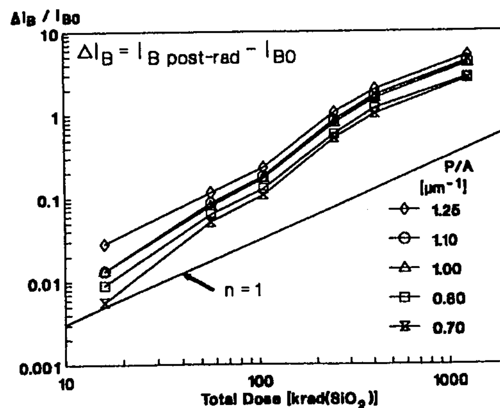

Fig.3 6. Total-dose and device-geometry dependencies of the excess base current measured at V_{BE}=0.7 V. I_{B0} is the pre-rad current. (After Nowlin et al. [8]).

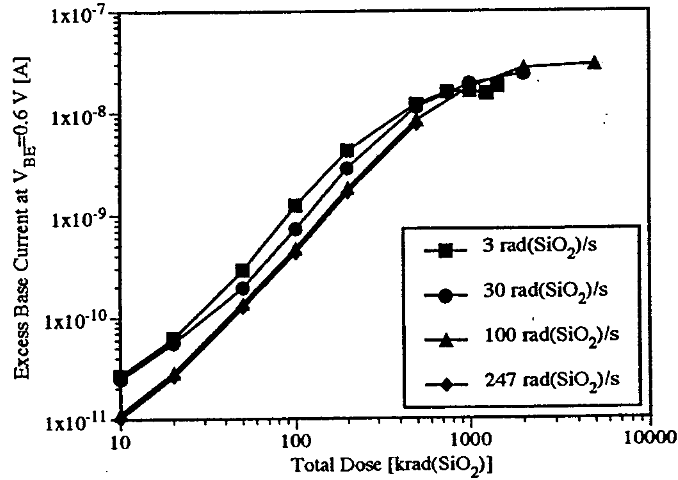

Fig. 3.7. Excess base current at V_{BE}=0.6 V versus total dose at four different dose rates. (After Kosier et al. [10]).

Perhaps the most striking feature in Fig. 3.7 is the dose rate dependence of the excess base current, indicating a *higher* degradation for *low* dose rates [6-8,10-11]. This is in contrast with what is known for MOS devices, where the damage generally increases with dose rate. The effect is more clearly evidenced in Fig. 3.8, where the low dose rate response saturates at ≈10 rad(SiO_2)/s for that particular type of devices [12]. In addition, the low dose rate effect is worst for zero bias irradiation, while reverse bias operation is worst case for high dose rate degradation in Fig. 3.9 [8]. The high dose region sets in around 150 rad(SiO_2)/s, where the excess base current becomes independent of this parameter [8] .

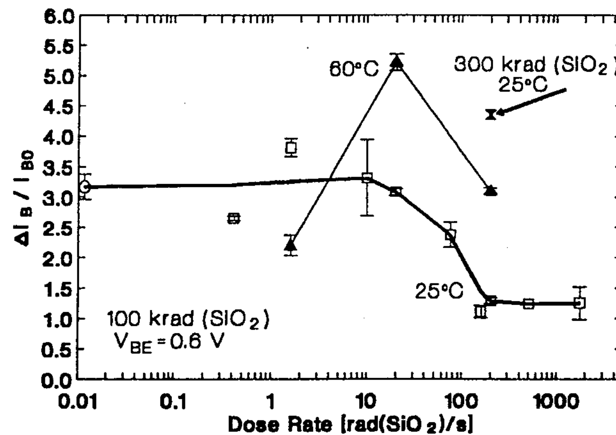

Fig. 3.8. Dose-rate response of the excess base current after irradiation to 100 krad(SiO_2) at 25 and 60°C. Also shown is a 200 rad(SiO_2)/s, 300 krad(SiO_2), 25°C data point representing a factor-of-3 overtest. (After Nowlin et al. [12]).

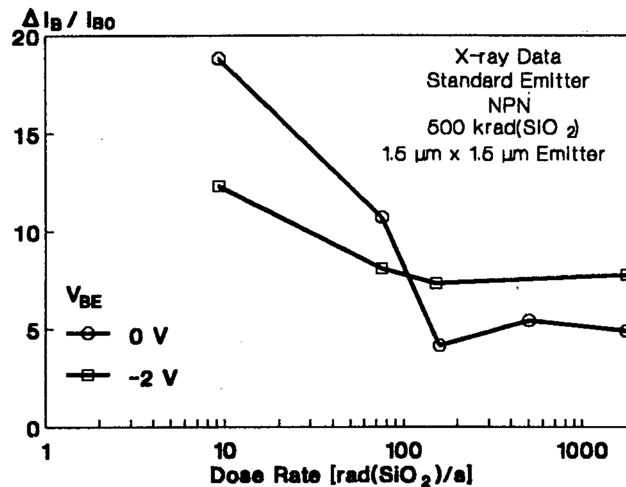

Fig. 3.9. Dose-rate dependence of the total-dose response of standard-emitter n-p-n devices irradiated in an X-ray source. (After Nowlin et al. [8]).

This low dose rate effect has large practical consequences for hardness assurance of modern bipolar space applications. In contrast to the case of the MOS system, the convenient standard laboratory tests at high dose rate do not provide a conservative estimate of the component and circuit degradation, but *underestimates* what can be expected for space radiation conditions. The alternative is to perform testing of BJTs at unpractical and lengthy (expensive) low dose rates. According to the MIL-STD-883D Test Method 1019.4, the low dose rate response can be simulated by applying a high temperature anneal, following a high-dose rate exposure. For bipolar transistors, this test method fails, since, as expected, the degradation anneals out, as evidenced by Fig. 3.10 [8]. In other words, high dose rate exposure plus high temperature anneal does not reproduce the enhanced degradation observed at low dose rates. Note also in Fig. 3.10 that at room temperature the annealing proceeds very slowly.

3.2.2 Basic Low Dose-Rate Degradation Mechanisms

It is clear from the above that the total-dose degradation in BJTs follows a different mechanism than in MOS devices. This occurs through from the different dose rate dependence. An additional factor that can play is that the oxide field during exposure is much lower in BJTs than in MOS transistors (typically ±1 MV/cm). Finally, as mentioned above, the screen oxide covering the base-emitter surface is generally rather thick (50 to 500 nm) and of poor(er) quality [8]. This calls for a radiation testing of such oxides under low bias. From the mid gap voltage shift shown in Fig. 3.11, it is clear that a larger hole trapping yield under zero bias follows for such field-oxides at low dose rates [8]. The extracted positive oxide charge in Fig. 3.12b nicely tracks the behavior of the excess base current of Fig. 3.12a, emphasizing the important if not dominant role played by the oxide trapped charge N_{OX} in the degradation of the BJTs [11].

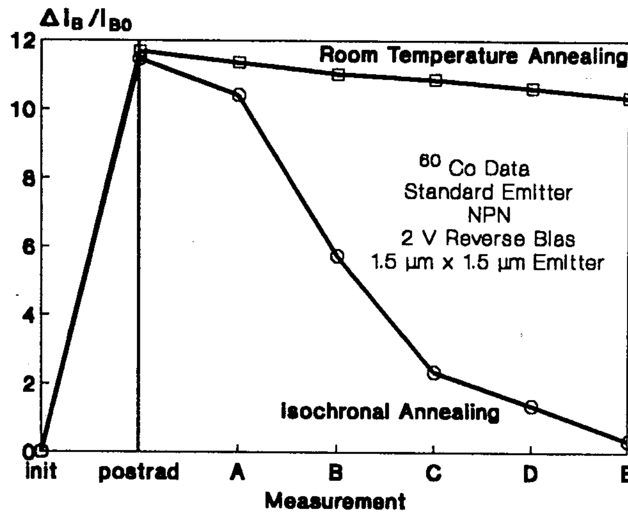

Fig. 3.10. Room-temperature and isochronal annealing response of reverse-biased, standard-emitter n-p-n transistors. All measurements were taken after exposure to 500 krad(SiO_2) (post-rad from ^{60}Co at 240 rad(SiO_2)/s, and after the isochronal anneal). The parts were annealed for 30 minutes at (A) 60°C, (B) 100°C, (C) 150°C, (D) 200°C and (E) 250°C. The room temperature parts were characterized at the same time as the isochronally annealed parts. (After Nowlin et al. [8]).

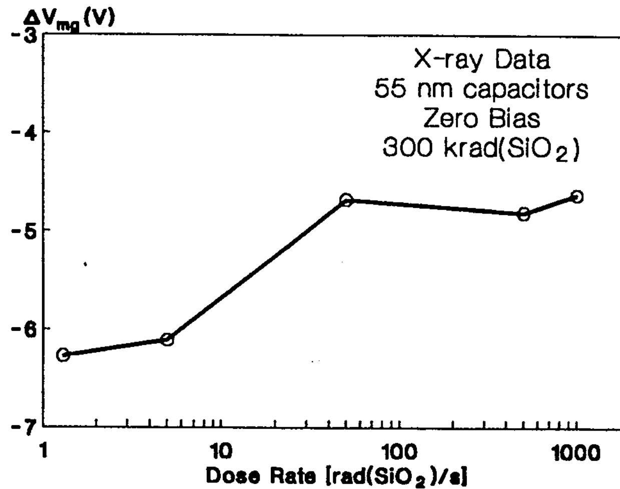

Fig. 3.11. Dose-rate dependence of the mid gap voltage shift in field-oxide capacitors with 55 nm oxides at 0 V bias. (After Nowlin et al. [8]).

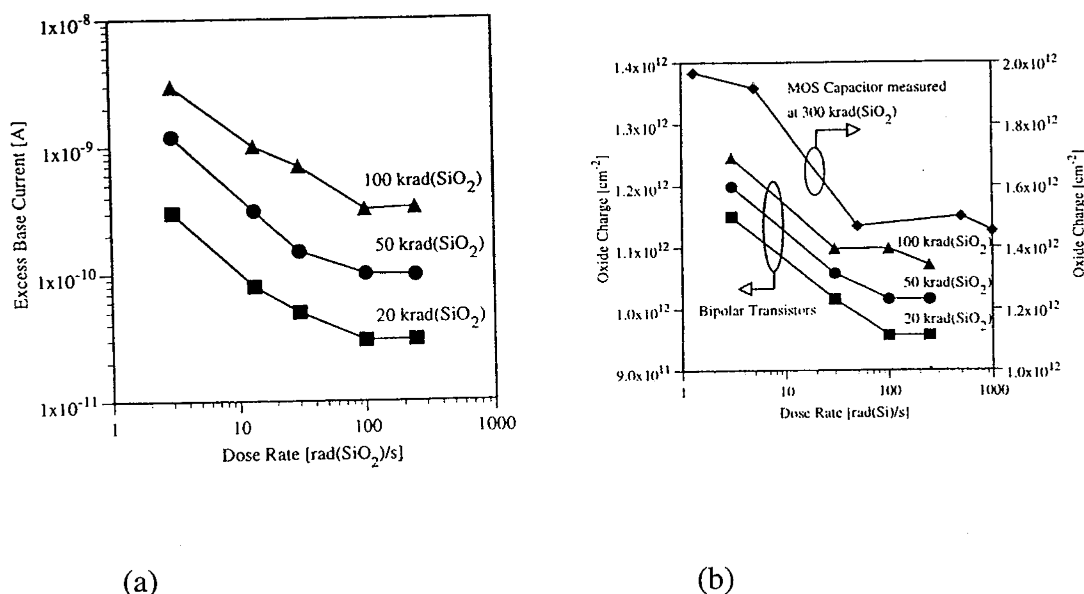

(a) (b)

Fig. 3.12 (a) Excess base current at V_{BE}=0.6 V versus dose rate and (b) oxide charge versus dose rate at various total doses. (After Wei et al. [11]).

The total dose damage in spacer, screen or sacrificial oxides, covering the base-emitter junction of a BJT has been studied in more detail by Fleetwood et al [13-14], using Thermally Stimulated Current (TSC) and C-V measurements. It has first of all been pointed out that the charge yield in such ion implanted and annealed spacer oxides is very high (close to 100%) compared with hardened oxides (≈0.1 to 1 % range). Also the role of electron trapping has been highlighted. A model has been proposed, which is schematically depicted in Fig. 3.13 [13] and explains why slightly more holes are trapped at low dose rates. Key in the model is the assumption that holes are trapped in delocalized metastable trapping centers (which can be related to ion implantation induced displacement damage; candidates are the so-called E_δ' centers, detected by ESR [B3]). The release of holes from these centers occurs on a time scale of seconds to hours. It has been shown that such centers are more abundant in soft oxides compared with hard ones. They also anneal at moderate temperatures (~50°C) [13]. An alternative model suggests that electron trapping in shallow traps explains the enhanced hole trapping at low dose rates in bipolar screen oxides [15]. At higher irradiation temperatures, the thermally activated release of the trapped electrons causes a reduction of the trapped hole yield at low dose rates and essentially removes the effect. Also the role of the non homogeneous fringing field at the edge of the base-emitter

junction has been pointed out [13,16]. The effect is shown to be more pronounced for p-n-p compared with n-p-n transistors.

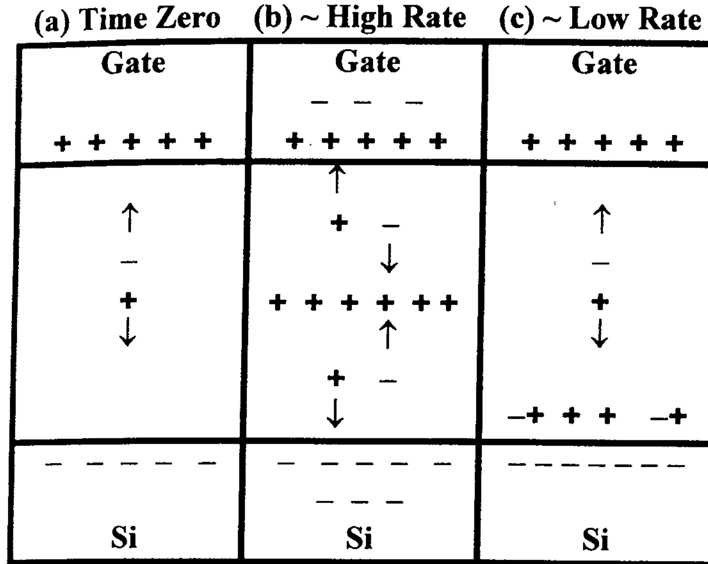

Fig. 3.13. Schematic illustration of electron and hole transport for three cases: (a) at the start of irradiation before trapped charge begins to build up, (b) during high-rate exposure, when holes are captured by metastable traps in the bulk of the SiO_2, causing space charge effects, and (c) during low-rate exposure, when some holes in metastable traps are emitted and transported to the SiO_2 interface. (After Fleetwood et al. [13]).

Another striking difference compared with the degradation of MOS type devices is the fact that repeated irradiation + anneal does not produce a hardening effect [17]. Instead, as evidenced by Fig. 3.14, a continuous degradation is observed, which saturates after a few irradiation + anneal cycles. In other words, after one (or more) irradiation + anneal steps, the radiation induced degradation becomes worse, for the same total dose. The trend is independent of the BJT geometry, or of the type of emitter (standard implanted or poly). P-n-p devices seem to be less susceptible compared with n-p-n. In order to explain this effect, surface stress measurements have been performed on similarly oxidized and metallized reference wafers [17]. The results of this analysis indicate that the interfacial compressive stress relaxes with increasing number of cycles. The interpretation given to these facts is that for lower compressive stress at the Si-SiO_2 interface, more interface traps are being created for the same total dose, thereby producing a larger excess base current and current gain degradation.

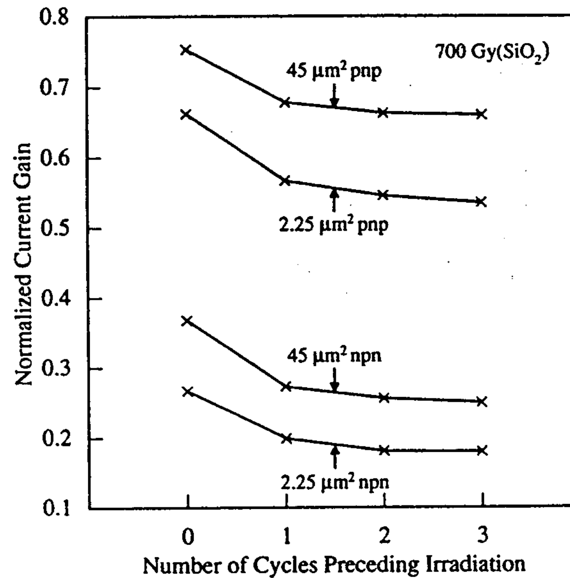

Fig. 3.14. Effect of radiation and anneal cycles on radiation-induced current gain degradation in a representative group of devices. Gain degradation increases with an increasing number of cycles independent of emitter geometry or polarity. All data were measured at V_{BE}=0.6 V. (After Witczak et al. [17]).

3.2.3 Charge Separation in BJTs

Total dose damage has two main effects in a bipolar transistor: first, the creation of oxide trapped charge changes the surface potential $\Psi_s(y)$at the interface of the spacer oxide and base-emitter junction. For an n-p-n transistor, the p-type base region becomes more depleted (Fig. 3.15) [18]. This enhances the peak surface recombination rate, which corresponds to the lateral position where the electron and hole densities at the surface are approximately the same. In order to determine the exact lateral position of the peak surface recombination rate, two-dimensional device simulations are indispensable [1,10,18-20]. A typical result is given in Fig. 16, for a certain V_{BE} and for different densities of oxide trapped charge N_{ox} [18].

A second contributing factor is the increase in the surface recombination velocity, given by Eq. (3.1), through the increase of the density of mid gap interface states D_{it}. Combining both factors, one can derive the surface recombination rate at a certain lateral position y, defined in Fig. 3.2 [1,B18]:

$$R_s(y) = \frac{n_i\, s_o \exp(\frac{qV_{BE}}{2kT})}{2\cosh[\frac{q}{kT}(\Psi_s(y) - \frac{V_{BE}}{2})]} \qquad (3.3)$$

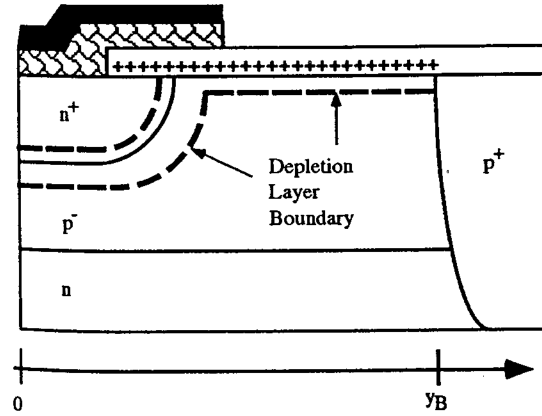

Fig. 3.15. Schematic cross section of the base-emitter junction showing the effect of oxide charge on the depletion layer. (After Koiser et al.[18]).

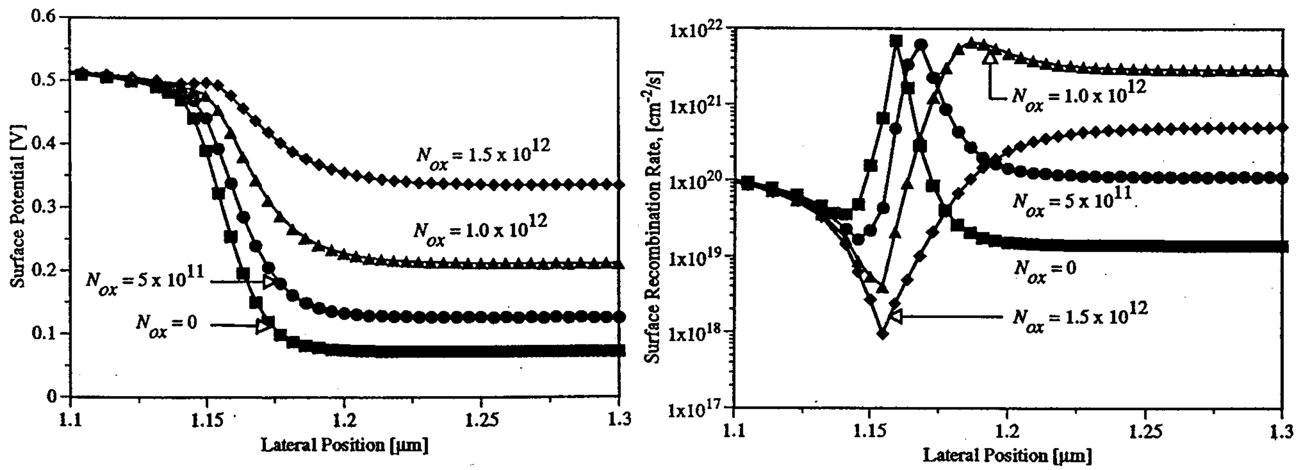

(a) (b)

Fig. 3.16. PISCES simulation results for the base junction, located at y=1.16 µm. V_{BE}=0.5 V with varying oxide charge in units of cm^{-2}. (a) Surface potential versus lateral position and (b) Surface recombination rate versus lateral position. (AfterKosier et al. [18]).

whereby $\Psi_S(y)$ is a function of N_{OX}. The band bending due to N_{OX} can be written in the depletion approximation [18]:

$$\Psi_{N_{ox}} = \frac{qN_{ox}^2}{2\varepsilon_S N_S} \tag{3.4}$$

with ε_S and N_S (in cm^{-3}) the silicon permittivity and doping density at the surface of the intrinsic base.
The peak recombination rate occurs for $\Psi_S(y)=V_{BE}/2$, so that

$$R_{speak}=\frac{1}{2}\, n_i\, s_o \exp(\frac{qV_{BE}}{2kT}) \tag{3.5}$$

Note that the peak recombination rate corresponds to an ideality factor n of exactly 2. The radiation-induced excess base current ΔI_B then follows from an integration over the whole base width (y=0 to y_B) of the sharp peaked function Eq. (3.3) (see Fig. 3.16).

Inspection of Eq. (3.5) tells us that both effects are intimately connected and affect the excess base current in an interactive and far from linear way. As a result, the excess base current shows initially a superlinear increase with dose (Figs 3.6 and 3.7) and eventually saturates for large total dose (Fig. 3.7) [10]. This is opposite to the case of a MOSFET, where the ΔV_{ox} and ΔV_{it} effects are additive, so that they can be fairly easy separated. This facilitates tremendously the physical modeling of the total-dose effects.

It has been demonstrated, however, that a similar kind of charge separation can be achieved for irradiated BJTs [18]. This is obtained in the following way. Looking more closely to the excess base current characteristics of Fig. 3.17, it is clear that for low total dose, two parts can be distinguished, corresponding to an ideality factor $1 < n < 2$ at low V_{BE}, while for high V_{BE}, n=2. The transition voltage V_{tr}, which is defined by the crossing point of the two linear fits in Fig. 3.17, is shown to be related to a critical oxide charge density, given by [18]:

$$N_{ox} = \sqrt{\frac{2\varepsilon_S N_S}{q}\left[\frac{q}{kT}\ln(\frac{N_S}{n_i}) - \frac{V_{tr}}{2}\right]} \tag{3.6}$$

and corresponds to the point where the oxide charge band bending of Eq. (3.4) is always equal or larger than $V_{BE}/2$. At this point, the maximum recombination rate is no longer occurring at the surface, but subsurface, as can be derived from the simulations of Fig. 3.16 and shown more explicitly in Fig. 3.18 [10]. Given the sharply peaked nature of R_S, the surface recombination will no longer contribute significantly to ΔI_B even if D_{it} shows a further increase with total dose. In other words, the excess base current will no longer be

affected by s_o, but by the base recombination lifetime, which is relatively insensitive to total dose (especially for X-ray exposures). This means that ΔI_B will saturate and furthermore exhibits an n=2. This PISCES simulations of Fig. 3.19 [10] further illustrate this.

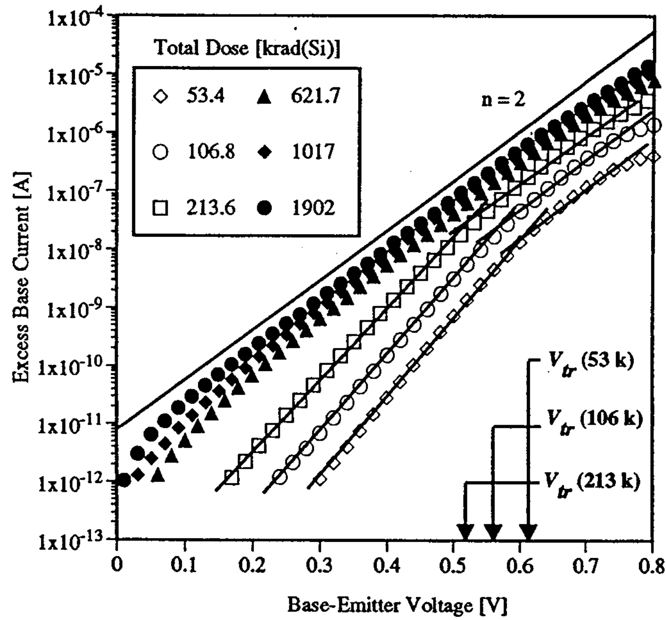

Fig. 3.17. Excess base current versus base-emitter voltage. (After Kosier et al [18]).

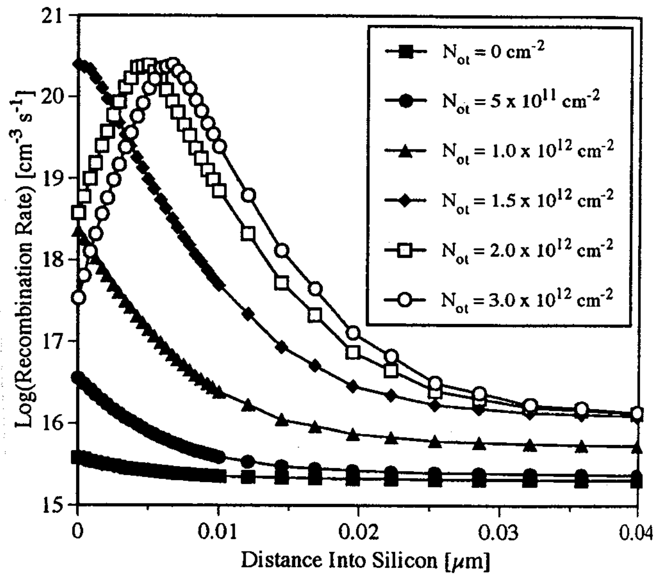

Fig. 3.18. PISCES-simulated recombination rate versus position normal to the interface for V_{BE}=0.5 V and various amounts of positive oxide charge. (After Kosier et al. [10]).

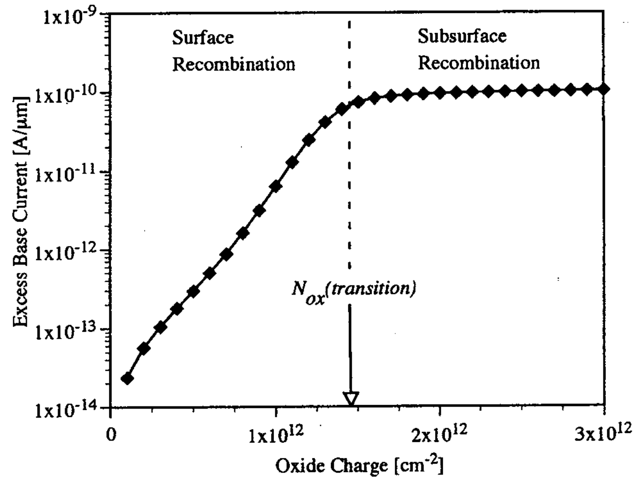

Fig. 3.19. PISCES-simulated excess base current versus positive oxide charge at V_{BE}=0.5 V. (After Kosier et al.[10]).

On the other hand, the lower n-value for lower total dose is explained by the fact that R_S is not constant, but varies with lateral position y along the base. Integrating Eq. (3.2) yields some effective (average) n value in that case. Another important consequence is that, while for low total dose and V_{BE} ($n < 2$) the excess base current scales with the device perimeter (Fig. 3.6), for n=2, the saturated excess base current will increase proportionally with the area of the transistor (Fig. 3.20) [20]. In conclusion, V_{tr} can be used as a measure for a certain oxide charge density in the spacer oxide.

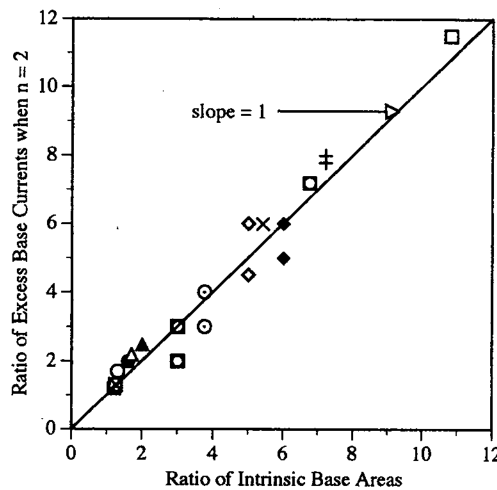

Fig. 3.20. Ratio of excess base current when n=2 versus ratio of intrinsic base areas. (After Kosier et al.[18]).

A value for the density of interface traps can be derived from the intercept of the exponential fit to the ΔI_B curves, corresponding to lower V_{BE} in Fig. 3.17, i.e. n<2. According to Eq. (3.3) or (3.4) for example, the intercept is proportional to s_o. It is clear from Fig. 3.17 that the intercept and, hence, s_o increases significantly with dose (Fig. 3.21). An alternative approach is to use a gated diode in forward operation [18], although the results may not be identical, like shown in Fig. 3.21. Because of this, preference is given to the intercept method.

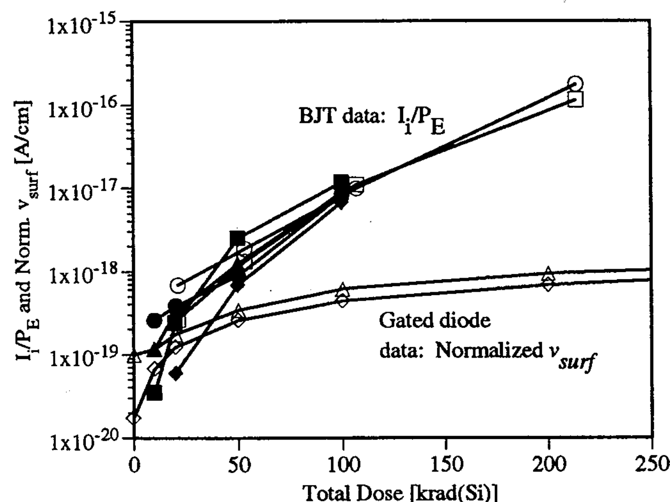

Fig. 3.21. Scaled intercept current and normalized surface recombination velocity versus total dose. (After Kosier et al. [18]).

Based on this analytical model, it is concluded that the key factor is the oxide trapped charge, since, combining Eqs (3.4) and (3.5), one obtains that [1,20]:

$$\Delta I_B \sim R_S \sim \exp([\frac{N_{OX}}{\sqrt{2}L_D N_S}]^2) \tag{3.7}$$

with L_D the extrinsic Debye length.

As mentioned above, for a certain type of poly emitter vertical transistors, a radiation-induced increase of the collector current is also found (Fig. 3.5) [9]. With the help of PISCES simulations, it was demonstrated that the origin of this increase is an enhancement of the effective emitter area, by an oxide trapped charge induced inversion of the p-base surface. This is illustrated in Fig. 3.22, showing the electron density in the emitter and p^- base region, for large N_{OX}. The excess collector current is then given by:

$$\Delta I_C = A_{EX} J_{EX} \tag{3.8a}$$

with A_{EX} the area of the "extrinsic" base (i.e. adjacent to the emitter) [9] and J_{EX} the corresponding current density. The upper bound for the effective emitter area is given by [9]:

$$A_{E,eff,max} = A_E + \frac{GN_{IN}}{GN_{EX}} A_{EX} \tag{3.8b}$$

with A_E the emitter area and GN_{IN},GN_{EX} the Gummel number for the "intrinsic" and for the "extrinsic" base, respectively.

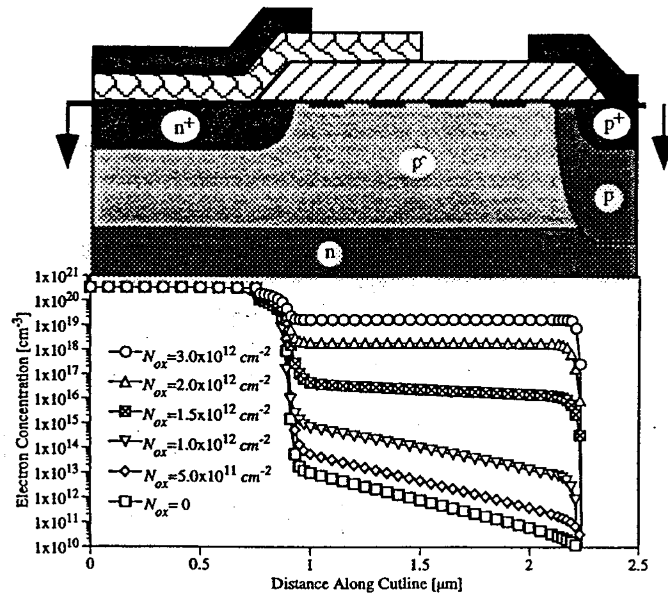

Fig. 3.22. PISCES simulated electron concentration along the oxide-silicon interface at V_{BE}=0.6 V versus increasing oxide charge. (After Wei et al. [9]).

3.2.4 Hardening Guidelines for Vertical BJTs

Based on the above insights, a few guidelines for practical bipolar technology and circuit hardening can be formulated [8,13]. These recommendations are:

i) to increase the surface doping density in the intrinsic base. As a result, a higher N_{OX} is necessary to deplete (or even invert) the surface (Eq. (3.6)) and according to Eq. (3.7) reduces significantly the total dose induced excess base current.

ii) to reduce the thickness of the screen or spacer oxide. This lowers in first instance the accumulated N_{OX}, the key factor in the damage process.

iii) to use dedicated sacrificial ion implantation oxides over the intrinsic base region, which are subsequently removed and/or to reduce the thermal budget to which the sacrificial oxide is subjected. A good quality spacer oxide can be grown/deposited in a later stage of the processing. This, of course, makes the bipolar (BiCMOS) process more complex and expensive.

iv) to optimise the design by using minimal P/A ratio devices, whenever possible. This is particularly useful for not too high total doses, below the saturation point of the excess base current. There, the ΔI_B is proportional with the device perimeter.

v) to design circuit operation for high(er) I_C (peak gain) operation. Higher V_{BE} operation corresponds to less ΔI_B and current gain degradation. Furthermore, the peak β shifts to higher base-emitter voltages upon irradiation (Fig. 3.4). Drawback is the higher power consumption which is often incompatible with the low power/low voltage applications of BiCMOS technologies.

vi) to reduce the intrinsic surface area between the base contact and the emitter. In fact, downscaling bipolar and BiCMOS technologies fulfills perfectly this requirement. It is, therefore, anticipated that scaled technologies will be more radiation tolerant, as they also have higher base doping densities and thinner spacer oxides. The use of a heterojunction device may also be a useful alternative [21].

3.2.5 Hardening Assurance and Testing

One particular problem of hardness assurance for bipolar devices and technologies for space is the assessment of the low dose rate effects in a cost-effective and meaningful way. One pathway, which has been pursued, is to replace radiation testing by reverse-bias hot-carrier degradation testing. In the past, it has been noted that in certain cases, there exists a similarity between both types of degradation, which mainly produces a current gain reduction, caused by excess base current [22-23]. Unfortunately, comparative studies have pointed out that the degradation mechanism is quite different in both cases [19-20,24]. As shown above, total dose damage occurs mainly through the creation of oxide trapped charge, while hot-carrier degradation proceeds by the creation of interface traps near the emitter-base junction [24], resulting in an excess base current with ideality factor 2.

An alternative is the use of high-temperate (• 60°C), high dose rate irradiations. According to the results of Fig.3. 8 [10], the resulting degradation is of the same order as the low dose-rate room temperature exposures. At the moment, this is considered a viable method for assessing low dose rate damage in bipolar components and circuits [25].

An important point to mention is also that the worst case testing at low dose rates is for zero bias, i.e. with all terminals grounded (see e.g. Fig. 3.9 [8]).

3.2.6 Bulk Damage in Vertical Transistors

So far, little displacement damage studies have been performed on modern BJTs [26-28], the main reason being that total dose damage is clearly first order priority. Still, there are a couple of reasons to study for example proton or electron irradiation effects. One reason is that for future deep submicron technologies, e^- [26-27] and ion-beam lithography may be applied. This exposes the wafers to displacement damage, which can, however, anneal during subsequent thermal processing. Fort space applications, proton damage is a potential problem.

The degradation of 0.5 μm BJTs fabricated in IMECs single poly BiCMOS has been studied in [28], with particular emphasis on the Gummel plots, static current gain and low-frequency (LF) noise. The latter parameter is important for analog (linear) applications (amplifiers, voltage regulators) and in addition for non-linear microwave applications, since the LF noise can determine the high-frequency phase noise. One MeV electron irradiation was compared with 59 MeV proton exposures (unbiased). Some clear differences have been noted, as illustrated by the results of Figs 3.23 and 3.24.

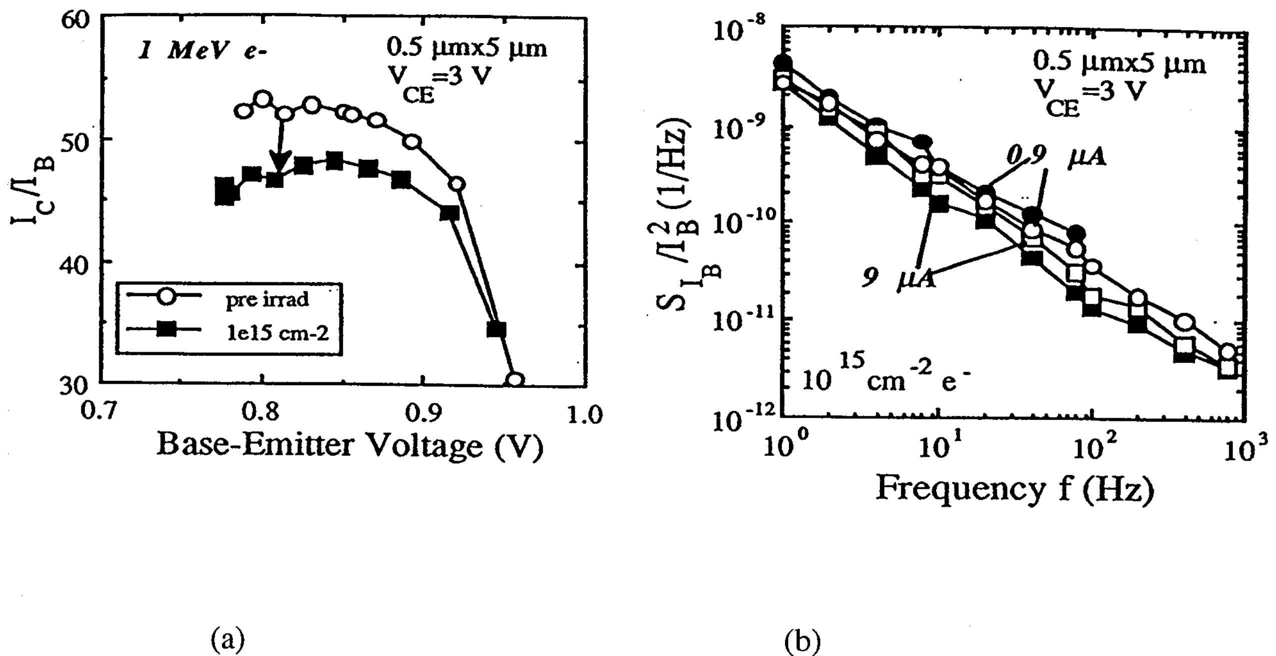

(a) (b)

Fig. 3.23. (a) Current amplification before (open) and after (closed) a 1 MeV 10^{15} cm^{-2} electron irradiation. (b) LF noise spectra before (open) and after (closed) the same irradiation, for a 0.5 μmx5 μm vertical n-p-n transistor. (After Simoen et al.[28]).

In both cases, the static characteristics have degraded (mainly the base current) (Fig. 3.23a and 3.24a). For the LF 1/f noise, on the other hand, e^- irradiations have little effect (Fig. 3.23b), while protons cause a marked increase of the flicker noise, at high V_{BE} (Fig. 3.24b). The latter effect is believed to indicate the creation of displacement damage in the base-emitter junction of the BJT, while for electron irradiations, total dose effects on the surface recombination current are most likely predominant. This is similar as for X-ray or γ-exposures.

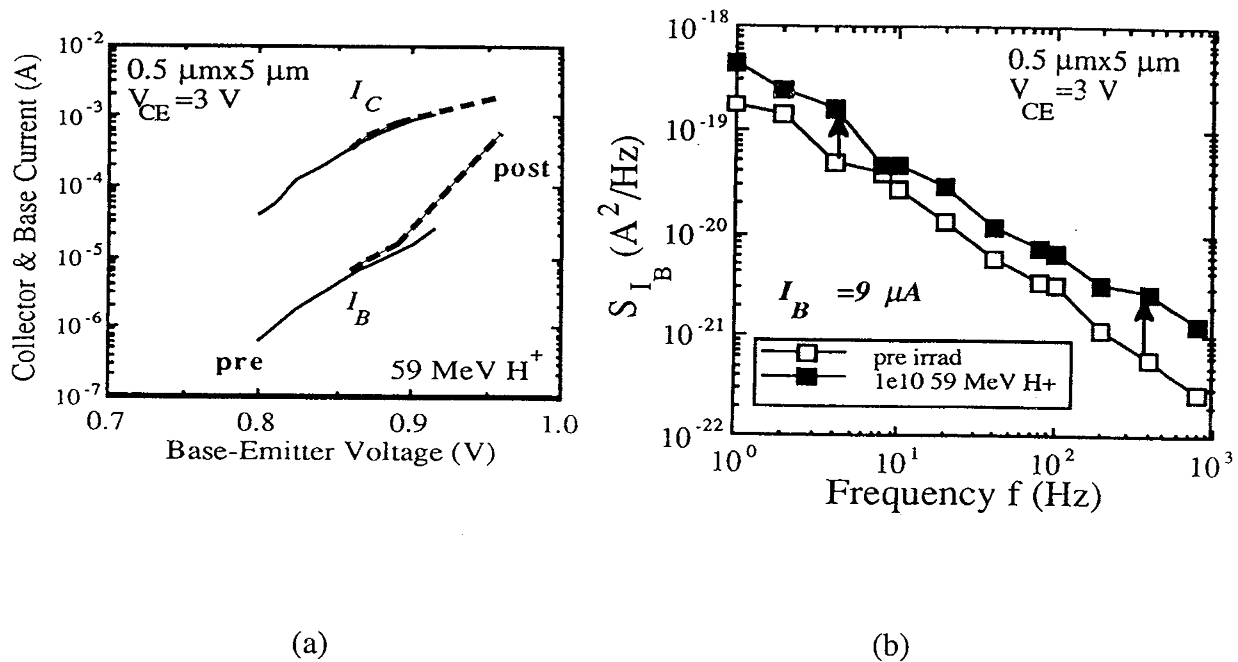

(a) (b)

Fig. 3.24. (a) Gummel plot before (full) and after (dash) a 10^{10} cm^{-2} 59 MeV proton irradiation. (b) LF noise spectrum before (open) and after (closed) the same irradiation, for a 0.5 µmx5 µm vertical n-p-n BJT. (After Simoen et al. [28]).

3.3 Lateral Transistors

3.3.1 Phenomenology

Although vertical p-n-p BJTs are significantly more radiation hard than their n-p-n counterparts, there are indications that certain types of p-n-p transistors in fact show more pronounced radiation-induced damage, particularly at low dose rates. This was derived from experiments on bipolar linear circuits and components [29-33]. Therefore, a systematic comparison of different types of p-n-p BJTs, depicted in Fig. 3.1, has been undertaken [34-37]. It is clear from Fig. 3.25 that the LPNP shows the most pronounced normalized current gain degradation, compared with the S- or V- type p-n-p transistor [34]. In addition, the low

dose rate effect is higher for the LPNP (Fig. 3.26). A typical feature for the degradation of the LPNP is the reduction of the collector current after total dose exposure, shown in Fig. 3.27. The post-irradiation base current in Fig. 3.27a shows an ideality factor n between 1 and 2 for a $V_{BE} < 0.7$ V and n=2 for $V_{BE} > 0.7$ V [34]. The excess base current of Fig. 3.28a increases with lower dose rate and follows roughly the same trend as the interface and oxide trapped charges in test capacitors, representative for the oxide above the base-emitter junction (Fig. 3.28b).

An important factor in the degradation of lateral p-n-p's is the doping density of the emitter [37]. Highly doped emitters show reduced excess base current for the same total dose, compared with lightly doped emitters (Fig. 3.29). The same observation applies for the degradation of the collector current (Fig. 3.30a) and of the normalised current gain (Fig. 3.30b).

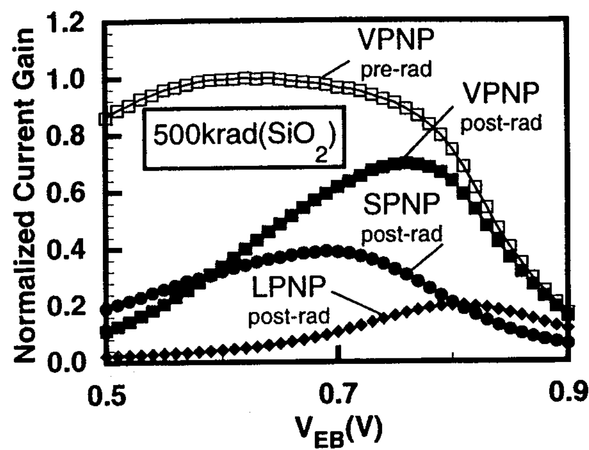

Fig. 3.25. Normalised current gain vs. V_{BE} for lateral (LPNP), substrate (SPNP), and vertical (VPNP) transistors for a total dose of 500 krad(SiO_2). Dose rate for VPNP devices is 158 and for LPNP and SPNP devices is 167 rad(SiO_2)/s. (After Schmidt et al. [34])

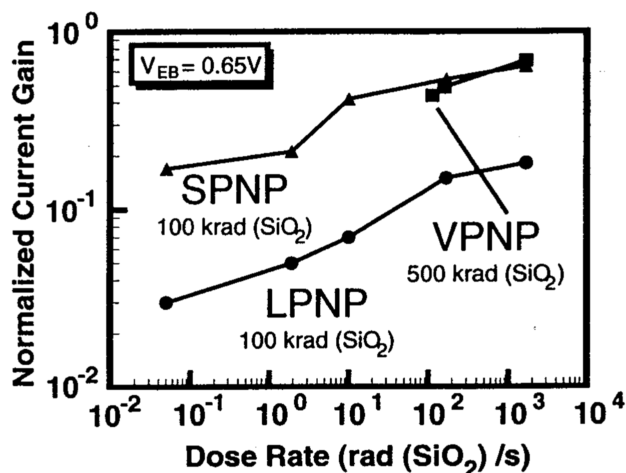

Fig. 3.26. Normalised current gain vs. dose rate for lateral (LPNP), substrate (SPNP), and vertical (VPNP) transistors. The total dose for the LPNP and SPNP devices was 100 krad(SiO_2), and the total dose for the VPNP device was 500 krad(SiO_2). (After Schmidt et al. [34]).

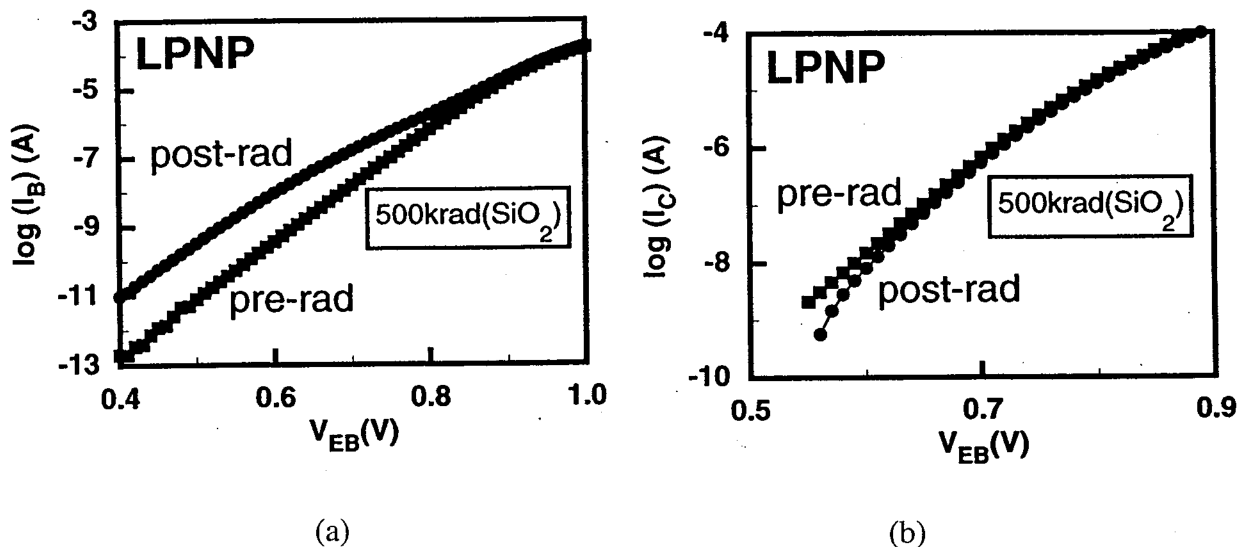

(a) (b)

Fig. 3.27. Gummel plots ((a) log I_B and (b) log I_C vs. V_{EB}) for the LPNP at a dose rate of 167 rad(SiO_2)/s to a total dose of 500 krad(SiO_2). (After Schmidt et al. [34]).

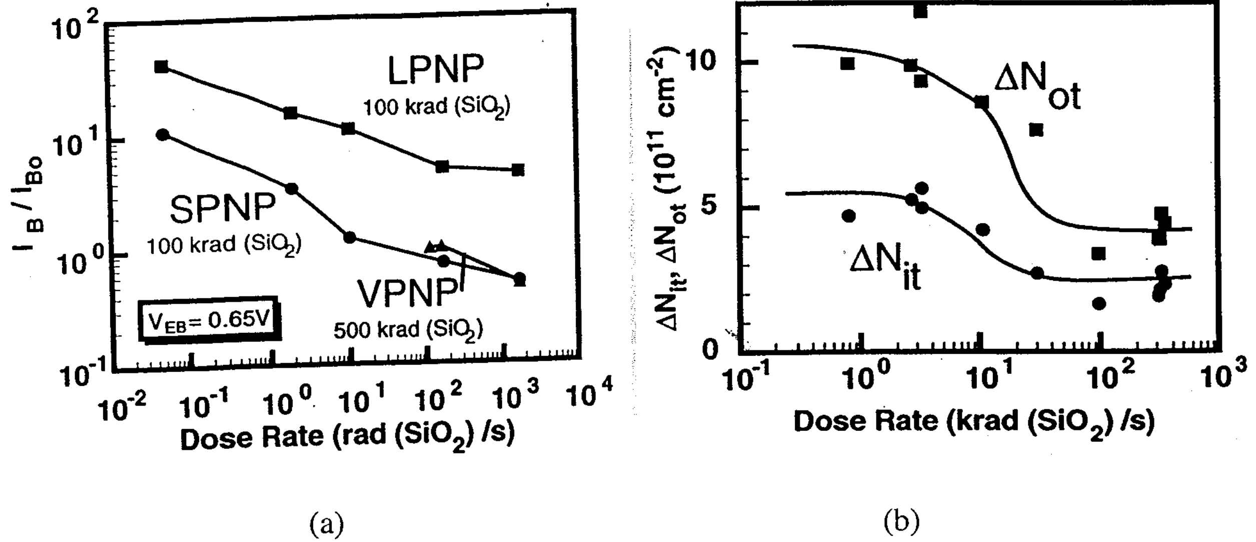

(a) (b)

Fig. 3.28. (a) Excess base current $\Delta I_B/I_B$ versus dose rate for the LPNP, SPNP and VPNP transistors. The Co-60 data at 0.5 rad(SiO_2)/s has been reduced by the factor 2.73 for comparison with the X-ray data. (b) Change in the number density of oxide trapped charge ΔN_{ot} and interface traps ΔN_{it} in test capacitors, representative of the oxide above the base-emitter junction in the LPNP transistors. (After Schmidt et al. [34]).

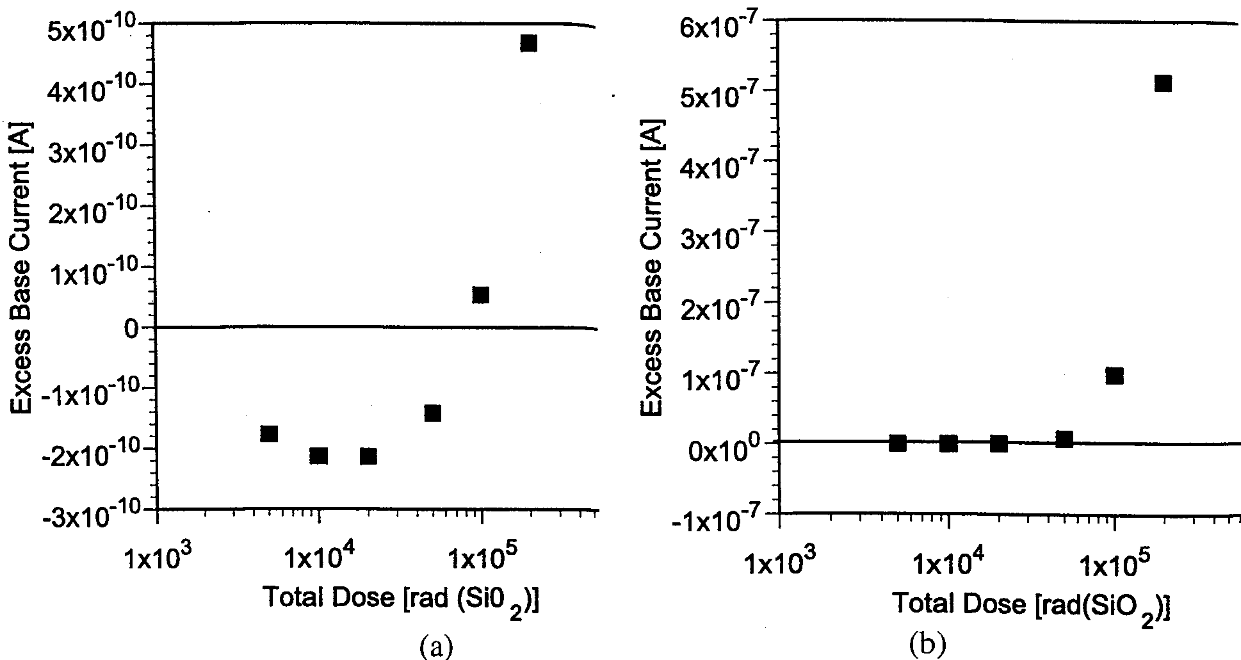

(a) (b)

Fig. 3.29. Excess base current vs. total dose for V_{BE}=0.6 V, a dose rate of 83.3 rad(SiO_2)/s for: (a) heavily-doped emitter and (b) lightly-doped emitter. (After Wu et al. [B37]).

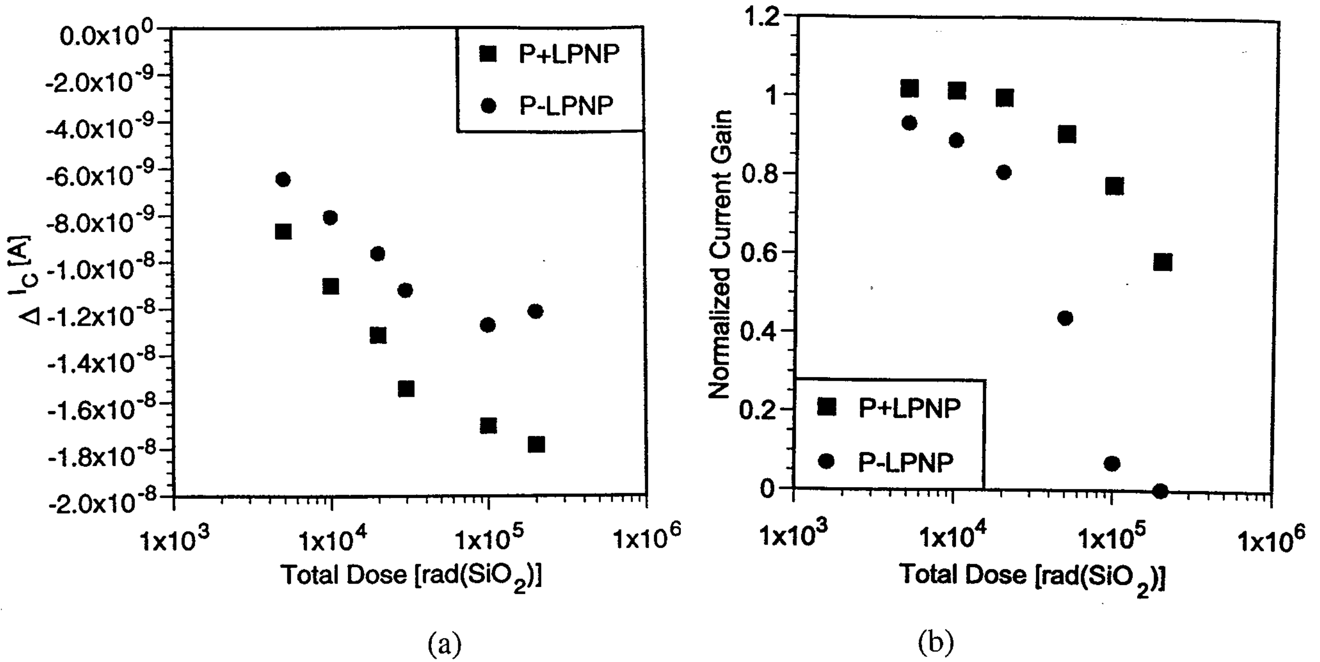

Fig. 3.30. (a) Change in collector current vs. total dose measured at V_{BE}=0.6 V and (b) normalised gain plotted vs. total dose for V_{BE}=0.6 V, for devices irradiated at a dose rate of 83.3 rad(SiO_2)/s. (After Wu et al. [37]).

3.3.2 Physical Mechanisms and Modeling

In order to understand the degradation behavior in an irradiated p-n-p BJT, one has to consider the impact of positive oxide trapped charge on the depletion (inversion) in the base and emitter, like in Fig. 3.31. The n-base will become accumulated, while the emitter gets depleted with increasing N_{ox} (total dose).

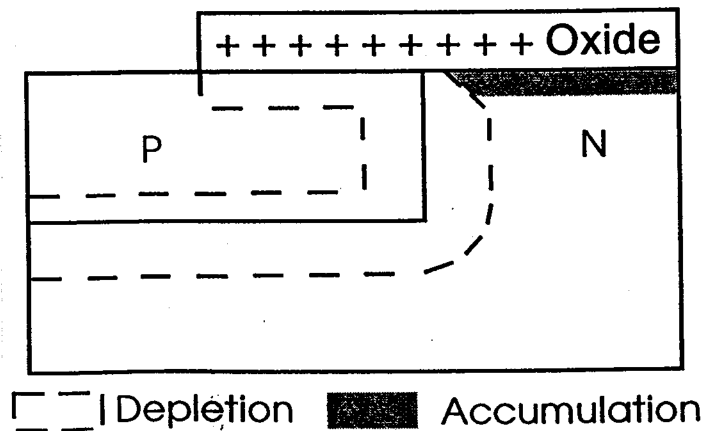

Fig. 3.31. Cross-section of the emitter base junction, showing depletion and accumulation regions in the presence of positive oxide charge. (After Wu et al[37]).

It should be kept in mind that depleting the surface region will enhance the surface recombination rate, while the opposite is true for accumulation. This implies that the surface recombination current will enhance in the p-type emitter and be reduced in the base. However, like in Fig. 3.32, one should in addition account for the radiation-induced increase in the density of interface traps [34]. The net result is that in the n-type base, the increasing N_{it} is more or less balanced by the N_{ot} induced accumulation. This explains the initial or negative reduction excess base current and the minimum with dose observed in Fig. 3.29a for the heavily doped LPNP [37]. No such effect is found for the lightly doped case (Fig. 3.29b). In the p-type emitter side, both effects should in principle interact with and enforce each other, similar as for the p-type base in an n-p-n device. The effect will be more pronounced for a lowly doped emitter compared with a highly doped one [37].

Two extra degradation mechanisms have to be considered for these p-n-p transistors [34]. The first one is related to the accumulation of the n-type base, which becomes an n^+ base. As shown by the PISCES simulations of Fig. 3.33, more electrons will be back-injected in the emitter through this effect, yielding an increase of the base current. A second effect of the accumulated base surface is that the holes will be pushed deeper in the substrate, leading to a longer 'effective' base. At the same time, more holes will recombine along their path, since they are moving in a heavier doped buried n^+ region, characterized by a lower recombination lifetime. This is represented by the PISCES results of Fig. 3.34 [34] and explains the reduction of the collector current shown in Figs 3.27 and 3.30. The strongly different radiation tolerance for L and S devices is related to the predominant direction of the hole flow: in the L transistor, it will essentially occur along the surface, will for the S device, only a fraction of the hole current will be lateral. The fact that the buildup of oxide trapped charge forces the holes to flow deeper in the base largely explains the susceptibility of LPNP to total dose degradation [34].

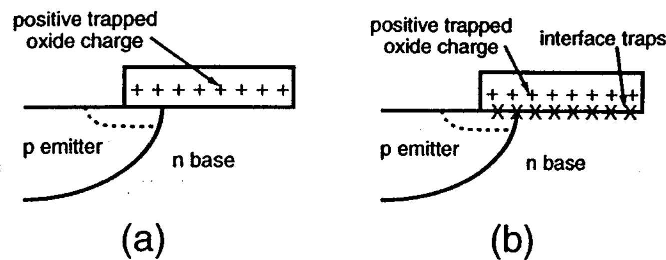

Fig. 3.32. Illustration of positive trapped oxide charge (a and b) and interface traps (b) over the emitter-base junction and the resulting expansion of the depletion region into the emitter. (After Schmidt et al. [34]).

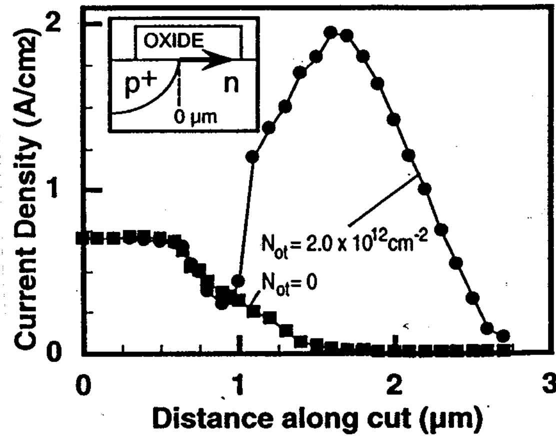

Fig. 3.33. SPISCES simulations of electron current density near the base-emitter junction that shows the effect of excess base current due to back-injected electrons. The cut-line (represented by the arrow) is just under the Si-SiO_2 interface below the base-emitter junction with the origin at the junction. (After Schmidt et al. [34]).

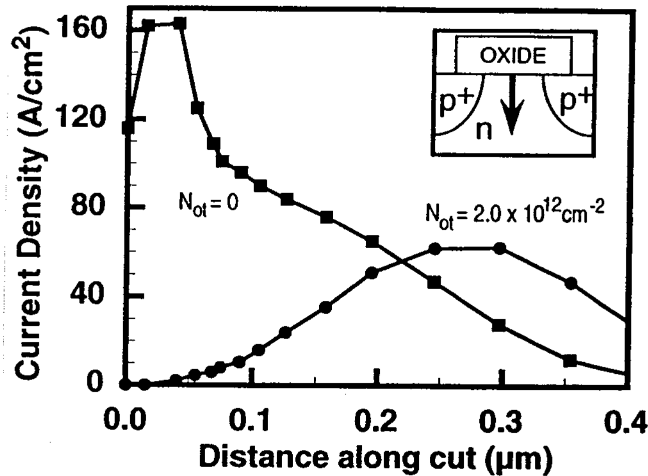

Fig. 3.34. SPISCES simulation of the hole current density midway between the base-emitter and the base-collector junctions at the Si-SiO_2 interface. This illustrates how N_{ot} alters the path injected holes must travel en route to the collector. The origin of the cut-line (represented by the arrow) is at the Si-SiO_2 interface. (After Schmidt et al. [B34]).

3.4 Conclusions

From the above, one can conclude that the main total dose damage mechanisms of modern bipolar transistors and circuits are quite well established and understood. The current gain degradation is mainly caused by the radiation-induced excess base current, which in turn is generated predominantly by the positive charging of the spacer oxide across the base-emitter junction. The specific nature of this oxide together with the low field present explains the higher degradation at low dose rates, compared with high dose rate irradiations. Identification of this mechanism also leads the way to improve the hardening of bipolar technologies. At the same time, it is expected that downscaling will enhance the radiation resistance. One critical point may be the hardness assurance testing, although performing the irradiations at high temperatures (around 100°C) can solve this.

Less is known about bulk damage effects by high-energy particles - a critical aspect for medium orbit satellites. Surely more experimental work needs to be done to study the main effects there and to identify possible displacement damage phenomena. It is not clear as yet whether dose rate plays an equal role for particle irradiations. This may be even more difficult to study, from an experimental viewpoint.

Another unknown is the possibility of processing induced plasma damage on the behavior of BJTs. Similar as for the gate oxide of a MOSFET, the spacer oxide can be degraded when subjected to a plasma. However, other damaging may mask such effects caused by the base implantation and emitter anneal. Plasma discharging will also depend largely on the presence of long metal or polysilicon lines on top of the spacer (or other vital) oxides.

References

[1] R.D. Schrimpf, "Recent advances in understanding total-dose effects in bipolar transistors", IEEE Trans. Nucl. Sci. **43**, 787 (1996).

[2] A.H. Johnston and R.E. Plaag, "Models for total dose degradation of linear integrated circuits", IEEE Trans. Nucl. Sci. **34**, 1474 (1987).

[3] G.P. Summers, E.A. Burke, C.J Dale, E.A. Wolicki, P.W. Marshall and M.A. Gehlhausen, "Correlation of particle-induced displacement damage in silicon", IEEE Trans. Nucl. Sci. **34**, 1134 (1987).

[4] C.J. Dale, P.W. Marshall, G.P. Summers and E.A. Wolicki, "Displacement damage equivalent to dose in silicon devices", Appl. Phys. Lett. **54**, 451 (1989).

[5] C. Dale and P. Marshall, "Displacement damage in Si imagers for space applications", SPIE Vol. **1447** *Charge-Coupled Devices and Solid State Optical Sensors II*, 70 (1991).

[6] E.W. Enlow, R.L. Pease, W.E. Combs, R.D. Schrimpf and R.N. Nowlin, "Response of advanced bipolar processes to ionising radiation", IEEE Trans. Nucl. Sci. **38**, 1342 (1991).

[7] R.N. Nowlin, E.W. Enlow, R.D. Schrimpf and W.E. Combs, "Trends in the total-dose response of modern bipolar transistors", IEEE Trans. Nucl. Sci. **39**, 2026 (1992).

[8] R.N. Nowlin, D.M. Fleetwood, R.D. Schrimpf, R.L. Pease and W.E. Combs, "Hardness-assurance and testing issues for bipolar/BiCMOS devices", IEEE Trans. Nucl. Sci. **40**, 1686 (1993).

[9] A. Wei, S.L. Kosier, R.D. Schrimpf, W.E. Combs and M. DeLaus, "Excess collector current due to an oxide-trapped-charge-induced emitter in irradiated NPN BJTs", IEEE Trans. Electron. Devices **42**, 923 (1995).

[10] S.L. Kosier, W.E. Combs, A. Wei, R.D. Schrimpf, D.M. Fleetwood, M. DeLaus and R.L. Pease, "Bounding total-dose response of modern bipolar transistors", IEEE Trans. Nucl. Sci. **41**, 1864 (1994).

[11] A. Wei, S.L. Kosier, R.D. Schrimpf, D.M. Fleetwood and W.E. Combs, "Dose-rate effects on radiation-induced bipolar junction transistor gain degradation", Appl. Phys. Lett. **65**, 1918 (1994)

[12] R.N. Nowlin, D.M. Fleetwood and R.D. Schrimpf, "Saturation of the dose-rate response of bipolar transistors below 10 rad(SiO_2)/s: Implications for hardness assurance", IEEE Trans. Nucl. Sci. **41**, 2637 (1994).

[13] D.M. Fleetwood, S.L. Kosier, R.N. Nowlin, R.D. Schrimpf, R.A. Reber, Jr., M. DeLaus, P.S. Winokur, A. Wei, W.E. Combs and R.L. Pease, "Physical mechanisms contributing to enhanced bipolar gain degradation at low dose rates", IEEE Trans. Nucl. Sci. **41**, 1871 (1994).

[14] D.M. Fleetwood, L.C. Riewe, J.R. Schwank, S.C. Witczak and R.D. Schrimpf, "Radiation effects at low electric fields in thermal, SIMOX, and bipolar-base oxides", IEEE Trans. Nucl. Sci. **43**, 2537 (1996).

[15] V.V. Belyakov, V.S. Pershenkov, A.V. Shalnov and I.N. Shvetzov-Shilovsky, "Use of MOS structures for the investigation of low-dose-rate effects in bipolar transistors", IEEE Trans. Nucl. Sci. **42**, 1660 (1995).

[16] V.S. Pershenkov, V.B. Maslov, S.V. Cherepko, I.N. Shvetzov-Shilovsky, V.V. Belyakov, A.V. Sogoyan, V.I. Rusanovsky, V.N. Ulimov, V.V. Emelianov and V.S. Nasibullin, "The effect of emitter junction bias on the low dose-rate radiation response of bipolar devices", IEEE Trans. Nucl. Sci. **44**, 1840 (1997).

[17] S.C. Witczak, K.F. Galloway, R.D. Schrimpf and J.S. Suehle, "Relaxation of Si-SiO_2 interfacial stress in bipolar screen oxides due to ionizing radiation", IEEE Trans. Nucl. Sci. **42**, 1689 (1995).

[18] S.L. Kosier, R.D. Schrimpf, R.N. Nowlin, D.M. Fleetwood, M. DeLaus, R.L. Pease, W.E. Combs, A. Wei and F. Chai, "Charge separation for bipolar transistors", IEEE Trans. Nucl. Sci. **40**, 1276 (1993).

[19] R.J. Graves, D.M. Schmidt, S.L. Kosier, A. Wei, R.D. Schrimpf and K.F. Galloway, "Visualisation of ionizing-radiation and hot-carrier stress response of polysilicon emitter BJTs", IEDM Tech. Dig., 233 (1994).

[20] S.L. Kosier, A. Wei, R.D. Schrimpf, D.M. Fleetwood, M.D. DeLaus, R.L. Pease and W.E. Combs, "Physically based comparison of hot-carrier-induced and ionizing-radiation-induced degradation in BJTs", IEEE Trans. Electron Devices **42**, 436 (1995).

[21] J.M. Roldan, G. Niu, W.E. Ansley, J.D. Cressler, S.D. Clark and D.C. Ahlgren, "An investigation of the spatial location of proton-induced traps in SiGe HBTs", IEEE Trans. Nucl. Sci. **45**, 2424 (1998).

[22] K.A. Jenkins and J.D. Cressler, "Electron beam damage of advanced silicon bipolar transistors and circuits", IEDM Tech. Dig., p. 30 (1988).
[23] K.A. Jenkins, J.D. Cressler and J.D. Warnock, "Use of electron-beam irradiation to study performance degradation of bipolar transistors after reverse-bias stress", IEDM Tech. Dig., 873 (1991).
[24] R.L. Pease, S.L. Kosier, R.D. Schrimpf, W.E. Combs, M. Davey and M. DeLaus, "Comparison of hot-carrier and radiation-induced increases in base current in bipolar transistors", IEEE Trans. Nucl. Sci. **41**, 2567 (1994).
[25] A.H. Johnston, C.I. Lee and B.G. Rax, "Enhanced damage in bipolar devices at low dose rates: Effects at very low dose rates", IEEE Trans. Nucl. Sci. **43**, 3049 (1996).
[26] K.A. Jenkins, "Frequency response of bipolar junction transistors after electron-beam irradiation", IEEE Trans. Electron Devices **36**, 1722 (1989).
[27] K.A. Jenkins and J.D. Cressler, "Electron-beam damage of self-aligned silicon bipolar transistors and circuits", IEEE Trans. Electron Devices **38**, 1450 (1991).
[28] E. Simoen, S. Decoutere, B. Merron, L. Deferm, C. Claeys, G. Berger, G. Ryckewaert, H. Ohyama and H. Sunaga, "High-energy particle irradiation effects in 0.5 μm BiCMOS polysilicon emitter bipolar junction transistors", in Proc. RADECS '97, Eds G. Barbottin and P. Dressendorfer, The IEEE (New York), 102 (1998).
[29] J. Beaucour, T. Carrière, A. Gach, D. Laxague and P. Poirot, "Total dose effects on negative voltage regulator", IEEE Trans. Nucl. Sci. **41**, 2420 (1994).
[30] A.H. Johnston, G.M. Swift and B.G. Rax, "Total dose effects in conventional bipolar transistors and linear integrated circuits", IEEE Trans. Nucl. Sci. **41**, 2427 (1994).
[31] S. McClure, R.L. Pease, W. Will and G. Perry, "Dependence of total dose response of bipolar linear microcircuits on applied dose rate", IEEE Trans. Nucl. Sci. **41**, 2544 (1994).
[32] A.H. Johnston, B.G. Rax and C.I. Lee, "Enhanced damage in linear bipolar integrated circuits at low dose rate", IEEE Trans. Nucl. Sci. **42**, 1650 (1995).
33] H. Barnaby, H.J. Tausch, R. Turfler, P. Cole, P. Baker, R.L. Pease, "Analysis of bipolar circuit response mechanisms for high and low dose rate total dose irradiations", IEEE Trans. Nucl. Sci. **43**, 3040 (1996).
[34] D.M. Schmidt, D.M. Fleetwood, R.D. Schrimpf, R.L. Pease, R.J. Graves, G.H. Johnson, K.F. Galloway and W.E. Combs, "Comparison of ionizing-irradiation-induced gain degradation in lateral, substrate and vertical PNP BJTs", IEEE Trans. Nucl. Sci. **41**, 1541 (1995).
[35] R.D.Schrimpf, R.J. Graves, D.M. Schmidt, D.M. Fleetwood, R.L. Pease, W.E. Combs and M. DeLaus, "Hardness-assurance issues for lateral PNP bipolar junction transistors", IEEE Trans. Nucl. Sci. **42**, 1641 (1995).
[36] D.M. Schmidt, A. Wu, R.D. Schrimpf, D.M. Fleetwood and R.L. Pease, "Modeling ionizing radiation induced gain degradation of the lateral PNP bipolar junction transistor", IEEE Trans. Nucl. Sci. **43**, 3032 (1996).
[37] A. Wu, R.D. Schrimpf, H.J. Barnaby, D.M. Fleetwood, R.L. Pease and S.L. Kosier, "Radiation-induced gain degradation in lateral PNP BJTs with lightly and heavily doped emitters", IEEE Trans. Nucl. Sci. **44**, 1914 (1997).

4. RADIATION EFFECTS IN SCALED CMOS

Since a few years, a strong tendency exists to replace hardened electronics for space by so-called "Custom's Of The Shelf" components (COTS), fabricated in a mainstream commercial CMOS technology. One strong motivation for this strategy is the expectation that scaled technologies should inherently be more radiation hard. This relies mainly on the fact that along with the electrical channel length L of the MOS transistors, also the thickness of the gate dielectric t_{ox} is reduced, for every next technology generation. Consequently the amount of positive trapped-hole charge during irradiation, will reduce accordingly. This follows from the expression for the threshold voltage (or flat band voltage) shift corresponding to radiation-induced hole trapping [1]:

$$\Delta V_{ot} = \Delta V_T = \frac{q}{\varepsilon_{ox}\varepsilon_0} [b(t_{ox}-2h_1)] \frac{t_{ox}}{2} \qquad (4.1)$$

with q the electron charge, ε_{ox} and ε_0 the dielectric constant of the gate oxide and of vacuum, respectively and b the fraction of the volume density of holes created throughout the oxide which become trapped to form fixed positive charge (hole yield). The parameter h_1 is the distance from the Si-SiO_2 interface into the oxide, where trapped holes can recombine with electrons tunneling from the substrate or from the gate. It is approximately equal to 3 nm for reasonable times t between irradiation and measurement (it varies according to ln t). Equation (4.1) is valid for positive gate bias during the exposure and shows a quadratic dependence of ΔV_{ot} on t_{ox}. It is also clear from Eq. (4.1) that for thin and ultra-thin oxides smaller than $2xh_1$ (~6 nm) essentially no net hole trapping will occur during irradiation, which is indeed found in practice [2]. In case a hole gets trapped near the interface under positive gate bias, it will immediately recombine with an electron tunneling from the substrate, thereby removing all fixed charge.

Based on this simple observation, one could come to the conclusion that all (deep) submicron CMOS technologies are radiation hard - particularly for low dose rate space applications, allowing some recovery of trapped charge during exposure - and no extra measures need to be taken anymore. Reality is of course somewhat more complicated than that, as will be reviewed below. Not only charge trapping but also interface state generation during and following irradiation is of concern. Particularly for scaled devices, this can lead to a non-homogeneous and more severe device degradation, as will be shown in paragraph 1. In addition, deep submicron processing utilizes a number of aggressive steps, which expose the gate dielectric to radiation damage - one can think of plasma (dry) etching, e-beam and X-ray lithography, etc. This can generate direct radiation damage or latent damage in the oxide which act as precursors for radiation induced traps, as will be discussed in the second part. Although radiation damage may be of concern for certain applications, reliability and lifetime issues are of more importance for CMOS devices and circuits. The need for a reliable gate dielectric for scaled technologies has triggered the development of alternatives, like nitrided and reoxidised nitrided oxides. Their response to radiation will be briefly discussed in section 3. For ultra thin oxides, some new radiation-induced phenomena occur, which may be an issue for large total doses (section 4). Finally,

device isolation is still the Achilles' heel with respect to hard devices. The fact that for deep submicron technologies commonly used LOCal oxidation of Silicon (LOCOS) is being replaced by so-called Shallow Trench Isolation (STI) puts the question of radiation hardness back on the blackboard. This and related issues will be dealt with in the final section.

4.1 Impact of Scaling on the Radiation Response

4.1.1 Gate Length Dependence

Early studies on the impact of radiation on short channel effects were rather controversial: while in some reports a change was observed [3-5], other studies did not reveal a noticeable effect [6-7]. Later it was found that it strongly depends on technological details, whether or not the short channel behavior is affected by irradiation [8-9]. In a first attempt to model this issue, Huang et al [4-5] considered the charge sharing concept, depicted in Fig. 4.1, in order to calculate the impact of positive fixed charge on the flat band and threshold voltage of a short channel n-MOSFET.

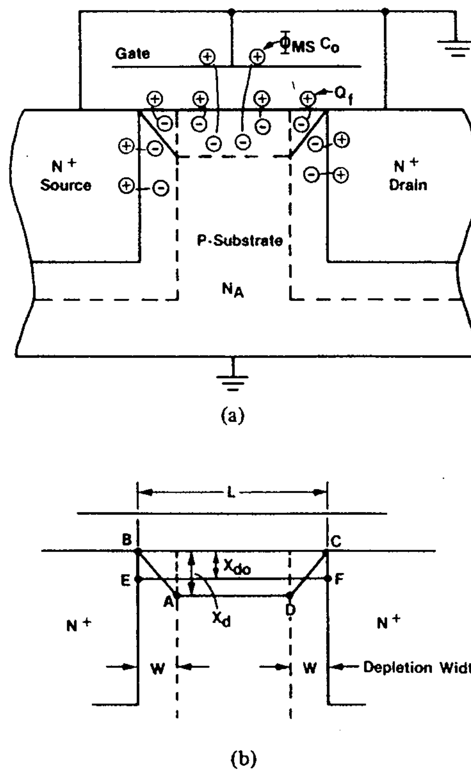

Fig. 4.1. Cross-sectional view of MOS model. (a) Pictorial view of charge sharing concept. (b) Geometry used for the calculations. (After Huang and Schrankler [4]).

They found that the corresponding change becomes:

$$\Delta V_T = \Delta V_{fb} = \frac{\Delta Q_{ot}}{C_{ox}} \frac{L}{L-W_d} \tag{4.2}$$

with C_{ox} the oxide capacitance per unit of area and ΔQ_{ot} a certain amount of trapped oxide charge (C/cm^2). As long as the device length L is much larger than the width of the source/drain depletion region W_d, the induced flat-band voltage shift is length independent, while an increased short channel effect is found from Eq. (4.2) for shorter devices. A stronger V_T shift has indeed been found for certain CMOS technologies, as shown in Fig. 4.2 [9]. In addition, the subthreshold leakage current (off-state leakage) also increases more severely for shorter n-channel transistors (Fig. 4.3). This means that the standby power consumption is higher for irradiated short channel transistors than for long devices. Studying in more detail the components contributing to the threshold voltage shift, i.e. the creation of positive oxide charge ΔV_{ot} and of negative interface charge (ΔV_{it}) in case of an n-MOSFET reveals that it is mainly ΔV_{ot} which increases for smaller L, while ΔV_{it} is relatively insensitive to this parameter [9]. In line with this ΔV_{ot} effect, the short p-channel counterparts show a more pronounced negative shift of the threshold voltage.

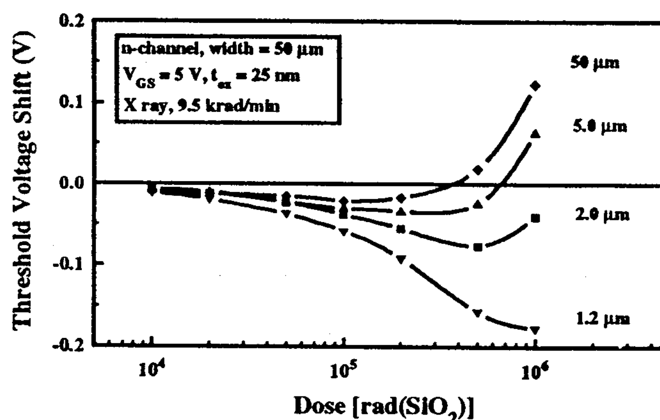

Fig. 4.2. ΔV_T for n-channel transistors irradiated to 1 Mrad(SiO_2) at 5 V with lengths of 50 µm to 1.2 µm and widths of 50 µm. (After Shaneyfelt et al. [9]).

The post-irradiation annealing of the trapped positive charge under 5 V gate bias appears to be similar for long and short devices, although the net V_T shift is markedly different (Fig. 4.4) [9]. The rebound observed in Fig. 4.4, whereby the threshold voltage of the n-MOSFET becomes larger (i.e. more positive) than before irradiation is less for a short channel compared with a longer channel device. This may be an advantage for shorter devices for the low dose rate environments, typical for space. However, the increase in off state leakage and power consumption may be a serious drawback, particularly for present-day low power/low voltage applications. Based on the low-frequency (LF) noise results shown in Fig. 4.5, it was concluded that for short-channels, there is an enhanced oxide trapped charge buildup [9]. This comes from the fact that the LF noise magnitude is proportional to the so-called near interface oxide traps, also called "slow" or "border" traps [10]. Note that the stronger radiation induced increase in the normalized noise (normalized

for the bias voltage and the device area A !) observed for the short channel transistors in Fig. 4.5 is an additional serious drawback for analogue applications of scaled technologies. The fact that more oxide trapping occurs for shorter lengths also demonstrates that Eq. (4.2) is too simple an approximation to describe the length dependence, since ΔQ_{ot} also varies with L.

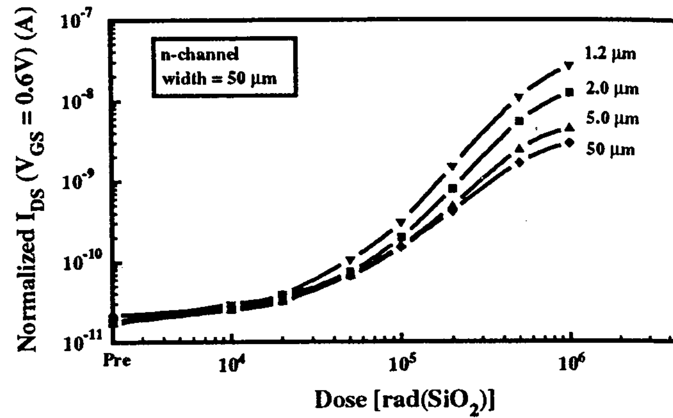

Fig. 4.3. Drain-to-source current at V_{GS}=0 V for the n-channel transistors. Note that the current has been normalized by L/W for transistor size. (After Shaneyfelt et al. [9]).

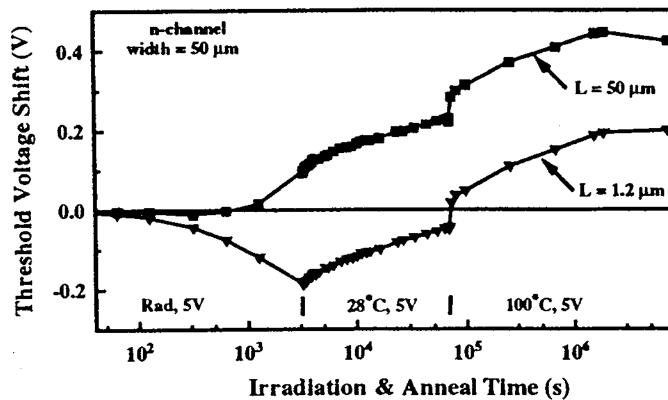

Fig. 4.4. ΔV_T for n-channel transistors with lengths of 1.2 and 50 µm, irradiated to 500 krad(SiO_2) and annealed at 28°C and 100°C. During irradiation and annealing, the gate bias was +5 V. (After Shaneyfelt et al. [9]).

It should finally be noted that the radiation response of narrow-width devices has also been studied in a number of cases (see e.g. Ref. 11).

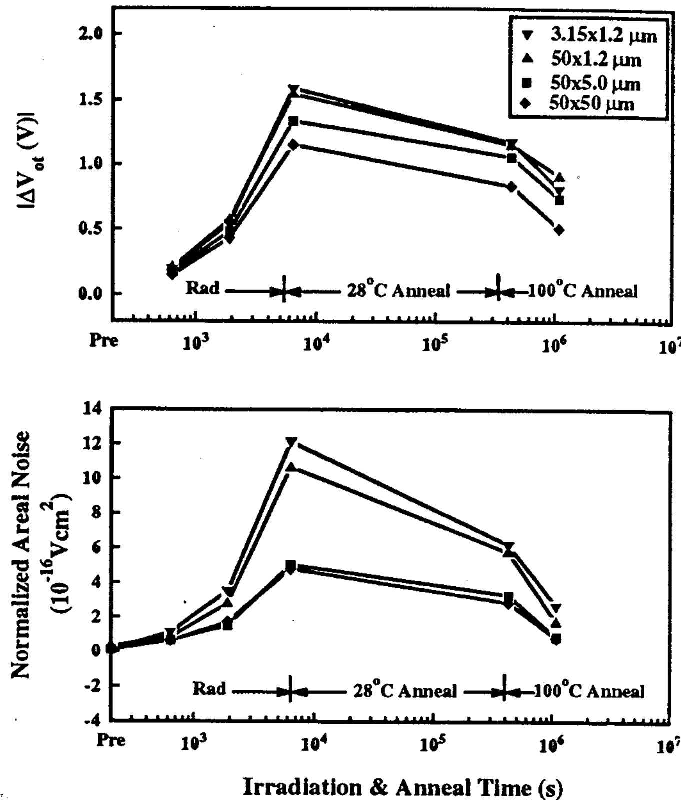

Fig. 4.5. ΔV_{ot} and normalized area noise power as a function of irradiation and anneal times for n-channel transistors. (After Shaneyfelt et al. [9]).

4.1.2 Non-Homogeneous Damaging

An additional factor which contributes to the enhanced degradation of short devices is the non-homogeneous nature of the damage along the channel, whereby clearly different densities of interface and oxide trapped charge have been found near the source and drain junctions [12-14]. This has been revealed by applying a number of new dedicated techniques with lateral resolution along the Si-SiO_2 interface, which are based on a modified charge pumping technique [12], the series resistance extraction of an L-array [13-14] and the study of the so-called gate-induced drain leakage (GIDL) current [13-14] (see next paragraph).

Figure 4.6 again illustrates the length dependence of the negative threshold voltage shift for n-MOSFETs with different 18 nm gate oxides: fluorinated, standard control dry oxide and a hardened oxide [14]. At the same time, the transconductance g_m is reduced

after irradiation, whereby the largest effect is seen for the shorter devices, and, for control oxides. Note that in Fig. 4.6 the control and fluorinated devices show a similar tendency, although the magnitude of the change is different, while the rad-hard MOSFETs in fact show opposite trend, with increased degradation for the shorter lengths. The latter is in line with previous observations for non-hardened oxides [5,9].

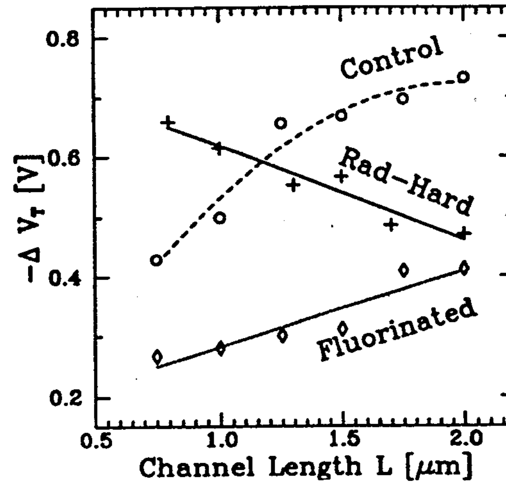

Fig. 4.6. Channel length dependent threshold voltage shifts in irradiated MOSFETs. During irradiation, a gate bias of +5 V with respect to the substrate was applied. t_{ox}=18 nm. (After Balasinski and Ma [14]).

Figure 4.7 represents the channel resistance R versus the channel length for the different gate oxides, before and after exposure to 1 Mrad(SiO_2) X-rays. After irradiation R is in first order given by [13]:

$$R = G^{-1} = \frac{L_{eff}-\Delta L}{W_{eff}} (\mu_{n,p}\, C_{ox}|V_{GS}-V_T|)^{-1} \tag{4.3}$$

with $\mu_{n,p}$ the electron (n) or hole (p) effective low-field mobility, L_{eff} and W_{eff} the effective (or electrical) length and width of the transistor. L_{eff} is equal to the designed (or mask) channel length minus a channel length reduction δL which is technology dependent, but constant for different L.

The ΔL in Eq. (4.3) corresponds to the edge region, adjacent to source/drain with a lower V_T than the bulk channel. This happens for example when more positive charge is trapped near the drain of an n-MOSFET (negative ΔL). If excessive negative (interface state) charge is created near the drain, a positive ΔL will be found, resulting in a shorter L_{eff} [13-14].

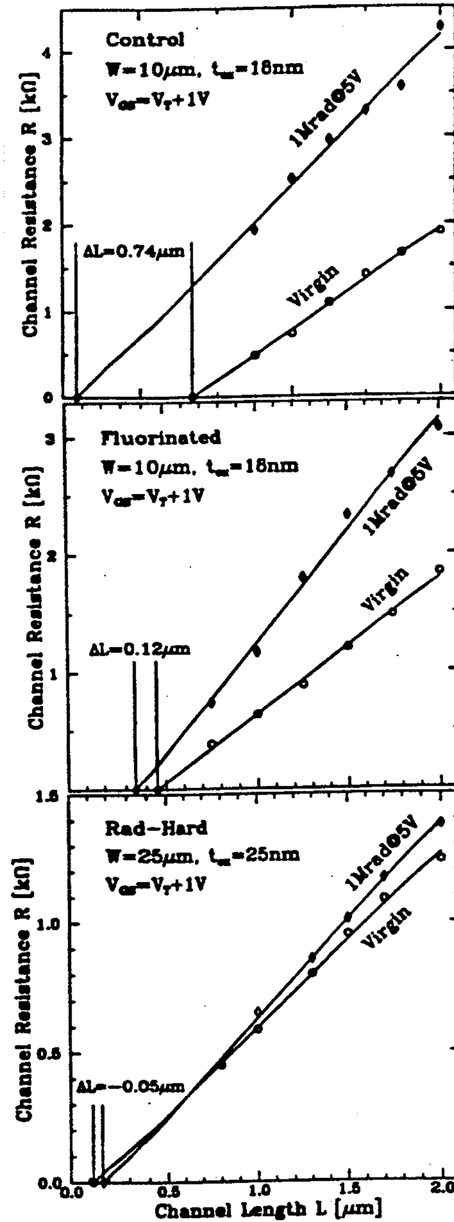

Fig. 4.7. Channel resistance as a function of channel length for virgin and irradiated MOSFETs from three lots: (a) Control, (b) Fluorinated and (c) Rad-Hard. The intercepts at the horizontal axis reveal the changes in the effective channel length. (After Balasinski and Ma [14]).

From Fig. 4.7 it is first of all derived that the slope of the post-rad curve is larger, indicating a degradation of the mobility, while the intercept with the x-axis has shifted by an amount ΔL, which strongly depends on the gate oxidation conditions. For the control and fluorinated case a positive ΔL points to an excessive negative charge near the source/drain, while a higher positive charge is expected for the rad-hard devices (negative ΔL).

The origin of this excessive charge near source and drain regions can be derived from the modified charge pumping analysis, which provides the lateral distributions of the interface and oxide traps (Fig. 4.8) [14]. It is clear that the control and fluorinated n-MOSFETs give rise to a lower trapped hole charge near the drain, while the opposite is observed for the radiation hard devices. In contrast, the density of negatively charged (acceptor) interface traps increases significantly when the drain is approached for control/fluorinated devices, while a more or less flat profile is found for the hard transistors (Fig. 4.8b). As a net result, more positive trapped charge is present for the hard n-MOSFETs, giving furthermore rise to a larger negative shift for the shorter device lengths in Fig. 4.5. This is due to the fact that for smaller gate lengths, the contribution of the edge regions to the overall degradation becomes more important. A similar argument holds for the control and fluorinated split. Additional computer simulations point out that the peak transconductance is extremely sensitive to the magnitude and position of the effective oxide charge near the junctions [14].

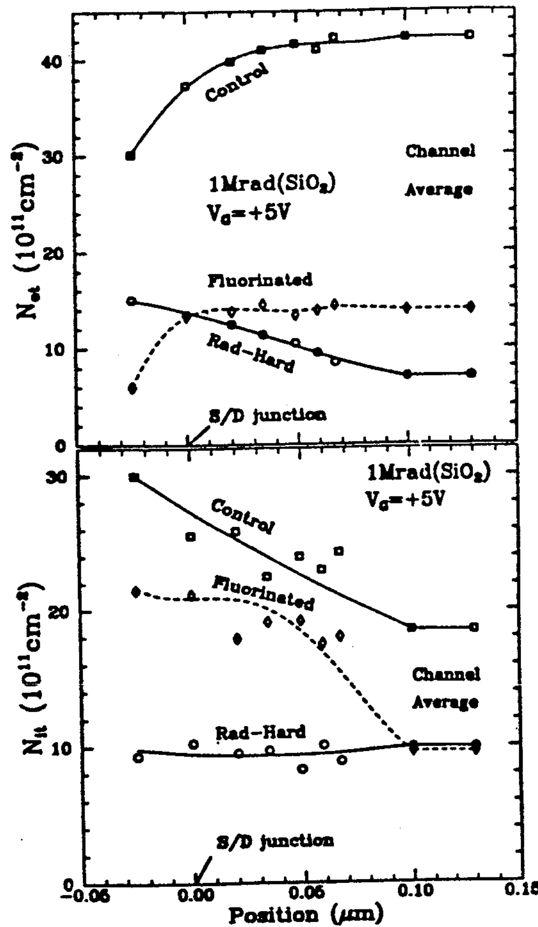

Fig.4.8. Lateral distribution of (a) oxide trapped charge, and (b) interface traps in the vicinity of the source or drain junction after 1 Mrad(SiO_2) irradiation at V_{GS}=+5 V. (After Balasinski and Ma [14]).

The origin of this non-uniformity is still unclear, since different mechanisms can be involved. One contributing factor is the difference in oxide field near the drain during the irradiation, related to the presence of the built-in field of the junction. Furthermore, the chemical oxide properties may be different close to source and drain, due to the presence of ion implanted dopants (As, B,...) in the oxide. In addition, there can be local variations in mechanical strain at the Si-SiO_2 interface, which is known to affect the generation of interface traps. Finally, there can be residual unannealed displacement damage in the oxide generated by previous device processing, i.e. coming from plasma etching and ion implantation.

It should finally be noted that in technologies using Lowly Doped Drain (LDD) structures covered by spacer oxides additional radiation-induced non uniformities in the degradation behavior can be created [15]. Omitting the LDD generally removes (lowers) this type of degradation.

4.1.3 Gate-Induced Drain Leakage (GIDL)

GIDL has emerged as a new constraint in miniaturizing MOSFET devices. Because it influences the drain current in the off state, it is of particular concern in low power circuits and DRAMs [16]. The GIDL current is observed when a gate bias is applied which accumulates the substrate, thus a negative V_{GS} for an n-MOSFET, attracting the holes to the interface. A field induced p^+-n^+ junction is hence created near the drain. Due to the large field existing there, tunneling of carriers from the p^+ to the n^+ region occurs, giving rise to an additional leakage current (GIDL), illustrated in Fig. 4.9 [16]. The GIDL current is basically independent of the device length L [17] and increases exponentially with |the absolute value of the gate overdrive voltage $|V_{GS}-V_T|$ as in Fig. 4.9.

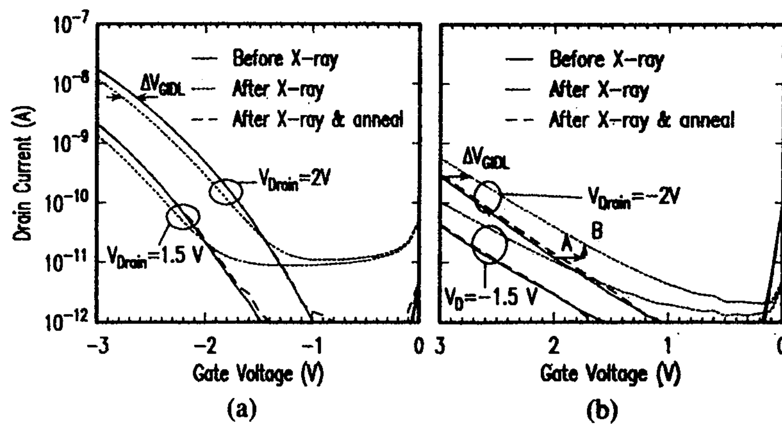

Fig. 4.9. Typical effect of a 0.5 J/cm^2 X-ray irradiation on GIDL in (a) n- and (b) p-channel MOSFETs with W/L=20 μm/0.65 μm, measured at V_{DS}=±1.5 V and ±2 V. In the n-channel device, the main effect of irradiation is a small parallel shift ΔV_{GIDL}. In the p-channel device, irradiation shifts the $I_D(V_{GS})$ characteristics - due to

trapped positive charges and positively charged interface states (A) - and increases the interface-state-assisted tunnel current (B). (After Acovic et al [16]).

After irradiation, the GIDL curve is shifted to more negative (n) or more positive (p) V_{GS} (Fig. 4.9). This shift is parallel for an n-channel device and is similar but in opposite direction, as the shift in the subthreshold I_D-V_{GS} curve, shown in Fig. 4.10a. This follows from the fact that [16]:

$$\Delta V_T = q\,(D_{itacceptor} - D^+_{ot})/C_{ox} \tag{4.4a}$$

$$\Delta V_{GIDL/given\ I_D} = q(-D_{itdonor} - D^+_{ot})/C_{ox} \tag{4.4b}$$

while, finally:

$$\Delta V_{mg} = -qD^+_{ot}/C_{ox} \tag{4.4c}$$

for the mid gap voltage shift, which corresponds to neutral interface traps (zero interface charge). $D_{itdonor}$, $D_{itacceptor}$ is the density of interface traps with donor and acceptor character, respectively. The former lie in the lower half of the band gap and are positively charged if the surface potential is below the level, while the acceptor states lie in the upper half and can be negatively charged or neutral, depending on the surface potential. In the case of GIDL (n-MOSFET) the surface potential is near the valence band and the donors are charged; the opposite holds when the MOSFET is operated in the subthreshold regime, where the acceptor interface charge is swept from zero to negative for increasing V_{GS}. The difference in shift between the GIDL and subthreshold I_D curve can be explained by this difference in underlying interface charge [16]. From this, it is concluded that in principle, the GIDL curve can be used in a similar way as the subthreshold characteristic to extract the oxide trapped charge near the drain after irradiation [13-4,16-17]. In fact, such a technique has first been developed to study interface-state generation by hot carriers in small MOSFETs.

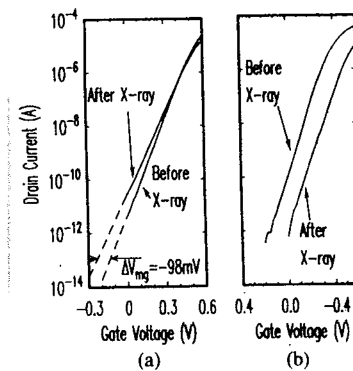

Fig. 4.10. Channel current in the MOSFETs of Fig. 4.9, at V_{DS}=±0.1 V. The dotted lines are extrapolated. In the n-channel device (a) the shift of V_T is 35 mV, and the subthreshold swing S increases from 78 to 92 mV/decade. In the p-channel device (b), ΔV_T=-211 mV and ΔS=3 mV/dec. (After Acovic et al. [16]).

For the p-channel devices, the shift of the post radiation curve in Fig. 4.9b is not parallel and also larger than for the n-MOSFETs [16]. This could point to the non-uniformity of the oxide trapped charge, already discussed above [14]. In addition, for low absolute gate bias, there is evidence for an excess GIDL after irradiation, which is more pronounced for the p-channel devices. It is believed that this is due an additional generation mechanism, whereby interface states assist the tunneling of carriers (ITAT=interface trap assisted tunneling) [16-17]. This causes the curves to shift vertically, while oxide trapped charge in first instance produces a horizontal shift, as indicated in Fig. 4.9. The larger impact of ITAT for p-channels suggest that probably a higher density of interface traps close to the conduction band is created by irradiation, compared with close to the conduction band, i.e. $D_{itacceptor} > D_{itdonor}$ [16].

Finally, from the annealing behavior, it is observed that the recovery proceeds faster for the oxide charge near the drain, as derived from GIDL experiments, compared with the charge in the central channel part [17].

4.2 Processing Induced Radiation Damage Effects

Already in the early days of submicron technologies it was realized that a number of processing steps could produce some form of radiation damage, which may not be removed totally by subsequent annealing [18]. This was shown to be the case for plasma or reactive ion etching (RIE), e-beam and X-ray lithography [19] and ion implantation through the gate oxide. While it is not clear yet whether e-beam, ion-beam or X-ray lithography will ever be used in a production environment (maybe somewhere in the sub 100 nm era), plasma and RIE etching is common practice nowadays. In the meantime, some other, new processing steps have emerged, which again raise concerns with respect to radiation damage. They will be critically reviewed in the following.

4.2.1 Plasma Damage

Typical submicron CMOS processes nowadays employ much plasma enhanced chemical vapor deposition and RIE steps, which could produce electrical stress and damage to the thin gate oxides. As a result, interface states and hole and electron traps are created by the Fowler-Nordheim (F-N) tunneling current flowing during the exposure to the plasma, which in a later stage can cause time-dependent dielectric breakdown (TDDB) and long term reliability problems. In addition, it is expected that also the radiation hardness of (sub)quarter micron CMOS could be at stake [20]. So far, little studies have addressed this issue. Nevertheless, from the cumulative probability plots of Fig. 4.11, it is immediately clear that plasma damaged devices show a large spread in the threshold voltage, which is on the average also shifted more than a non-plasma exposed wafer. Associated with the large spread and shift in V_T is a similar spread in the subthreshold slope S. The correlation between the two parameters is represented in Fig. 4.12 [20]. This suggests an enhanced hole trapping and interface state generation in plasma damaged devices, therefore, seriously jeopardizing the radiation tolerance.

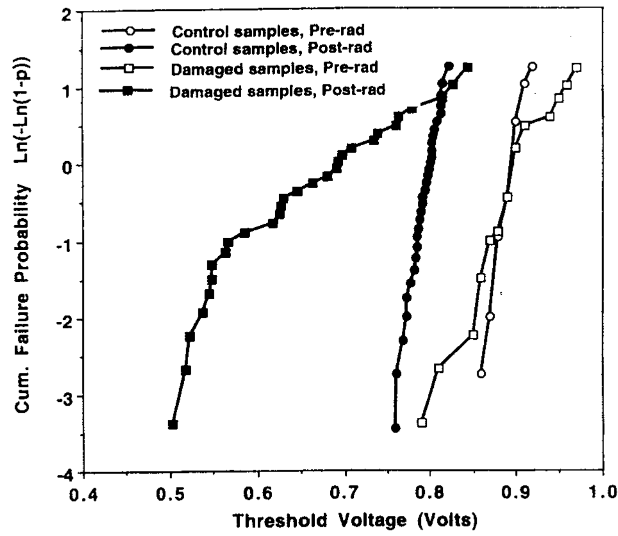

Fig. 4.11. Cumulative probability plots of threshold voltage (V_T) distribution of control and plasma-damaged samples before and after a total dose irradiation to 1 Mrad (SiO_2). NMOS devices were biased at V_{GS}=5 V and V_{DS}=V_{BS}=0 V during the irradiation. Large negative V_T shift indicates positive charge trapping in the plasma-damaged oxide. (After Yue et al. [20]).

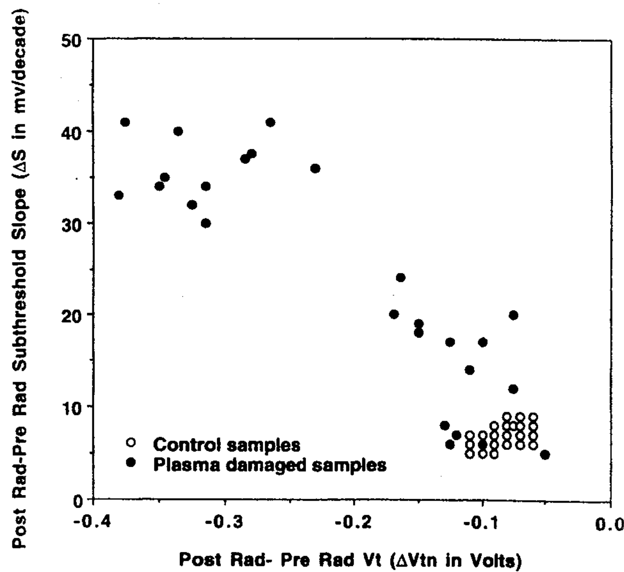

Fig. 4.12. Correlation between radiation induced threshold voltage shift (ΔV_T) and subthreshold swing shift (ΔS) with both control and plasma damaged samples. Results indicate enhanced hole trap and interface trap on plasma-damaged devices. (After Yue et al. [20]).

4.2.2 Rapid Thermal Annealing (RTA)

It is well-known that the total dose hardness of an oxide depends critically on the thermal history after oxide growth. For example, furnace annealing of the gate oxide at temperatures above 925°C can significantly degrade the radiation tolerance [21-27]. It has also been observed that the addition of a small amount of O_2 to an inert post-oxidation annealing (POA) reduces the buildup of trapped positive charge due to hot electrons or ionizing radiation [25-27]. Unfortunately, there exists usually a trade-off between, on the one hand, optimizing the quality of the oxide with respect to native fixed charge and interface states and, on the other hand, improving its radiation tolerance. In general, radiation resistant gate oxides have poorer initial quality and vice versa [27].

Nowadays, Rapid Thermal Annealing (RTA) is routinely used in submicron processing, amongst others for the activation of dopants after ion implantation and this to maintain a shallow junction depth of source and drain. Further downscaling actually reduces also the junction depths, which puts severe constraints on the allowable overall thermal budget. RTA is a powerful tool to cope with these limitations. During RTA, the temperature of a wafer is ramped in a short time (seconds) from room temperature to a value between 850 and 1050°C typically, where it is held for some annealing time (a few seconds) and then quickly cooled again. One may wonder if such a drastic procedure will affect the radiation hardness, especially since only the top surface of the wafer is heated significantly and there may exist a substantial temperature gradient across the wafer surface [27-28].

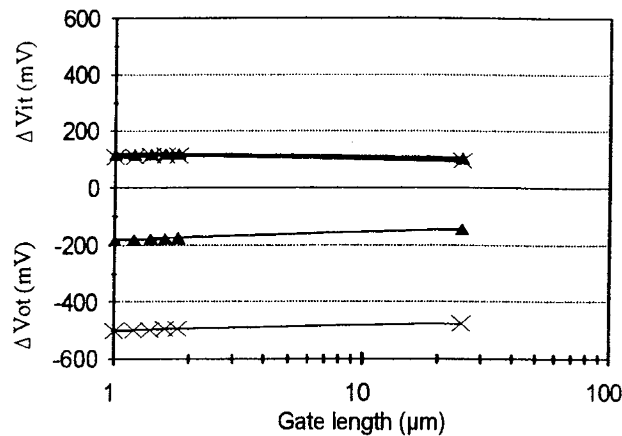

Fig. 4.13. Interface trap (ΔV_{it}) and oxide charge (ΔV_{ot}) contributions to the V_T shift after 1 Mrad(SiO_2) versus gate length of NMOS transistor from wafers with 1050 °C RTA (X) and without RTA (triangles). t_{ox}=18 nm, covered by a polysilicon gate. (After Flament et al. [28]).

The results of Fig. 4.13 immediately teaches us that RTA has a strong impact on the oxide trapped charge in furnace grown 18 nm oxides, but little influence on the radiation-induced interface states. At the same time, the device-to-device spread of ΔV_{ot} across a wafer is large(r), especially for the higher RTA temperatures, whereby the shifts are worst at the wafer periphery. This may be partially related to the non uniformity of the temperature during RTA, which can be controlled to within 20°C for the case studied [28]. The impact of the RTA temperature on the radiation response is better illustrated in Fig. 4.14, showing the largest negative V_T shift for the highest RTA temperature.

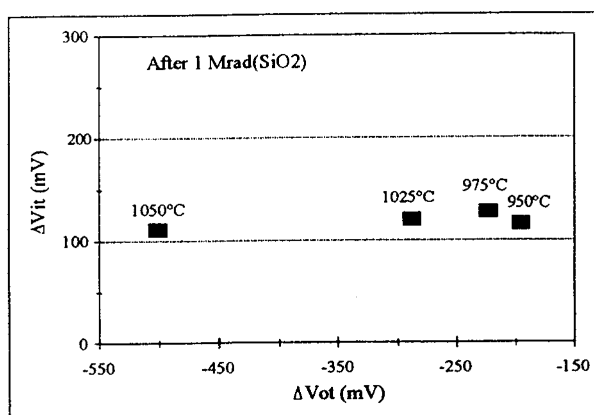

Fig. 4.14. ΔV_{it}-ΔV_{ot} plot for various RTA conditions in NMOS transistors. (After Flament et al. [28]).

In Fig. 15, the effect of an RTA post oxidation anneal on the V_T shift is compared with a PO furnace anneal. In both cases, negligible impact is observed up to a certain maximum temperature, while the hardness drops sharply beyond that. For RTA, this maximum occurs around 975°C [28]. Figure 4.15 implies that for a small temperature variation across a wafer during RTA, a strong spread in radiation response can occur for annealing temperatures beyond that. A similar behavior has been noted before for PO annealed 22-25 nm RT oxides grown at 1075°C [27]. In order to pinpoint the mechanism underlying the observations, the Arrhenius plot of Fig. 4.16 is very instructive. The same defect creation activation energy E_a of ≈3 eV has been found for both RTA and FA devices, strongly suggesting that it is an intrinsic oxide property which is responsible for the observed hardness degradation behavior.

The 3 eV activation energy comes close to the activation energy for the out-diffusion of interstitial oxygen to the adjacent Si substrate (≈2.54 eV), whereby oxygen vacancies are left behind near the interface. The latter centers have been shown to be responsible for the hole trapping, leading to the subsequent formation of *E'* paramagnetic centers, which can be detected by room temperature Electron Spin Resonance (ESR). The shift in temperature threshold between RTA and FA is then related to the time necessary for

sufficient oxygen atoms to leave the oxide. Since the time during RTA is restricted, a higher temperature is required to create a similar amount of oxygen vacancies. The dispersion observed across a wafer can be explained partly by assuming a temperature gradient. However, an additional factor (thermal stress ?) needs to be invoked, in order to explain the large magnitude of the spread

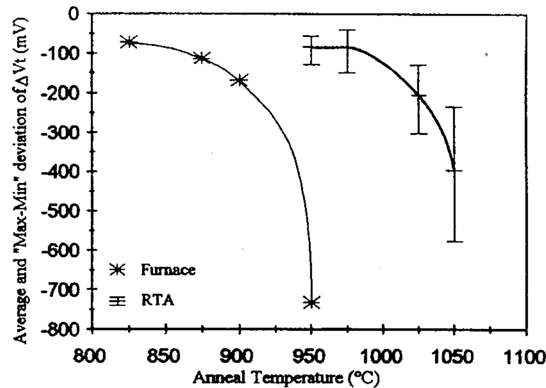

Fig. 4.15. V_T shift after 1 Mrad(SiO_2) versus anneal temperature for NMOS transistor. (After Flament et al. [28]).

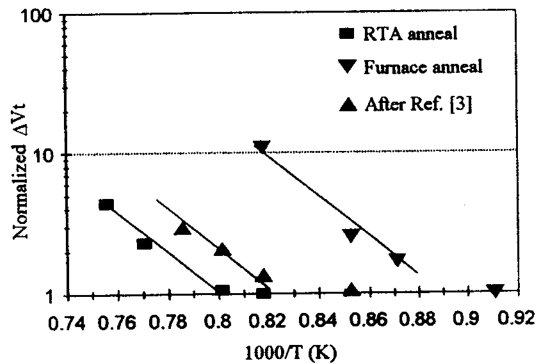

Fig. 4.16. Arrhenius plot of V_T shift after 1 Mrad(SiO_2) for NMOS transistor. t_{ox}=18 nm. (After Flament et al. [28]).

4.2.3 Gate Material and Contacting

Optimizing submicron CMOS requires in many cases the use of a double polysilicon gate material, in order to balance the properties of the n- and p-channel devices. For n-MOSFETs the standard n^+ poly is applied to the gate, while a surface channel p-

MOSFET is obtained if a B doped p^+ polysilicon gate is fabricated. This is in contrast to the classical n^+ single-poly p-MOSFET which has rather a buried channel character and, therefore, a worse control over the short-channel effects. The use of a double poly technology has a further implication, namely, one has to switch over to silicidation instead of Al metallisation of the gate. The latter would lead to a p-n junction in the polysilicon interconnect line.

The implementation of a p^+ poly gate brings about two major changes: first, there is the workfunction difference, which is about equal to the silicon band gap (≈1.12 eV). Second, the doping of the polysilicon is usually achieved by a B ion implantation, which might introduce B in the oxide, especially during the subsequent activation anneal of the dopants. These two factors can change the hardness of the oxide [29]. A thorough investigation has shown that p^+ poly gate devices actually show a better radiation response over a wide range of processing conditions, i.e., B implant dose. This is represented in Fig. 4.17a. A slightly different trend is observed with respect to the radiation-induced formation of interface states in the upper half of the band gap. There seems to exist an optimum implantation dose for B implanted n^+ poly (Fig. 4.17b), which was processed to compare with their p^+ counterparts to separate out the effect of the B implantation, from the change in work function difference on the radiation behavior. It was also observed that maximum ΔV_{it} was obtained for zero field during the exposure [29].

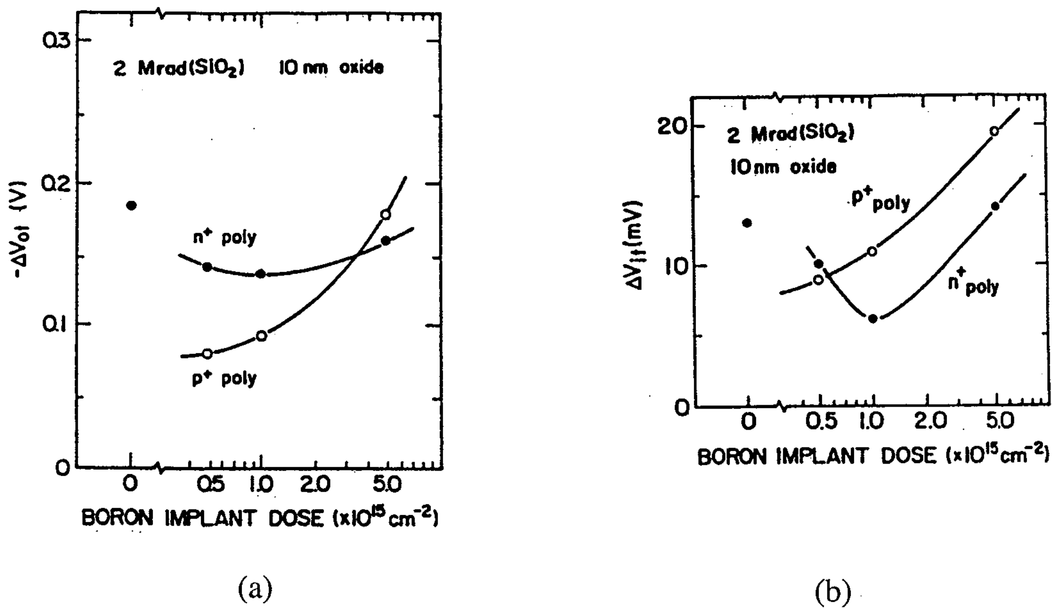

Fig. 4.17. Voltage shifts due to oxide trapped charge (a) and due to interface states (b) as a function of B implantation dose for the p^+ and n^+ gate capacitors with 10 nm oxides. The data represent the maximum voltage shifts with respect to applied bias. (After Yoshii et al. [29]).

The net result of ΔV_{ot} and ΔV_{it} is strongly in favor of the p^+ polysilicon compared with the commonly used n^+ material, so that p^+ p-MOSFETs are significantly harder than n^+ p-MOSFETs in older technology generations. The presence of the B in the oxide seems to play a certain role in the hardening, as found from the B implanted n^+ capacitors. It is speculated that B related (electron) traps could enhance electron-hole recombination during irradiation, so that less holes are available for subsequent deep trapping in oxygen vacancies near the interface. The trend for increasing hole trapping with increasing B dose could point to the presence of increasing residual ion implantation damage. The better behavior at higher doses for the n^+ poly could come from a further damage annealing during the subsequent P-diffusion doping used there. The increase of interface state formation with dose is probably related to the presence of Si-B bonds, which can break up to leave behind a silicon dangling bond (DB) [29].

Recently, interest in replacing polysilicon by amorphous silicon, deposited at lower temperatures has risen [30]. It has been shown that this affects the formation of interface states following ionizing irradiation: a significant reduction of D_{it} has been reported for amorphous gates. The improved hardness is assigned to the role of the mechanical stress associated with the amorphous gate. It is believed that a higher compressive stress is created in the oxide, after the gate dopant drive in, compared with polysilicon gates. On the other hand, annealing of polysilicon gates above 875°C lowers the hardness of the capacitor [24]. It has been demonstrated that for sufficiently high temperature anneals, the morphology of the polysilicon grains changes markedly, resulting probably in a different local stress.

The role of mechanical stress on interface state formation and hole trapping has been further studied by Kasama et al. [31-32], for different silicide-gate electrodes. It was found that compressive stress reduces both parameters and is in principle independent on the silicide material, for the same annealing conditions. The effect is most pronounced for interface-state generation and thin oxides. On the other hand, if the gate metallisation or back-end processing produces tensile stress, an increased interface state generation can result upon irradiation, which may show up a strong geometry (length) dependence [8].

4.3 Alternative Gate Dielectrics

4.3.1 Doped Oxides

The integrity of the gate oxide is sensitive to the post oxidation annealing temperature and ambient. Generally, annealing in an inert ambient is used, whereby the addition of a small amount of O_2 can increase the total dose hardness [27]. Furthermore, it has been found that the addition of a small amount of impurities during oxidation (Cl [33], F [34-35],...) can have a beneficial effect on the radiation response. It turns out that for most additives, an optimum exists, which implies that the gate oxidation conditions need to be well-controlled. An example is given in Fig. 4.18 for 18 nm F implanted gate oxides [35], demonstrating that the best response with respect to interface state generation is obtained

for a dose around $2x10^{15}$ cm^{-2}. It is believed that the presence of F or Cl at the interface changes the local bond strain distribution. A possible mechanism leading to the reduced strain is the interaction of a F atom with a strained Si-O bond, forming Si-F bonds and a non-bridging oxygen bond, resulting in a local strain relaxation. When excessive amounts of F (or Cl) are incorporated, too many non-bridging O-bonds are formed, which cancel the positive effect of strain relaxation [35].

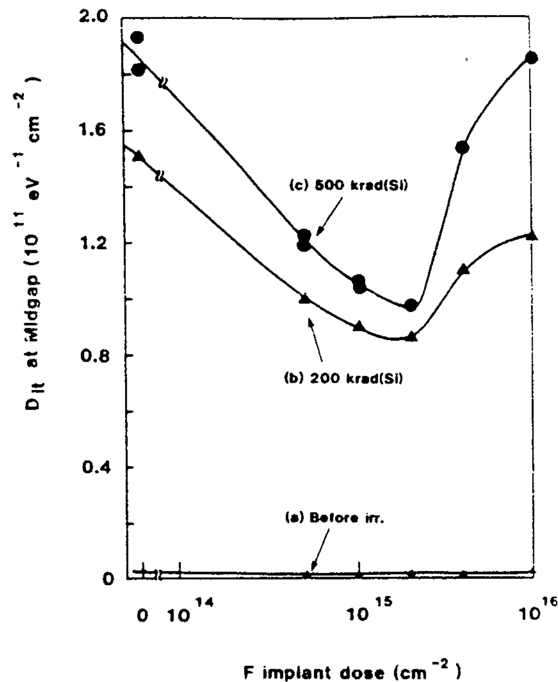

Fig. 4.18. X-ray radiation-induced mid gap interface state trap density as a function of fluorine implantation dose. Gate bias was kept floating during the irradiation. t_{ox}=18 nm. (a) Before irradiation; (b) after 200 krad(Si) radiation and; (c) after 500 krad(Si) radiation. (After Nishioka et al. [35]).

4.3.2 Nitrided (NO) and Reoxidised Nitrided Oxides (RNO)

The rate of scaling the device feature size is much stronger than the reduction in operating voltage. As a consequence, electrical fields in the oxide and near the drain become progressively higher, subjecting the MOS devices to hot carrier effects. This endangers the integrity and the lifetime of the oxide, so that there is a need for more reliable, hot carrier hard dielectrics. Early studies indicated that nitrided oxide (NO) could replace standard oxides for scaled technologies, as a harder, more reliable alternative [36-40]. Nitridation of the oxide is usually achieved by annealing the oxide in ammonia (NH_3), using either classical furnace, or rapid thermal annealing [40]. The latter allows a better control of the nitridation conditions and thermal budget. Besides that, nitrided oxides offer some other substantial advantages [39]: it has proven to be a good barrier for dopant diffusion (B, P, O,...). Nitrogen incorporation in the oxide increases the dielectric constant of the film, allowing a thicker layer to exhibit the same capacitance as a thinner oxide and

thus permitting higher gate voltages before breakdown. Nitrided oxides show furthermore a lower incidence of low field breakdown. Finally, there were early indications that NO holds promise as a hard(er) gate dielectric, which is not only of interest to space or military applications, but also in view of the application of plasma etching, e-beam or X-ray lithography [41], etc.

However, NO has also some substantial drawbacks, which limits large-scale implementation. First, it has been noted that NO oxides show a larger fixed oxide and interface trap charge under certain processing conditions [39 and references therein]. In addition, the presence of a large density of native electron traps (ET) can cause considerable electron trapping under hot-carrier or FN stressing conditions. These native ET are assumed to be related to the presence of substantial amounts of H or N close to the interface (see below for more details about the microscopic nature). Due to enhanced Coulombic scattering at these additional charge centers, the maximum effective mobility of carriers will be smaller in NO compared with standard oxides, resulting in a lower maximum transconductance for a MOSFET. The reduction is more pronounced for n- than for p-channel devices, due to the presence of the ETs [42]. Since both type of devices are affected, it is a strong evidence that the related near-interface oxide traps have an amphoteric character, i.e. they communicate with both inversion-layer holes and electrons. On the other hand, the mobility degradation with increasing gate bias V_{GS} is less pronounced for NO, resulting in a higher transconductance for high transverse electric fields than for standard oxides.

In order to improve the initial characteristics of NO, one can apply an additional reoxidation, either furnace [42] or rapid-thermal [43]. This is often abbreviated as RNO, although ONO or ROXNOX are also used frequently. The reoxidation reduces part of the excess fixed charges and ET, although not completely, while maintaining sufficient nitrogen concentration near the interface to preserve the advantages of NO. This is illustrated in Fig. 4.19, showing Auger (AES) profiles of NO and RNO oxides [42]. NO oxides contain a nitrogen peak at the Si-SiO_2 interface and at the surface (poly-gate) of the dielectric. For sufficiently heavy nitridations, the N concentration in the bulk of the oxide also increases. Reoxidation removes the surface peak and the bulk nitrogen, while the interface peak becomes smaller, compared with NO. In most cases, heavy nitridation and RNO create a high oxygen concentration layer at the interface, which plays a crucial role in the hardening of the gate dielectric.

Although NO and RNO have strong potential for achieving hard gate dielectrics, the resulting radiation response strongly depends on the processing details and usually requires an optimalisation. An example is presented in Fig. 4.20, showing the impact of the nitridation temperature and time on the radiation-induced flat band voltage change due to oxide trapped holes [39]. From these results follows that heavier nitridations (i.e. higher temperatures or longer times) are required to achieve hardness improvement, while light nitridations yield no improvement or even increase the hole trapping and interface state generation [39,44]. However, reoxidation of fairly light nitridations may result in a superior dielectric with respect to radiation damage [45]. Several groups have undertaken a systematic study of nitridation and reoxidation conditions on the radiation hardness, for which the Reader is referred to [44-49].

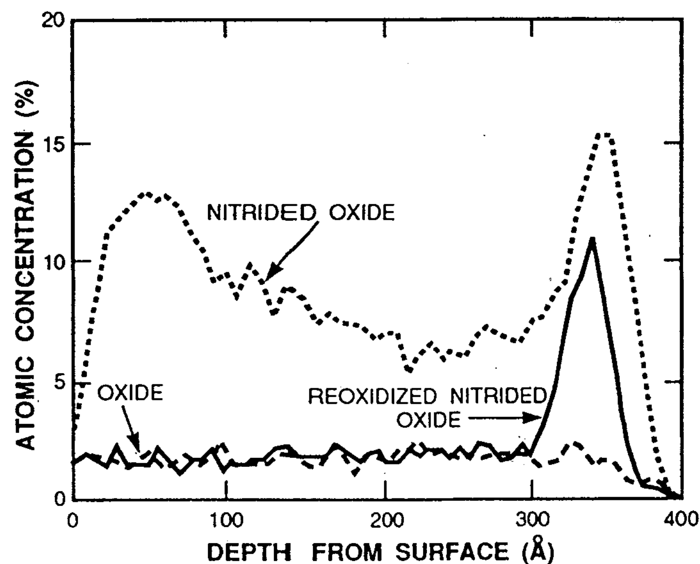

Fig. 4.19. Depth profiles of nitrogen concentration in oxide, nitrided oxide and reoxidised nitrided oxide, as measured by Auger electron spectroscopy. (After Dun and Wyatt [42]).

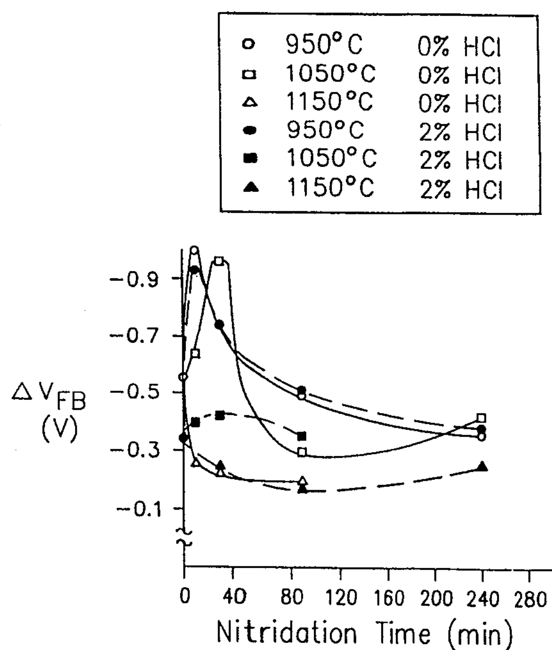

Fig. 4.20. Radiation-induced flat band voltage shift vs. nitridation time for 25 nm oxides grown in a dry O_2 ambient. Nitridation temperature and HCl content of oxidation ambient are shown in the inset. Dose is 100 Mrad. (After Ruggles and Monkowski [39]).

The degradation of the gate dielectric by ionizing radiation typically consists of hole trapping near the interface by already present neutral traps (with a hole capture cross section σ_p 10^{-13} to 10^{-14} cm^2) and the creation of interface traps. Electron trapping is usually negligible, since the native ET have an electron cross section which is typically three orders of magnitude smaller ($\sigma_n \sim 10^{-18}$ cm^2). This may no longer be the case for NO, where large densities of grown-in ET exist. Morover, radiation may create neutral ET with an electron cross section in the range 10^{-15} to 10^{-17} cm^2, which can become a reliability problem for downscaled MOSFETs, since they trap injected hot electrons [1]. Direct creation of other types of new trapping centers by displacement in the dielectric is rather uncommon.

Detailed studies of the hole trapping mechanisms in NO and RNO have been undertaken by a number of groups [50-53]. One unusual phenomenon was the observation that for RNO hole trapping was largest for negative gate bias during exposure (Fig. 4.21) [50]. For standard and NO gate dielectrics, maximum radiation-induced hole trapping occurs for positive gate bias with respect to the substrate, whereby the holes are pushed to the interface. The near interface region is characterized by a deficiency of oxygen and strained Si-O bonds, giving rise to a maximum concentration of neutral hole trapping centers (oxygen vacancies most likely). The fact that RNO behaves differently strongly suggests a different profile of pre-existing hole traps. Analyzing the midgap voltage shift leads to the schematic picture of Fig. 4.22, whereby the concentration of hole traps in the oxide peaks towards the gate and silicon interface, with the largest density near the gate interface (region between 3 and 7 nm of the gate) [42,50]. Another feature, which can be derived from Fig. 4.21, is that the capture cross section of the hole traps is much smaller in NO compared with RNO. This follows from the rapid saturation of the midgap voltage shift for RNO, while a continuous increase with dose is found for NO.

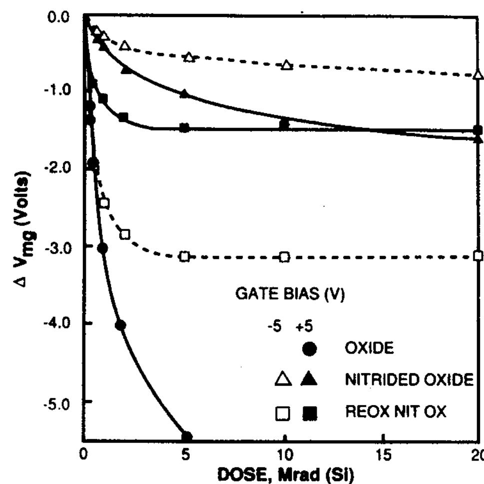

Fig. 4.21. Mid gap voltage shift versus dose for oxide, nitrided oxide and reoxidised nitrided oxide capacitors irradiated with positive and negative applied gate bias. (After Dunn [50]).

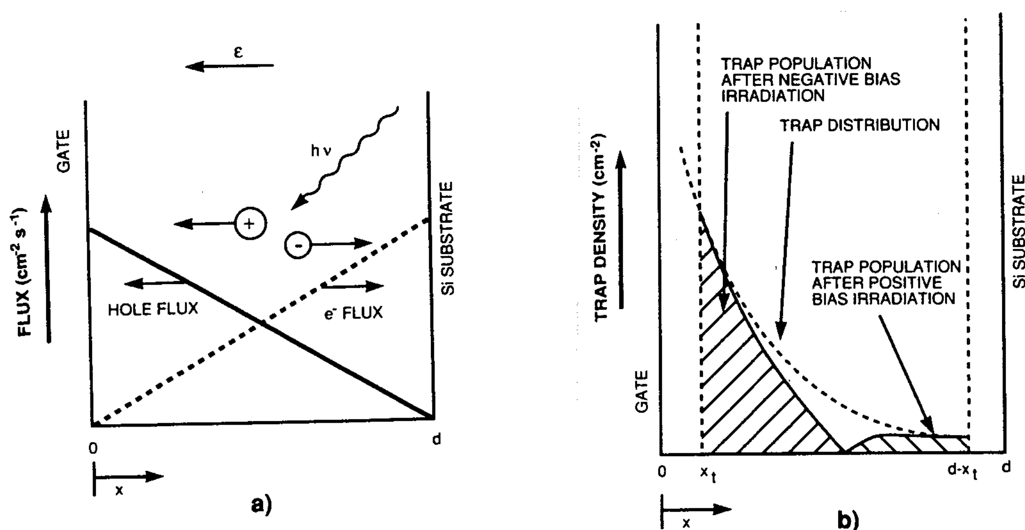

Fig. 4.22. (a) Hole and electron flux in an ideal trapless dielectric during irradiation with gate biased negatively. (b) Qualitative description of hole trap population in reoxidised nitrided oxide following positive and negative bias irradiations. (After Dunn [50]).

Part of the slow positive charging of NO dielectrics can be related to slow donor states, which may be created and ionized during electrical stress or irradiation [51]. Slow donor states are shown to be responsible for a reversible, bias- and temperature-dependent charge relaxation. The number of slow donor states is a function of the nitridation and reoxidation conditions. Using optimized conditions, RNO dielectrics can be grown with essentially no slow donor states and, hence, with little relaxation [51].

Detrapping studies of positive charge after irradiation have revealed some further interesting observations [52]. Figure 4.23 compares the detrapping behavior of irradiated 36 nm RNO with standard oxides, as a function of the gate bias and this for a 1 hour room temperature 'anneal'. For positive gate bias during the anneal, hardly any detrapping is found for RNO, which is indicated by the unannealed fraction remaining 1.0. This implies that also no interface traps are being created. For the standard oxide, increasing detrapping is found for more positive gate bias, which is in line with the electron tunneling mechanism at the Si-SiO_2 interface. This follows also from the ln t time dependence of the unannealed fraction at a constant gate bias [52]. Indeed, for positive gate bias, electrons can tunnel from the substrate in trapped hole centers, which have their maximum density near this interface. As a result, the trapped hole is neutralized by the captured electron, either permanently or reversibly, in the case of a switching oxide trap [54]. For negative gate bias, on the other hand, negligible detrapping is expected and found for standard oxides. For RNO, increasing detrapping is observed for more negative gate bias, confirming that the oxide trapped charge is mainly in the upper half of the dielectric, close to the gate electrode.

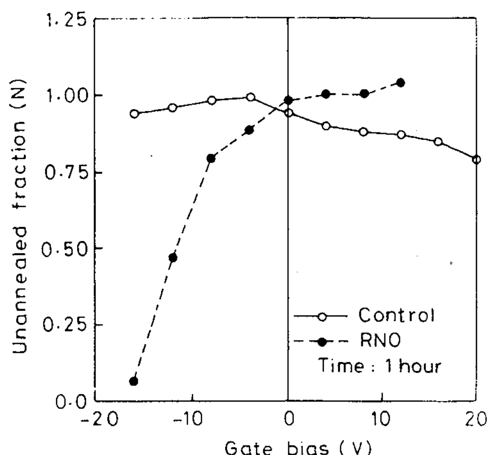

Fig. 4.23. Field detrapping of the radiation-induced trapped charges in control oxide as well as in RNO devices at different gate bias conditions. (After Mallik et al. [52]).

From isochronal detrapping experiments, whereby the temperature is varied for a fixed annealing time (10 min.) without application of bias here [52], one can derive an effective energy distribution of the discharging hole traps. As can be seen from Fig. 4.24, a completely different spectrum is found for RNO, showing a much more peaked behavior, centered around a higher average activation energy of around 0.96 eV. From this it is concluded that the traps which are found in conventional oxides are removed in RNO, whereas a new type of hole trap is introduced by the RNO process [52]. Finally, it has been observed that both the density and σ_p of the RNO hole traps are quite different from control oxides. The hole capture cross section is significantly larger (7.9 x 10^{-12} cm^2) and the density markedly smaller in RNO compared with a standard oxide [53].

One of the advantages of NO (RNO) is the absence of interface state generation during and following irradiation or high-field/hot-carrier stress. However, this only applies for optimized processing conditions, as illustrated by Fig. 4.25 [55,56]. This is further evidenced by the time evolutions of Figs 4.26a and b, corresponding to control and RNO oxide [57]. While there is a power law (t^m) dependent delayed D_{it} formation in the control oxide, it does not occur at all for the RNO. Furthermore, exposure to hydrogen after irradiation does not create additional interface traps or a reduction in trapped positive charge, this in contrast to control oxides [57].

Different mechanisms have been proposed for the absence of D_{it} formation, which are based on the two main models for interface trap buildup [56,58]. In the electron-hole recombination model, it is assumed that first a hole needs to be trapped in a near-interface oxide trap, which subsequently captures an electron, giving rise to a bonding reconfiguration which creates silicon dangling bonds at the interface (P_b centers). For light

nitridations, the presence of N creates strained Si-O bonds at the interface, which can act as a hole trapping center and are therefore thought to be precursors of the radiation-induced interface traps [56]. Heavy nitridation or reoxidation shifts the nitrogen peak away from the interface in the oxide and, hence, the corresponding trapping centers, while an oxidation of the interface occurs. In addition, it is believed that the presence of nitrogen in the oxide compensates the compressive stress at the interface. However, as pointed out by Yount et al, one should not overestimate the stress factor for NO and RNO dielectrics; these Authors assign only a minor role to stress in the radiation degradation of the Si-SiO_2 interface [59]. In their view, it is the absence of *E'* centers (oxygen vacancies) which reduces the hole trapping and probably the reduced D_{it} formation.

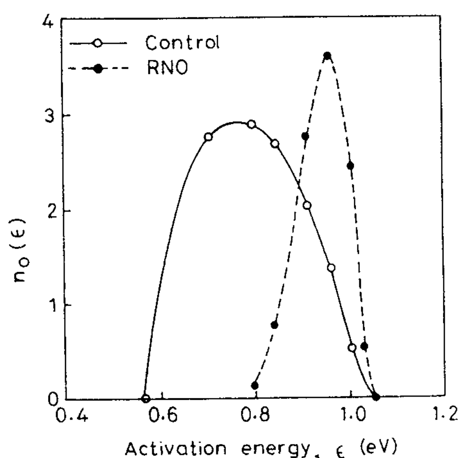

Fig. 4.24. Activation energy distribution of annealing of the radiation-induced trapped charges in control oxide as well as in RNO devices. (After Mallik et al. [52])

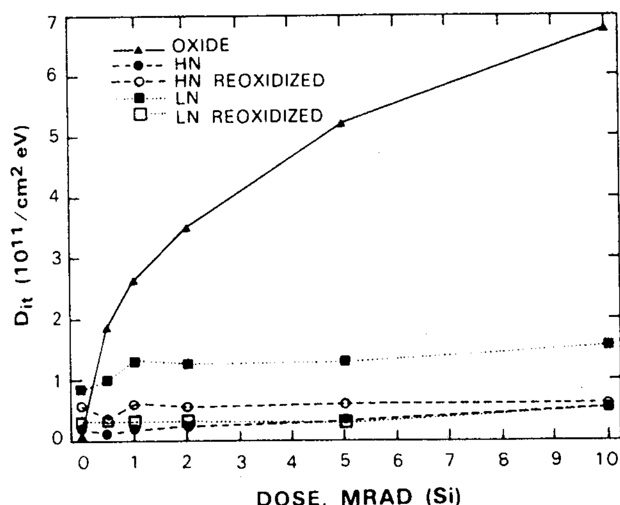

Fig. 4. 25. Mid gap interface state densities in MOS capacitors after exposure to 10 keV X-rays. (After Dunn [55]).

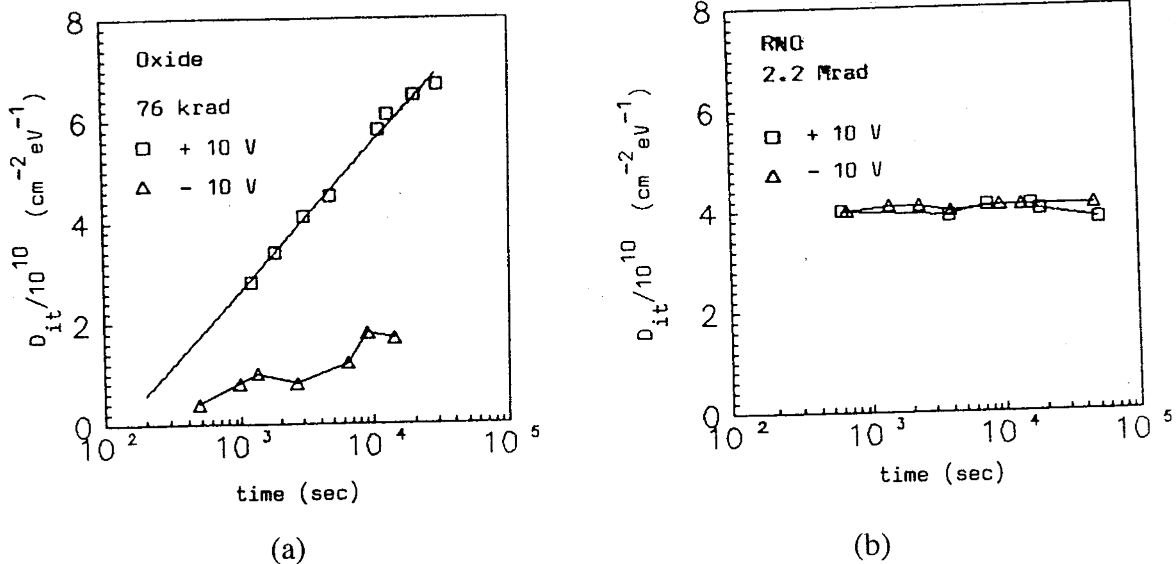

Fig. 4.26. (a) Time evolution of ΔD_{it} for dry oxide after a radiation dose of 76 krad(Si). The capacitors were biased at ±10 V after irradiation. D_{it} before irradiation was 10^{10} $cm^{-2}eV^{-1}$ and just after irradiation $8x10^{10}$ $cm^{-2}eV^{-1}$. (b) Time evolution of ΔD_{it} for RNO after a radiation dose of 2.2 Mrad(Si). The capacitors were biased at ±10 V after irradiation. D_{it} before irradiation was $2x10^{10}$ cm^2eV^1. (After Bhat and Vasi [57]).

Although the electron-hole recombination model may be partly responsible, it has recently been shown that hydrogen plays a definite role in the interface state generation or its absence in NO and RNO [58]. On the one hand, one would expect an effect of the high density of H present in NO [56], if the H-diffusion model were responsible for the radiation-induced D_{it} formation. The result of Fig. 4.27 clearly demonstrates that effectively interface states are being generated in RNO, if exposed to a hydrogen plasma and subsequently subjected to photoelectron injection at fields below the impact ionization threshold of ≈10 MV/cm in SiO_2. The main difference is that the rate of D_{it} increase is much lower in RNO compared with standard oxides. In fact, the rate of B passivation in the underlying silicon substrate nicely tracks the D_{it} curves, indicating that the same basic phenomenon determines the simple first-order kinetics of both effects. It is believed that the key factor is the diffusion of radiation released neutral hydrogen H^0 towards the interface, where it reacts with a passivated P_b center (P_b-H) to create a Si dangling bond and H_2. The presence of the nitrogen peak close to the Si-SiO_2 interface retards the hydrogen diffusion and operates thus as a diffusion barrier, similar as for other impurities like B and oxygen. Lighter reoxidation leaves a higher peak concentration (4 %) than the heavier RNO (2 %), explaining its larger efficiency in retarding/blocking the hydrogen diffusion. Another conclusion of this work is that the interface chemistry is not affected by RNO [58]. In other words, it is believed that the same density and type of interface trap precursor sites is

present in control or RTO dielectrics, which explains the strong correlation of the curves in Fig. 4.27.

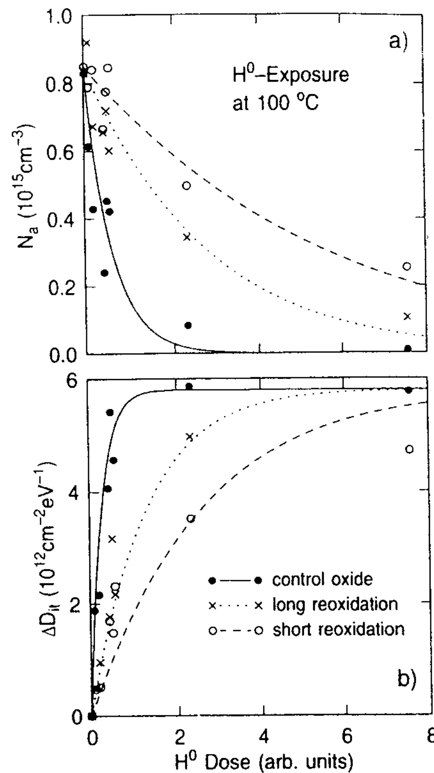

Fig. 4.27. Comparison of the doping density passivation in the depletion region of p-type (boron-doped) silicon (a) and of the interface state buildup at the silicon/oxide interface (b) as a function of the atomic hydrogen (H^0) dose from a remote hydrogen plasma. Exposures were performed at 100°C. In each case, samples with three different oxides are compared. (After Cartier et al. [58]).

While in standard thermal oxides electron trapping during irradiation is negligible, this may no longer be the case for NO, where it is known that a large density of ET is introduced during nitridation. In fact, trapped electrons could be responsible for a partial compensation of the trapped hole charge and, therefore, lowering ΔV_{ot} and enhancing the hardness of the oxide [60]. Detailed investigations have demonstrated that, although there is some electron trapping the effect is of second order (10 to 20 % of the hole trapping, typically). This is illustrated by Figs. 4.28 and 4.29. In Fig. 4.28, the isochronal detrapping of radiation-induced charge is plotted versus temperature. Up to point A in the RNO curve, the behaviour is dominated by hole detrapping, which shows a different temperature dependence for both types of oxide. This can be explained by the different energy distribution of the hole traps in both cases and shown in Fig. 4.24 [52]. This hole detrapping is shown to be independent of the magnitude of the field during irradiation, but depends heavily on its polarity (Fig. 4.29). At point A, full compensation occurs between the trapped positive and negative charge for RNO. On the other hand, no sign changing, is found for control oxides.

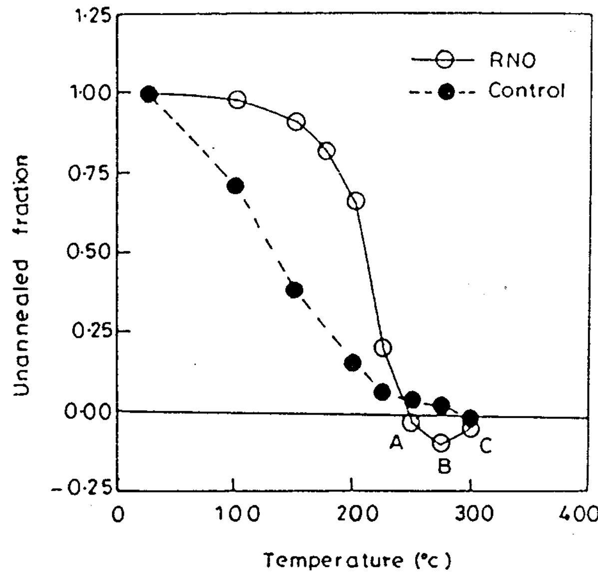

Fig. 4.28. Results of isochronal detrapping experiments following irradiation under floating gate for RNO (36 nm) and conventional dry oxides (33 nm). The values of ΔV_{mg} were -0.7 and -1.66 V for RNO and dry oxides, respectively. (After Mallik et al. [60]).

Further hole detrapping in RNO takes place from A to B in Fig. 4.28. The fact that the unannealed fraction changes sign (super-recovery) in the RNO indicates that electron trapping during exposure does occur. From B to C also the electrons become finally detrapped at higher temperatures, suggesting also another energy distribution for these centers. Holes in RNO are completely detrapped around 275°C, while this occurs around 300 °C for the electrons. It has also been demonstrated that the fraction of electron trapping is independent of the field direction during irradiation. This is opposite to the case of hole trapping, which shows maximum intensity in RNO for the most negative bias during exposure (Fig. 4.21) [50]. The amount of trapped negative charge, however, strongly depends on the bias during irradiation. Highest electron trapping occurs for zero field (floating gate), whereby a region of minimum potential is created by trapped holes, which stimulates electron trapping in the neighborhood. This is not the case for high fields. In addition, the low electron capture cross section of the traps reduces strongly with oxide field for high E_{ox}, explaining negligible electron trapping [60].

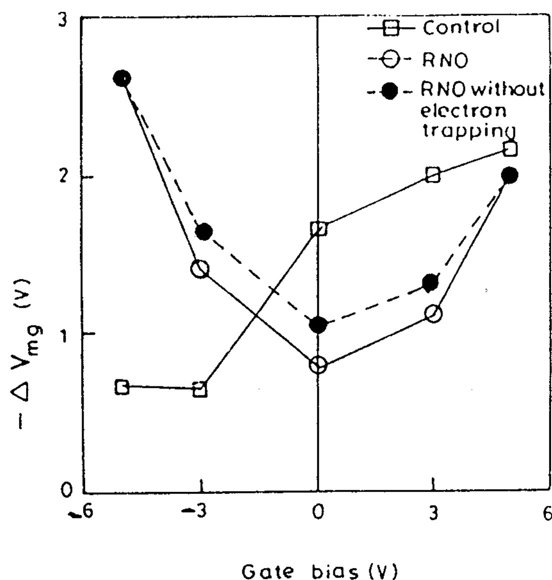

Fig. 4.29. Mid gap voltage shift as a function of gate bias during irradiation for 1 Mrad(Si) dose. Solid curves represent experimental ΔV_{mg} whereas dotted curve represents estimated ΔV_{mg} if there would not have been any electron trapping. (after Mallik et al. [60]).

Finally, Fig. 4.29 elucidates the role and impact of electron trapping for RNO dielectrics, showing maximum impact for zero fields and negligible effect for high fields, for both polarities. Note also that RNO shows highest hole trapping for negative gate bias during exposure and is, therefore, less suitable for such operation conditions, compared with control oxides [60].

Further studies have indicated that nitridation creates neutral hole and electron traps, which can be reduced by reoxidation [61], in a selective way, whereby traps with an electron capture cross section of 10^{-17} cm^2 are maintained, while ET with lower cross sections are removed [62]. One particular reliability issue is the creation of neutral electron traps (NET), following irradiation [1]. This is especially of concern under positive gate bias operation [63]. However, it has been demonstrated that for RNO, NET formation is successfully suppressed. This is assigned to the presence of the nitrogen peak close to the silicon interface, which blocks the diffusion of H^+, believed to be necessary for the NET creation.

The effect of irradiation on transistor mobility and maximum transconductance of RNO devices has been studied in a number of cases [42,64,65]. It has been found that after irradiation and subsequent low-temperature anneal, a higher inversion layer mobility is observed for RNO n-MOSFETs than before irradiation. Additional LF noise studies indicate that radiation + annealing removes near interface electron traps in RNO, which cause Coulombic scattering and an accompanying reduction of the mobility. The optimum

annealing temperature is around 400°C [64]. Similar effects are observed for the corresponding p-channel devices, although to a lesser extent. This confirms that the near-interface oxide trap responsible for the observations has an amphoteric character, but is much less efficient in trapping holes. It has furthermore been shown that after irradiation, the effective mobility of irradiated RNO transistors is superior to control n-MOSFETs [65] and may even improve after exposure (without anneal). One of the factors contributing to this improvement is the fact that hole trapping in RNO happens mainly at the gate interface [50], while in contrast, for standard oxides the trapped-hole charge is mainly at the silicon interface. This is related to the profile of the responsible traps, which shows opposite behavior for both types of dielectrics, as shown in Fig. 4.22.

It should be remarked that the subthreshold slope of irradiated RNO MOSFETs hardly degrades, indicating negligible buildup of interface states [42,65]. This is also confirmed by charge pumping measurements.

Finally, the charge trapping in thermal and nitrided oxides at low temperatures has been studied by Boesch and Dunn [66]. From these experiments, it is concluded that RNO has a potentially better total dose hardness for cryogenic applications, particularly under moderately high-field operation conditions.

In the foregoing, only the impact on the macroscopic properties of nitridation on the gate insulators has been addressed. Microscopic information on the structure of the responsible defects can also be obtained, using the Electron Spin Resonance (ESR) technique [67]. So far, the paramagnetic centers represented in Fig. 4.30 have been firmly identified at the interface or in the oxide of irradiated (or high-field stressed) gate dielectrics. At the same time, the obtained spin density allows to derive the corresponding absolute concentration to within a factor of 2. Trap density profiles can be measured by ESR on back etched oxides, gradually thinning the sample.

From ESR studies on irradiated films it has been derived that nitridation creates bridging N precursors (c in Fig. 4.30). RNO also shows these radiation induced bridging N traps together with overcoordinated nitrogen centres, represented by d in Fig. 4.30. The impact of the reoxidation time on the different trap species is shown in Fig. 4.31. From this, it is concluded that reoxidation lowers the density of bridging N precursors, which are therefore believed to correspond to the main native electron traps in NO films [67]. Nitridation reduces significantly the number of *E'* centers (holes trapped in an oxygen vacancy, giving rise to a paramagnetic unpaired electron), while reoxidation produces larger *E'* ESR signals. However, *E'* is not the dominant hole trap in RNO films [7]. This follows for example from the defect profiles shown in Fig. 4.32. While the *E'* centers show a pronounced increase near the silicon interface (position 0 Å) for the 'oxide', a flat profile is found for the NO and RNO case. One might at first sight speculate that the *E'* centers in RNO could be (partly) responsible for the radiation-induced hole trapping. However, further experiments show completely different behavior with 'normal' oxygen-vacancy related *E'* centers [67]. For example, no change is observed in the paramagnetism (density,...) of *E'* in RNO after the photoinjection of electrons. If these centers were positively charged like in conventional oxides, electrons would be readily trapped with a large cross section, rendering the center diamagnetic and thus undetectable for ESR

observation. This strongly suggests that RNO *E'* centers are charge neutral and probably single dangling bonds (b in Fig. 4.30)- not vacancies as in thermal oxides.

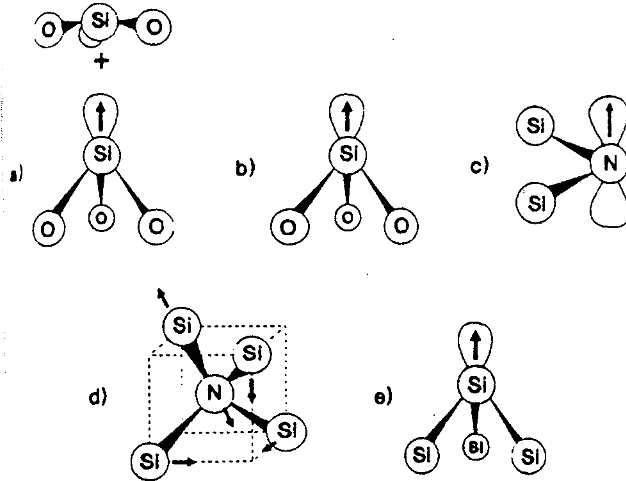

Fig. 4.30. Schematic diagram of the paramagnetic defects observed in irradiated gate dielectric films: (a) positive *E'* center associated with an oxygen vacancy; (b) neutral *E'* center; (c) bridging nitrogen center; (d) overcoordinated nitrogen center (arrows indicate direction of Jahn-Teller distortion) and (e) P_b center. It is unclear whether the overcoordinated and bridging nitrogen defects are bonded only to silicon defects. (After Yount et al. [67]).

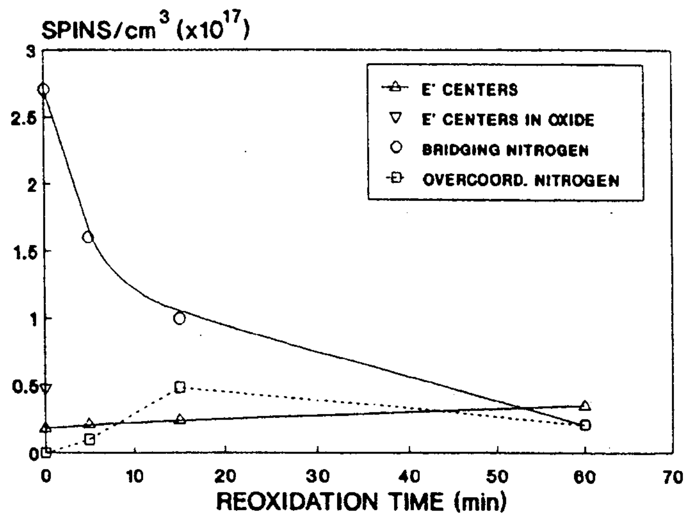

Fig. 4.31. Defect density versus reoxidation time. (After Yount et al. [67]).

Figure 33 shows the bridging N center profiles for NO and RNO films; they are thought to be responsible for the significant electron trapping in irradiated NO and to a lesser extent in RNO. This leaves us with the question which centers are responsible for the hole trapping near the gate electrode in RNO? A possible candidate is the overcoordinated N center, which shows an increasing profile towards the gate [67]. It is expected, however, that this is rather unlikely, given the expected donor nature of the group V nitrogen element. Another important finding is that after hydrogenation both the *E'* hole traps and the N-related defect centres disappear from ESR observation after a 10 minute exposure to forming gas anneal [67]. This implies that the N-related defects quickly react with the H_2, thereby lowering the effective diffusivity (mobility) of hydrogen. This can be a key process in the reduction of interface state buildup and supports the results of Cartier et al. [58].

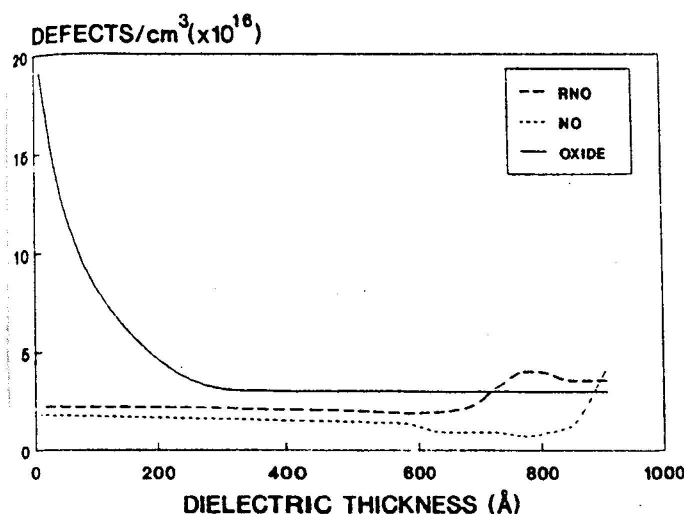

Fig. 4.32. *E'* distribution in oxide, NO and 15RNO samples. Distribution curves are approximations based on etchback data. (After Yount et al. [67]).

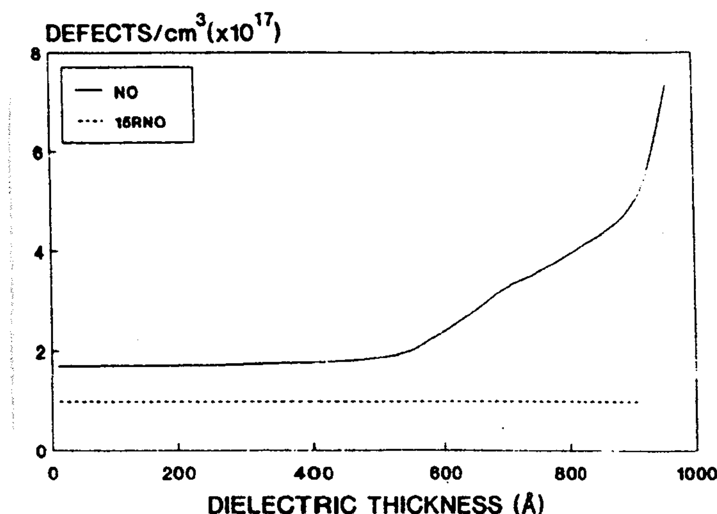

Fig. 4.33. Bridging nitrogen distribution in NO and 15RNO samples. Distribution curves are approximations based on etchback data. (After Yount et al. [67]).

4.3.3. N_2O or Nitrous Oxides

Recently, interest has developed to grow thin and ultra-thin oxides in an N_2O atmosphere (nitrous oxide or oxynitrides), rather than in NH_3 [68-72]. This offers several advantages: first, less hydrogen is introduced compared with NO. Second, the starting quality with respect to fixed charge, electron traps and interface traps is equal compared to conventional oxides. Next, a nitrogen peak is only found at the silicon interface, not at the surface or in the oxide bulk, as seen in Fig. 4.34. Different processing schemes have been proposed [68-72], whereby a repeated thermal oxidation in N_2O [71], or a two-step oxidation in O_2 followed by N_2O shows some advantages, compared with a single N_2O growth. In the latter case, the thickness of the grown layer saturates at rather low values, due to the reduced diffusion of oxygen across the nitrogen barrier at the interface [72]. In addition, little or no pre-radiation degradation of the maximum transconductance and the effective mobility has been noted [70,72]; even an improvement can be found for optimised nitridation conditions [70].

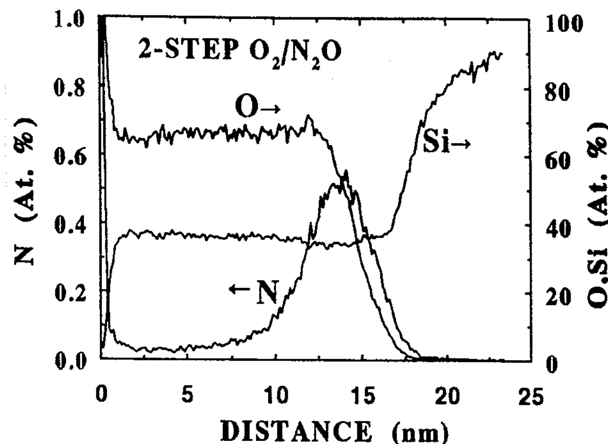

Fig. 4.34. SIMS N, Si and O profiles of a 14 nm thick 2 step O_2/N_2O oxynitride. The N peak is at the Si-SiO_2 interface with a maximum N concentration of ~0.5 at. %. (After Saks et al. [72]).

In addition to the advantageous initial quality of the oxynitrides, also the radiation response is improved compared with thermal oxides [68-72]. It has been shown that both the oxide trapped charge and the interface state generation due to ionization damage is reduced. An example is given in Fig. 4.35 [69], showing a smaller transconductance degradation for N_2O-nitrided. Remark also the length dependence in the figure, whereby a higher degradation is found for the shorter transistors, in line with earlier reports [9,14] (see e.g. Fig. 4.4). It has also been observed that N_2O oxides show an enhanced resistance against NET formation [69].

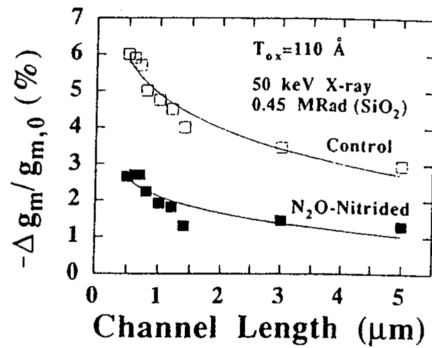

Fig. 4.35. Normalised peak g_m degradation ($\Delta g_m/g_{m,0}$) due to X-ray irradiation as a function of channel length for n-MOSFETs with control and N_2O-nitrided gate oxides. (After Lo et al. [69]).

The impact of the gate dielectric for ≈8 nm gate dielectrics is represented in Fig. 4.36 [71], showing the superior behaviour of N_2O (2-time) oxides. It is mainly the interface state buildup, which is improved, while the hole trapping is equivalent as for thermal oxides [72]. This points to the fact that the chemistry and structure of the near interface oxide region, where the border traps reside is clearly different for oxynitrided layers [72-74], whereby it is assumed that less oxygen vacancies are present, while stronger Si-N bonds may replace the strained Si-O bonds.

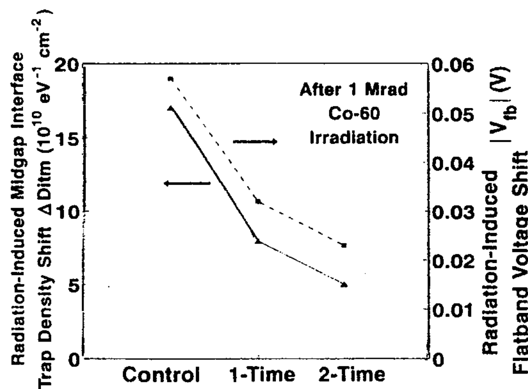

Fig. 4.36. Radiation-induced mid gap interface trap density shift ΔD_{itm} and flatband voltage shift $|\Delta V_{fb}|$ for control, one-time N_2O grown and two-time repeated N_2O-grown samples. (After Wu and Hwu [71]).

4.4. Ultra-Thin Oxides

Present-day 0.18/0.25 μm technologies have a gate oxide thickness in the range 4 to 5 nm. Further downscaling will lead to a further reduction of t_{OX}. However, it is expected that when the fundamental tunneling limit around 2-2.5 nm is reached, one will have to look for alternative gate dielectrics with a higher dielectric constant, in order to lower the direct tunnel current through the thin gate. Hereby is silicon nitride a first candidate. From a viewpoint of total dose damage, the tunneling limit has already been trespassed [2]. For a thickness below twice the electron tunneling limit (2x3 nm=6 nm) essentially no trapped holes will be retained in the oxide during irradiation. So far the good news. However, some new radiation-induced problems and drawbacks may arise in ultra-thin oxides, which motivate a deeper investigation.

4.4.1 Radiation Induced Leakage Current (RILC)

Recent investigations have shown that irradiated thin oxides can show an enhanced gate leakage current density J_g at low gate biases, before the onset of the classical FN tunneling current, which remains unaffected by the exposure [2,75-76]. An example is given in Fig. 4.37 [2].

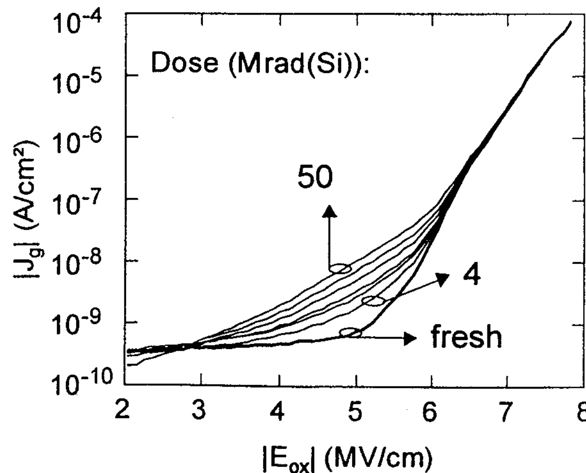

Fig. 4.37. Negative J_g-E_{OX} curves measured before (fresh) and after irradiation for various doses ranging from 4 to 50 Mrad(Si). (After Ceschia et al. [2])

There exists a large similarity with stress induced leakage current (SILC) generation. This typically occurs for high total doses (several tens of Mrad). The excess leakage current density J_e after irradiation or electrical stress is represented separately in Fig. 4.38, whereby clearly two slopes in the J_e versus E_{OX} curves are seen. Furthermore, from the plot it is derived that a law similar as for FN tunneling, can represent RILC for the two parts of the curve. The kink in the J_e characteristics defines a critical field E_k whereby the leakage

current mechanism changes. This E_k depends on the oxide thickness, as shown in Fig. 4.39 [2]. In analogy with the SILC mechanism, it is assumed that RILC originates from a trap-assisted tunneling of carriers through the oxide barrier, as represented in Fig. 4.40. Neutral traps, induced by the stress or the irradiation are thought to be responsible. The kink in the leakage current characteristics corresponds to a change in the barrier seen by the electron in the oxide trap, which is shown in Fig. 4.40. In other words, for fields below E_k, the trapped electron experiences a trapezoidal barrier, while this becomes a triangular barrier for higher fields exceeding E_k. From the magnitude of E_k shown in Fig. 4.39, it is derived that the tunneling process is inelastic, whereby the carrier looses an energy $\Delta E \approx 1$ eV through the excitation of phonons, when it becomes trapped.

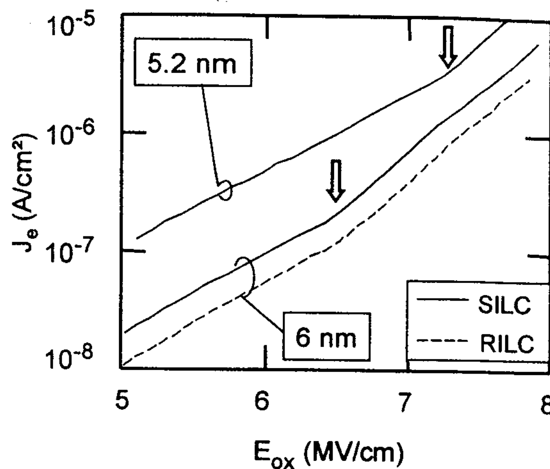

Fig. 4.38. Excess current after irradiation or electrical stress for two different oxide thickness (5.2 and 6 nm). (After Ceschia et al. [2]).

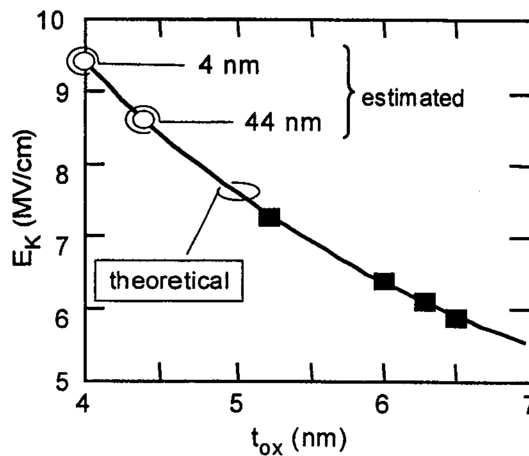

Fig. 4.39. Critical field E_k as a function of t_{ox}. Closed squares represent experimental data, while open dots indicate the expected values for t_{ox} = 4 nm and 4.4 nm. For to thin oxides, the FN dominates the overall gate current, so that it is difficult if not impossible to extract the RILC contribution. (After Ceschia et al. [2]).

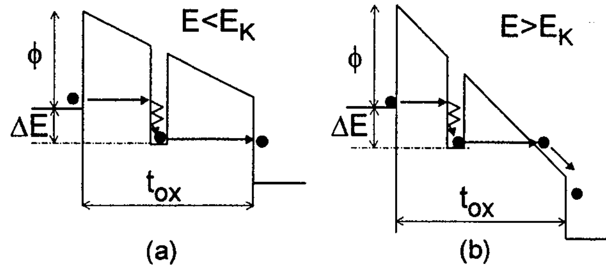

Fig. 4.40. Inelastic trap-assisted tunneling for (a) $E_{ox} < E_k$ and (b) $E_{ox} > E_k$. (After Ceschia et al. [2]).

The RILC shows a clear dependence on the bias during the irradiation (Fig. 4.41), indicating that the neutral trap formation is gate bias dependent. The RILC is most pronounced for zero (low) field during the exposure, yielding a homogeneous neutral trap distribution. For more asymmetric distributions, the trap assisted tunneling probability from the gate to the trap, or from the trap to the silicon will be lowered. From the observed field dependence, it is concluded that the underlying traps are not related to displacement damage, but rather require trapping of a charged species, which is released by the irradiation. A possible candidate is hydrogen.

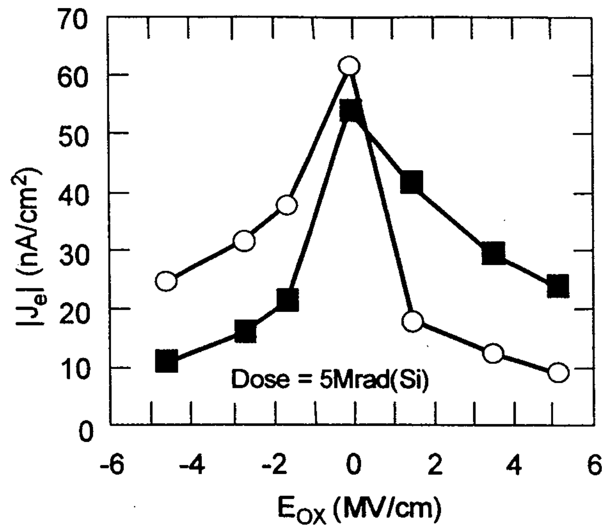

Fig. 4.41. Excess current read at $|E_{ox}|$=5MV/cm for different gate voltages applied during irradiation for t_{ox}=4 nm (o=positive RILC; closed squares is negative RILC, i.e. measured with a negative bias on the gate). (After Ceschia et al. [2]).

The RILC kinetics is given in Fig. 4.42, showing a power law dependence on the dose, whereby the exponent is close to 0.9. This is similar as the interface state buildup variation

with dose in thermal oxides, whereby the exponent is in the range 0.7-0.8 typically. As can be seen in Fig. 4.42, the magnitude of the RILC is determined by the gate oxide thickness and by the operational bias [2]. It has finally been noted that radiation can also create so-called quasi- or soft breakdown, which is an irreversible (i.e. permanent) damage of the oxide, whereby a local leakage current path has been created in the dielectric. This precedes catastrophic (hard) breakdown where the insulating function of the gate is lost permanently.

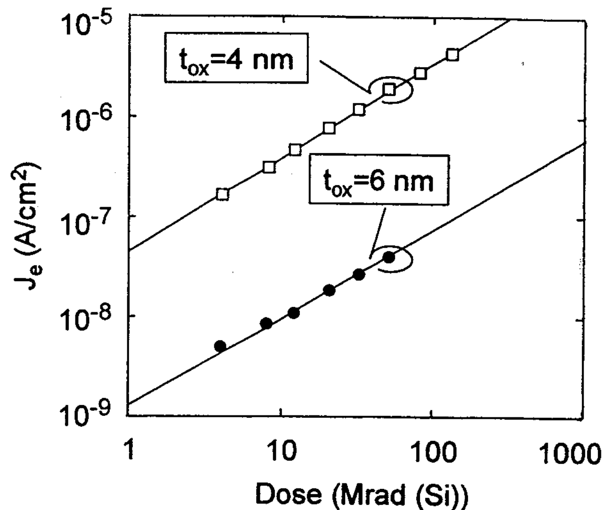

Fig. 4.42. RILC kinetics (negative excess current) for t_{OX}=4 nm (open squares) and 6 nm (closed circles). (After Ceschia et al. [2]).

4.4.2 Single Event Gate Rapture

Scaled technologies imply a thinner gate and higher oxide fields during operation. E_{OX} values in excess of 5 MV/cm may be expected for technologies approaching 0.1 μm feature sizes [77]. Recently, concern has risen that single event gate rapture (SEGR) may become the dominant catastrophic failure mechanism for space-based electronics at the 256 Mbit level and beyond. However, a recent study has indicated that for thin oxides the SEGR susceptibility in fact improves considerably [77]. The basic reason is that the breakdown field increases in thin dielectrics since less defect creation occurs through hot carriers. Only for devices operating at fields well in excess of 5 MV/cm, SEGR can become of concern.

4.5 Device Isolation

So far, isolation between active devices was achieved by growing a thick field oxide, using the so-called LOCal Oxidation of Silicon (LOCOS) concept, depicted in Fig. 4.43 (top). However, the lateral encroachment of the thick field oxide, giving rise to the bird's beak limits the scalability of LOCOS-based device isolation, so that for 0.25 μm and beyond, alternatives like shallow trench isolation (STI) become attractive (Fig. 4.43c). As

the thickness of the field oxide is much larger than of the gate, much more hole trapping will occur, leading to appreciable device and circuit degradation. In this part, recent advances in the radiation degradation of LOCOS and STI isolation will be summarized.

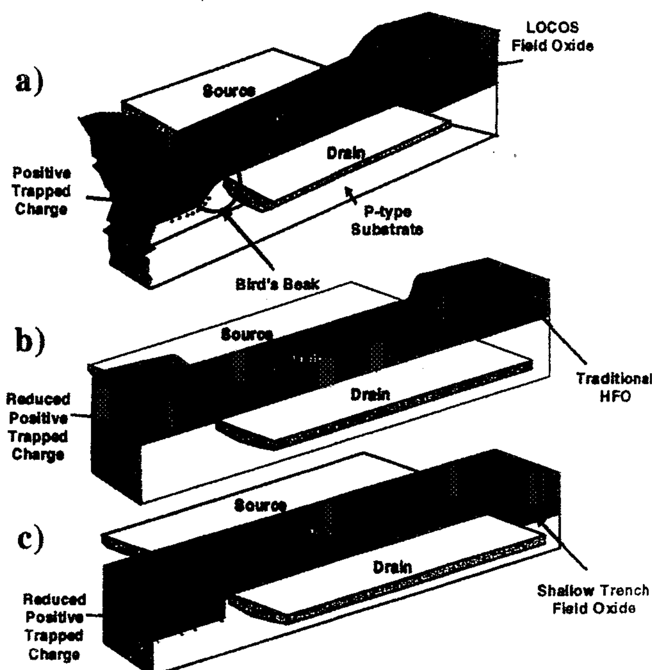

Fig. 4.43. The top cross section (a) illustrates LOCOS isolation that is commonly used for commercial CMOS technologies. The middle cross section (b) shows a tradional hardened field-oxide isolation. The bottom cross section (c) illustrates shallow trench isolation used in deep submicron technologies.

4.5.1 LOCOS Isolation

A typical cross section of a field oxide used in a 0.7 - 0.8 μm CMOS technology near the gate edge is shown in Fig. 4.44 [78]. It is clear that due to the thickness variation of the field oxide, the degradation will also be non-uniform and a distinction needs to be made between the contribution of the different regions. In first approximation, one can consider the field oxide with a polysilicon gate on top of it as a parasitic capacitor or transistor adjacent to the active devices [78-79]. Recently, large progress has been made in the understanding of the device degradation associated with the field devices, using a combination of device simulation and appropriate analysis techniques, like a modified charge pumping technique [79]. The parasitic leakage current associated with a field transistor is composed of different contributions, which are summarized in Fig. 4.45. From these studies, it is concluded that the main source of degradation is associated with the bird's beak region. There, a higher density of trapped charge and a higher creation of interface traps is found (Fig. 4.46). This is ascribed to the higher mechanical stress in the bird's beak region. In fact, also before irradiation, a larger D_{it} exists typically there. It has

finally been observed that similar border traps occur in the different parts of the field oxide [9]

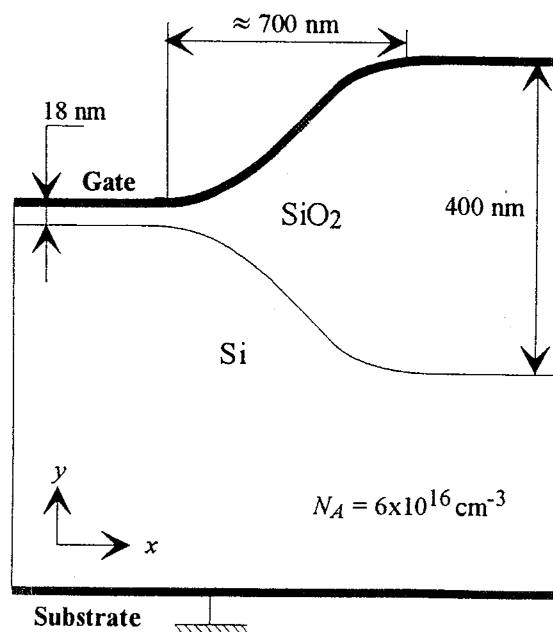

Fig. 4.44. Simulated LOCOS structure. (After Brisset et al. [78]).

In order to harden the field oxide, different approaches can be taken. Generally, impurities have been in-diffused or implanted, to create electron traps in the thick oxide. Electron trapping during irradiation will partially compensate for the hole trapping and, therefore, lowers the net negative flat band or threshold voltage shift of the parasitic field transistor. Such dopants can be N, or P. Recently, also interest developed for F-doped field oxides for hardening purposes [80]. Figure 4.47 shows clearly the improvement observed using F-doped field oxides. As a result, the parasitic subthreshold edge leakage for regular n-MOSFETs is reduced significantly. The basic reason is that the field V_T is less degraded by the irradiation [80]. An optimum dose of around $5x10^{14}$ cm^{-2} exists, for that particular processing. The improvement is observed for both positive and negative gate bias. Similar results have been obtained for irradiated gated diodes, which show a lower increase of the radiation-induced surface-generation related leakage current with increasing F dose [80]. This points to a reduced interface state buildup.

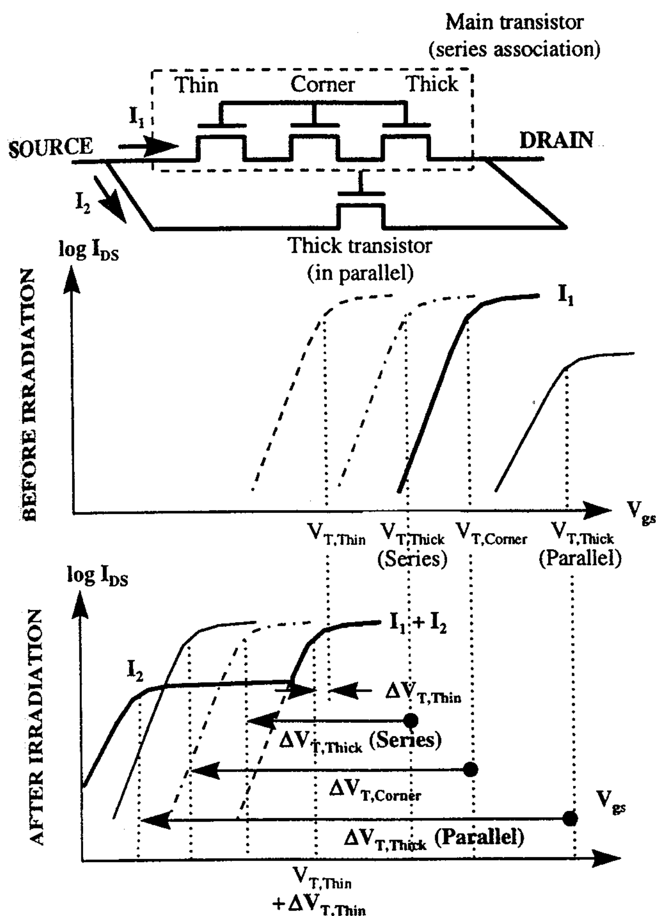

Fig. 4.45. Schematic illustration of total dose effects on $I_D(V_{GS})$ characteristics of overlap LOCOS transistors. The main transistor corresponds to the series association of the so-called thin, corner and thick devices. The so-called thick transistor, in parallel with the main structure, represents a parasitic structure turned on by irradiation. (After Flament et al. [79]).

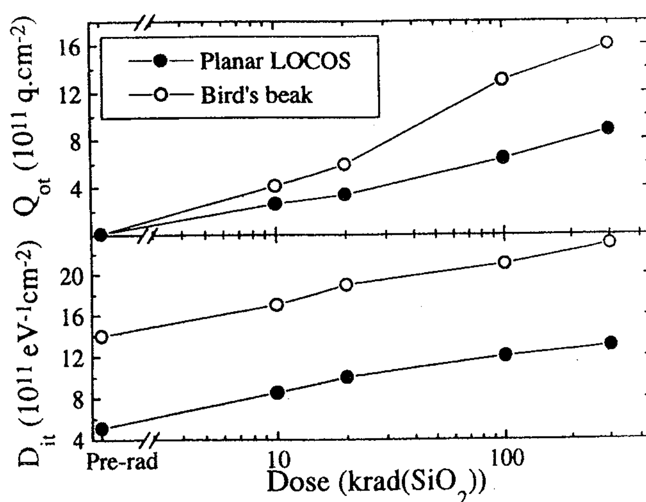

Fig. 4.46. Total dose evolution of Q_{ot} and D_{it} in bird's beak and planar LOCOS regions of the overlap transistor. (After Flament et al. [79]).

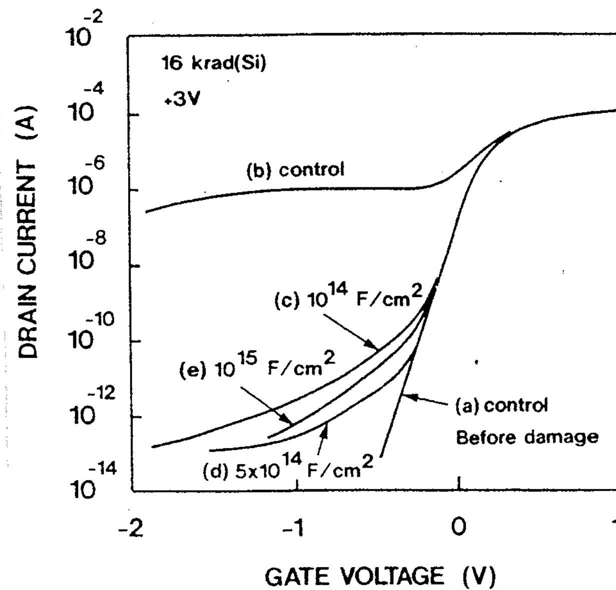

Fig. 4.47. Drain current vs gate voltage curves for n-MOSFETs (L=1.0 μm and W=10 μm) surrounded by LOCOS field oxides before (curve a) and after X-ray irradiation with a gate voltage during irradiation of +3 V (curve b-e). The curves (a) and (b) represent the control before (curve a) and after (curve b) irradiation, respectively. The field oxide F-implant dose is specified for each device (curves c-e). (After Nishioka et al. [80]).

4.5.2 Shallow Trench Isolation

Commercial (sub) 0.25 μm CMOS technologies routinely use STI instead of the LOCOS based isolation. STI consists of a shallow trench, typically, 500 nm deep or so, which is afterwards filled by a deposited oxide. According to Fig. 4.48, at least two leakage paths exist - one along the sidewalls of a single device, leading to subthreshold leakage; a second one in between devices, whereby the parasitic field transistor is turned on. In order to stick as closely as possible to the COTS principle, one could imagine that an STI based commercial technology is hardened by replacing the filling oxide by a hardened type of dielectric. This requires the smallest amount of changes of the commercial technology [81]. However, as evidenced by Fig. 4.49, such an approach does not work. While in a standard type of technology, the implemented hardened field oxide can withstand total doses up to 1 Mrad(SiO_2), this is not the case in a STI approach. Already at 30 krad (and +5 V on the gate during the exposure) significant subthreshold leakage is noted in Fig. 4.49. In addition, 16 kbit SRAMs fabricated in this technology fail around 80-100 krad(SiO_2). The reason for this unexpected degradation is related to the high electric fields existing in the corners of a shallow trench [81]. Using 3-dimensional simulations, one can demonstrate that the profiles of the trenches play a crucial role in this. It turns out that a slight overfilling of the trenches with oxide, so that its level is higher than that of the active region, shows the best total dose

hardness (Fig. 4.50), because it generates a reduction of the corner field and the associated radiation-induced leakage.

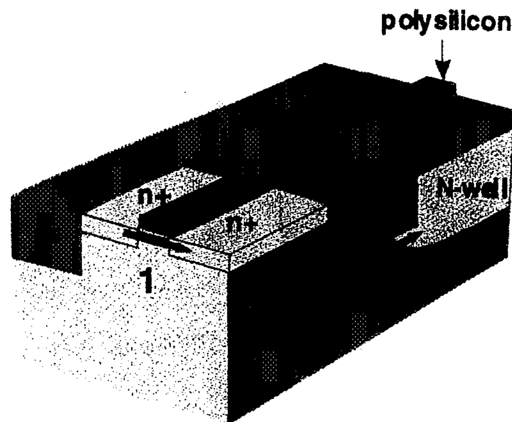

Fig. 4.48. Arrows indicate two possible parasitic leakage current paths in shallow trench technology. (After Shaneyfelt et al. [81]).

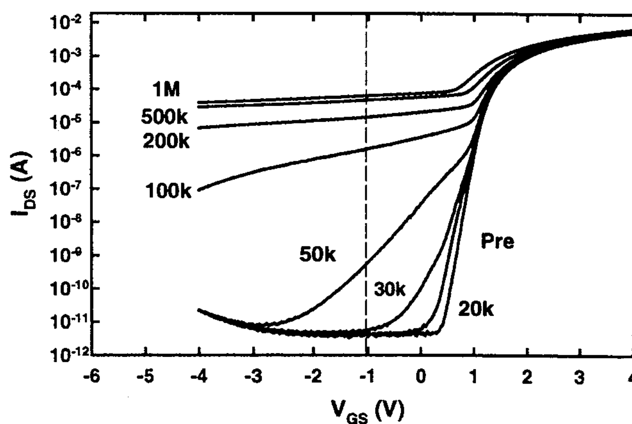

Fig. 4.49. Subthreshold I-V curves for n-channel transistors irradiated at room temperature in steps of 1 Mrad(SiO_2) using 10 keV X-rays at 167 rad(SiO_2)/s. (After Shaneyfelt et al. [81]).

Further (or alternative) measures that could be taken consist of an increase of the field implantation and optimizing the pull-back of the active regions from the trenches [81]. It turns out that increasing the field implantation dose does not really improve the radiation hardness, especially if the implantation has been done through the filled trenches. Residual ion implantation damage and/or dopants in the oxide are believed to act as trapping centers for radiation-induced charges. It is recommended to avoid ion implantation through the trench oxide for applications requiring total dose hardness. Pull-back of $\approx$0.3 μm yields better hardness at the expense of packing density and chip area. It has been demonstrated that by carefully optimizing the STI process hardness levels up to several Mrad(SiO_2) can be achieved [81].

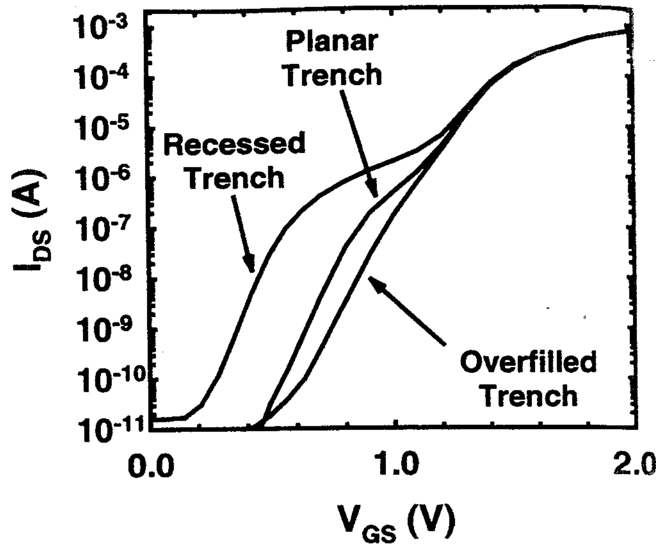

Fig. 4.50. Simulated I-V characteristics for three different trench profiles. For the overfilled trench profile, the trench insulator extends 100 nm above the trench corner. (After Shaneyfelt et al. [81]).

4.6. Conclusions

With the trend of reducing the thickness of the gate dielectric or even replacing it by harder alternatives, whereby N_2O oxynitrides show the best performance, it is expected that scaled submicron technologies can withstand increasing levels of total dose irradiation. To a certain extent, this also goes for the shallow-trench isolation used nowadays, although this requires a careful optimalization of the processing steps. Clearly more work needs to be done in this respect to screen all potential hardness problems and solutions. In line with the COTS philosophy, hardening commercial technologies should be done with as few as possible process modifications, rather than taking measures for extreme hardness levels.

From the above follows that there may exist some 'second order' problems related to the frequent use of certain processing steps like plasma etching, RTA, etc... In many cases, research is developing rapidly, mainly from a viewpoint of manufacturing and reliability/lifetime. The hardness issue comes generally second place, but shows many common points of interest with oxide integrity and lifetime aspects. This means that some of the results and improvements obtained there can be directly translated to the hardness issue.

It is hard to foresee, whether the application of (sub) 100 nm CMOS will bring about some new radiation-induced degradation mechanisms. Although RILC and SEGR may occur, it is expected that this will only be the case for extreme conditions, which are not typical for the space environment. They are, therefore, at the moment more of academic interest. However, shrinking of the device area can have a deleterious impact on transient behavior of circuits, like latch-up and single event upsets, since the charge requires to upset a node scales along.

References

[1] M. Walters and A. Reisman, "Radiation-induced neutral electron trap generation in electrically biased insulated gate field effect transistor gate insulators", J. Electrochem. Soc. **138**, 2756 (1991).
[2] M. Ceschia, A. Paccagnella, A. Cester, A. Scarpa and G. Ghidini, "Radiation induced leakage current and stress induced leakage current in ultra-thin gate oxides", IEEE Trans. Nucl. Sci. **45**, 2375 (1998).
[3] S. Share and R.A. Martin, "Effects of ionizing radiation on short-channel thin-oxide (200-Å) MOSFETs", IEEE Trans. Electron Devices **22**, 619 (1975).
[4] J.S.T. Huang and J.W. Schrankler, "Flat-band voltage dependence on channel length in short-channel threshold model", IEEE Trans. Electron Devices **32**, 1001 (1985).
[5] J.W. Schrankler, R.K. Reich, M.S. Holt, D.H. Hu, J.S.T. Huang, G.D. Kirchner and H.L. Hughes, "CMOS scaling implications for total dose radiation", IEEE Trans. Nucl. Sci. **32**, 3988 (1985).
[6] J.Y. Chen, D.O. Patterson and R. Martin, "Radiation hardness on submicron NMOS", IEEE Trans. Nucl. Sci. **28**, 4314 (1981).
[7] P.K. Bhattacharya and A. Reisman, "A study of X-ray damage effects on short channel behavior of IGFETs", J. Electron. Materials **19**, 727 (1990).
[8] J. Scarpulla, A.L. Amram, V.W. Gin, T.C. Morse and K.T. Nakamura, "Gate size dependence of the radiation-produced changes in threshold voltage, mobility, and interface state density in bulk CMOS", IEEE Trans. Nucl. Sci. **39**, 1990 (1992).
[9] M.R. Shaneyfelt, D.M. Fleetwood, P.S. Winokur, J.R. Schwank and T.L. Meisenheimer, "Effects of device scaling and geometry on MOS radiation hardness assurance", IEEE Trans. Nucl. Sci. **40**, 1678 (1993).
[10] D.M. Fleetwood, "Border traps in MOS devices", IEEE Trans. Nucl. Sci. **39**, 269 (1992).
[11] M.C. Peckerar, D.B. Brown, H.C. Lin and D.I. Ma, "Modeling total dose effects in narrow-channel devices", IEEE Trans. Electron Devices **30**, 1159 (1983).
[12] W. Chen, A. Balasinski and T.-P. Ma, "Lateral distribution of radiation-induced damage in MOSFETs", IEEE Trans. Nucl. Sci. **38**, 1124 (1991).
[13] A. Balasinski and T.-P. Ma, "Ionizing radiation damage near CMOS transistor channel edges", IEEE Trans. Nucl. Sci. **39**, 1998 (1992).
[14] A. Balasinski and T.-P. Ma, "Impact of radiation-induced nonuniform damage near MOSFET junctions", IEEE Trans. Nucl. Sci. **40**, 1286 (1993).
[15] D.C. Pantelakis, D.F. Hemmenway, N. van Vonno and T.J. Sanders, "Freeze-out characteristics of radiation hardened n^+ polysilicon gate CMOS transistors", IEEE Trans. Nucl. Sci. **38**, 1289 (1991).
[16] A. Acovic, C.C.-H. Hsu, L.-C. Hsia, A. Balasinski and T.-P. Ma, "Effects of X-ray irradiation on GIDL in MOSFETs", IEEE Electron Device Lett. **13**, 189 (1992).
[17] N.C. Das, V. Nathan, R. Tallon and R.J. Maier, "Radiation effects on gate induced drain leakage current in metal oxide semiconductor transistors", J. Appl. Phys. **72**, 4958 (1992).
[18] R.A. Gdula, "The effects of processing on radiation damage in SiO_2", IEEE Trans. Electron Devices **26**, 644 (1979).

[19] C. C.-H. Hsu, L.K. Wang, M.R. Wordeman and T.H. Ning, "Hot-electron-induced instability in 0.5-μm p-channel MOSFETs patterned using synchrotron X-ray lithography", IEEE Electron Device Lett. **10**, 327 (1989).
[20] J. Yue, E. Lo and M. Flanery, "Total dose radiation response of plasma-damaged NMOS devices", IEEE Electron Device Lett. **18**, 532 (1997).
[21] K.G. Aubuchon, "Radiation hardening of PMOS devices by optimization of thermal SiO_2 gate insulator", IEEE Trans. Nucl. Sci. **17** (1971).
[22] W.R. Dawes, Jr., G.F. Derbenwick and B.L Gregory, "Process technology for radiation-hardened CMOS integrated circuits", IEEE J. Solid State Circuits **SC11**, 459 (1976).
[23] P.S. Winokur, E.B. Erret, D.M. Fleetwood, P.V. Dressendorfer and D.C. Turpin, "Optimizing and controlling radiation hardness of Si-gate CMOS process", IEEE Trans. Nucl. Sci. **32**, 3954 (1985).
[24] J.R. Schwank and D.M. Fleetwood, "Effect of post-oxidation anneal temperature on radiation-induced charge trapping in metal-oxide-semiconductor devices", Appl. Phys. Lett. **53**, 770 (1988).
[25] C.H. Seager and W.K. Schubert, "Hole trapping in oxides grown by rapid thermal processing", J. Appl. Phys. **63**, 2869 (1988).
[26] K. Hofmann, D.R. Young and G.W. Rubloff, "Hole trapping in SiO_2 films annealed in low-pressure oxygen atmosphere", J. Appl. Phys. **62**, 925 (1987).
[27] W.K. Schubert, "Comparison of the effects of post-oxidation anneals on the initial properties and the radiation response of rapid thermally processed oxides", J. Appl. Phys. **69**, 3159 (1991).
[28] O. Flament, J.L. Leray, F. Martin, E. Orsier, J.L. Pelloie, R. Truche and R.A.B. Devine, "Effect of rapid thermal annealing on radiation hardening of MOS devices", IEEE Trans. Nucl. Sci. **42**, 1667 (1995).
[29] I. Yoshii, K. Hama and K. Maeguchi, "Radiation effects on p^+ poly gate MOS structures with thin oxides", IEEE Trans. Nucl. Sci. **36**, 2124 (1989).
[30] K.-S. Chang-Liao and C.-C. Chuang, "Improvement of radiation hardness in poly-Si gate MOS capacitor by use of amorphous-Si", Electron. Lett. **30**, 1540 (1994).
[31] K. Kasama, F. Toyokawa, M. Tsukiji, M. Sakamoto and K. Kobayashi, "Mechanical stress dependence of radiation effects in MOS structures", IEEE Trans. Nucl. Sci. **33**, 1210 (1986).
[32] K. Kasama, M. Tsujiki and K. Kobayashi, "Correlation between mechanical stress and hydrogen-related effects on radiation-induced damage in MOS structures", IEEE Trans. Nucl. Sci. **34**, 1202 (1987).
[33] Y. Wang, Y. Nishioka , T.P. Ma and R.C. Barker, "Radiation and hot-electron effects on SiO_2/Si interfaces with oxides grown in O_2 containing small amounts of trichloroethane", Appl. Phys. Lett. **52**, 573 (1988).
[34] Y. Nishioka, K. Ohyu, Y. Ohji and T.-P. Ma, "Channel length and width dependence of hot-carrier hardness in fluorinated MOSFETs", IEEE Electron Device Lett. **10**, 540 (1989).
[35] Y. Nishioka, K. Ohyu, Y. Ohji, N. Natsuaki, K. Mukai and T.P. Ma, "The effect of fluorine implantation on the interface radiation hardness of Si-gate metal-oxide-semiconductor transistors", J. Appl. Phys. **66**, 3909 (1989).

[36] M.L. Naiman, F.L. Terry, J.A. Burns, J.I. Raffel and R. Aucoin, "Properties of thin oxynitride gate dielectrics produced by thermal nitridation of silicon dioxide", IEDM Tech. Dig., pp. 562-564 (1980).
[37] F.L. Terry, Jr., R.J. Aucoin, M.L. Naiman and S.D. Senturia, "Radiation effects in nitrided oxides", IEEE Electron Device Lett. **4**, 191 (1983).
[38] R.K. Pancholy and F.M. Erdmann, "Radiation effects on oxynitride gate dielectrics", IEEE Trans. Nucl. Sci. **30**, 4141 (1983).
[39] G.A. Ruggles and J.R. Monkowski, "An investigation of fixed charge buildup in nitrided oxides", J. Electrochem. Soc. **133**, 787 (1985).
[40] R. Sundaresan, M.M. Matloubian and W.E. Bailey, "Rapid-thermal nitridation of SiO_2 for radiation-hardened MOS gate dielectrics", IEEE Trans. Nucl. Sci. **33**, 1223 (1986).
[41] G.J. Dunn, "Effect of synchrotron X-ray radiation on the channel hot-carrier reliability of reoxidized nitrided silicon dioxide", IEEE Electron Device Lett. **12**, 8 (1991).
[42] G.J. Dunn and P.W. Wyatt, "Reoxidized nitrided oxide for radiation-hardened MOS devices", IEEE Trans. Nucl. Sci. **36**, 2161 (1989).
[43] G.Q. Lo, D.K. Shih, W. Ting and D.L Kwong, "Effects of post-nitridation anneals on radiation hardness in rapid thermal nitrided gate oxides", Appl. Phys. Lett. **55**, 2405 (1989).
[44] M. Severi, L. Dori, M. Impronta and S. Guerri, "Process dependence of hole trapping in thin nitrided SiO_2 films", IEEE Trans. Electron Devices **36**, 2447 (1989).
[45] G.J. Dunn, R. Jayaraman, W. Yang and C. G. Sodini, "Radiation effects in low-pressure reoxidised nitrided oxide gate dielectrics", Appl. Phys. Lett. **52**, 1713 (1988).
[46] Y.-L. Wu and J.-G. Hwu, "Improvement in radiation hardness of reoxidised nitrided oxide (RNO) in the absence of post-oxidation anneal", IEEE Electron Device Lett. **14**, 1 (1993).
[47] W.-S. Lu, K.-C. Lin and J.-G. Hwu, "Process dependence of radiation hardness of rapid thermal reoxidised nitrided gate oxides", IEEE Trans. Electron Devices **40**, 1597 (1993).
[48] K. Neumeier and H.P. Bruemmer, "A systematic investigation of the influence of processing parameters on the radiation hardness of reoxidised nitrided oxides", In Proc. RADECS '95, The IEEE (New York), pp. 131-136 (1996).
[49] W.-S. Lu, C.-H. Chan and J.-G. Hwu, "A systematic study of the inital electrical and radiation hardness properties of reoxidised nitrided oxides by rapid thermal processing", IEEE Trans. Nucl. Sci. **42**, 167 (1995).
[50] G.J. Dunn, "Hole trapping in reoxidised nitrided silicon dioxide", J. Appl. Phys. **65**, 4879 (1989).
[51] K.S. Krisch, B.J. Gross and C.G. Sodini, "Positive-charge trapping in nitrided oxide and reoxidised nitrided oxide", J. Appl. Phys. **70**, 2185 (1991).
[52] A. Mallik, J. Vasi and A.N. Chandorkar, "The nature of the hole traps in reoxidised nitrided oxide gate dielectrics", J. Appl. Phys. **74**, 2665 (1993).
[53] A. Mallik, A.N. Chandorkar and J. Vasi, "Capture cross section of hole traps in reoxidised nitrided oxide measured by irradiation", Solid-State Electron. **38**, 1851 (1995).
[54] J.F. Conley, Jr., P.M. Lenahan, A.J. Lelis and T.R. Oldham, "Electron spin resonance evidence that E'_γ centers can behave as switching oxide traps", IEEE Trans. Nucl. Sci. **42**, 1744 (1995).

[55] G.J. Dunn, "Generation of interface states in nitrided oxide gate dielectrics by ionising radiation and Fowler-Nordheim stressing", Appl. Phys. Lett. **53**, 1650 (1988).
[56] V. R. Rao and J. Vasi, "Radiation-induced interface-state generation in reoxidised nitrided SiO_2", J. Appl. Phys. **71**, 1029 (1992).
[57] N. Bhat and J. Vasi, "Interface-state generation under radiation and high-field stressing in reoxidised nitrided oxide MOS capacitors", IEEE Trans. Nucl. Sci. **39**, 2230 (1992).
[58] E. Cartier, D.A. Buchanan and G.J. Dunn, "Atomic hydrogen-induced interface degradation of reoxidised-nitrided silicon dioxide on silicon", Appl. Phys. Lett. **64**, 901 (1994).
[59] J.T. Yount, P.M. Lenahan and P.W. Wyatt, "The effects of thermal nitridation and reoxidation on the interfacial stress and structure of silicon dioxide gate dielectrics", J. Appl. Phys. **77**, 699 (1995).
[60] A. Mallik, J. Vasi and A.N. Chandorkar, "Electron trapping during irradiation in reoxidized nitrided oxides", IEEE Trans. Nucl. Sci. **40**, 1380 (1993).
[61] R.J. Krantz, J. Scarpulla and J.S. Cable, "Total dose-induced charge buildup in nitrided-oxide MOS devices", IEEE Trans. Nucl. Sci. **38**, 1746 (1991).
[62] A.J. de Castro, M. Fernandez and J.L. Sacedon, "Effects of thermal nitridation on the radiation hardness of the SiO_2/Si interface", J. Appl. Phys. **73**, 7465 (1993).
[63] V. Ramgopal Rao, D.K. Sharma and J. Vasi, "Neutral electron trap generation under irradiation in reoxidized nitrided gate dielectrics", IEEE Trans. Electron Devices **43**, 1467 (1996).
[64] G.J. Dunn, B.J. Gross and C.G. Sodini, "Radiation-induced increase in the inversion layer mobility of reoxidized nitrided oxide MOSFETs", IEEE Trans. Electron Devices **39**, 677 (1992).
[65] A. Mallik, J. Vasi and A.N. Chandorkar, "A study of radiation effects on reoxidized nitrided oxide MOSFETs, including effects on mobility", Solid-State Electron. **36**, 1359 (1993).
[66] H.E. Boesch, Jr. and G.J. Dunn, "Hole transport in SiO_2 and reoxidized nitrided SiO_2 gate insulators at low temperature", IEEE Trans. Nucl. Sci. **38**, 1083 (1991).
[67] J.T. Yount, P.M. Lenahan and G.J. Dunn, "Electron spin resonance study of radiation-induced point defects in nitrided and reoxidized nitrided oxides", IEEE Trans. Nucl. Sci. **39**, 2211 (1992).
[68] H. Hwang, W. Ting, B. Maiti, D.-L. Kwong and J. Lee, "Electrical characteristics of ultrathin oxynitride gate dielectric prepared by rapid thermal oxidation of Si in N_2O", Appl. Phys. Lett. **57**, 1010 (1990).
[69] G.Q. Lo, A.B. Joshi and D.L. Kwong, "Radiation hardness of MOSFETs with N_2O-nitrided gate oxides", IEEE Trans. Electron Devices **40**, 1565 (1993).
[70] Y.-L. Wu, K.-M. Kuo and J.-G. Hwu, "Reduction of radiation-induced degradation in n-channel metal-oxide-semiconductor field-effect transistors (MOSFETs) with gate oxides prepared by repeated rapid thermal N_2O annealing", Jpn. J. Appl. Phys. **33**, L916 (1994).
[71] Y.-L. Wu and J.-G. Hwu, "Improvement in radiation hardness of gate oxides in metal-oxide semiconductor devices by repeated rapid thermal oxidations in N_2O", Appl. Phys. Lett. **64**, 3136 (1994).
[72] N.S. Saks, M. Simons, D.M. Fleetwood, J.T. Yount, P.M. Lenahan and R.B. Klein, "Radiation effects in oxynitrides grown in N_2O", IEEE Trans. Nucl. Sci. **41**, 1854 (1994).

[73] D.M. Fleetwood and N.S. Saks, "Oxide, interface, and border traps in thermal, N_2O, and N_2O-nitrided oxides", J. Appl. Phys. **79**, 1583 (1996).
[74] C.J. Anthony, M.J. Uren and V. Nayar, "Radiation hardness of N_2O grown oxynitrides assessed using the conductance technique", Appl. Phys. Lett. **69**, 2104 (1996).
[75] A. Scarpa, A. Paccagnella, F. Montera, G. Ghibaudo, G. Pananakakis, G. Ghidini and P.G. Fuochi, "Ionizing radiation induced leakage current on ultra-thin gate oxides", IEEE Trans. Nucl. Sci. **44**, 1818 (1997).
[76] A. Candelori, A. Paccagnella, M. Cammarata, G. Ghidini and P.G. Fuochi, "Fowler-Nordheim characteristics of electron irradiated MOS capacitors", IEEE Trans. Nucl. Sci. **45**, 2383 (1998).
[77] F.W. Sexton, D.M. Fleetwood, M.R. Shaneyfelt, P.E. Dodd and G.L. Hash, "Single event gate rupture in thin gate oxides", IEEE Trans. Nucl. Sci. **44**, 2345 (1997).
[78] C. Brisset, V. Ferlet-Cavrois, O. Flament, O. Musseau, J.L. Leray, J.L. Pelloie, R. Escoffier, A. Michez, C. Cirba and G. Bordure, "Two-dimensional simulation of total dose effects on NMOSFET with lateral parasitic transistor", IEEE Trans. Nucl. Sci. **43**, 2651 (1996).
[79] O. Flament, J.L. Autran, P. Paillet, P. Roche, O. Faynot and R. Truche, "Charge pumping analysis of radiation effects in LOCOS parasitic transistors", IEEE Trans. Nucl. Sci. **44**, 1930 (1996).
[80] Y. Nishioka, T. Itoga, K. Ohyu, M. Kato and T.-P. Ma, "Radiation effects on fluorinated field oxides and associated devices", IEEE Trans. Nucl. Sci. **37**, 2026 (1990).
[81] M.R. Shaneyfelt, P.E. Dodd, B.L. Draper and R.S. Flores, "Challenges in hardening technologies using shallow-trench isolation", IEEE Trans. Nucl. Sci. **45**, 2584 (1998).

5. GaAs BASED FIELD EFFECT TRANSISTORS FOR RAD HARD APPLICATIONS

The high electron mobility of GaAs and related III-V compounds renders these materials very suitable for high-speed digital and microwave/millimeter wave applications. The superior operation frequency combined with low high-frequency noise and power dissipation has been exploited for the development of satellite and other telecommunications systems. In this respect, the extreme radiation hardness quoted for these materials is an invaluable plus point: total dose radiation tolerance levels up to 1 Grad(GaAs) have been observed, which is at least two orders of magnitude better than for hardened Si-based technologies. Nowadays, InP is more and more replacing GaAs substrates. However, the use of the semi-insulating (SI) substrates brings about some specific radiation effects, which jeopardize the correct functioning of devices and circuits. Therefore, in a first paragraph, the relevant material properties and the structure of the Metal-Semiconductor Field-Effect Transistor (MESFET) and the High Electron Mobility Transistor (HEMT), also called Modulation Doped FET (MODFET) will be described. Next, the results of macroscopic displacement damage studies in GaAs will be summarized and compared with the NIEL concept. In a third part, the radiation response and hardening of MESFETs will be presented, followed next by the behavior of HEMTs. Finally some conclusions are drawn and suggestions for future work formulated. In this context, it should be remarked that IMEC has developed an InP based MMIC (Monolithic Microwave Integrated Circuit) technology in the frame of several ESA programs.

5.1 GaAs Material Properties and Device Structures

5.1.1 III-V Substrates and Native Defects

MESFETs and HEMTs are usually fabricated on SI (Semi-Insulating) GaAs substrates grown by the Liquid Encapsulation Czochralski (LEC) technique, which are known to be more radiation tolerant than Cr doped material [1]. The semi-insulating nature of the material is a result of the native donor trap called EL2, approximately 0.75 eV below the conduction band, i.e. close to mid gap. It is attributed to an As_{Ga} antisite defect, as determined by EPR measurements [2-3] or a complex involving the antisite. In fact, its exact nature is still a matter of controversy and intense research [3-6]. The partial compensation of the deep EL2 donor by acceptor levels from trace impurities introduced during the crystal growth [7] or by the Ga-sublattice related acceptors [2] pins the Fermi level near the mid gap, yielding a semi-insulating substrate.

The radiation hardness of SI GaAs is a result of the antisite hardness (immovability) [7]. Examples are given in Fig. 5.1a and Fig. 5.1b, representing the EL2 concentration derived from DLTS versus the fluence Φ for neutron (n) [8] and electron (e^-) exposure [9], respectively. However, as can be derived from Fig. 5.1a, EL2 can be created during proton or neutron irradiation [3,6,8-11], particularly at higher fluences. The EL2 introduction is, however, not monotonous with fluence but shows a rather complex behavior [6,10]. For large displacement damage, giving rise to defect clusters, interactions between shallower

traps (like EL6) and EL2 start to occur, which alter the electrical properties of the center. If neighboring point defects occur within 10 nm of each other (typical size of the damage cluster along the track of an ion path), the emission path of captured electrons is changed. Phonon-assisted tunneling to the shallower trap may become possible, from which the carrier is subsequently emitted to the conduction band. This mechanism is thought to be responsible for the U-band levels in heavily neutron or ion irradiated (implanted) GaAs [3,10]. As a result, the true EL2 concentration can only be found after annealing the other radiation damage at 600°C. Grown-in EL2 centers are thermally very stable and are reported to anneal at 800°C or higher. Additional EL2 in excess of a thermodynamic grown-in equilibrium concentration tends to disappear in the 500-600°C range [10].

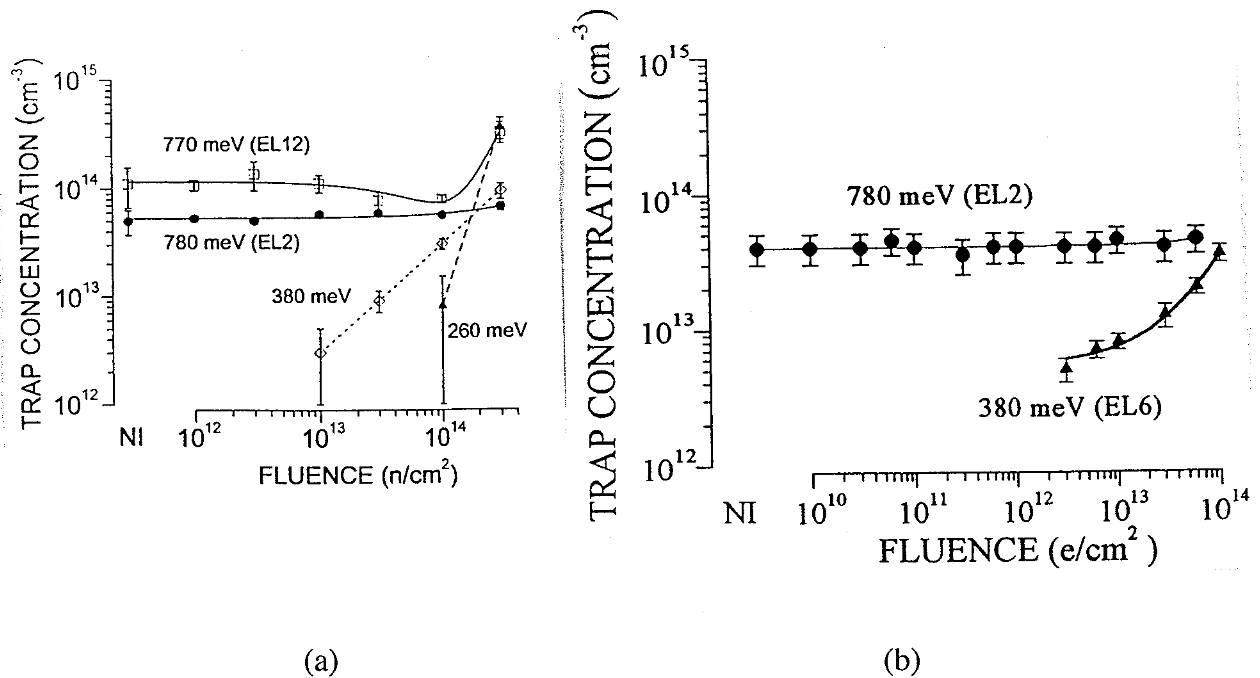

Fig. 5.1. (a) Trap concentrations as a function of neutron fluence in n-type GaAs. Note that the EL2 trap is practically independent of 1 MeV equivalent neutron irradiation up to 10^{14} n/cm^2. The EL12 trap tends to decrease in the range 3×10^{12} to 10^{14} n/cm^2. The peak at 380 meV from the conduction band is the EL6 acceptor and its introduction rate is 0.3 cm^{-1}. A significant density of EL14 level (260 meV) develops at 3×10^{14} n/cm^2. NI stands for not irradiated. (After Jorio et al. [8]). (b) Trap concentration as a function of 7 MeV electron fluence. (After Khanna et al. [9]).

It is known for some time that when for instance a light pulse is shined upon GaAs, EL2 can be transferred into a metastable excited state by absorption of a photon (which can be a γ as well), according to the reaction:

$$EL2^{o} + h\nu \rightarrow EL2^{*} \quad (5.1)$$

whereby $EL2^o$ is the neutral charge state and EL2* the charged metastable state. This leads to long photo-transients in the drain current of a FET since the electrons, after tunneling into the substrate traps activated by the irradiation, are subsequently emitted back into the conduction band thermally [7]. The transient time constant is dependent on the type of trap (which can also be a deep radiation induced defect). This (optical) irradiation stimulated SI substrate trapping causes several parasitic effects in the FET characteristics, like back- and sidegating [12-14], which will be described in more detail later. A related effect is the persistent photo-quenching (PPQ) in the capacitance of a reverse biased junction diode, which is considered to be a fingerprint of EL2 [6].

With respect to the basic radiation defects in GaAs, the situation is far more complex than in the case of a group IV semiconductor. Native defects exist in both the Ga and As sublattice, i.e. an arsenic vacancy (V_{As}) and interstitial (As_i), or the Ga counterparts (V_{Ga} and Ga_i) should be considered, like in Fig.5.2, representing the formation energies of native GaAs defects as a function of the Fermi level in the band gap [15]. In addition, As_{Ga} or Ga_{As} antisite defects are present and nearest neighbor pairs between a vacancy and the antisite defect can be formed as well (simple Frenkel pairs). These native defects are also the primary displacement damage defects formed upon irradiation, with γ's, electrons, neutrons or ions [2]. Depending on the stability of the primary defects and on the energy transferred, more complex (and more stable) radiation defects can be created, like E1 to E3 in n-type GaAs. In electron irradiated p-type material, two hole traps H0 and H1 are observed typically [2], which are thought to correspond to other charge states of the electron traps observed in n-type material. Additional levels occur for proton or neutron irradiations [2-6,8-11], like the U-band, EL6, EL12, etc, which correspond to higher order defects/complexes. Some of the well-known deep levels in GaAs are represented schematically in Fig. 5.3 [8], while their nature and thermal stability is summarized in Table 5.1 [2].

From Fig. 5.2, one can also derive the charge state of the defects as a function of the Fermi level. The EL2 level thus corresponds with the $2^+/1^+$ donor state, although it is claimed that the As_{Ga} should be a double donor [2] giving rise to a second (higher) level in the band gap. It is also clear from Fig. 5.2 that the basic defects in the As sub-lattice have a donor character, whereby the group V element in an excess position gives up one or more of its valence electrons to the conduction band. The opposite is true for the Ga sub-lattice showing predominant acceptor nature of its associated defects. This dual nature of the basic radiation defects explains to a large extent the carrier compensation observed after irradiation of both n- and p-type GaAs [16-17], which become more intrinsic and even show up type inversion for high fluences [16].

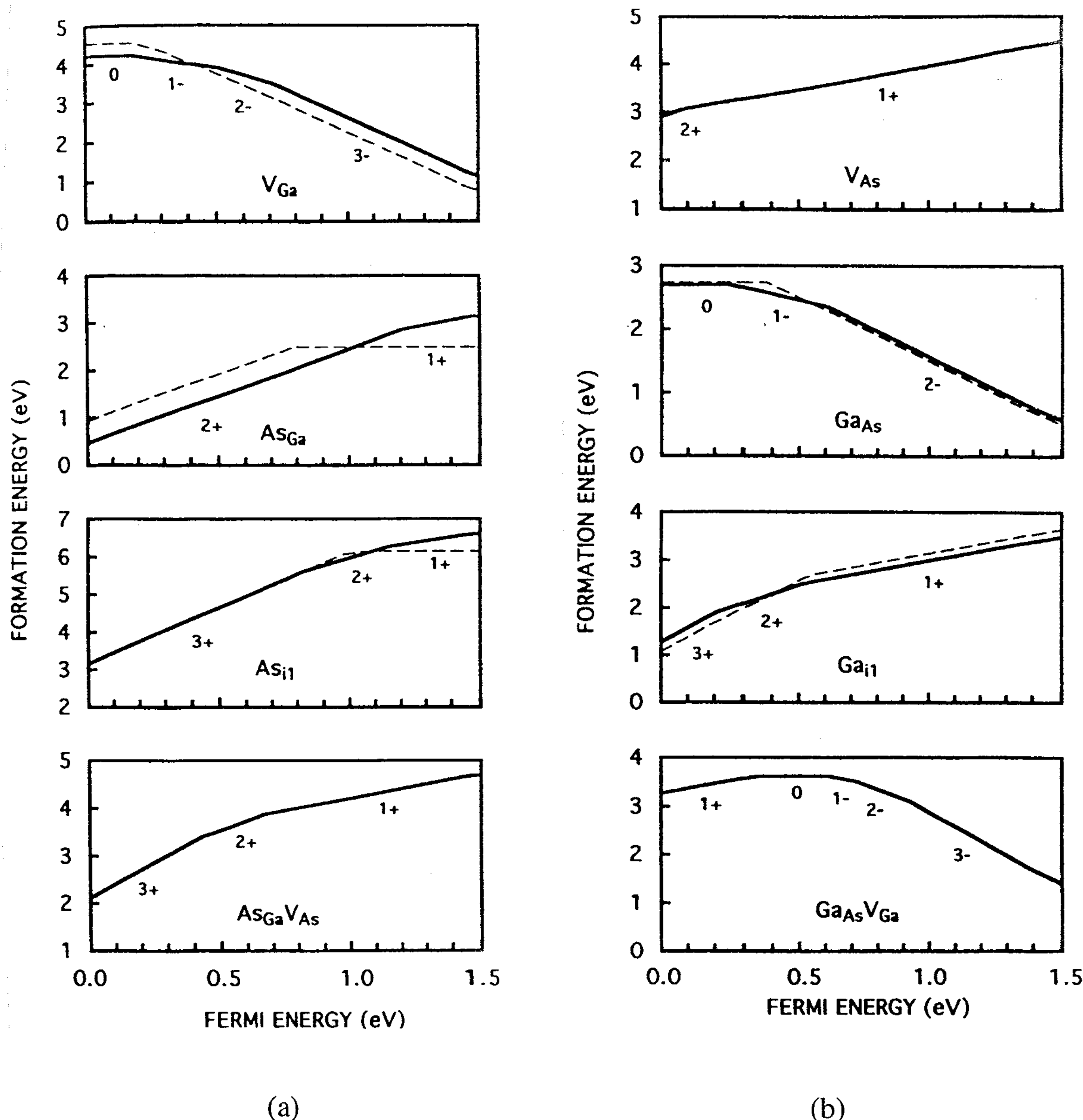

Fig.5.2. Formation energies of native defects associated with As-rich (a) and with Ga-rich (b) GaAs as a function of the Fermi level, measured from the valence band edge. (After Luken and Morrow [15]).

From Table 5.1, a few interesting observations can be made. First, most of the identified primary radiation defects are related to the As sub-lattice, which are in many cases of a donor nature. The Ga-related native defects are not so well documented. One reason is that most of the radiation studies have been performed on the technological more relevant n-type (or SI) material. DLTS on a n-GaAs Schottky or a p-n junction easily reveals the electron trap levels (E or EL), but it is much more difficult if not impossible to detect the minority carrier hole traps. It has also been argued that the primary Ga defects, i.e. V_{Ga} or V_{Ga}-Ga_i may not be stable in p-type GaAs, due to the different charge state (Fermi level) of the centers [16]. The Ga vacancy can transform in the more stable As_{Ga}-V_{As} by simple nearest neighbor hop. The substitional-interstitial pair can directly

recombine if the V_{Ga} is positively charged. It is furthermore clear that the nature and identity of many of the native defects is still controversial and not always firmly established. For example, the charge state(s) of V_{As} is still a matter of debate, assigning both double acceptor [2,10] and double donor character to the E1,E2 levels. In the meantime, the gallium vacancy has been positively identified using low temperature photoluminescence (PL) [17-18]. It turns out to be a shallow acceptor, which correlates well with the degradation of a number of macroscopic material parameters, like the electron mobility. Such shallow acceptors could be also partially responsible for the carrier removal or compensation in irradiated n-type GaAs [16,17].

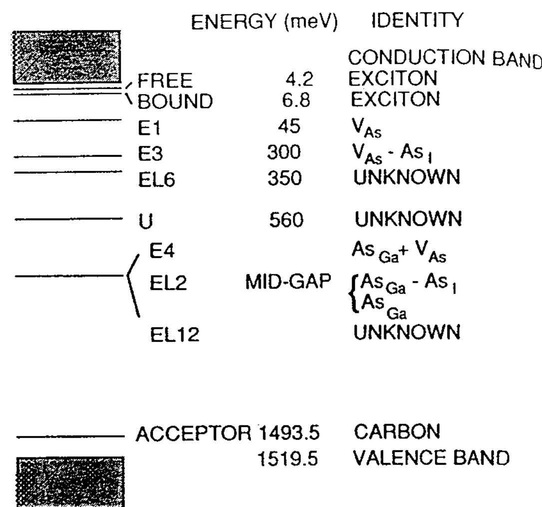

Fig. 5.3. The energy level diagram of some mid gap states in gallium arsenide. Some of the levels have been obtained in as grown samples, others in neutron irradiated GaAs. (After Jorio et al. [8]).

Regarding the thermal stability of the primary radiation defects, it can be concluded that - as far as the information is available - the native defects anneal around 200-300°C, while higher order defects, found after proton or neutron irradiation anneal at higher temperatures (400-500°C) [10]. EL6 and the U band disappear around 500°C. This means that after a 500 °C anneal most of the irradiation induced deep levels have dissolved, leaving EL2 as the dominant deep center [10].

In the ternary wide gap AlGaAs layers used in HEMT devices, a similar situation exists, where the native DX centers are predominantly present for an Al content larger than 22 % [19], showing also radiation hardness. An example is given in Fig. 5.4 for He ion irradiations. No change in the DLTS spectrum is observed after an exposure to 7.6×10^{11} cm^{-2} 5 MeV He ions [20]. These deep donor DX centers are a complex of a donor impurity (D) and an unknown (X) native defect [19]. Like EL2, metastable behavior can be induced by various excitation mechanisms, which provoke long term transients in the device characteristics.

Table 5.1. Characteristic properties of the intrinsic defects as deduced from DLTS and thermal stability. (After Bourgoin et al. [2]).
*according to Look and Sizelove [16] V_{As} is a double donor, in agreement with Fig.5.2.

Defect	DLTS	Thermal Stability T_{ann} (^{o}C)
V_{As}	$E1=E_c-0.045$ eV (2-/-)* $E2=E_c-0.14$ eV (-/0)	--
V_{As}-As_i	$E3=E_c-0.30$ eV $E5=E_c-0.96$ eV $H0=E_v+0.06$ eV $H1=E_v+0.25$ eV	220
As_{Ga} Ga_{As}	EL2 (?) $E_v+0.077$ eV (0/-) $E_v+0.23$ eV (-/2-)	>950
$As_{Ga}+V_{As}$	$E4=E_c-0.76$ eV (+/2+) •$E_c-0.35$ eV (0/+)	
As_i		≈200

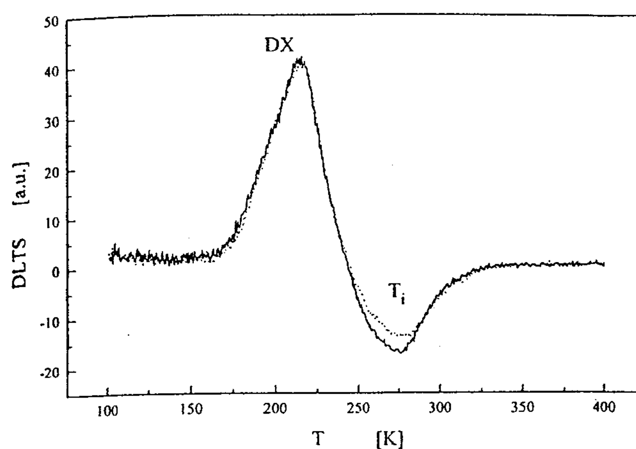

Fig.5.4. Typical drain current DLTS before irradiation (dashed line) and after a fluence of $7.6x10^{11}$ 5 MeV He ions. (After Papaioannou et al. [20]).

5.1.2 MESFET Structure and Operation

The structure of a MESFET is schematically shown in Fig. 5.5a: in the SI substrate, a highly doped n-layer is fabricated either by Si ion implantation or by epitaxial deposition of a several μm thick layer, which is contacted by the n^+ source and drain region. In many cases, a lowly p-doped buffer layer is deposited on top of the SI substrate before the creation of the channel layer (Fig. 5.5a). It is generally assumed that a Gaussian carrier profile is obtained for an ion implanted device, like in Fig. 5.b consequences for the hardness of the FETs. Typical doping densities are in the range 1 to $5x10^{17}$ cm^{-3}, depending on the application. For an epitaxial layer, the constant doping level is mostly lower than the maximum doping peak in an implanted device. The reason is that the gate leakage current of the reverse biased Schottky diode should be kept small. For higher surface n-doping densities, the barrier height will be lowered and hence the leakage increased [21]. The application envisaged will also dictate to some extent the use of an implanted or an epitaxial channel. Finally, on top of the doped n-layer, a metal gate (Au-based) is formed.

In the threshold region of a uniformly doped MESFET, the source-drain current satisfies the relation:

$$I_{DS} = \frac{Z\mu_{eff}\varepsilon}{2d_n L}(V_{GS} - V_T)^2 \tag{5.2}$$

with Z the gate width, L the length, d_n is the channel depth (order ≥0.5 μm), ε is the permittivity of GaAs, μ_{eff} the effective electron mobility and V_{GS} the gate to source voltage. Using the gradual channel approximation, the threshold voltage V_T obeys in first instance:

$$V_T = V_{bi} - \frac{qd_n^2 N}{2\varepsilon} = V_{bi} - V_P \tag{5.3}$$

Hereby is N the channel carrier density (in cm^{-3}), q the elementary charge and V_{bi} the built-in potential of the gate junction. The pinch-off voltage V_P corresponds to the potential necessary to deplete the channel layer. The threshold voltage can according to Eq. (5.2) be obtained by extrapolating $\sqrt{I_{DS}}$ to zero V_{GS}, for constant V_{DS} in the linear region.

In case of an implanted profile, a modified theory has been derived [22], starting from the general expression:

$$V_P = V_{bi} - \frac{q}{\varepsilon}\int_{x_o}^{x_c} xN(x)dx \tag{5.4}$$

with x_o the start of the channel and x_c the end, while x_c-x_o=d_n is the channel width. For a constant profile N(x)=constant, Eq. (5.3) is found immediately, for x_o=0. The integral has been worked out also for a Gaussian implantation carrier profile [22].

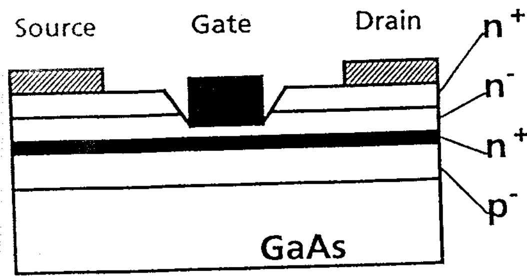

(a) Cross-sectional view

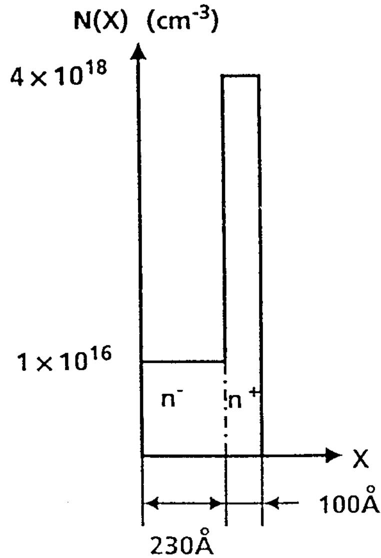

(b) Carrier depth profile

(a)

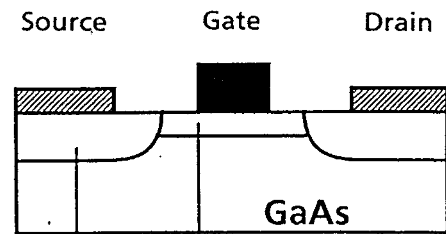

(a) Cross-sectional view

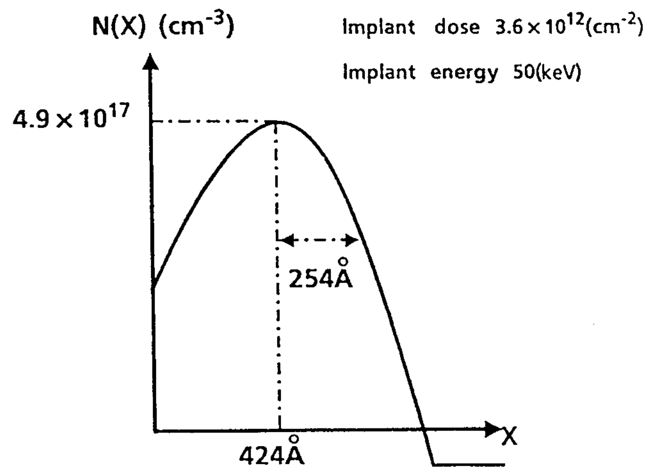

(b) Carrier depth profile

(b)

Fig. 5.5. A conventional GaAs MESFET structure (a) and a proposed radiation hard architecture (b). (After Nishiguchi et al. [21]).

For device and circuit simulations, Eq. (5.2) is too simplistic to describe the full I_{DS}-V_{DS} curve in the whole drain bias range. A suitable empirical model, which has been utilized to simulate the impact of radiation damage is given by [23]:

$$I_{DS} = \beta' (V_{GS}-V_T)^n \tanh(\alpha' V_{DS}) (1+\lambda V_{DS}) \qquad (5.5)$$

β' sets the saturation current (flat level at large V_{DS}), α' models the initial slope (linear region, small V_{DS}) and accounts for the higher mobility in linear operation. The exponent n is usually assumed to be 2, but can also be considered as a fitting parameter and λ is the channel length modulation parameter and models the output conductance of the transistor. It often takes the form:

$$\lambda = \frac{\lambda_o}{1 + K(V_{GS} - V_T)} \qquad (5.6)$$

with λ_o and K fitting parameters.

For analog applications the low-frequency (LF) noise is an important parameter. This even applies for micro and millimeter-wave non-linear circuits, where the phase noise of an oscillator is determined by the LF noise. Fig. 5.6 illustrates the possible sources of LF noise in a GaAs MESFET [24]. It could be (1) the metal-semiconductor interface; (2) the free surface region between source and gate and drain and gate (ungated region), which is frequently covered by a passivation layer (SiO_2 for example); (3) the neutral channel region; (4) the gate depletion region and (5) the channel-substrate depletion region. It has been shown that the dominant source of 1/f noise is generation-recombination (GR) by trap levels in the depletion region [24]. By studying the impact of the substrate type (SI versus Cr doped) and the effect of the presence of a buffer layer, it was concluded that the main source of LF noise is the substrate. It is not clear whether the GR noise is predominantly generated in region (4) or (5). On the other hand, it was also observed that the surface contribution to the noise generation is small. Finally, it has been found that the input noise voltage varies according to $1/\sqrt{L}$, with L the device length. This is in line with GR noise generated in the depletion region of the MESFET [24]. For L<0.5 μm, the noise varies according to 1/L.

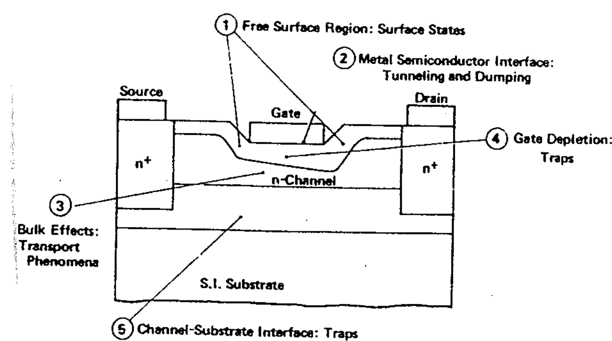

Fig. 5.6. Possible sources of 1/f noise in a GaAs MESFET. (After Su et al. [24]).

5.1.3 HEMT Structure and Operation

The layer scheme of a lattice matched Si doped AlGaAs HEMT is represented in Fig. 5.7a [25], while a pseudomorphic HEMT (P-HEMT), where the lattice mismatch between the GaAs substrate and the InGaAs channel layer is larger is shown in Fig. 5.7b [26]. For not too large gate biases, charge transport from source to drain is by the two-dimensional electron gas (2-DEG) existing at the GaAs/(undoped)wide-gap InGaAs interface. The carriers are provided by the highly doped AlGaAs (or InGaAs) donor layer (typically 10^{18} cm^{-3} donors), which is offset from the channel by the lowly doped AlGaAs spacer layer. The fact that the 2-DEG electrons are seperated from the charged donor atoms in the highly doped layer reduces strongly the Coulombic scattering contribution to the mobility, so that effectively high mobility transport occurs in the channel. This becomes particularly pronounced for cryogenic temperature operation, where Coulomb scattering is relatively more pronounced. The GaAs buffer layer is undoped but has in practice a slight p-type character (i.e. contains a net acceptor density). At higher gate biases, also the low-mobility donor layer will contribute to the drain current, which gives rise to a degradation of the effective mobility and hence of the device transconductance g_m. The band diagram of a GaAs HEMT is represented in Fig. 5.8, defining also the relevant device parameters. More complex layer schemes are sometimes used, for example with an extra AlGaAs buffer layer on top of the SI substrate, whereon the p-GaAs channel layer is deposited [20,27]. This extra heterojunction has been shown to provide improved resistance against ionizing radiation-induced photoconductivity (back-gating and transients).

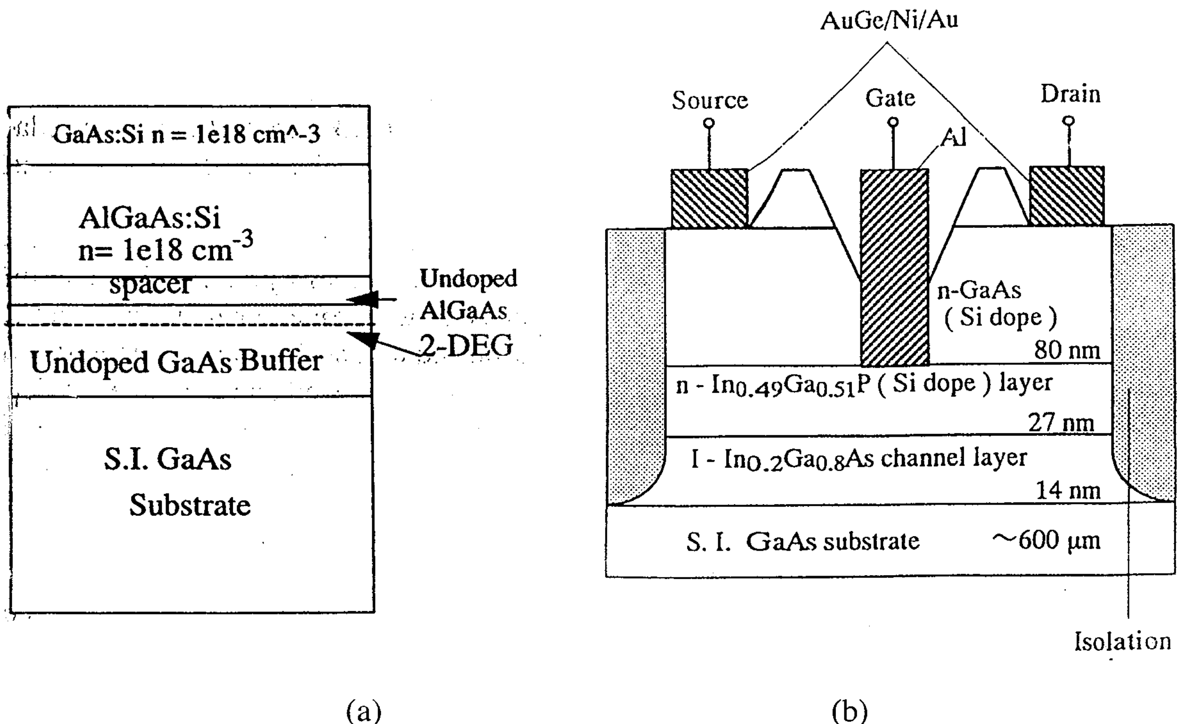

Fig. 5,7. (a) Schematic cross-section of an AlGaAs/GaAs HEMT (After Subramanian et al. [25]) and (b) of a pseudomorphic HEMT. (After Ohyama et al. [26]).

The on voltage of a HEMT is determined by a number of parameters. In the depletion approximation, it can be shown that the electric field at the heterojunction interface is given by [28]:

$$F_i = \frac{-V_{off} - E_F + V_{GS}}{d_n + d_s} \tag{5.7}$$

Hereby is d_n the doped AlGaAs(n) layer and d_s the spacer layer thickness, E_F (in volts) the Fermi level relative to the bottom of the quantum well and V_{off} is the voltage which annihilates the channel charge, and given by:

$$V_{off} = \phi_m - \Delta E_c - V_{A1} \tag{5.8}$$

ϕ_m is the Schottky barrier height and ΔE_c is the conduction band discontinuity at the AlGaAs/GaAs interface. For radiation damage studies, it is generally assumed that the latter two parameters are not affected by the irradiation [20,28]. This has been verified experimentally for ΔE_c under γ-irradiation, yielding a constant value of ≈0.165 eV up to 40 Mrad(GaAs) [25].

Finally, V_{A1} in Eq. (5.8) is the potential drop across the AlGaAs layer. For a homogeneously doped layer, V_{A1} is given by Eq. (5.3) and is equal to minus the pinch-off voltage ($-V_P$). For radiation damage studies, it is only V_G', given by:

$$V_G' = V_{GS} - \phi_m - \Delta E_c \tag{5.9}$$

which needs to be considered. For the calculation of E_F, it is generally assumed that only the first quantum level in the 2-D well is occupied [20,28], which simplifies the analysis considerably. Based on that, it can be shown that the 'threshold' voltage defined in Eq. (5.9) is a function of the AlGaAs (N) and the GaAs (N_A) doping density and of the geometry (AlGaAs donor and spacer layer thickness d_n+d_s) [28]. This results finally in a non-linear relationship between the gate bias close to threshold and the electron density in the 2-DEG N_S [20]:

$$V_{GS} = \frac{q(d_n+d_s)N_s}{\varepsilon} + (\phi_m - \Delta E_c - V_P) + \frac{kT}{q}\ln[\exp(\frac{qN_s}{DkT}) - 1] + \alpha_0(N_s + N_A^*)^{2/3} \tag{5.10}$$

k is Boltzmann's constant, T the absolute temperature, N^*_A is the surface acceptor density in the GaAs buffer layer (in cm^{-2}), D is the density of states of the 2-DEG and equal to $3.24x10^{17}$ $m^{-2}V^{-1}$ [20] and α_0=$2.5x10^{-12}$ eV $m^{4/3}$. Equation (5.10) gives a satisfactory approximation for N_S values below $5x10^{11}$ cm^{-2} [20].

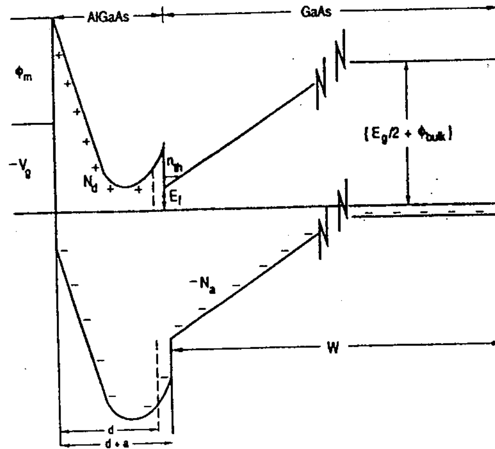

Fig. 5.8. Band diagram of a HEMT structure with Schottky contact, with barrier height ϕ_m, under gate bias V_{GS}. AlGaAs donors and unintentional acceptors (density N_a) are assumed to be completely ionised. Near the threshold, the Fermi level (dash-dot line) lies below the bottom of the 2-DEG well. (After Krantz et al. [28]).

5.2 Macroscopic and Microscopic Displacement Damage Effects in GaAs

5.2.1 Macroscopic Displacement Damage in GaAs

Exposure to high-energy particle or photon irradiation causes a degradation of the electrical parameters of GaAs layers. The main effects are a reduction of the carrier density termed carrier removal and a reduction of the mobility, caused by displacement damage. The reduction of the carrier density is a net result of carrier trapping by radiation induced trap levels and charge compensation by created defects with opposite character [16]. For very high fluences, even type inversion occurs [16]. The mobility degradation is caused by Coulombic scattering at charged centers, which include the created traps. The carrier removal rate $-dN/d\Phi$ for not too large fluences is constant, leading to an empirical law [29]:

$$N = N_o (1-a_N \Phi) \tag{5.11}$$

with Φ the particle fluence, N_o the starting carrier density and a_N a damage parameter. Similarly, for the mobility, derived for example from Hall measurements on exposed epitaxial layer structures or bulk samples, one can write:

$$\frac{1}{\mu} = \frac{1}{\mu_o}(1 + b_\mu \Phi) \qquad (5.12)$$

with μ_o the initial mobility.

The damage parameters a_N and b_μ have been derived from irradiations of simple "resistors" or Hall structures and yielded the following relationship with starting doping density, both for bulk and epitaxial samples, for fast neutron exposure [29]:

$$a_N = 7.2 \times 10^{-4}\ N_0^{-0.77} \qquad (cm^2) \qquad (5.13)$$

$$b_\mu = 7.8 \times 10^{-6}\ N_0^{-0.64} \qquad (cm^2) \qquad (5.14)$$

The corresponding carrier removal rate is represented in Fig. 5.9 and shows an increase for higher starting doping density. From Fig. 5.9, a value ranging from 6 to 10 cm^{-1} is derived for a doping density typical for the channel of a MESFET or of a HEMT.

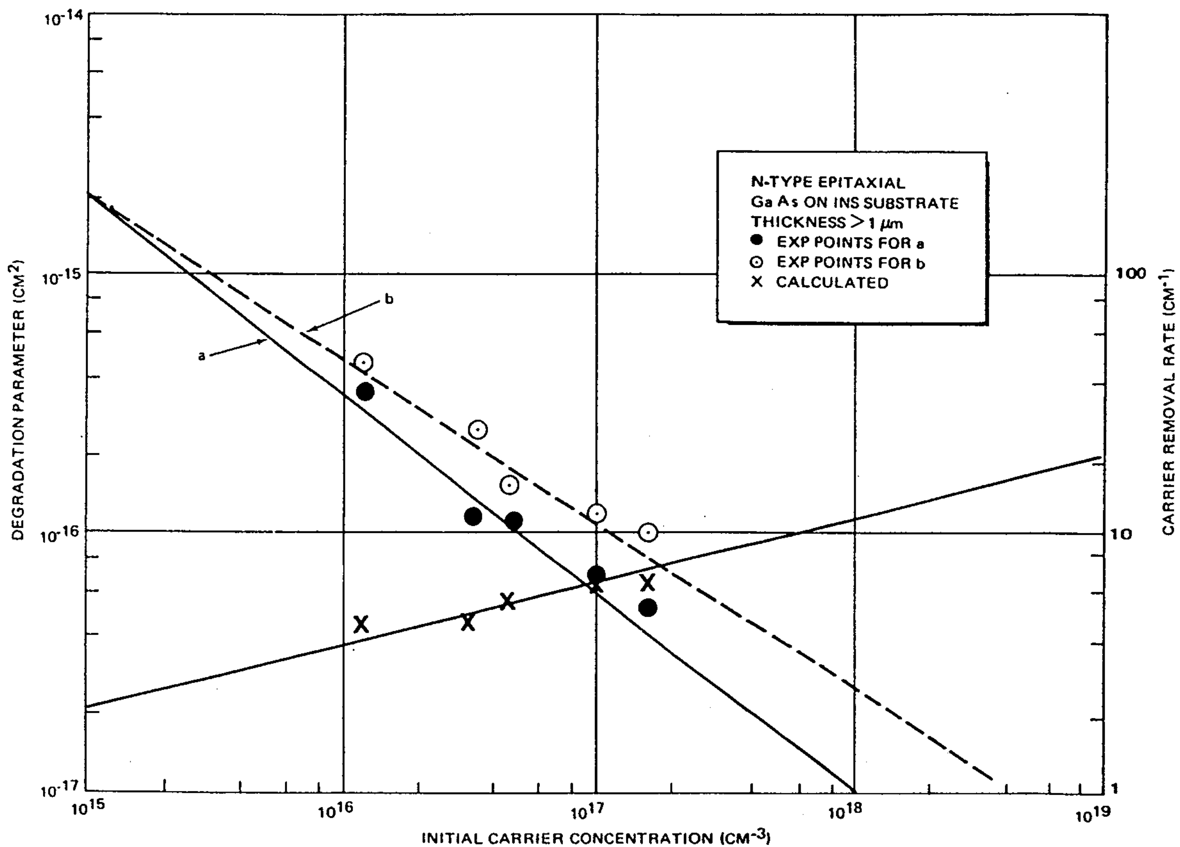

Fig. 5.9. Degradation parameters a_N and b_μ and carrier removal rate versus initial carrier concentration for epitaxial n-type GaAs. (After Behle and Zuleeg [29]).

The damage parameters have been studied for epitaxial GaAs for other particle irradiations as well [30-33] and also for ion implanted resistors [31]. A striking result is that the damage factor for carrier removal is more than 1 decade larger for implanted resistors compared with epitaxial (or bulk) ones (Fig. 5.10). The damage factor also shows a superlinear dependence on doping density, suggesting that higher implanted GaAs should be more radiation tolerant, than for lower implant doses.

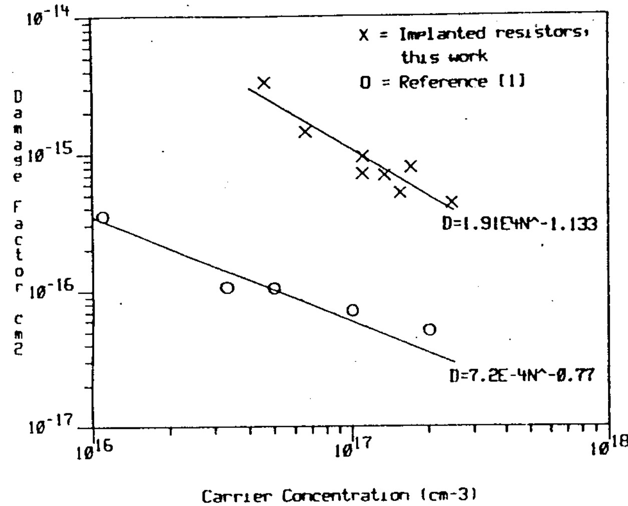

Fig. 5.10. The resistor damage factor as a function of carrier concentration under neutron bombardment for implanted and epitaxial uniformly doped resistors. (After Campbell et al. [31]).

Gamma irradiation of GaAs generates similar carrier removal and mobility degradation, as demonstrated in Fig. 5.11, versus total dose [21]. For the carrier removal, the following empirical relationship has been obtained [21]:

$$\Delta N = 9.92 \times 10^{5} \, D_{\gamma}^{1.17} \ \mathrm{cm}^{-3} \qquad (5.15)$$

with D_γ the total dose. The carrier removal rate was found to be independent of the initial carrier concentration N_o.

The damage factors defined above provide a good empirical description of the macroscopic displacement damage for fairly large total doses or fluences. However, it has been observed on several occasions that certain electrical/optical bulk properties of GaAs improve for moderate radiation fluences [34-38]. This has been found for the maximum mobility, the minority carrier lifetime, the carrier concentration, the exciton lifetime and the PL intensity [37]. This improvement becomes clear especially after annealing the irradiated samples at 550°C and is ascribed to a so-called radiation-induced 'ordering' effect,

suggesting a restructuring of the lattice. The energy deposited during irradiation may induce configuration modification, which can result in a lower energy state of the crystal. Another possibility is the stimulated gettering of impurities and defects at surface or interface sites. An example is given in Fig. 5.12 [38], showing the maximum low-temperature mobility (occurring at ≈90 K), in function of the neutron fluence. An increase of μ_{max} is observed until a fluence of 10^{13} n/cm^2, for irradiated and annealed samples. No increase is noted for unannealed samples.

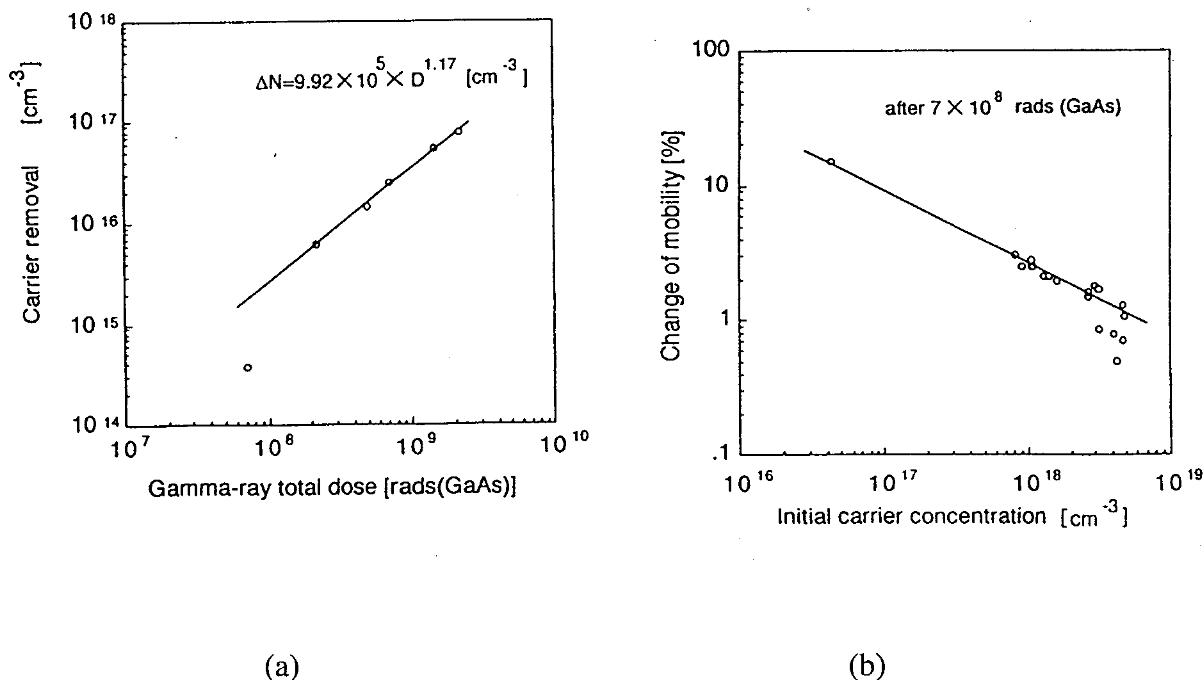

(a) (b)

Fig. 5.11. Carrier removal with γ-ray irradiation (a) and density dependence of mobility degradation with γ-ray irradiation. (After Nishiguchi et al. [21]).

Figure 5.13a demonstrates that for the high fluence range, the empirical law of Eq. (5.12) is in first approximation valid. In the same fluence range, it has also been found that the irradiation induced gallium vacancy acceptor concentration, detected by PL, increases linearly with fluence (Fig. 5.13b) [38]. These two facts establish a clear correlation between the radiation induced degradation of a macroscopic parameter (μ_{max}) and a primary radiation defect in n-type GaAs.

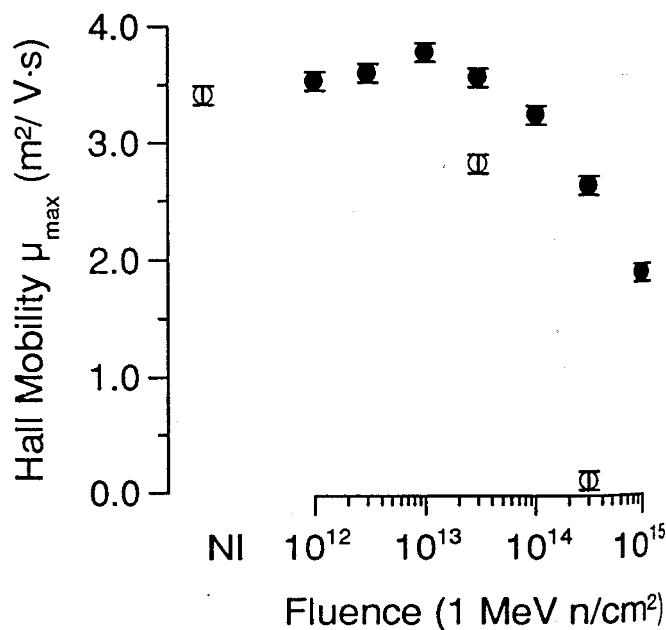

Fig. 5.12. μ_{max} as a function of fluence. For annealed samples (closed circles), it goes through a maximum at 10^{13} n/cm^2. This increase did nor occur for the samples which were irradiated but not annealed. (After Jorio et al. [38]).

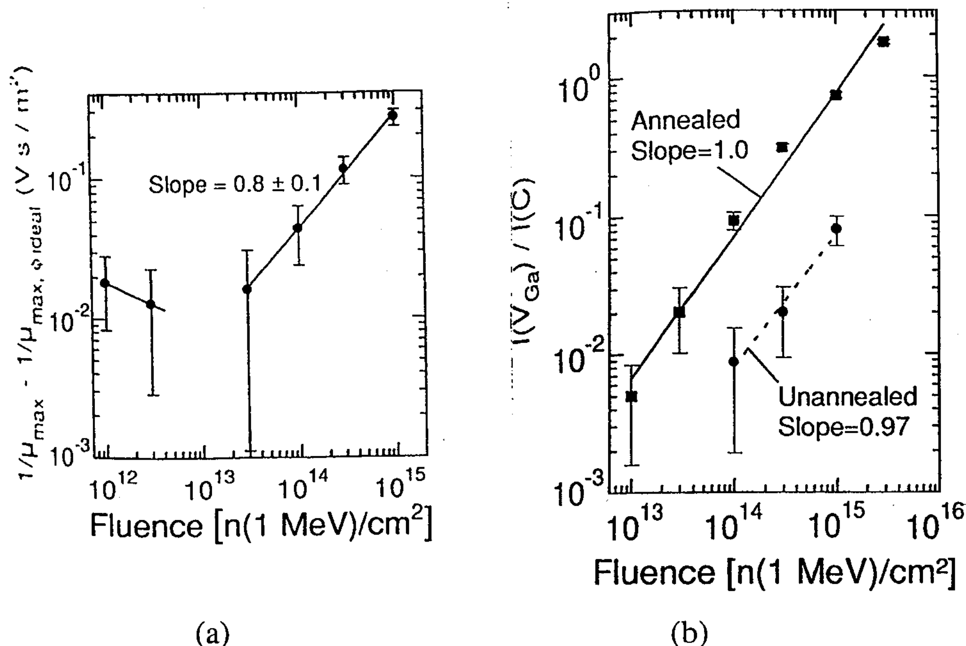

(a) (b)

Fig. 5.13. (a) $(1/\mu_{max}-1/\mu_{max,\Phi ideal})$ as a function of fluence. The measured slope of 0.8±0.1 in the degradation regime for large neutron fluences suggests that Eq. (12) holds in first instance. (b) Normalised PL intensity $I(V_{Ga})/I$(carbon) as a function of fluence. V_{Ga} is observed in the non annealed samples between 10^{14} and 10^{15}n/cm^2, whereas in the annealed samples at Φ between 10^{13} and 3×10^{15} n/cm^2. (After Jorio et al. [38]).

5.2.2 Microscopic Displacement Damage Modeling

In order to relate the radiation induced degradation of a macroscopic parameter, to the microscopic lattice damage created by a high-energy particle, one can use a number of numerical physics-based models to calculate the interactions between the projectile and the target. Particularly the Non Ionising Energy Loss (NIEL) concept has proved its value in the last decade, for different semiconductor materials. It basically considers the energy which is deposited in the lattice by non-ionising interactions, which include elastic (Rutherford scattering) and non-elastic nuclear interactions. The latter will prevail at higher energies.

Summaries of the different results obtained on n- and p-type GaAs and for a wide range of particles and energies are given in Fig. 5.14, showing a linear correlation with the non-ionizing energy deposition (NIEL) [33]. However, the energy of the primary knock-on atoms (PKA's) corresponding to Fig. 5.14 is in fact quite low (50 to 200 eV), while the maximum transferred PKA energy in GaAs can be as high as 2 MeV. This is much larger than the corresponding values for Si (300 keV). For such high maximum energies, nuclear inelastic interactions should be considered. For example, in the case of high energy proton irradiations, high energy inelastic nuclear interactions (PKA's) become important above 10 MeV H^+ and dominate for energies higher than 60 MeV. Experimental evidence is provided by the results shown in Fig. 5.15, for high-energy proton exposures, showing the normalised resistance change of a GaAs resistor, as a function of fluence. While the initial slope is approximately constant and can be described by:

$$\frac{R}{R_o} = 1 + K_R \Phi \qquad (5.16)$$

with K_R the resistance damage factor, for higher Φ, a superlinear degradation is found [33].

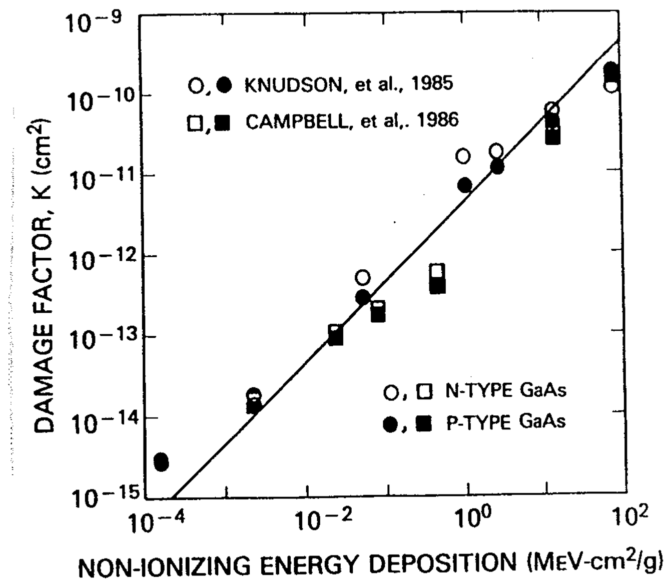

Fig. 5.14. A plot showing the linear dependence of the damage factors for GaAs JFETs and resistors on nonionizing energy deposition. The data comes from Refs 30 and 31. (After Summers et al. [33]).

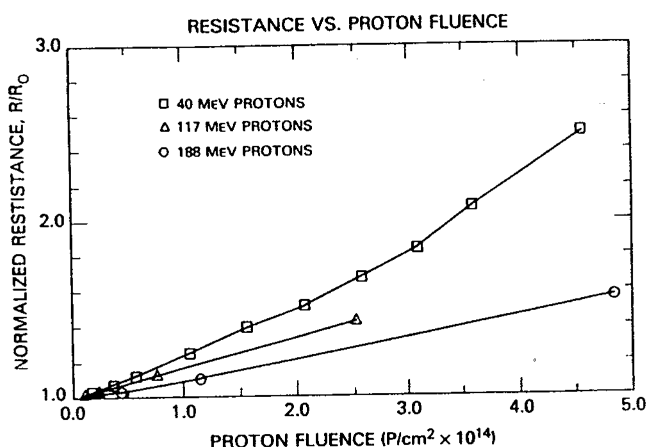

Fig. 5.15. Variation in reduced resistance of ion implanted n-type GaAs as a function of proton fluence for 40, 117 and 188 MeV protons. (After Summers et al. [33]).

The likeliness of high-energy recoils at high particle energies for GaAs implies that the total non-ionizing energy S_d should be calculated from [33]:

$$S_d = \frac{N_{av}}{A}(\sigma_c E_e + \sigma_i E_i) \tag{5.17}$$

where the σ's are the cross sections, the E's are effective average recoil energies for elastic (e) and inelastic (i) recoils, N_{av} is Avogadro's number and A the gram atomic weight of the target. The result is depicted in Fig. 5.16, showing a good agreement between NIEL and the (linear) resistance damage factor, if account is made for the non-local energy deposition of energetic PKA's, which penetrate much deeper in the substrate than the extent of the implanted or epitaxial resistors. It should also be remarked that the proton energy dependence of the carrier removal rate and the mobility are similar, as derived from Hall measurements, at least for protons up to 63 MeV [32].

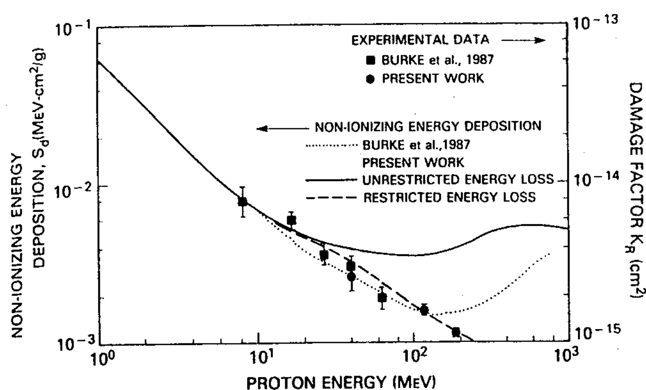

Fig. 5.16. NIEL versus proton energy according to different approximations, compared with the experimental damage factors for implanted resistors. The restricted energy loss curve results when the energy of the residual recoils is arbitrarily limited to 500 keV, i.e. recoils having a range less than the active depth of the resistor. (After Summers et al. [33]).

5.2.3 Correlation with Radiation Defects

The successful correlation established between the NIEL (or TRIM simulations) and the macroscopic damage opens up strong perspectives for the prediction and simulation of radiation damage in III-V electronics and enables to reduce considerably the amount of testing. Nevertheless, such a correlation is not that obvious, since the material properties are affected in the first place by stable radiation defects, which are only fractions of the total amount of Frenkel pairs initially formed. Furthermore, the defects responsible for the degradation must not necessarily be simple (primary) defects but can be complexes or larger aggregates. Therefore, for a full understanding of the problem, one should identify the critical defects, which is not an obvious task.

As mentioned above, one of the first successful identifications of critical radiation induced defects was the gallium vacancy, correlating well with the mobility degradation [38]. In addition, the correlation between the radiation induced formation of V_{Ga} and the NIEL has been extensively studied by Khanna et al [17], using PL, which is a relative technique. The signal peak associated with V_{Ga} is resulting from electron-hole recombination through a donor (D) and a nearby V_{Ga} shallow acceptor (close to the valence band). Its formation has been investigated for a broad range of substrate doping densities (n-GaAs: 10^{15} up to 10^{18} Si/cm^3) and irradiating particles: electrons, neutrons, protons, lithium, deuteron and oxygen. A comparison with ^{60}Co γ-irradiation was also performed. In general, the spectral PL intensity after irradiation reduces with increasing fluence. This points to the creation of deep(er) trap centers, which cause a non-radiative GR of electron-hole pairs and thus compete with the PL optical recombination transitions. However, annealing at 550°C removes most of this deep level damage and increases again the PL signal [21].

From these studies, a good correlation between the relative density of the primary defects V_{Ga} and the NIEL was derived as a function of particle fluence (Fig. 5.17). Also TRIM, which basically calculates the number of vacancies formed along the trajectory of the projectile yields a qualitative agreement. Interestingly, the V_{Ga} was observed for high dose γ-irradiations as well, indicating that indeed displacement damage is formed due to the energetic secondary Compton electrons. It has furthermore been observed that the formation of the gallium vacancy is strongly dependent on the starting material.

Another interesting fact is the observation of the Si_{As} shallow acceptor in PL, which is displaced from its original Ga donor site. This is a direct mechanism for carrier removal, whereby dopant atoms are incorporated in a simple radiation induced defect and are lost for providing electrons to the channel. In fact, due to the acceptor nature, an additional charge compensation effect occurs [16], removing a second charge per Si_{As}. It also illustrates clearly the amphoteric nature of the silicon dopant. Both defects are coupled to each other, through the reaction [17]:

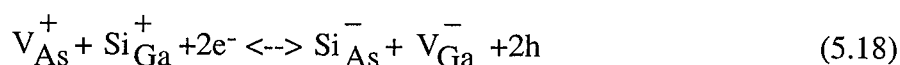

$$V_{As}^{+} + Si_{Ga}^{+} + 2e^{-} \leftrightarrow Si_{As}^{-} + V_{Ga}^{-} + 2h \qquad (5.18)$$

The creation of As vacancies by displacement will push the reaction to the right. The fact that the PL density of both Si_{As} and V_{Ga} increases strongly for neutron irradiations after 550°C anneal points to the fact that these centers are probably involved in larger irradiation induced complex defects or defect pairs [38].

Looking at Fig. 5.17, it is clear that at high energies, the Rutherford mechanism, predicting a 1/E dependence (E the particle energy) is no longer followed. A larger damage rate is found than calculated in Fig. 5.16, both by NIEL or by TRIM [17]. In contrast to the interpretation of Summers et al. [33], it is believed that this higher damage rate above ≈10 MeV for protons could be caused by a secondary displacement cascade, associated with high energetic PKA's. From the neutron irradiations, it is derived that they are more damaging than electron exposures and give rise to larger defect complexes clustered along the neutron track, which most likely incorporate the V_{Ga} and Si_{As}. These could for instance be defects related to the well-known U-band, which is not formed in electron or gamma irradiated GaAs and anneals at approximately 450-500°C [10]. These thermal recombination centres are deeper in energy and, therefore, quench the PL signal.

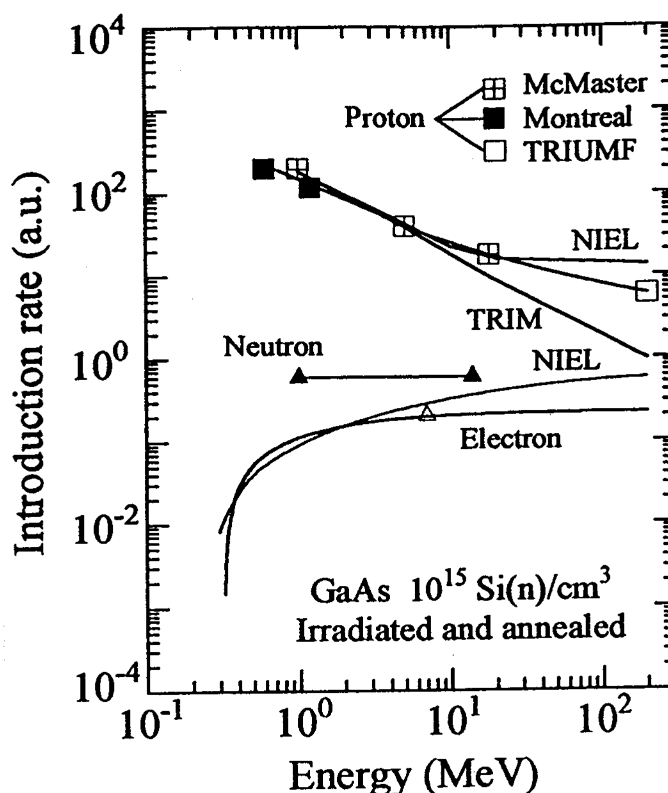

Fig. 5.17. The introduction rate of V_{Ga} in irradiated and annealed samples (A) doped to 10^{15} cm^{-3}. The agreement for the proton experiments with NIEL and TRIM is satisfactory for E < 10 MeV. There is only one experimental point for electron irradiation, for which the NIEL and the Darwin-Rutherford calculations have been included. (After Khanna et al. [17]).

5.3 Radiation Damage and Hardening in GaAs MESFETs

5.3.1 Displacement and Ionization Damage in FETs

In first instance, a MESFET can be considered as a "bulk" type of device, whereby charge transport occurs through a channel which is at some distance from the Schottky contact interface. It will therefore be mainly degraded by displacement damage effects in the channel region. Only in the ungated source-gate and drain-gate region, the carriers may be exposed to the surface and, hence, to charging in a passivation dielectric layer if present or to interface state creation. Furthermore, ionization can also induce some typical trapping and transient response in the SI substrate, so that total dose and dose rate effects should be considered as well, particularly on a circuit level [39]. However, most of the important device and circuit parameters will be predominantly affected by displacement damage. Therefore, a large part of the studies so far have concentrated on this issue.

The radiation response of MESFETs has been studied since the early eighties, whereby both high-energy particle (neutrons, electrons) [22-23,39-42] and γ-irradiations [21,42-43] have been performed. It should be remarked that in the latter case, the degradation is qualitatively similar, since energetic secundary and Compton electrons are generated, which can have energies up to 0.6 to 1.1 MeV [41]. The latter again create the necessary displacement damage for carrier removal and mobility degradation. Finally, also the combined effect of neutron/gamma irradiations showed some interesting features [44].

The degradation of the main MESFET parameters, namely, mobility μ_{eff}, pinch-off voltage V_P and carrier removal is illustrated in Figs 5.18a to 5.18c [41], for different types of devices, after exposure to gamma's and 1 MeV electrons. It is seen that the epitaxial FETs show a lower degradation than the ion-implanted devices, although the doping density is approximately the same ($\approx 2 \times 10^{17}$ cm^{-3}). This is in line with the resistor results of Fig. 5.10 [31]. It is generally assumed that the degradation of the pinch-off voltage is proportional to the carrier removal rate and inversely proportional to the original doping density. In other words [22,41]:

$$\frac{dV_p/d\Phi}{V_{Po}} = \frac{dN/d\Phi}{N_o - N} = 1 - a_N\Phi \tag{5.19a}$$

V_{Po} and N_o are the original pinch-off voltage and doping density and a_N the damage factor for carrier removal, defined in Eq. (5.11).

Likewise, for the mobility [22]:

$$\frac{1}{\mu} = \frac{1}{\mu_o}(1 + b_\mu\Phi) \tag{5.19b}$$

while for the transconductance [22]:

$$\frac{g_m}{g_{mo}} = \frac{N\mu}{N_o\mu_o} = \frac{(1-a\Phi)}{(1+b\Phi)} \tag{5.19c}$$

and for the drain current [22]:

$$\frac{I_{DS}}{I_{DSo}} = \frac{N^2\mu}{N_o^2\mu_o} = \frac{(1-a\Phi)^2}{(1+b\Phi)} \tag{5.19d}$$

Again, b_μ is the mobility degradation factor; the symbols with an o subscript are pre-irradiation values.

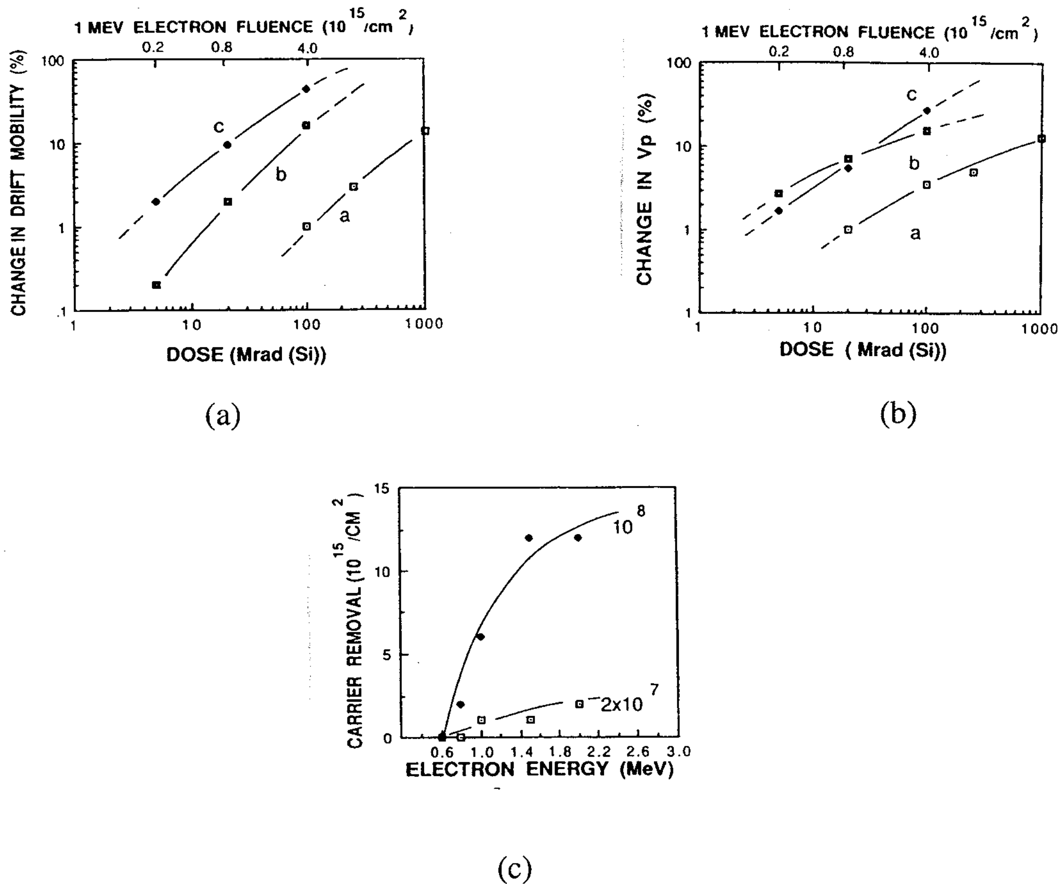

Fig. 5.18. (a) Percent degradation in mobility versus fluence and dose for γ– and 1-MeV e^- irradiation of vapor phase epitaxy (VPE) and ion-implanted material. Curve a: VPE, γ (dose abscissa); curve b: VPE, e^- irradiation (dose and fluence abscissa); curve c: implant, e^- irradiation (dose and fluence abscissa). (b) Percent degradation in pinch-off voltage versus dose and fluence for γ and 1-MeV e^- irradiations of FATFETs (=50 μm long) on VPE and implanted GaAs. Curve a: VPE, γ (dose abscissa); curve b: VPE, e^- irradiation (dose and fluence abscissa); curve c: implant, e^- irradiation (dose and fluence abscissa). (c) Carrier removal at $2x10^7$ (curve a) and 10^8 rad(Si) (curve b) for different e^- energies in FATFETs fabricated on GaAs epitaxial layers. (After Meulenberg et al. [41]).

From Fig. 5.18c it is derived that given the average Compton electron energy of 300 keV within the devices, only a few gamma created electrons will produce atomic displacements, explaining their lower effectiveness apparent in Figs 5.18a and 5.18b. The higher degradation found for implanted FETs is first of all explained by the presence of (shallow) unannealed Si implantation damage, which becomes electrically activated by the irradiation [7].

The lower radiation tolerance of an implanted MESFET technology has been further elaborated by Janousek et al. [22]. An example of the threshold voltage degradation for a neutron irradiated implanted FET is given in Fig. 5.19 versus fluence. As can be seen the change in V_P (or V_T) is much larger than can be predicted by Eq. (5.19a) for a uniform doping density and certainly non-linear with fluence.

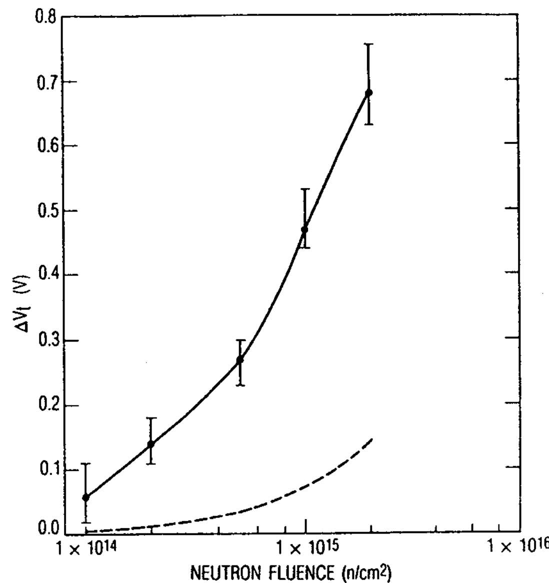

Fig. 5.19. Shift in threshold voltage as a function of neutron fluence (solid line). Predicted shift in threshold voltage using theory for a uniform profile (broken line). The solid dots are the average of the data. (After Janousek et al. [22]).

A model has been developed based on a Gaussian doping profile and including a local doping density dependent carrier removal rate of the form [22]:

$$a_N(x) = a_{No}\, N(x)^{-\nu} \tag{5.20}$$

which is equivalent to a carrier removal rate:

$$a^*(x) = a_{No}\, N(x)^{1-\nu} \tag{5.21}$$

It is not only shown that the irradiation can change the shape and width of the profile (channel), but in order to explain the measured V_T shift one has to assume a carrier removal rate which is larger for implanted FETs than the value of 6 cm^{-1} standardly assumed for 10^{17} cm^{-3} doped n-GaAs [29], with a value of 20 cm^{-1} closer to the observations. This is in line with other observations for implanted technologies [22], yielding rates between 10 and 100 cm^{-1}. This higher removal rate can be associated with the nature of neutron-induced defects formed in ion-implanted/annealed material versus epitaxial material. It is finally shown that only for low neutron fluences the threshold voltage of implanted MESFETs can be described by a simple linear relationship with fluence (Eq. (5.19a)). On the other hand, the uniform doping of an epitaxial layer may lead to a substantial hardening of the technology

The combined effect of neutron and gamma irradiation on implanted MESFETs has been studied by Chang et al. [44]. In the standard experiment, the neutron-irradiated sample was first annealed at 150°C in air for 30 min before the application of a γ-exposure to $2x10^7$ rads. This agrees with the onset of the 150-225°C annealing stage of radiation-induced point defects (simple primary defects). A second stage occurs at 400-450°C and is thought to correspond to larger "clustered" damage (U band, EL6,...) [10], expected for neutron irradiations, not for γ's. A typical result of this procedure is shown in Fig. 5.20. For moderate neutron doses, a slight improvement of the device transconductance is noted - the same applies for γ-doses up to $5x10^6$ rad(GaAs). This is in line with the results shown in Fig. 5.12 for the Hall mobility [37-38] of GaAs.

As can be noted in Fig. 5.20, annealing produces a slight recovery of the characteristics. However, a subsequent γ-irradiation gives rise to an enhanced degradation in the high neutron fluence range. This degradation is not caused by the γ-irradiation alone, as experimentally verified. It is concluded that there exists some latent damage (neutral defects) in neutron exposed material which becomes activated (i.e. filled by charge carriers) by the gamma's [44]. For low to moderate neutrons fluences, the device degradation will be governed by the carrier removal, since b_μ is negligibly small (mobility degradation factor). For high neutron fluences, on the other hand, where b_μ is no longer negligible, the mobility degradation becomes the predominant degradation mechanism for the transconductance and the drain current (see Eqs (5.19)).

Another important observation is that the experimental carrier removal rate is linear with Φ only for fluences up to $\approx 10^{15}$ cm^{-3} (Fig. 5.21), in line with the observations of Janousek et al. [22]. For the largest fluences, the removal rate becomes smaller than expected from Eq. (5.11) or (5.19a). The Authors propose a model, which is valid, for the whole neutron fluence range and which not only considers carrier removal but also carrier (donor) generation, in order to explain the reduced V_T change. This is achieved in the following way [44]:

$$\frac{V_P}{V_{Po}} = \frac{N}{N_o} = \frac{(1 - a_N \Phi)}{(1 + a_N'^k \Phi)} \qquad (5.22)$$

Fitting Eq. (5.22) to the data shows that k=1 and a'≈a, so that one can write:

$$\frac{V_{Po}}{V_P} = \frac{N_o}{N} = 1 + a_N \Phi \qquad (5.23)$$

and for the carrier removal rate:

$$\frac{dN}{d\Phi} = \frac{a_N}{N_o} N^2 \qquad (5.24)$$

Equation (5.24) predicts a quadratic dependence of the carrier removal rate on N, which is indeed found experimentally in Fig. 5.22. The values in Fig. 5.22 are in agreement with other results, which predict larger values than 6-10 cm^{-1} for implanted GaAs with a doping density of 10^{17} cm^{-3} [22].

Using the carrier removal rates after neutron and after the combined n/γ irradiation, one can distinguish between the contributions of point defects and defect clusters, as shown in Fig. 5.23. While the point defects show a 1 to 1 slope with the number of disappearing carriers, a slope of two (or more) is found for the defects clusters, implying that at least two carriers are captured in these neutron-related centers. This suggests thus larger defects, which are expected to be more thermally stable than the point defects and therefore correspond with the 400-450°C annealing stage.

These observations help to understand the difference in effects induced by gamma's (very moderate) and by energetic neutrons (more pronounced) in GaAs MESFETs. The gamma photons and the secondary and Compton electrons are seen as being rather ineffective in producing carrier trapping effects in GaAs other than a moderate number of shallow trapping levels very near the conduction band [44] (and valence band [17]). These shallow trapping levels coincide with the ones corresponding to unannealed implantation damage and are activated thermally at room temperature - they are responsible for the room temperature conduction. Annealing at 150°C enables to stabilize the shallow levels, resulting in no significant difference in the device performance, between pre- and post γ-irradiation.

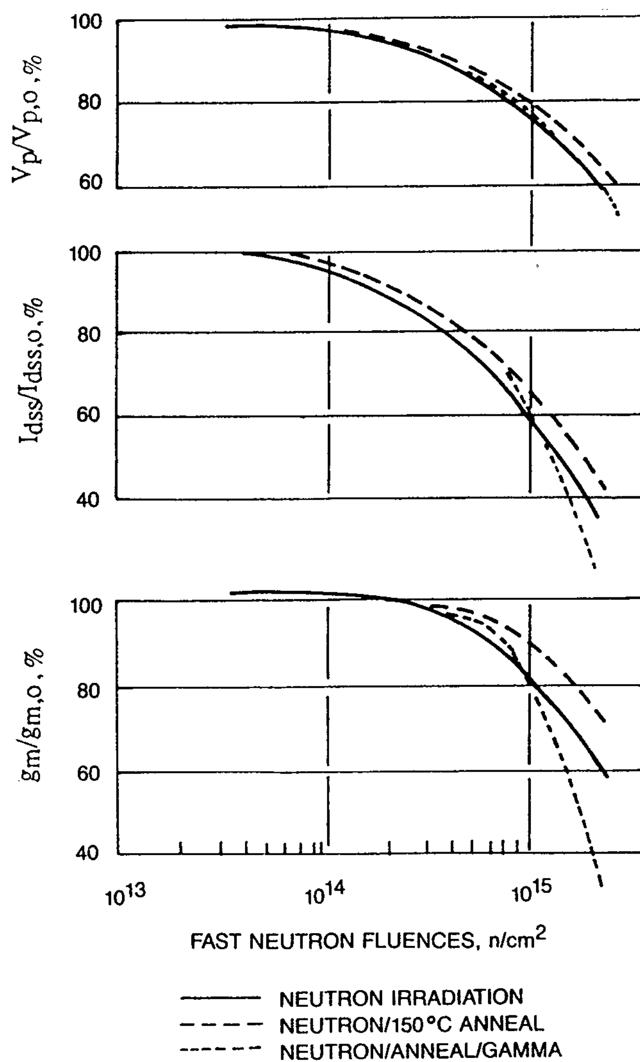

Fig. 5.20. Percentage reductions in device parameters. (After Hang et al. [44]).

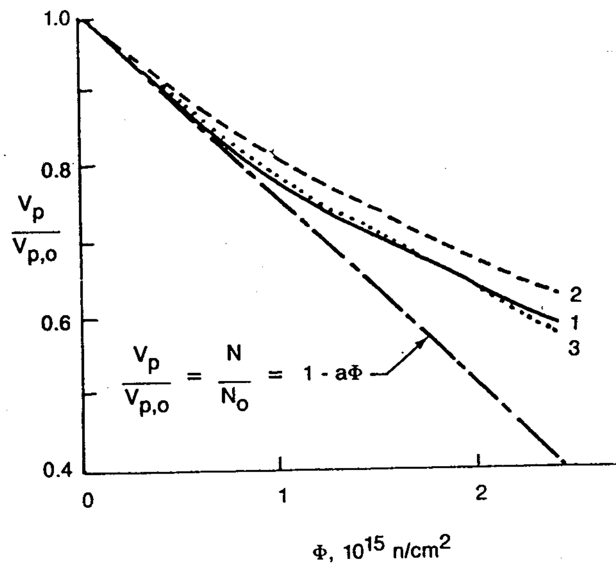

Fig. 5.21. Carrier removal by neutrons. 1=neutrons; 2=neutrons + annealing and 3=neutrons/anneal/gamma's. (After Chang et al. [44]).

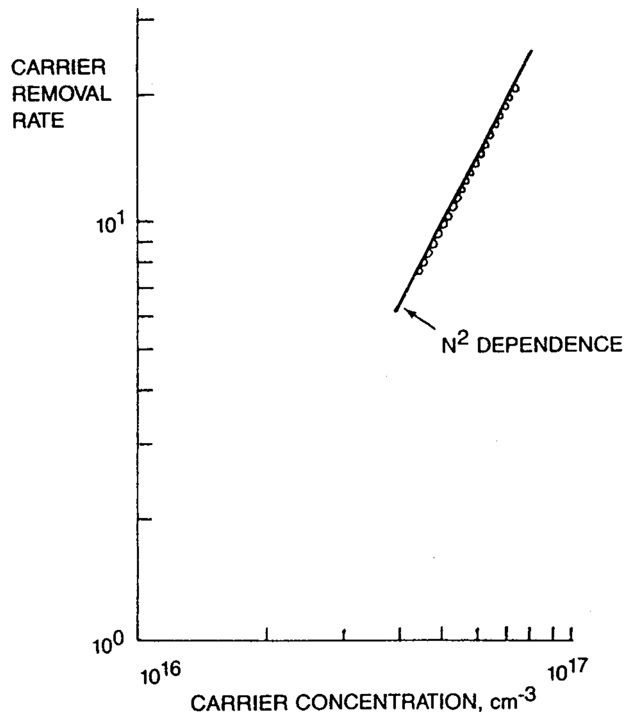

Fig. 5.22. N^2 dependence of the carrier removal rate. (After Chang et al. [44]).

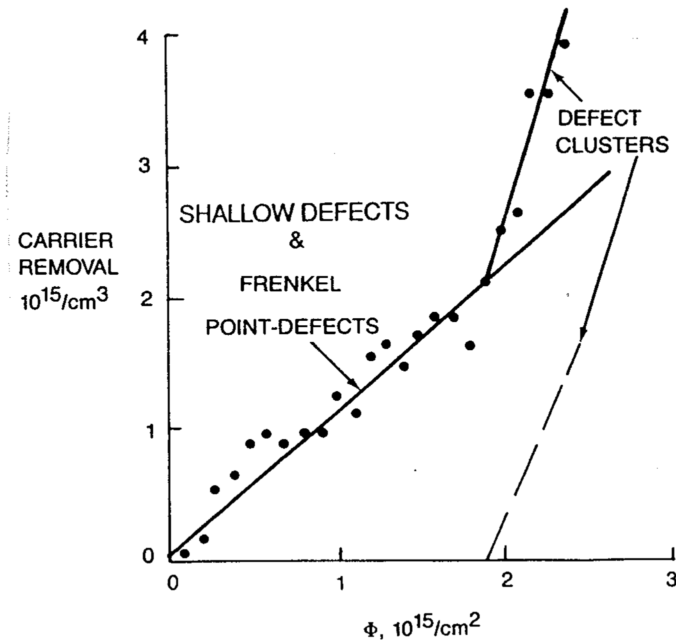

Fig. 5.23. Defect buildup versus neutron fluence. (After Chang et al. [44]).

Exposure to energetic neutrons, however, leads to the production of more permanent defects, which continue to grow in number with increasing fluence and may even coalesce into defect clusters at sufficient fluence. These centers are sufficiently deep so that charge carriers trapped in them become permanently lost for conduction. At the same time, these charged (cluster) defects are responsible for a significant mobility degradation through Coulombic scattering, which becomes the dominant degradation mechanism at high neutron fluences. Shallow levels, on the other hand, are at room temperature ineffective in reducing the electron mobility. It has also been shown that beside the shallow radiation induced defects, one needs to assume two other types of centers, in order to fully interpret the observed degradation behavior. For moderate neutron fluences, deep-level permanent Frenkel type of point defects are generated linearly with fluence and capable of trapping one carrier. Beyond a certain fluence threshold, in addition, larger aggregates of point defects may be formed, with each cluster capable of trapping two (or more) charge carriers. They also produce the largest effect on mobility [44].

A final remark is that due to this synergistic effect of a combined neutron/gamma exposure, one may wonder how a MESFET device/circuit will behave in a mixed radiation environment.

Recently, interest has emerged for the impact of radiation on the LF noise performance of MESFETs [7,45-46]. It has been observed that the 1/f noise voltage of a MESFET follows both a $1/\sqrt{L}$ [24] and a $1/\sqrt{W}$ dependence [46]. It was observed that the LF noise after γ-exposure increases with accumulated total dose (Fig. 5.24), for frequencies

above 1 kHz. In that frequency range, a clear GR noise component develops, which points to the creation of radiation-induced shallow traps or the stimulation of already-present shallow levels, like unannealed Si ion-implantation-related damage [7]. The displacement of Si donor to a Ga site introduces shallow acceptor levels [17] which can cause such a high-frequency GR noise. The broad frequency range suggests a distribution of different shallow levels. The LF part of the spectrum << 1 kHz is thought to be dominated by EL2-like deep levels and remains unchanged here [46].

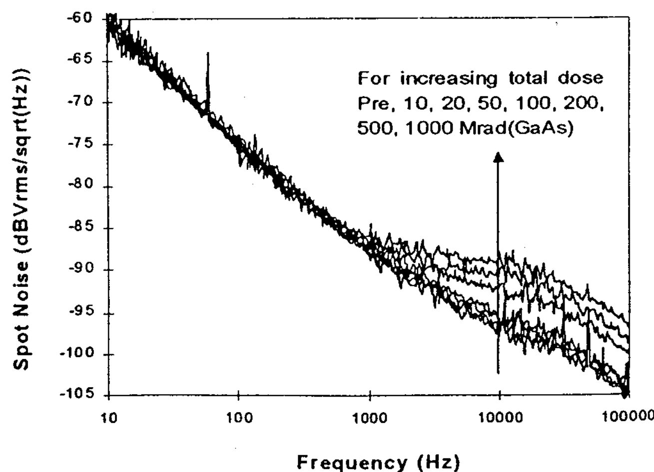

Fig. 5.24. 1x600 μm GaAs MESFET spot noise for various total dose, post-irradiation at test set output. (After Hiemstra et al. [46]).

Another issue is the dose rate effect *during* the exposure, illustrated by Fig. 5.25. It is seen there that the LF noise degrades severely for increasing dose rate [46]. The phenomenon saturates for a dose rate in the range 150 krad/hour (Fig. 5.26a), which is ascribed to the fact that the range of stimulated traps (selected time constants) is narrowed down, while at low dose rates, a broad range of time constants (energy levels) is excited. In addition, the concentration of traps is finite, leading to the observed saturation at high dose rates. However, the effect of the dose rate reduces for higher accumulated doses (Fig. 5.26b) [7]. At the same time, noise spikes at low frequencies (range 10 - 100 Hz) have been reported [7], which correspond to the irradiation induced stimulation of the deep level traps (this could be substitutional oxygen donors on an As site, having a similar energy level as EL2, which may 'anneal' under irradiation, and are known to anneal at rather low temperatures [7]). These LF noise peaks increase for increasing dose rates and are believed to be due to a sidegating effect, whereby the deep level traps are excited by the exposure over the whole substrate. Sidegating is the effect where the substrate next to the MESFET can affect its performance, while back- or selfgating is related to the substrate below the channel. No saturation of this detrimental sidegating effect, causing noise peaks, has been noted.

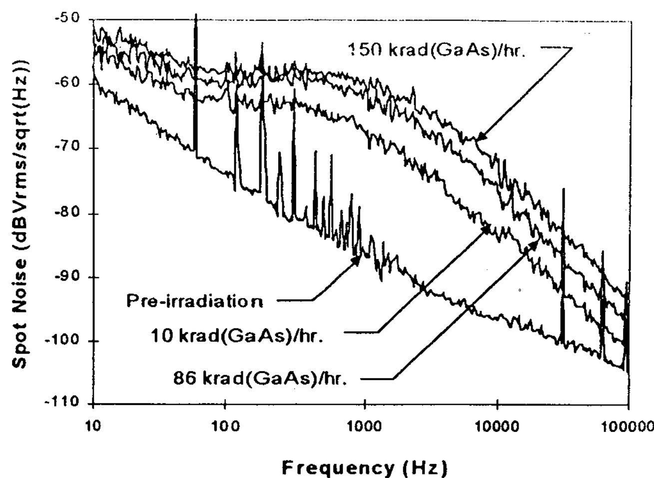

Fig. 5.25. 1x300 μm GaAs MESFET spot noise for various dose rates at the onset of irradiation at test set output. (After Hiemstra et al. [46]).

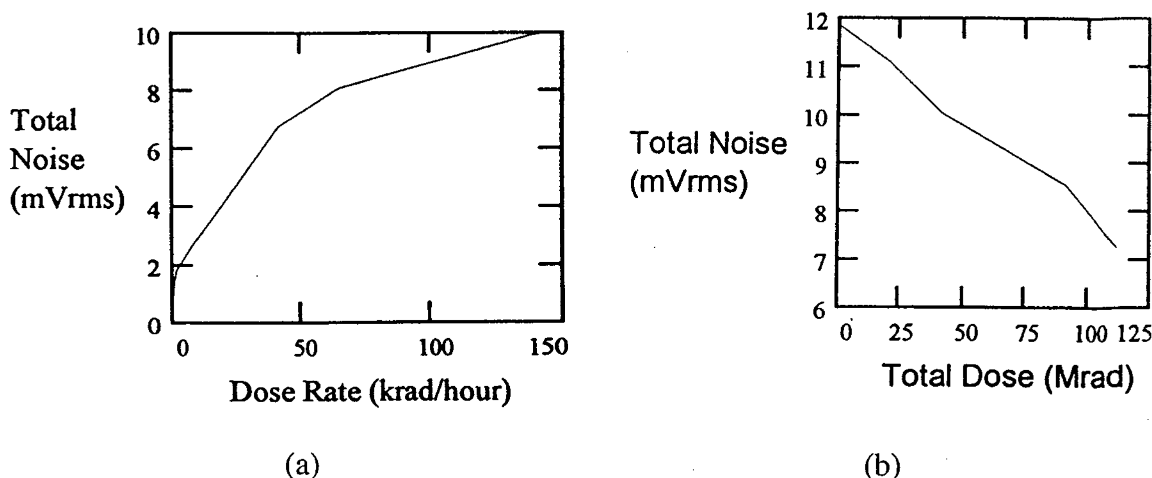

Fig. 5.26. (a) Dose rate dependent total noise and (b) total noise during irradiation versus total dose. (After Hiemstra [7]).

In order to improve the dose rate dependent 1/f noise, a few measures can be taken. A better performance could be achieved by the implementation of an epitaxially grown buffer layer between the substrate and the implanted active area. An alternative approach involves controlling the state of the semi-insulating substrate by applying a substrate contacted process, which provides a die backside metallization pattern below the device channels. Application of an appropriate bias eliminates backgating [7].

The impact of cryogenic irradiations in the range 100 K and higher has been studied by Shaw et al. [47]. The a_N and b_μ damage factors have been studied as a function of temperature, for 3 MeV protons. The results are represented in Fig. 5.27a and 5.27b,

showing that the carrier removal rate is a factor 2.5 larger for 100 K irradiations, compared with RT. The same applies for the mobility degradation (Fig. 5.27b). Thermal annealing experiments revealed a clear annealing stage at 270 K, while no apparent recovery for $T_{anneal} < 225$ K was found (Fig. 5.28) [47]. However, this annealing was only found for the carrier density N and not for the mobility. Comparing the annealing behaviour of resistors and MESFETs it is shown that the recovery of a resistor above 225 K is approximately half of the FET's, which can be explained by the different annealing behaviour of μ and N. The observed annealing stage is in agreement with earlier published work [48-49] related to the observation of deep level traps and carrier removal, measured by DLTS and C-V, respectively. Two acceptor levels at E_V+0.25 eV (H1?) and E_V+0.42 eV have been observed after 120 K 1 MeV proton irradiation of n-type GaAs, showing an annealing stage at ≈280 K. It is suggested that the corresponding defects are related to Ga displacements, possibly a deep state of V_{Ga}, or a mixed divacancy (see Fig. 5.2). They are thus shown to be responsible for carrier removal for low temperature irradiations. Additional charged centers should mainly cause the mobility degradation. Other annealing stages of radiation induced defects have been reported at 180 K, 235 K, 280 K and 520 K [47-49].

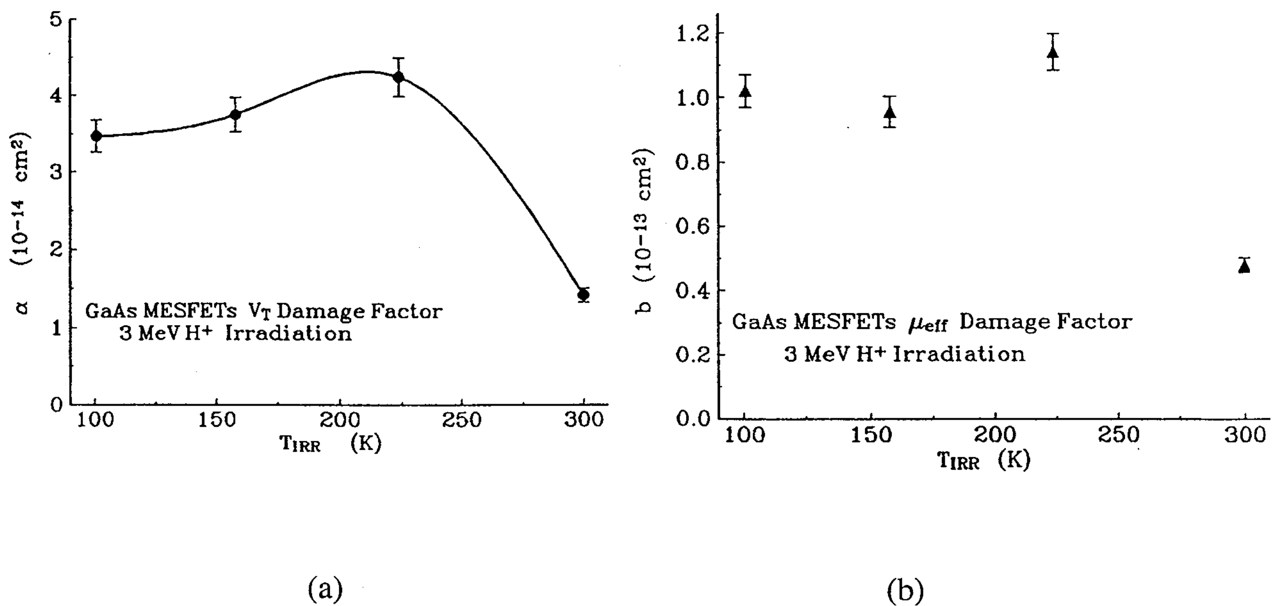

(a) (b)

Fig. 5. 27. (a) V_T damage factor versus irradiation temperature T_{IRR} and (b) corresponding μ_{eff} damage factor. There is no strong T_{IRR} dependence for temperatures below T_{IRR} ~ 224 K. (After Shaw et al. [47]).

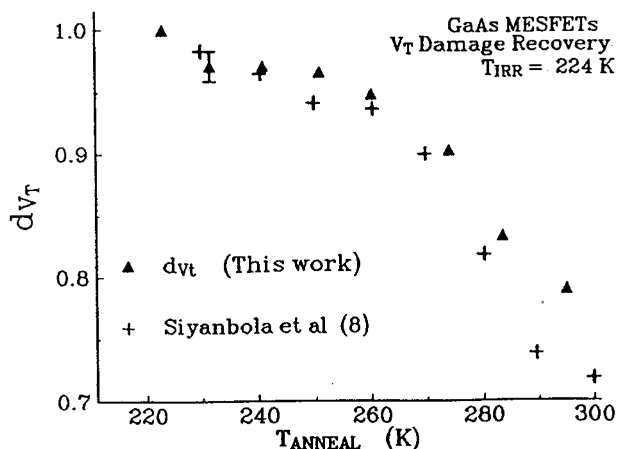

Fig. 5.28. Recovery of the differential change in threshold voltage versus isochronal annealing temperature, plotted with the annealing data of Siyanbola et al. [49]. The results are qualitatively similar. (After Shaw et al. [47]).

By studying the transient phenomena in the gate capacitance or the drain current, it is possible to perform a kind of deep-level spectroscopy on an irradiated MESFET [20],[50]. This should enable the identification of the trap levels in the channel region responsible for the device degradation. Beside DLTS like techniques, it has been demonstrated that the study of the frequency dispersion of the transconductance g_m or of the channel conductance g_D provides an alternative way to study radiation-induced deep levels. The advantage is that the study can be performed at one temperature (e.g. RT), whereby the frequency of the small-amplitude excitation signal applied for example to the gate is varied in a broad range. This allows to identify the presence of the U band at E_C-0.5 eV and EL14 at E_C-0.2 eV after 6 MeV (average energy) neutron exposure [50]. The presence of EL2 (E_C-0.79 eV) was also detected before and after irradiation, showing no change. Furthermore, also the gate to source current may be an important monitor for radiation damage in a MESFET [50]. In general, a reduction of the gate current was observed in both polarities. This indicates that no deep generation centers were created in the depletion region. The behavior suggests a compensation of the donor levels in the channel by radiation induced acceptors, giving rise to a reduction of the tunneling current in reverse bias.

Several studies have considered the effect of displacement damage (carrier removal and mobility degradation) on MESFET based circuits [23,39-43,51]. One of the basic building blocks for digital circuits is a ring-oscillator consisting of a number of inverters. Studies of neutron irradiated inverters show that the noise margins and gain increase after exposure (Fig. 5.29). Especially the high noise margin improves dramatically (Fig. 5.30). The characteristic becomes also more centered (symmetrical) which explains in first instance the improvement of the invertor performance. This also suggests an easy way for

radiation hardening of digital MESFET circuits, whereby the initial inverter should have its switching point to the right of the optimum center point.

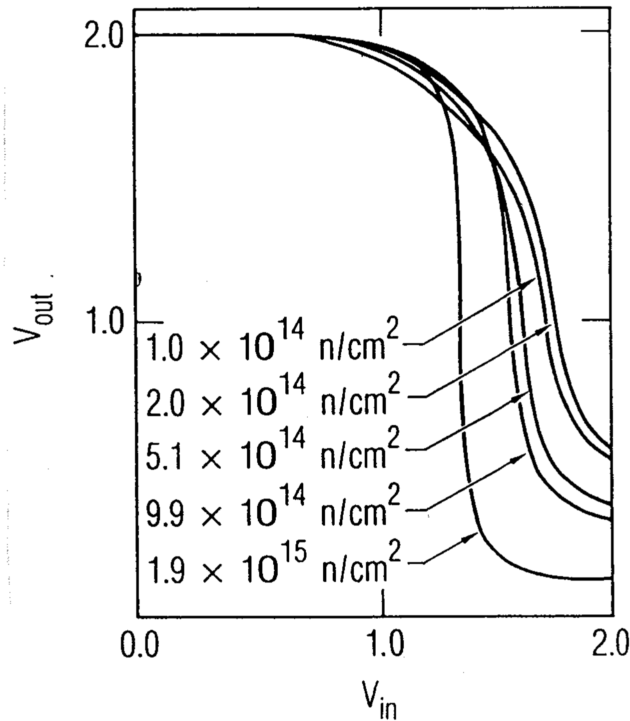

Fig. 5.29. Measured SDFL inverter characteristics as a function of neutron fluence. (After Bloss et al. [23]).

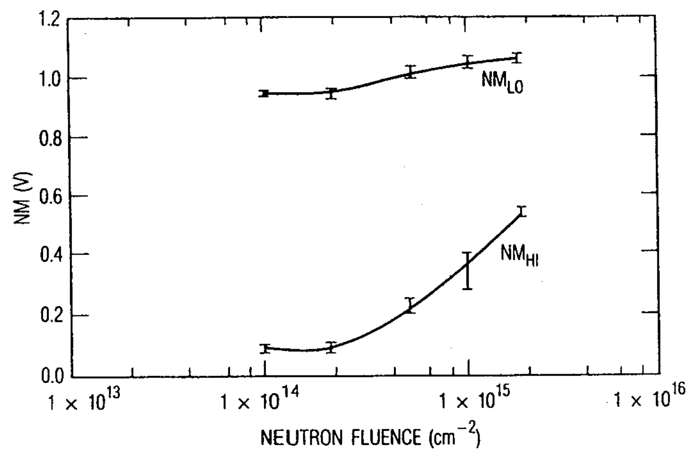

Fig. 5.30. High and low noise margins of SDFL inverters as a function of neutron fluence determined from measured data. Note the increase of the noise margins for higher neutron fluences. (After Bloss et al. [23]).

The fact that the threshold voltage of the FETs becomes more positive causes the observed changes in Fig. 5.29. In addition, the output conductance (in saturation) of the individual FETs improves (becomes larger), giving rise to a flatter I_D-V_{DS} curve [46] and steeper inverter characteristics. In other words, the short-channel effect improves upon irradiation. This is related to the fact that the SI substrate becomes more compensated upon irradiation - thus more resistive. This reduces substrate currents and carrier injection, back- and sidegating coupling and kink effects, giving rise to the higher R_{out}.

It is concluded that although the threshold voltage and the transconductance of individual devices is severely degraded after exposure to $\approx 2\times10^{15}$ cm^{-2} neutrons, the logic circuits will still be functional, under extreme radiation conditions [23]. However, the speed of operation will degrade significantly, as seen from the drastic increase of the ring oscillator gate delay in Fig. 5.31a. A slight improvement is seen upon illuminating the circuit; this is because of the ionization of deep radiation-induced traps by the incident photons. The observed speed degradation follows exactly the observed degradation of the FET transconductance with fluence (Fig. 5.31b) [23].

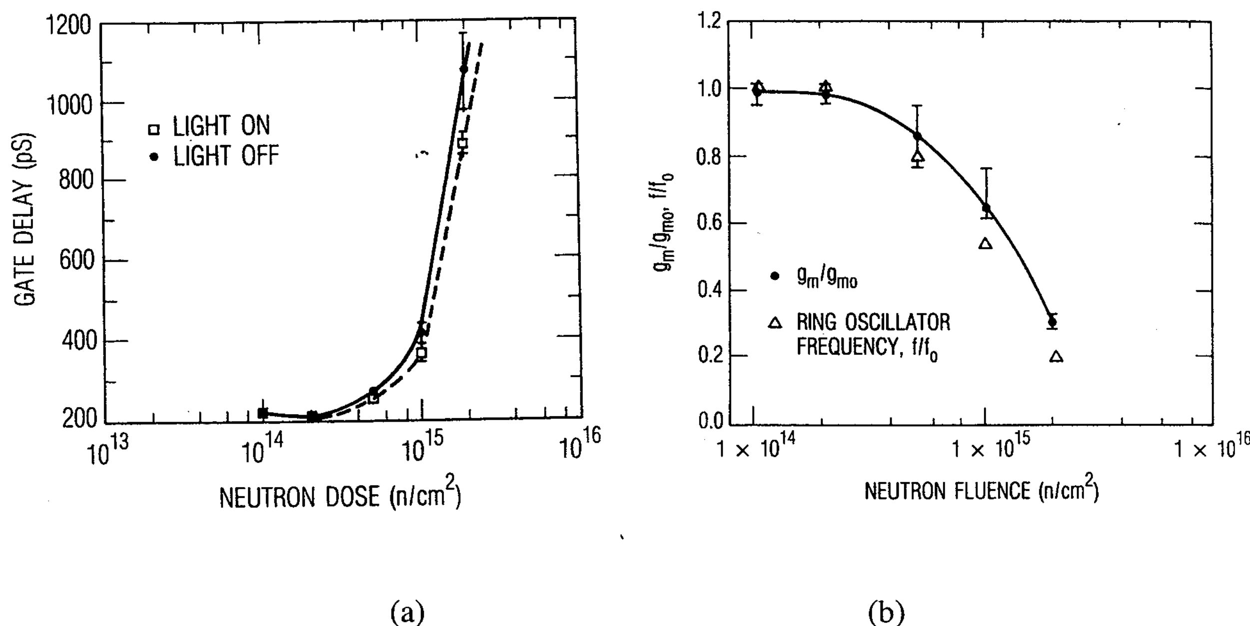

(a) (b)

Fig. 5.31. (a) Measured gate propagation delays of 13-stage ring oscillator as a function of neutron fluence and (b) measured fractional transconductance degradation of GaAs FET and frequency degradation of a 13-stage ring oscillator as a function of neutron fluence. (After Bloss et al. [23]).

The high frequency performance of irradiated MMIC circuits (amplifiers) has been reported for example by Meulenberg et al. [41]. In that work, a broad-band distributed

amplifier, using an ion-implanted technology was compared with a K_a band power amplifier on epitaxial material. Fig. 5.32a and 5.32b shows the gain degradation in the GHz range for both amplifiers, after 10^8 rad(Si) 1-MeV electron irradiation. The gain reduction is more pronounced at the high frequency end, while being negligible for the lower frequencies.

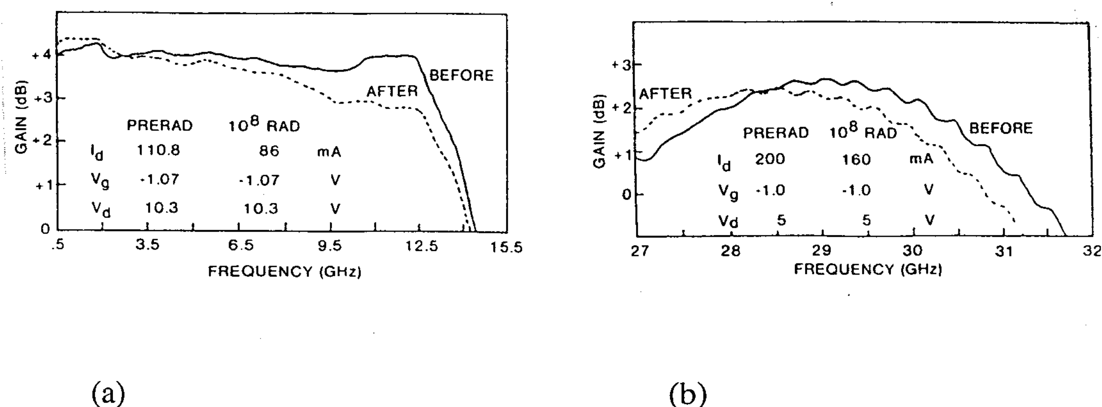

(a) (b)

Fig. 5.32. (a) Performance of MMIC distributed amplifier before and after 1-MeV electron irradiation (10^8 rad(Si)), biased for pre-irradiation gain flatness. (b) Performance of K_a-band MMIC amplifier. (After Meulenberg et al. [41]).

It has also been observed that the transient response upon a high dose rate electron (or γ-pulse) is quite different for the two circuits [41]. The implanted amplifiers show a faster, higher-amplitude peak after 10^8 rad(Si) 1-MeV electrons, while the opposite is true for the epitaxial circuit. It is concluded from this that a number of factors contribute to these phototransients, related to design aspects (distributed finger gate), the operation mode (applied voltage), the passive circuit components and to the material/technology. The origin of the transients is the substrate, whereby the buffer layer in the epitaxial material plays the major role. It is even suggested that pre-exposure to a slight dose can be used as a hardening technique against the transient effect for epitaxial technologies [41]. This results in a more resistive (compensated) p-type buffer layer. The same could in principle be obtained by lightly p-type doping the buffer layer. Other suggestions have been the implementation of an extra AlGaAs layer at the back of the structure [20,27], or using a thinner substrate.

The temperature dependence of these transient effects has been studied by Anderson [51], showing that for neutron irradiated MMIC circuits, the induced damage levels provoke long time transients at low temperature operation. A final ionization related circuit effect is the occurrence of single event upsets for which the Reader is referred to the Review by Zuleeg [39].

5.3.2 HEMTs

The basic radiation damage mechanisms in GaAs/AlGaAs HEMTs have been studied by a number of groups [20,25,28,52-55]. The analysis of the basic displacement damage effect on the threshold voltage is based on Eqs (5.7)-(5.10). Starting from there, the radiation induced change can be modeled by [28]:

$$\Delta V_T = \Delta V'_{Ga}\,\Phi\,[1 - V_{A1}\,(a_N N/N_A^2)/\Delta V'_{Ga}] \qquad (5.25)$$

with a_N the carrier removal rate in the AlGaAs, $V_{A1} = -q\,N\,d_n^2/2\varepsilon$ the threshold shift due to the AlGaAs layer and $\Delta V'_{Ga}$ depends on the GaAs material parameters as described in Ref. 28. Equation (5.25) predicts a linear change of the threshold voltage with fluence, which is valid in the low fluence range. A slightly modified theory has been developed in [20,54], whereby only the net acceptor concentration in the GaAs buffer layer is considered. From Fig. 5.33 follows that the degradation of the threshold voltage of a HEMT is a complex function, composed of different contributions. Figure 5.34 shows the different terms, whereby it is clear that the carrier removal in the AlGaAs layer only contributes for 2.5 % in the whole fluence range. The major impact comes from the change in the Fermi level and the change in the field at the interface due to the redistribution of the charge in the GaAs buffer [28].

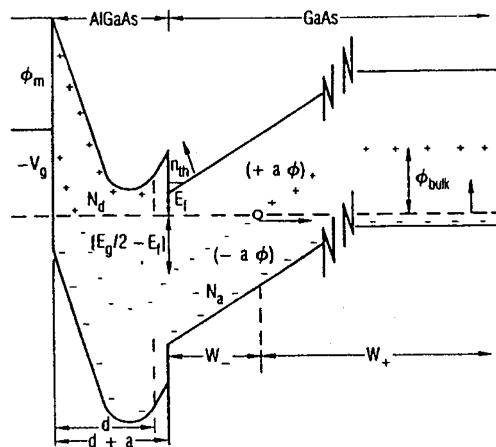

Fig. 5.33. Post-irradiation band diagram of a typical MODFET structure. W_- is the extent of the depletion region in the GaAs in which the traps are below the Fermi level. W_+ is the extent of the region in which the traps lie above the Fermi level. (After Krantz et al. [28]).

Typical degradation of the I-V characteristics for neutron irradiation is given in Figs 5.35 and 5.36 [54]. The degradation of the drain saturation current is given by a sublinear law [54]:

$$I_{DSS} = I_{DSSo}\,(1-\beta_I \Phi^{\delta}) \tag{5.26}$$

where δ=0.425, for neutron irradiations, this in contrast to the case of He ion irradiation which produces a linear reduction [20]. Such a non-linear law is thought to be caused by a change in conduction mechanism for increasing neutron fluence, whereby the original 2-DEG quantum well transport is overtaken by conduction in the AlGaAs doping layer. This is related to the carrier removal within the 2-DEG upon irradiation.

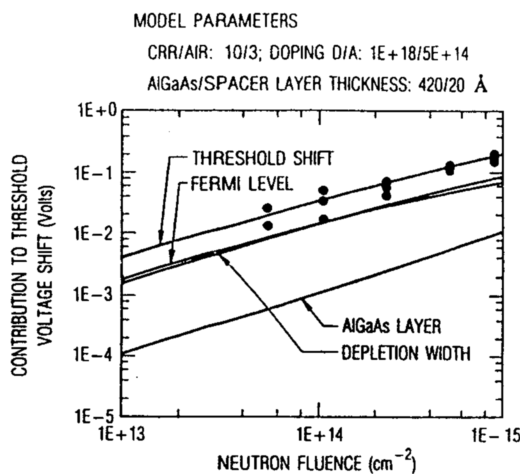

Fig. 5.34. Contributions of the threshold voltage shift versus neutron fluence. For the modeling, a carrier removal rate of 10 cm^{-1} is assumed in the AlGaAs, while a GaAs acceptor introduction rate of 3 cm^{-1} is considered. (After krantz et al. [28]).

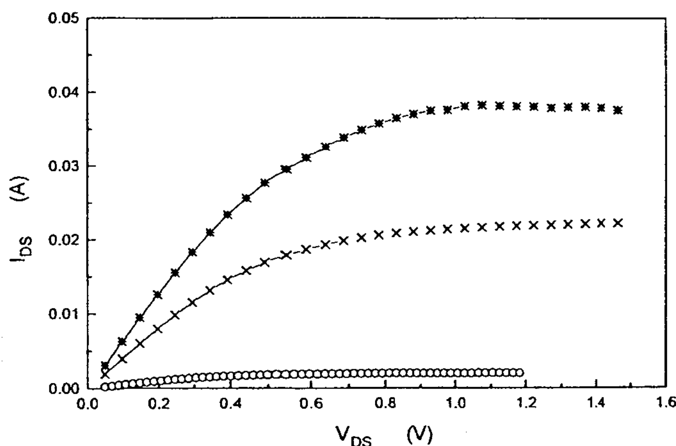

Fig. 5.35. Dependence of I_{DS}-V_{DS} (V_{GS}=0 V) characteristics on the radiation fluence. (*) before irradiation; (x) after a fluence of 10^{15} n/cm^2 and (o) after a fluence of 1.7×10^{16} n/cm^2. (After Papastamatiou et al. [54]).

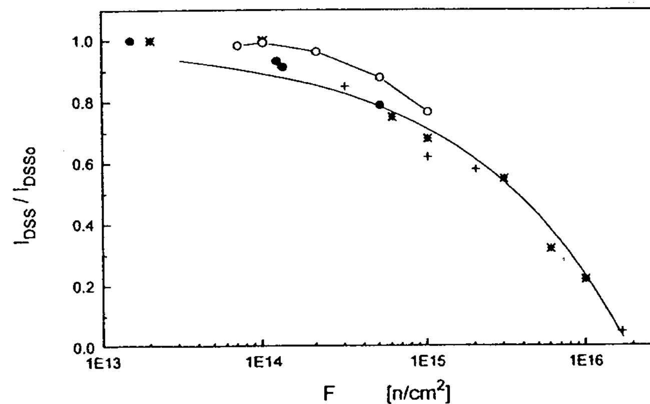

Fig. 5.36. Dependence of the HEMT drain saturation current versus radiation fluence for (*) structure A. (+) structure B with a backside AlGaAs layer and (o) data from [56], and (o) transconductance degradation from [57]. (After Papastamatiou et al. [54]).

The reduction of the 2-DEG concentration is represented in Fig. 5.37. It is found to decrease linearly with fluence (Fig. 5.38), giving rise to a damage constant of $6x10^{-17}$ cm^{-2} [54] (neutrons) or $2.5x10^{-13}$ cm^2 (He ions) [20]. Furthermore, using C-V measurements on large area (long) HEMTs enables to determine the carrier profile in the AlGaAs/GaAs heterojunction [20], yielding the result of Fig. 5.39. The heavy ion irradiation used there clearly reduces the carrier concentration in the AlGaAs donor layer and in the 2-DEG. The carrier removal rate following from fitting the threshold voltage model to the experimental data gives rise to values in the range 100 cm^{-1} (n) to $2x10^5$ cm^{-1} (He ions) which is much larger than what is commonly assumed for III-V compounds (i.e. 10 cm^{-1} [28]). DLTS of high fluence irradiated structures revals the presence of a number of deep traps at 0.46 eV (DX), 0.59 eV and 0.62 eV from the conduction band, which are thought to be responsible for the carrier removal in the donor layer [54]. However, the dominant factor in the degradation of the 2-DEG is the change in the buffer layer doping density (charge redistribution) and the creation of interface traps at the AlGaAs/GaAs interface [20,28,54].

The behavior of the mobility is shown in Fig. 5.40. It is seen there that for low 2-DEG densities, the mobility increases due to screening of Coulombic interaction, followed by a peak. At higher carrier densities, part of the conduction takes place in the highly doped AlGaAs, which is characterized by a lower mobility [20,54]. The 2-DEG mobility degrades almost linearly with fluence, which is correlated with the creation of charged gallium vacancies (acceptors) in the GaAs layer [17].

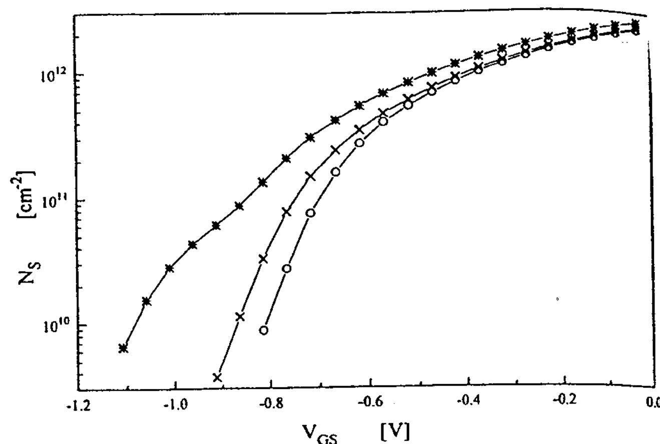

Fig. 5.37. Dependence of 2-DEG concentration on the gate bias (full squares) before irradiation and after a fluence (o) of $3x10^{15}$ n/cm^2 and (*) $6x10^{15}$ n/cm^2. (After Papastamatiou et al. [54]).

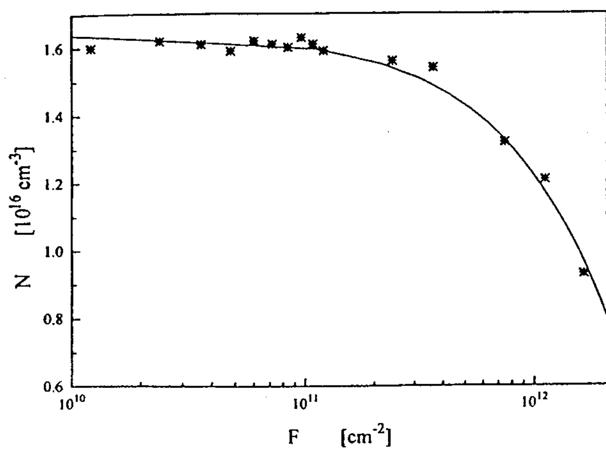

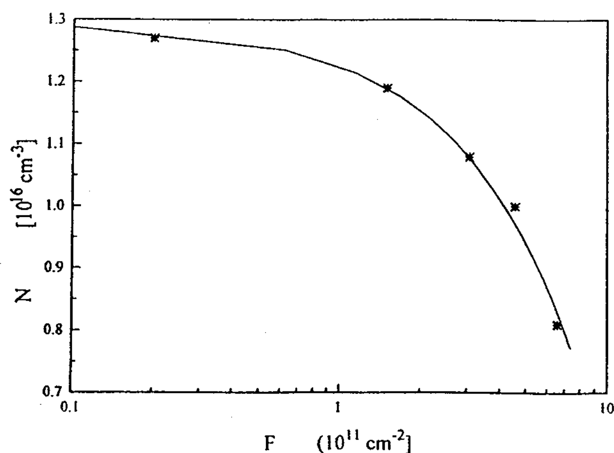

(a) (b)

Fig. 5.38. (a) Dependence of the 2-DEG carrier concentration on the radiation fluence. The continuous line corresponds to a linear fit. (b) Dependence of the AlGaAs donor layer carrier concentration on the radiation fluence. The continuous line corresponds to a linear fit. (After Papaioannou et al. [20]).

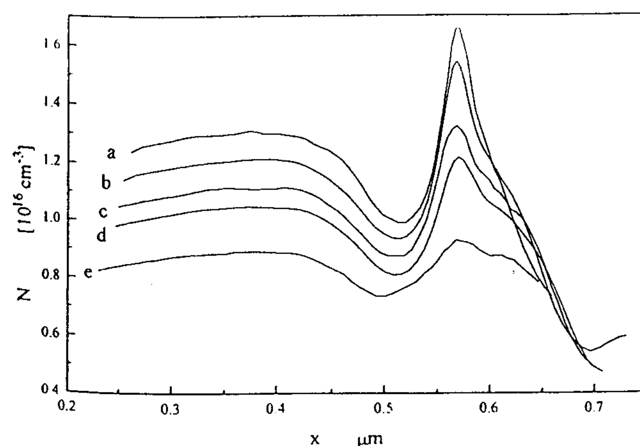

Fig. 5.39. Profile of an AlGaAs/GaAs heterojunction obtained from C-V characteristics (a) before irradiation, (b) after a fluence of 3.8×10^{11} cm^{-2}, (c) after a fluence of 7.6×10^{11} cm^{-2}; (d) a fluence of 1.1×10^{12} cm^{-2} and (e) after a fluence of 1.5×10^{12} cm^{-2}. (After Papaioannou et al. [20]).

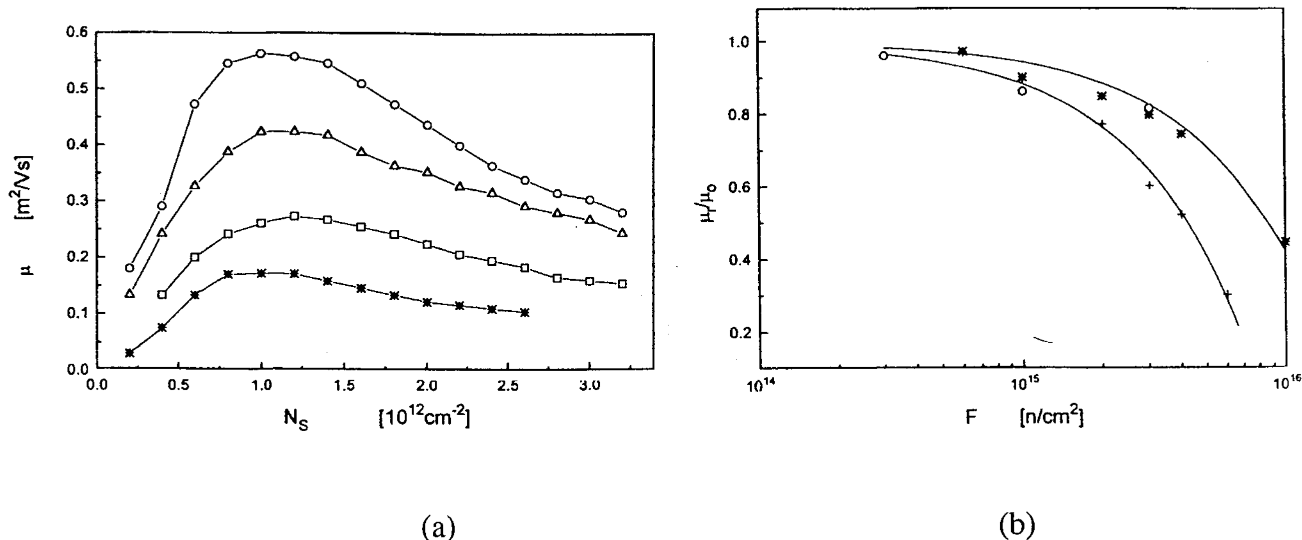

Fig. 5.40. Typical dependence of the mobility on the sheet carrier concentration: (o) before irradiation and after a fluence of (triangles) 6×10^{14} n/cm^2, (squares) 3×10^{15} n/cm^2 and (*) 6×10^{15} n/cm^2. (b) Dependence of the normalized mobilities to their pre-irradiation values, on the radiation fluence (*) standard structure, (+) structure with additional back side AlGaAs layer to reduce the photo-transients, and (o) of GaAs, whose data were obtained from Ref [38]. (After Papastamatiou et al. [54]).

Another cause for mobility degradation is the creation of charges and the increase in roughness at the AlGaAs/GaAs interface [20,54]. Evidence for the latter has been obtained in [25]: according to the analysis of the results of Fig. 5.41 a surface charge density at the n-GaAs/n-AlGaAs interface of ≈-10^{11} cm^{-2} is created after exposure to 40 Mrad γ's. The induced charges provoque a reduction of the electron mobility by Coulomb scattering. The mobility damage factor amounts to 0.59×10^{-13} cm^{-2} (n) [54] and 4.25×10^{-13} cm^{-2} (He ions) [20]. However, a strong impact of the device structure has been observed [20,54]. While the addition of a back AlGaAs interface layer doubles the mobility damage coefficient in the case of neutron exposure [54], a reduction of it is seen for HEMTs with a Low Temperature (LT) deposited AlGaAs donor and spacer layer. A better radiation hardness is thus obtained in the latter case (Fig. 5.42) [20]. It is thought that the presence of additional background bulk and interface defects introduced during the low temperature growth causes this improvement, requiring a larger radiation induced charge to compensate for it. The penalty is a lower initial device and material quality.

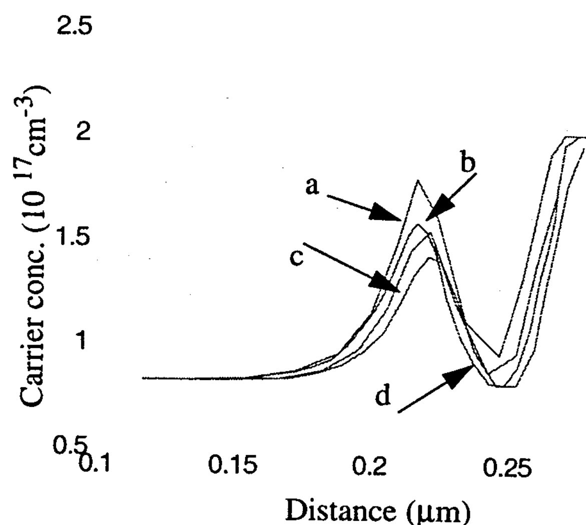

Fig. 5.41. Measured carrier concentration profiles of a GaAs/AlGaAs single heterojunction structure for different gamma ray irradiation doses: (a) unirradiated; (b) 1.0 Mrad (c) 10.0 Mrad; (d) 40 Mrad. (After Subramanian et al. [25]).

An additional diagnosis for radiation induced defects is the study of the drain current as a function of (low) temperature [20,53-54]. An example of the impact of neutron exposure is shown in Fig. 5.43. At large radiation fluences, a drastic reduction of the current is observed, corresponding to a change in conduction mechanism. For curve c in Fig. 5.43, the 2-DEG conduction has vanished and current is flowing through the donor layer. In other words, it behaves as an AlGaAs MESFET. From the I_{DS}-T characteristics information concerning the trapping mechanisms can be extracted, as indicated in Fig. 5.43. A thermally activated current is observed corresponding to two activation energies (0.05 and 0.18 eV). It is furthermore derived that the deeper level shows a donor nature [54].

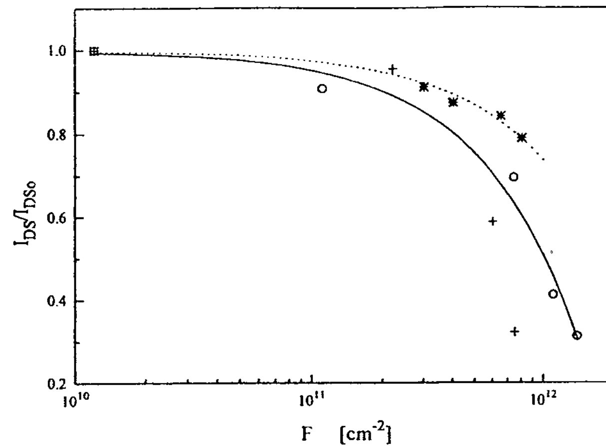

Fig. 5.42. Relative degradation of drain saturation current vs alpha particle fluence for (+) a D-mode HEMT; (b) a commercially available one, and (*) a HEMT with low-temperature donor and spacer layers. The continuous and dotted lines represent fitting curves to the linear degradation model. (After Papaioannou et al. [20]).

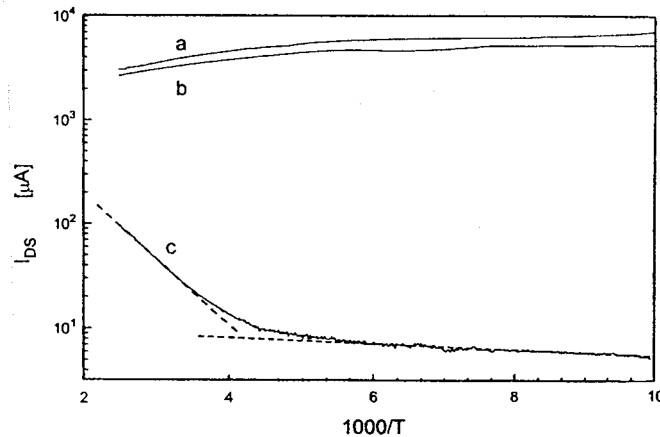

Fig. 5.43. Temperature dependence of the drain current of a conventional HEMT. All curves were obtained at V_{GS}=0 V and V_{DS} = 50 mV: (a) before irradiation; and after a fluence of (b) $3x10^{14}$ n/cm^2, and (c) $1.7x10^{17}$ n/cm^2. In (c), the dotted lines result from fitting of the experimental data to a thermally activated drain current with activation energies of 0.18 and 0.05 eV. (After Papastamatiou et al. [54]).

In addition to the channel properties, it has been observed that also the device parasitics are degraded upon irradiation [20,54]. This is particularly valid for the series resistance R_{SD}, which comes from the ungated source to gate and gate to drain regions plus the contact resistance. One can generally write for the total resistance:

$$R_T = R_{SD} + R_{chan} \tag{5.27}$$

with R_{chan} given by:

$$R_{chan} = \mu(N_S)\frac{qN_S Z}{L} \tag{5.28}$$

R_{SD} depends on the device geometry, doping levels and the fabrication process. Irradiation causes generally an increase of R_{SD} as shown in Fig. 5.44 for different HEMT structures, after He exposure [20]. The change is small for low fluences, but once a threshold surpassed, the increase is fast. For neutron exposure, a linear increase with fluence has been reported [54]. Such behavior can not simply be explained by carrier removal only and other mechanisms need to be considered: for example chemical reactions with Au metallization at the ungated surface could play a role [52].

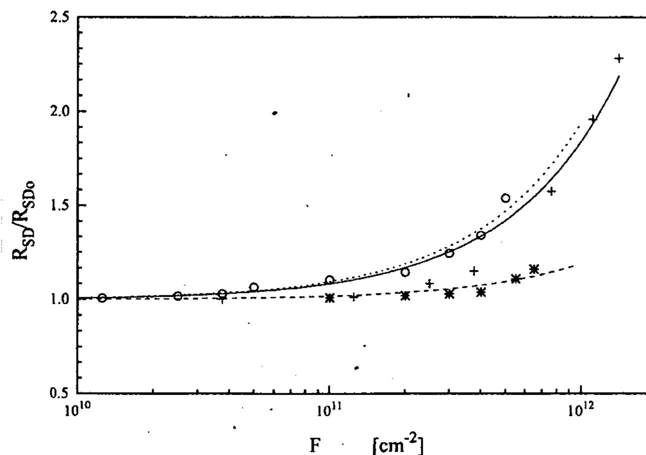

Fig. 5.44. Variation of the normalised series resistance to their values before irradiation vs He ion radiation fluence for (o) a standard structure, (+) a HEMT with a back AlGaAs layer and (*) a LT-HEMT. (After Papaioannou et al. [20]).

In order to explain the degradation of the threshold voltage a refined charge control model has been developed [20,53-54] with three fitting parameters: the thickness of the AlGaAs donor layer d_n, the donor layer pinch-off voltage V_P and the net acceptor layer

density N_A^* per unit of area in the GaAs buffer layer [20,53-54]. Based on the model, a good fit with the experimental data can be found, in function of the fluence. An example is given in Fig. 5.45 [54]. The resulting N_A^* versus neutron fluence is represented in Fig. 5.46, showing a reduction of the net acceptor concentration. It is a general observation that the slightly p-type GaAs buffer layer becomes more intrinsic after irradiation. Based on the linear relationship between ΔN_A^*, one can define a corresponding damage factor β_μ which equals $4.2x10^{-7}$ for conventional HEMT structures and about $1.4x10^{-6}$ for HEMTs with an additional buffer layer and this for neutron exposures [54].

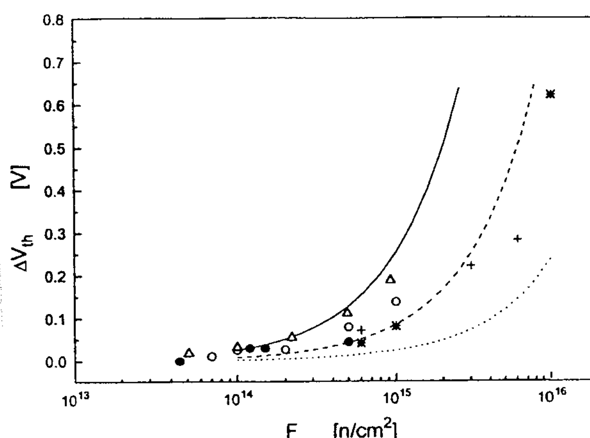

Fig. 5.45. Variation of threshold voltage with the radiation fluence for devices which data were obtained from literature and devices with a conventional structure (*) and (+) and additional AlGaAs buffer layer. The theoretical curves were obtained using a carrier removal rate (dotted) of 30 cm^{-1}, (dashed) 100 cm^{-1} and (continuous) 300 cm^{-1}. (After Papastamatiou et al. [54]).

It has been demonstrated that also γ-irradiation causes displacement damage in HEMTs [25,53]. Additionally, surface passivation of the ungated regions with SiO_2 for example can play a definite role in increasing the radiation tolerance for total dose γ's [25]. This is illustrated in Fig. 5.47 for a GaAs/AlGaAs modulation doped structure without (a) and with (b) passivation. The degradation is mainly found for the electron mobility. In the same work [25], it has been found that the GaAs/AlGaAs interfaces are quite stable and robust against radiation damage. GaAs/InGaAs/GaAs quantum well structures show some impact of the irradiation on the symmetry of the carrier profiles (Fig. 5.48). This is interpreted as being due to a slight rearrangement by In diffusion in the well during irradiation. The peak charge density, however, remains approximately constant, suggesting a negligible increase of the interface charge density, which is already high at the beginning.

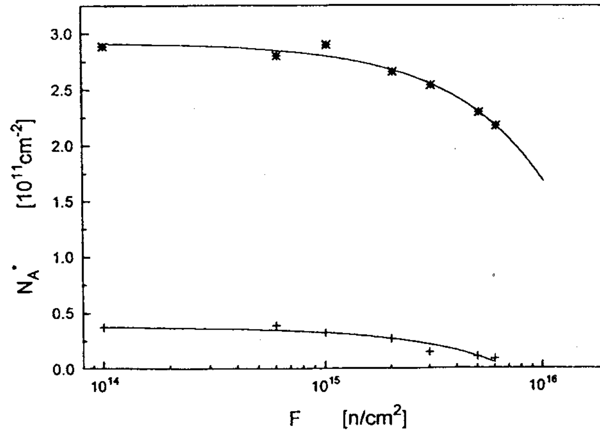

Fig. 5.46. Buffer layer, equivalent net acceptor concentration N_A^* per unit area versus radiation fluence (*) conventional HEMT and (+) HEMT with an additional AlGaAs buffer layer. (After Papastamatiou et al. [54]).

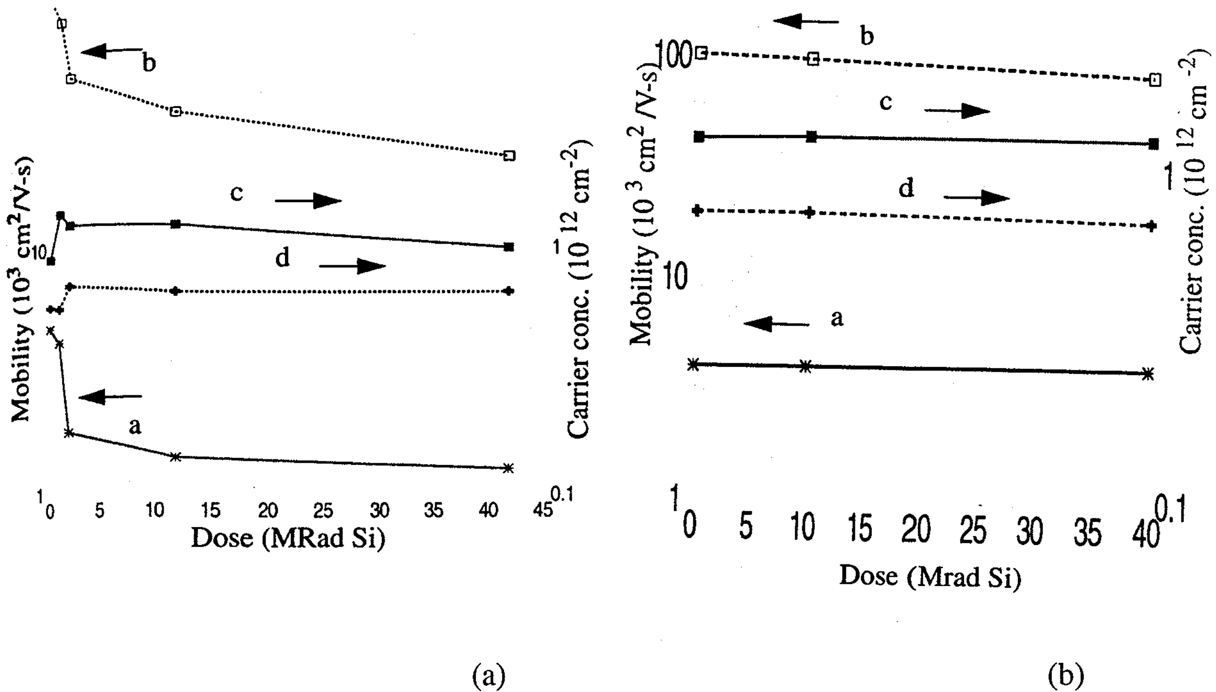

Fig.5. 47. Gamma irradiation dose dependence of Hall mobility at 300 K (a) and 77 K (b) and carrier concentration at 300 K (c) and 77 K (d) of a GaAs/AlGaAs modulation doped heterostructure sample without SiO_2 passivation (A) and with SiO_2 passivation (B). (After Subramanian et al. [25]).

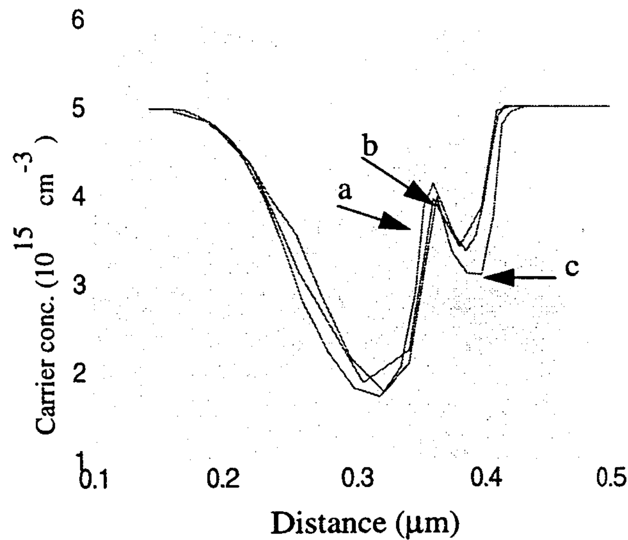

Fig. 5.48. Measured carrier concentration profiles of GaAs/InGaAs/GaAs quantum well structure for different gamma irradiation doses: (a) unirradiated; (b) 10 Mrad and (c) 40 Mrad. (After Subramanian et al. [25]).

The impact on HEMT based circuits and MMICs has been the subject of a few studies [57-58]. Inverters still work properly after a neutron fluence of 10^{15} n/cm^2, as can be judged from the result of Fig. 5.49 [57]. The inverter characteristic becomes slightly more steep, while the noise margins drop by about 200 mV for 10^{15} n/cm^2. Figure 5.50 shows the degradation of the propagation delay with neutron fluence, which is more pronounced for 77 K operation. The reason for this larger sensitivity at cryogenic temperatures is the higher mobility and the relatively larger degradation upon exposure [57].

A general observation is also that HEMT devices and circuits are generally more radiation tolerant than MESFETs (see e.g. [58]).

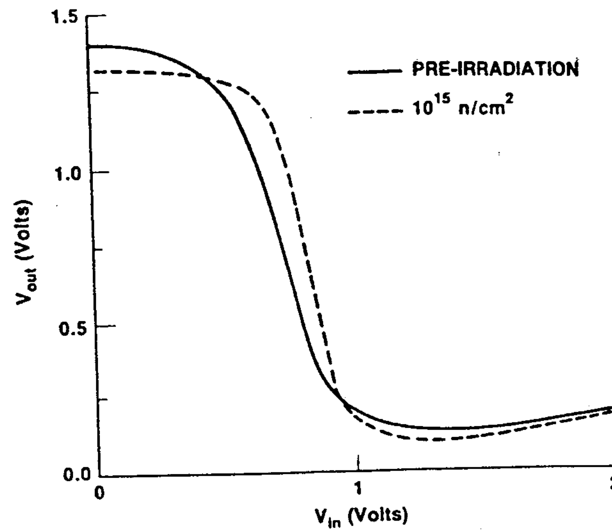

Fig. 5.49. SFFL inverter characteristics comparing pre-irradiation curve to curve following 10^{15} n/cm^2. (After Janousek et al. [57]).

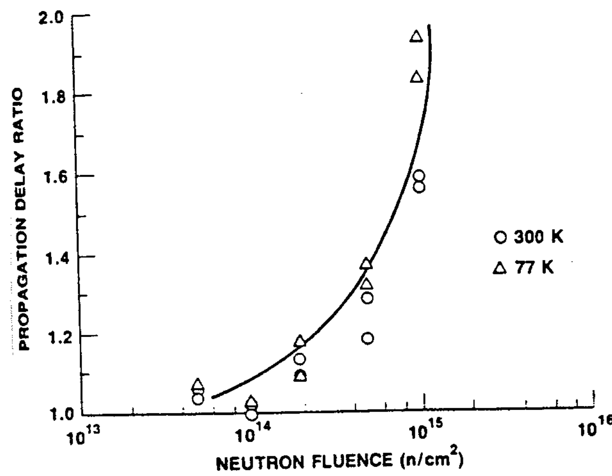

Fig. 5.50. Propagation delay degradation (normalised to the pre-radiated propagation delay) of the HEMT ring oscillator circuits as a function of neutron fluence at 300 K and 77 K. (After Janousek et al. [57]).

5.4 Conclusions

GaAs and related compounds surely have a hardness advantage of several decades compared with Si electronics and are, therefore, the technologies of choice for heavy radiation environments. In addition, a proper choice of substrate, technology and device structure further boost the radiation performance of GaAs MMICs. Less is known for more recent InP based technologies, which thus requires some testing. On the other hand, the fundamental understanding of for example the displacement damage is reasonably well developed and some of the critical radiation defects have been positively identified. Furthermore, the NIEL concept describes quite accurately the damage coefficients with particle energy for not too large energies. However, for larger energies allowing inelastic nuclear interactions, a discrepancy exists between the calculated NIEL and the variation of the observed device performance degradation. This is certainly a point which requires further investigation.

References

[1] W.T. Anderson and S.C. Binari, "Radiation effects in GaAs devices and ICs", IEEE Int. Reliability Proc., pp. 316-319 (1983).

[2] J.C. Bourgoin, H.J. von Bardeleben and D. Stiévenard, "Native defects in gallium arsenide", J. Appl. Phys. **64**, R65 (1988).

[3] G. Guillot, "EL2-related studies in irradiated and implanted GaAs", Revue Phys. Appl. **23**, 833 (1988).

[4] S. Makram-Ebeid and P. Boher, "Defect pairs and clusters related to the EL2 centre in GaAs", Revue Phys. Appl. **23**, 847 (1988).

[5] J.C. Bourgoin and M. Lannoo, "A critical look at EL2 models", Revue Phys. Appl. **23**, 863 (1988).

[6] P.N. Brunkov, V.S. Kalinovsky, V.G. Nikitin and M.M. Sobolev, "Generation of the EL2 defect in n-GaAs irradiated by high energy protons", Semicond. Sci. Technol. **7**, 1237 (1992).

[7] D.M. Hiemstra, "Dose rate total dose dependence of the 1/f noise performance of a GaAs operational amplifier during irradiation", IEEE Trans. Nucl. Sci. **42**, 1615 (1995).

[8] A. Jorio, C. Rejeb, M. Parenteau, C. Carlone and S.M. Khanna, "Radiation induced carrier enhancement and intrinsic defect transformation in n-GaAs", J. Appl. Phys. **74,** 2310 (1993).

[9] S.M. Khanna, C. Rejeb, A. Jorio, M. Parenteau and C. Carlone, "Electron and neutron radiation-induced defects in gallium arsenide", IEEE Trans. Nucl. Sci. **40**, 1350 (1993).

[10] H.H. Tan, J.S. Williams and C. Jagadish, "Characterization of deep levels and carrier compensation created by proton irradiation in undoped GaAs", J. Appl. Phys. **78**, 1481 (1995).

[11] A. Jorio, C. Carlone, M. Parenteau, C. Aktik and N.L. Rowell, "Formation of EL2, As_{Ga} and U band in irradiated GaAs: effects of annealing", J. Appl. Phys. **80**, 1364 (1996).

[12] H. Gorankin, M. Birritella, W. Seelbach and R. Vaitkus, "Backgating and light sensitivity in ion implanted GaAs integrated circuits", IEEE Trans. Electron Devices **29**, 845 (1982).

[13] S. Subramanian, P. Bhattacharyaj, K. Staker, C. Church and M. Badawi, "Geometrical and light-induced effects on backgating in ion implanted GaAs MESFETs", IEEE Trans. Electron Devices **32**, 28 (1985).

[14] T. Carruthers, W. Anderson and J. Weller, "Optically induced backgating transients in GaAs FETs", IEEE Electron Device Lett. **6**, 580 (1985).

[15] K.M. Luken and R.A. Morrow, "Formation energies and charge states of native defects in GaAs: a selected compilation from the literature", Semicond. Sci. Technol. **11**, 1156 (1996).

[16] D.C. Look and J.R. Sizelove, "Defect production in electron-irradiated, n-type GaAs", J. Appl. Phys. **62**, 3660 (1987).

[17] S.M. Khanna, A. Jorio, C. Carlone, M. Parenteau, A. Houdayer and J.W. Gerdes, Jr., "Particle dependence of the gallium vacancy production in irradiated n-type gallium arsenide", IEEE Trans. Nucl. Sci. **42**, 2095 (1995).

[18] A. Jorio, A. Wang, M. Parenteau, C. Carlone, N.L. Rowell and S.M. Khanna, "Optical identification of the gallium vacancy in neutron irradiated gallium arsenide", Phys. Rev. B **50**, 1557 (1994).

[19] P.M. Mooney, "Deep donor levels (DX centers) in III-V semiconductors", J. Appl. Phys. **67**, R1 (1990).

[20] G.J. Papaioannou, M.J. Papastamatiou and A. Christou, "He ion radiation effects in high electron mobility transistors", J. Appl. Phys. **78**, 3066 (1995).

[21] M. Nishiguchi, T. Hashinaga, H. Nishizawa, H. Hayashi, N. Okazaki, M. Kitagawa and T. Fujino, "Radiation tolerant GaAs MESFET with a highly-doped thin active layer grown by OMVPE", IEEE Trans. Nucl. Sci. **37**, 2071 (1990).

[22] B. Janousek, W.E. Yamada, R.J. Krantz and W.L. Bloss, "Neutron radiation effects in GaAs ion-implanted metal-semiconductor field-effect transistors", J. Appl. Phys. **63**, 1678 (1988).

[23] W.L. Bloss, W.E. Yamada, A.M. Young and B.K. Janousek, "Characteristics of GaAs MESFET inverters exposed to high energy neutrons", IEEE Trans. Nucl Sci. **35**, 1074 (1988).

[24] C. Su, H. Rohdin and C. Stolte, "1/f noise in GaAs MESFETs", IEDM Tech. Dig., pp. 601-604 (1983).

[25] S. Subramanian, A. Sarkar, L. Ungier and S.M. Goodnick, "Integrity of III-V heterojunction interfaces under gamma irradiation", IEEE Trans. Nucl. Sci. **44**, 1862 (1997).

[26] H. Ohyama, E. Simoen, S. Kuroda, C. Claeys, Y. Takami, T. Hakata H. Sunaga, "Impact of high energy particles on InGaP/InGaAs pseudomorphic HEMTs", IEEE Trans. Nucl. Sci. **45**, 2861 (1998).

[27] W.T. Anderson, M. Simons, W.F. Tseng, J.A. Herb and S. Bandy, "Transient radiation effects in AlGaAs/GaAs MODFETs", IEEE Trans. Nucl. Sci. **34**, 1669 (1987).

[28] R.J. Krantz, W.L. Bloss and M.J. O'Loughlin, "High energy neutron irradiation effects in GaAs modulation-doped field effect transistors (MODFETs): Threshold voltage", IEEE Trans. Nucl. Sci. **35**, 1438 (1988).

[29] A.F. Behle and R. Zuleeg, "Fast neutron tolerance of GaAs JFETs operating in the hot electron regime", IEEE Trans. Electron Devices **19**, 993 (1972).

[30] A.R. Knudson, A.B. Campbell, W.J. Stapor, P. Shapiro, G.P. Mueller and R. Zuleeg, "Radiation damage effects of electrons and H, He, O, Cl and Cu ions on GaAs JFETs", IEEE Trans. Nucl. Sci. **32**, 4388 (1985).

[31] A.B. Campbell, A.R. Knudson, W.J. Stapor, G. Summers, M.A. Xapsos, M. Jessee, T. Palmer, R. Zuleeg and C.J. Dale, "Particle damage effects in GaAs test structures", IEEE Trans. Nucl. Sci. **33**, 1435 (1986).

[32] E.A. Burke, C.J. Dale, A.B. Campbell, G.P. Summers, T. Palmer and R. Zuleeg, "Energy dependence of proton-induced displacement damage in gallium arsenide", IEEE Trans. Nucl. Sci. **34**, 1220 (1987).

[33] G.P. Summers, E.A. Burke, M.A. Xapsos, C.J. Dale, P.W. Marshall and E.L. Petersen, "Displacement damage in GaAs structures", IEEE Trans. Nucl. Sci. **35**, 1221 (1988).

[34] L.W. Aukerman and R.D. Graft, "Annealing of electron-irradiated GaAs", Phys. Rev. **127**, 1576 (1962).

[35] M. Parenteau, C. Carlone and S.M. Khanna, "Damage coefficient associated with free exciton lifetime in GaAs irradiated with neutrons and electrons", J. Appl. Phys. **71**, 3747 (1992).
[36] H. Ghamlouch, M. Aubin, C. Carlone and S.M. Khanna, "Electron irradiation of GaAs: Improvement of transport properties and observation of DX-like centers at ambient temperature", J. Appl. Phys. **74**, 4357 (1993).
[37] S.M. Khanna, C. Rejeb, A. Jorio, M. Parenteau, C. Carlone and J. W. Gerdes, Jr., "Electron and neutron radiation-induced order effect in gallium arsenide", IEEE Trans. Nucl. Sci. **40**, 1350 (1993).
[38] A. Jorio, M. Parenteau, M. Aubin, C. Carlone, S.M. Khanna and J.W. Gerdes, Jr., "A mobility study of the radiation induced order effect in gallium arsenide", IEEE Trans. Nucl. Sci. **41**, 1937 (1994).
[39] R. Zuleeg, "Radiation effects in GaAs FET devices", Proc. IEEE **77**, 389 (1989).
[40] W.T. Anderson, M. Simons, A. Christou and J. Beall, "GaAs MMIC technology radiation effects", IEEE Trans. Nucl. Sci. **32**, 4040 (1985).
[41] A. Meulenberg, H.-L. A. Hung, K.E. Peterson and W.T. Anderson, "Total dose and transient radiation effects on GaAs MMICs", IEEE Trans. Nucl. Sci. **35**, 2125 (1988).
[42] H. Derewonko, A. Bosella, G. Pataut, D. Perié, J.L. Pinsard, C. Sentubery, C. Verbeck, P. Bressy and P. Augier, "Evaluation of GaAs low noise and power MMIC technologies to neutron, ionizing dose and dose rate effects", IEEE Trans. Nucl. Sci. **43**, 837 (1996).
[43] M.A. Listvan, P.J. Vold and D.K. Arch, "Ionizing radiation hardness of GaAs technologies", IEEE Trans. Nucl. Sci. **34**, 1664 (1987).
[44] J.Y. Chang, M.H. Badawi and A. DeCicco, "Neutron/gamma induced damage mechanisms and synergistic effects in GaAs MESFETs", IEEE Trans. Nucl. Sci. **36**, 2068 (1989).
[45] M. Citterio, S. Rescia and V. Radeka, "Radiation effects at cryogenic temperatures in Si-JFETs, GaAs MESFET, and MOSFET devices", IEEE Trans. Nucl. Sci. **42**, 2266 (1995).
[46] D.M. Hiemstra, A.A. Kizeevi, L.Z. Hou and C.A.T. Salama, "Dose rate and total dose dependence of low frequency noise performance, I-V curves and sidegating for GaAs MESFETs", IEEE Trans. Nucl. Sci. **45**, 2616 (1998).
[47] G.J. Shaw, M.A. Xapsos, B.D. Weaver and G.P. Summers, "Low temperature proton irradiation of GaAs MESFETs", IEEE Trans. Nucl. Sci. **40**, 1300 (1993).
[48] W.O. Siyanbola and D.W. Palmer, "Low temperature annealing of deep electron traps produced by proton irradiation of n-GaAs", Semicond. Sci. Technol. **5**, 7 (1990).
[49] W.O. Siyanbola and D.W. Palmer, "Electronic energy levels of defects that anneal in the 280-K stage in irradiated n-type gallium arsenide", Phys. Rev. Lett. **66**, 56 (1991).
[50] G. Meneghesso, A. Paccagnella, D.V. Camin, N. Fedyakin, P. Pessina and C. Canali, "Study of neutron damage in GaAs MESFETs", IEEE Trans. Nucl. Sci. **44**, 840 (1997).
[51] W.T. Anderson, J. Gerdes and J.A. Roussos, "Temperature dependent GaAs MMIC radiation effects", IEEE Trans. Nucl. Sci. **40**, 1735 (1993).
[52] M.J. O'Loughlin, "Radiation effects in high electron mobility transistors: Total dose gamma irradiation", IEEE Trans. Nucl. Sci. **34**, 1808 (1988).

[53] N. Arpatzanis, M. Papastamatiou, G.J. Papaioannou, Z. Hatzopoulos and G. Konstandinides, "The gamma ray radiation effects in high-electron-mobility transistors", Semicond. Sci. Technol. **10**, 1445 (1995).

[54] M. Papastamatiou, N. Arpatzanis, G.J. Papaioannou, C. Papastergiou and A. Christou, "Neutron radiation effects in high electron mobility transistors", IEEE Trans. Electron Devices **44**, 364 (1997).

[55] E. Dupont-Nivet and M. Pasquali, "Neutron effects on HEMT devices", Proc. RADECS '91, The IEEE (New York), pp. 189-193 (1992).

[56] J.F. Ziegler, J.P. Biersack and U. Littmark, The Stopping and Range of Ions in Solids, New York: Pergamon, p. 120 (1987).

[57] B.K. Janousek, R.J. Krantz, W.L. Bloss, W.E. Yamada, S. Brown, R.L. Remke and S. Witmer, "Characteristics of GaAs heterojunction FETs (HFETs) and source follower FET logic (SFFL) inverters exposed to high enery neutrons", IEEE Trans. Nucl. Sci. **36**, 2223 (1989).

[58] W.T. Anderson, A.R. Knudson, A. Meulenberg, H.L. Hung, J.A. Roussos and G. Kiriakidis, "Heavy ion total fluence effects in GaAs devices", IEEE Trans. Nucl. Sci. **37**, 2065 (1990).

6. OPTO-ELECTRONIC COMPONENTS FOR SPACE

Photonics systems are ideally suited for space applications for a number of reasons: there is the high bandwidth and speed of operation, the immunity for electromagnetic interference and high reliability, low power consumption and cost and above all, light weight. Given the direct band gap, yielding a high quantum efficiency and the superior radiation tolerance of GaAs and related compounds, III-V opto-electronic components are the technology of choice for applications in a broad wavelength range, going from 700 to 1600 nm, whereby operation at 1300 nm is particularly suitable for fiber optics, since it corresponds to maximum radiation hardness of the mono-mode fibers. In this chapter, the behavior of modern III-V opto-electronic components is described and problem areas defined. First, a description of the most promising device structures and their operation parameters is presented and this for Light Emitting Diodes (LED), Laser Diodes (LD), on the one hand, and Photodiodes or Photodetectors (PD), on the other. A brief discussion of optocouplers is also given. Next, the fundamental and material issues related to radiation degradation are pointed out, followed by a discussion of recent irradiation studies of LEDs, LDs, PDs and optocouplers. A summary and the identification of issues requiring further studies conclude the chapter.

6.1 Opto-Electronic Components

6.1.1 Light Emitting Diodes (LEDs) and Laser Diodes (LDs)

Early LEDs were based on amphoteric Si-doped or Zn-doped GaAs, active in the range 850-950 nm [1-3]. However, better radiation tolerance was observed for GaAsP based diodes, emitting in the 850 nm region [4]. Also good radiation resistance was observed for high radiance GaAlAs (820 nm) and InGaAsP (1300 nm) LEDs [3]. The improvement of epitaxial growth techniques allows to deposit nowadays complex layer structures, with sharp interfaces and steep concentration and composition gradients. Modern LEDs are therefore often based on Quantum Well (QW) structures in for example the InGaAs/GaAs/AlGaAs system, active around 875 nm, as represented in Fig. 6.1 [5].

Recently, interest has developed for the wavelength range around 1300 nm, which is the λ of choice for immunity to radiation induced attenuation of optical fibers [5]. In that case, InGaAsP is the preferred material for fabricating an LED.

The operation of an LED is characterized by the light output L versus the applied forward bias. L relies heavily on the forward current flowing through the device, which may have different dependencies on forward bias, as shown in Fig. 6.2. The light output is proportional to the radiative recombination current and degrades if the non-radiative recombination current increases. The latter occurs when deep-level generation-recombination (GR) centers are induced by displacement damage. L can be represented by [3-4]:

$$L = C_2 \tau \exp\left(\frac{qV_F}{kT}\right) \qquad (6.1)$$

with τ the carrier lifetime, composed of a radiative (τ_r) and a non-radiative (τ_{nr}) part, i.e.:

$$\tau^{-1} = \tau_r^{-1} + \tau_{nr}^{-1} \tag{6.2}$$

q is the electron charge, k Boltzmann's constant and T the absolute temperature. C_2 is a constant and V_F the applied forward bias. The forward current density J_F, on the other hand, obeys:

$$J_F = \frac{C_2}{\sqrt{\tau}} \exp(qV_F / kT) \tag{6.3}$$

or:

$$J_F = \frac{C_5}{\sqrt{\tau}} \exp(qV_F / 2kT) \tag{6.4}$$

Equation (6.3) applies if the current is diffusion dominated (n=1), while Eq. (6.4) goes for space charge recombination controlled current (n=2).

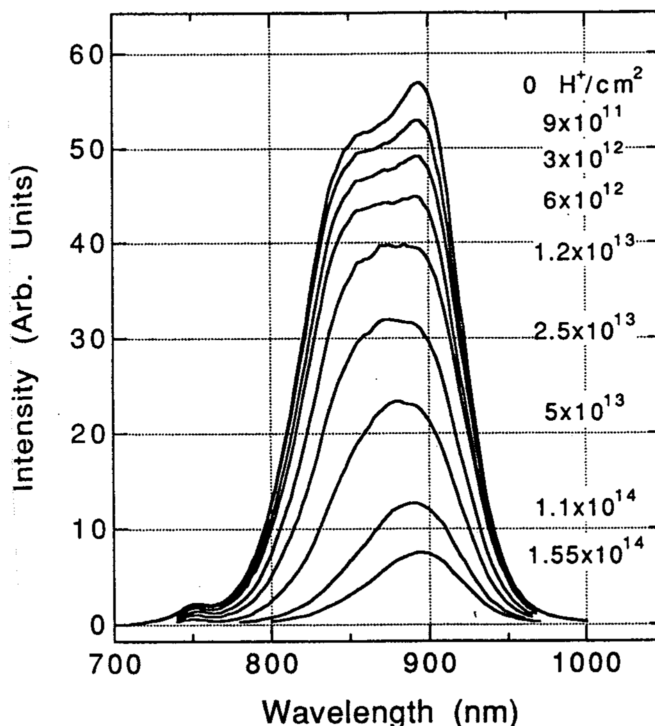

Fig. 6.1. Change of the typical dual-QW LED structure as a function of accumulated proton fluence when operated at 100 mA and 20 °C during irradiation. The spectra were taken with the proton beam momentarily blocked. (After Evans et al. [5]).

Remark that given the large current levels at which the diodes are operated, a significant power is dissipated in the resistive part of the structure, causing a certain amount of self-heating. Since the band gap of the materials reduces for higher temperature, the central wavelength of the electroluminescence spectrum will shift to longer values if this occurs. This is particularly true for LDs; measuring the spectral line shift, therefore, provides a means to determine the local device temperature. Note also that the creation of non-radiative GR centers during exposure increases the power dissipation, since the band-gap energy is released through the emission of phonons (=heat). This heat loading effect may reduce L in a radiation environment, as will be explained in more detail below [7].

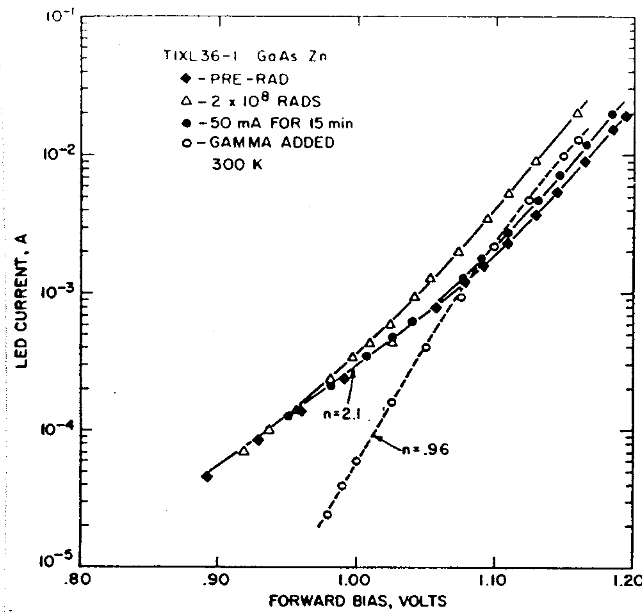

Fig. 6.2. Pre- and post-irradiation current-voltage characteristics of a typical Zn-diffused GaAs LED. The dashed curve is the difference between pre- and post-irradiation I_F-V_F curves. The n values refer to the proportionality : $I_F \bullet \exp(qV_F/nkT)$. Note that application of forward bias returns the I_F-V_F curve to nearly its pre-irradiation characteristic. (After Barnes [2]).

For high-power and high-speed (e.g. high data rates) applications, LDs are more appropriate than LEDs [6]. The higher speed of LDs is related to the low carrier lifetimes, which are in the range of 10^{-11} s during the lasing action, i.e. for stimulated photon emission, which is several orders larger than for LEDs (range 1 ns typically) [7]. From this simple fact, one can immediately derive that LDs are expected to be more radiation tolerant than LEDs, if the dominant lifetime degradation is due to displacement in the substrate. This follows from Eq. (6.2), where for small initial τ_r, a much larger fluence is required and, hence, a larger density of radiation-induced GR centers to bring τ_{nr} to the same order of magnitude. This trend was indeed found for early-generation components [7].

There exists different types of III-V based LDs, consisting of a single or multiple QWs. A typical structure is represented in Fig. 6.3, featuring a QW active region sandwiched between GaAlAs layers, with higher Al content (higher band gap) [7]. The LD of Fig. 6.3 contains an array of active stripes, wherein the current is confined by an ion (hydrogen for example) implantation. This creates high resistive isolation regions, separating the different arrays. Another possibility is to fabricate a broad-area device, where the active region is a single current-carrying QW stripe, defined by an oxide insulator. A multiple quantum well (MWQ) structure is represented in Fig. 6.4 [8]. The LDs of Figs 6.3 and 6.4 are horizontal cavity lasers, which emit their photons in the plane of the junction (Fig. 6.4b). Vertical-cavity surface-emitting lasers (VCSELs) emit their light perpendicularly to the junction (Fig. 6.5) [9] and can be directly modulated at rates in excess of 10 GHz. They can be used to transmit signals through space or in multimode optical fibers, thereby showing great potential for optical interconnects. Again, the lateral current confinement can be achieved either by oxidation or by proton implantation.

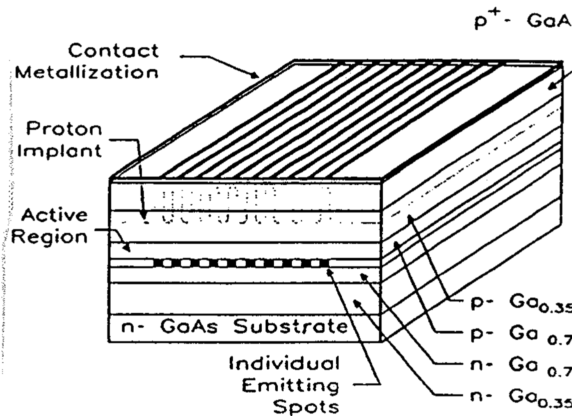

Fig. 6.3. Structure of the semiconductor laser diode array. (After Carson and Chow [7]).

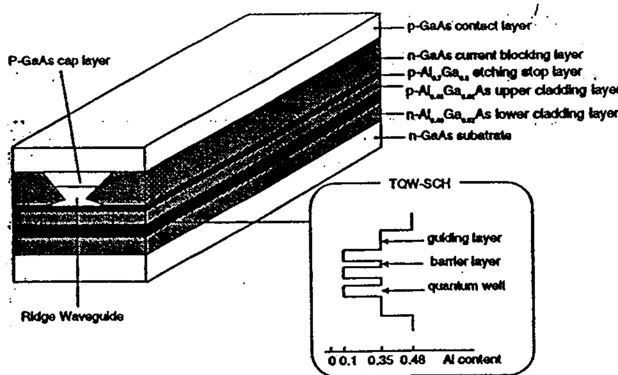

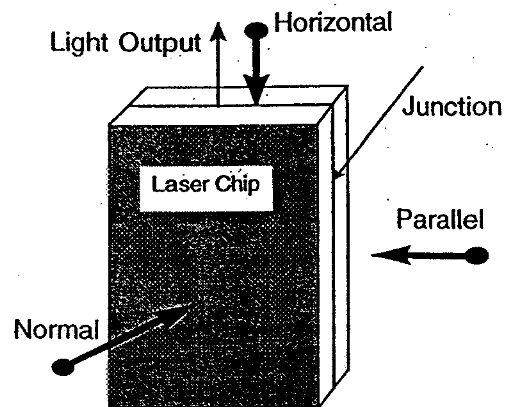

(a) (b)

Fig. 6.4. (a) Schematic structure of the laser diode and (b) of the proton incident directions. (After Zhao et al. [8]).

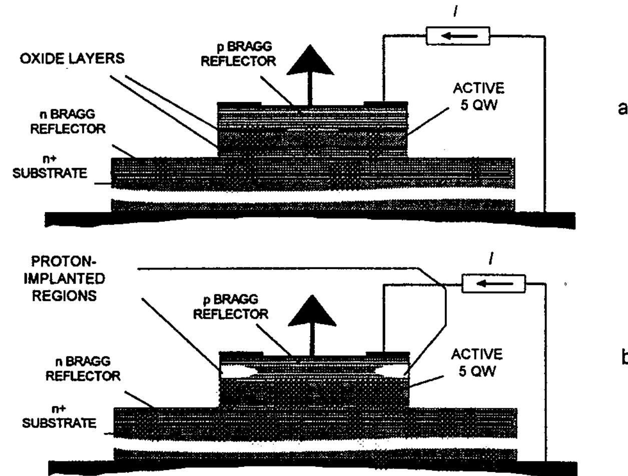

Fig. 6.5. Structure of VCELs. The resonant cavity is vertical, with the mode confined between two Bragg reflectors made up of quarter-wave stacks of AlGaAs with the Al concentration varying between high and low values. In the center of a one-wavelength-thick undoped region, there are 5 GaAs quantum wells where there is optical gain. Two types of lasers were investigated: (a) lasers with the lateral current confinement provided by edge-oxidized layers with very high Al content, and (b) lasers with current apertures defined by proton implantation. (After Paxton et al. [9]).

The light output or optical power L of a LD varies with the diode current passing through the junction, as in Fig. 6.6 [8]. Important parameters are the threshold current I_{th} for lasing action, separating the region of spontaneous emission (LED action) from the stimulated emission at high diode current. It can be expressed as [8]:

$$I_{th} \propto (\tau_r/\tau)\ [\alpha + \ln(1/\rho)/l_c] \qquad (6.5)$$

with a the cavity loss coefficient (cm^{-1}), assumed to be unaffected by irradiation in first instance [7]. ρ is the facet reflectance and l_c the cavity length (cm). The optical power above threshold is given by [7]:

$$L = \eta\ (I_{op} - I_{th}) \qquad (6.6)$$

with η the slope efficiency in mW/mA (i.e. in first instance given by $\partial L / \partial L_{opt}$). I_{op} is the operation current (mA). For the linear characteristics of Fig. 6.6, η is a constant. On the other hand, VCSELs suffer from thermal roll-over, as evidenced by Fig. 6.7 [9]. This is related to the fact that in a VCSEL, a temperature change (by selfheating at higher I_{op}) causes the cavity resonance and gain peak to move to longer wavelengths. Increasing self-

absorption of created photons for example by created defects can degrade the slope efficiency [7-9].

An important remark is that for most of the LED and LD structures, the active region is several μm below the surface of the device. This has to be taken into account when calculating the local energy deposition or NIEL going into displacements at the site of the (M)QW junction [5].

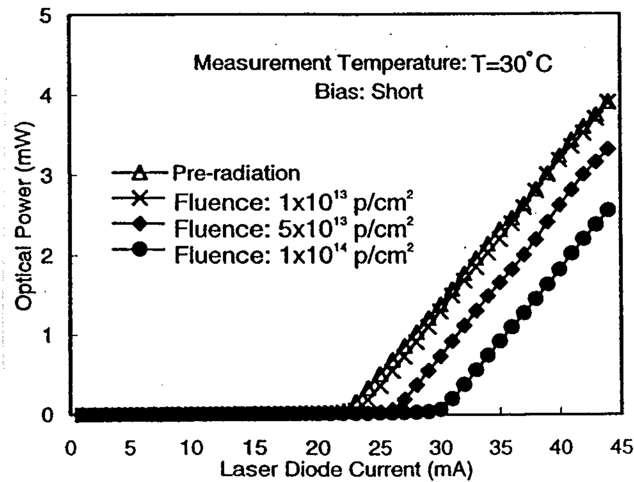

Fig. 6.6. L versus I_{op} characteristics for devices shorted during irradiation. (After Zhao et al. [8]).

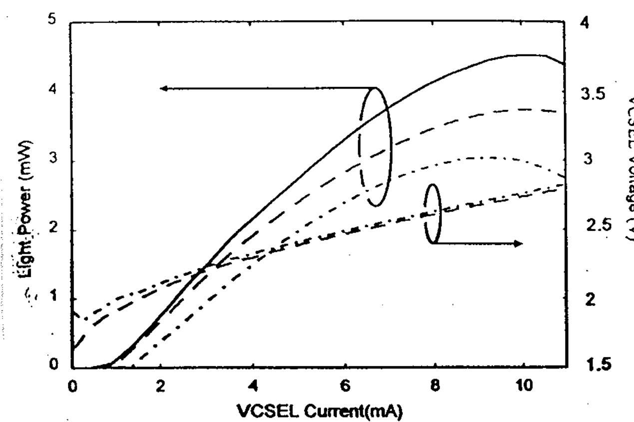

Fig. 6.7. Light-current and voltage-current curves for a VCSEL. (After Paxton et al. [9]).

6.1.2 Photodetectors

Depending on the spectral region, different types of photodetectors can be used. In some cases, a silicon p-i-n diode or a bipolar phototransistor is preferred, because it can be fabricated monolithically with the necessary signal amplifier. However, direct gap III-V materials based PD offer certainly advantages compared with silicon. For example, $In_{0.47}Ga_{0.53}As$ is infrared sensitive, since the band gap is ≈0.75 eV, so that wavelengths in the range 900 to 1600 nm can be absorbed. The layers can, furthermore, be deposited lattice matched on InP SI substrates. A typical structure for such a p-i-n diode is shown in Fig. 6.8 [10].

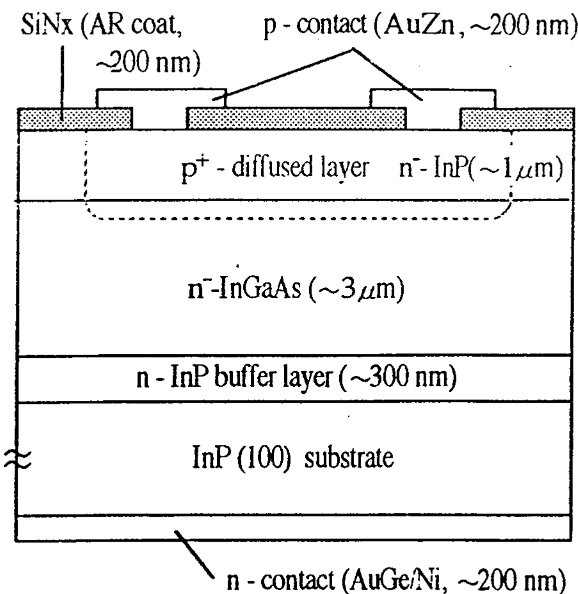

Fig. 6.8. Schematic representation of an $In_{0.53}Ga_{0.47}As$ p-i-n photodiode. (After Ohyama et al. [10]).

Another emerging technology is the so-called Quantum Well Infrared Photodetectors (QWIP's), which are large monolithic two dimensional detector arrays, for wavelengths > 2 μm. In the future, they may replace the existing HgCdTe material, which has problems in detecting long wavelengths >15 μm and also in working in a very low background photon environment [11]. These problems are related to the difficulties in growing highly uniform and defect free stable HgCdTe material. A further advantage is that for multispectral imaging, the peak response wavelength of a QWIP can be tuned by changing the externally applied bias across the AlGaAs/GaAs multistack of different one color QWIPs (Fig. 6.9). Thus QWIPs could provide multispectral imagery by suitable bias

voltage across a given fabricated device. In addition, it has been demonstrated that an LED can be integrated on the same chip, with each detector in the QWIP array. A combined QWIP-LED can be used as a wavelength converter from the mid to far infrared (QWIP) to the near infrared wavelengths emitted by the LED coupled to the QWIP. This technology has the potential of improved performance - because of better quality layers and lower dark currents - ease of production and cost reduction, compared with their present-day competitors for mid to far infrared camera's.

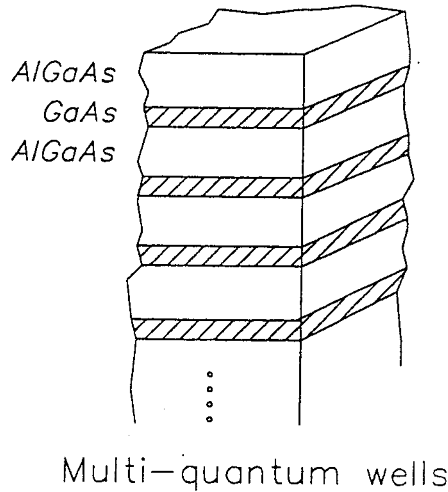

Fig. 6.9. Schematic of nmthick GaAs/AlGaAs multiple layers in a QWIP structure. (After Khanna et al. [11]).

Important operational parameters of a PD are the dark current, the low-frequency noise and noise equivalent power (NEP) and the optical responsivity, which is determined by the charge collection efficiency. Although a PD is a device with a surface-active layer (junction), the light is absorbed much deeper in the material. The absorption coefficient $\alpha(\lambda)$ depends on the wavelength of the light. The light intensity in the detector material follows an exponential law with distance from the surface (x=0):

$$I(x) = I(0) \exp(-\alpha(\lambda)x) \tag{6.7}$$

so that $x=1/\alpha(\lambda)$ corresponds to the distance where the light intensity drops to 1/e of its value at the surface. Electron-hole pairs are thus generated at depths much larger than the reverse biased photodiode depletion region, so that the carriers have to diffuse to the active region to be collected. The collection efficiency, therefore, strongly depends on the diffusion minority carrier length $L_n=\sqrt{D_n\tau}$. D_n is the (electron) diffusion constant. The photoresponse will begin to be affected when the lifetime is reduced to the point where $L < 3\alpha(\lambda)$ [12]. From this, it is concluded that both photodiodes and LEDs/LDs are in first instance determined by the same material parameter, namely the minority carrier lifetime.

This implies that these classes of devices are predominantly prone to displacement radiation damage and less, if at all, to ionization effects. Therefore, some kind of correlation with NIEL is anticipated, which will be discussed in the next section.

6.1.3 Optocouplers

Optocouplers form an essential part in many photonics systems. They provide a DC isolation between circuit blocks, which increases the reliability of space-born instruments [12]. Optocouplers are generally constructed of two dies, separated by an optically transparent but electrically isolated medium. Information is transferred by light generated by an LED (or LD) and sensed by a photodetector, as represented in Fig. 6.10 [13], showing two different arrangements. In Fig. 6.10b, the isolating medium is for example a silicone coupling compound. The detector is followed by an amplifier stage [12].

The important figure of merit for an optocoupler is the Current Transfer Ratio (CTR) which gives the ratio of the detector current to the LED current and is thus a combined quantity, which not only depends on the sending and the receiving components, but also on the coupling medium. The radiation response of an optocoupler is thus rather complex and generally combines permanent and ionisation/transient radiation effects [12].

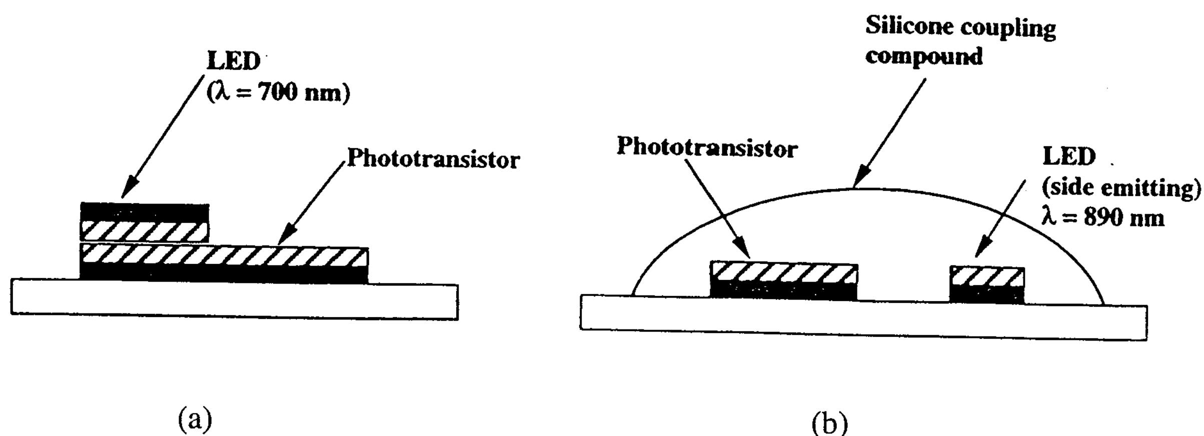

Fig. 6.10. Physical configuration of two different optocouplers. (After Rax et al. [13]).

6.1.4 IMEC activities

IMEC is actively involved in the development of InGaAs infrared photodetectors and has a long-standing reputation in the field of III-V opto-electronics (lasers, LEDs) fabricated by Metal-Organic Chemical Vapor Deposition (MOCVD) (INTEC - Gent). Since a few years, the impact of radiation on the performance of InGaAs photodetectors, fabricated by Japanese Research Groups has been studied intensively, in collaboration with Prof. Ohyama and co-workers [10]. Presently, activities are shifting towards the study of the degradation of InGaAsP QW laser diodes.

6.2 Basic Radiation Effects and Material Issues

6.2.1 Damage Factors and NIEL

From Eqs (6.1) to (6.4) clearly follows that the recombination lifetime of the active material plays a dominant role in the operation of opto-electronic components. Quite often, the degradation of these devices under irradiation is described by a lifetime damage coefficient (or factor), which is defined by [14]:

$$K_\tau = (1/\tau - 1/\tau_0)/\Phi \qquad (6.8)$$

with Φ the particle fluence and τ_0 the initial recombination lifetime. Constant K_τ suggests that the reciprocal lifetime increases proportionally with fluence, which was verified experimentally for proton irradiated GaAs LEDs, in the energy range 1 to 500 MeV. The result of this study is summarized in Figs 6.11 and 6.12 [14]. In the proton fluence and particle range studied, the change in inverse lifetime shows a linear relationship with fluence (Fig. 6.11). A value of 1.06×10^{-4} cm^2/s was obtained at an incident energy of 9.0 MeV (corrected energy 8.0 MeV). Comparing this with the calculated NIEL shows a good agreement in Fig. 6.12. This clearly demonstrates that the lifetime degradation is due to displacement damage. Deviations occur, however, for proton energies above 150 MeV, showing lower measured damage factors than predicted by the restricted energy loss model developed in Ref. 15. One possible interpretation is that the clustered damage, which is created by highly energetic Primary Knock-on Atoms (PKA's) is less effective in reducing lifetime, than the point defects induced at lower proton energies.

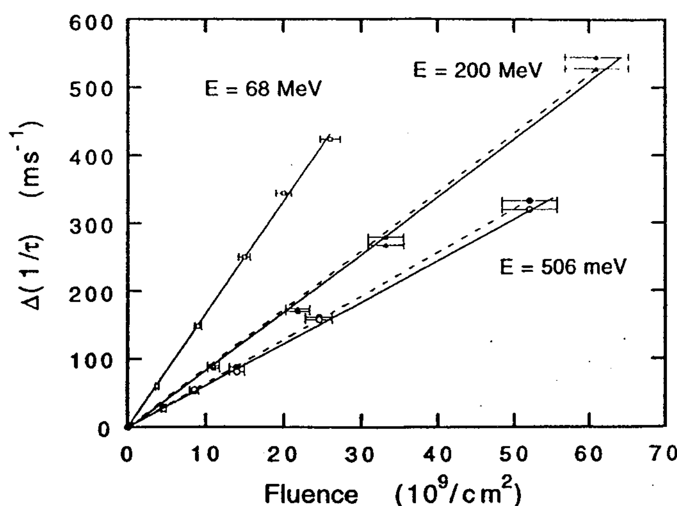

Fig. 6.11. Typical curves of the reciprocal lifetime with proton fluence. For 200 and 506 MeV protons, the two sets of points represent irradiations from the front (solid lines) and from the rear (dashed lines). (After Barry et al. [14]).

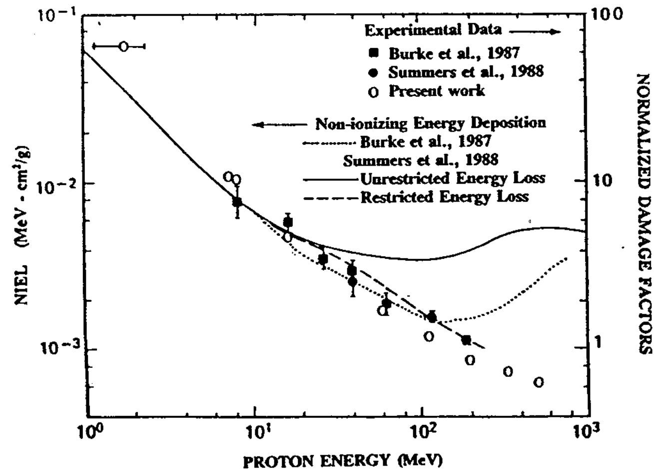

Fig. 6.12. Lifetime damage factors (open circles) fitted at 10 MeV to the calculated NIEL versus proton energy of [15]. The right-hand ordinate is normalized at 10^{-15} n/cm^2 in [15], and at 10^{-5} cm/s in this work. (After Barry et al. [14]).

Not only the recombination lifetime of irradiated opto-electronic components scales with NIEL, but also the generation lifetime, derived from the reverse dark current of InGaAs photodetectors. This is illustrated in Fig. 6.13 [6]. This implies that the increase in leakage current of pin diodes is fully due to the created displacement damage centers, which will be discussed in more detail below. One important remark, however, is that not necessarily the same radiation induced centers determine both the generation and the recombination lifetime. The former will be governed by near mid gap levels, while for recombination, it is mainly the ratio of the capture cross sections for minority and majority carriers which will define the efficiency of the trap.

Based on these observations, it has been proposed to use the damage factor in GaAs LEDs as an alternative method for displacement damage monitoring [16], instead of using epitaxial or implanted resistors, JFETs, etc...Given the sensitivity of the light output L, this monitor should be particularly suited for the low fluence range (or low γ dose) and is therefore complementary to the resistor based methods. Furthermore, the damage in an LED is purely due to lattice displacements, while negligible ionization damage occurs. Care has to be taken that during the measurement of the light output, no self-annealing occurs. It is recommended to operate the device at low currents (1 to 10 % of the normal operation current). The light output damage factors ($\tau_0 x K_\tau$) obtained in the study, were in the range of $6x10^{-7}$ rad^{-1} (for ^{60}Co), indicating a detection limit of 5 to 10 krad(GaAs) [16]. For 1 to 2 MeV neutrons, a $K_\tau \tau_0$ product $\approx 10^{-12}$ cm^2 was obtained, which is 3 to 4 times higher than the data derived in earlier studies on similar devices. This is related to the higher

recombination lifetime τ_0 (higher material quality), which was found to be 800 ns for the radiative lifetime, to be compared with previous values of 270 ns. This supports the observation that the better the starting material quality, the poorer the radiation tolerance is [3-4].

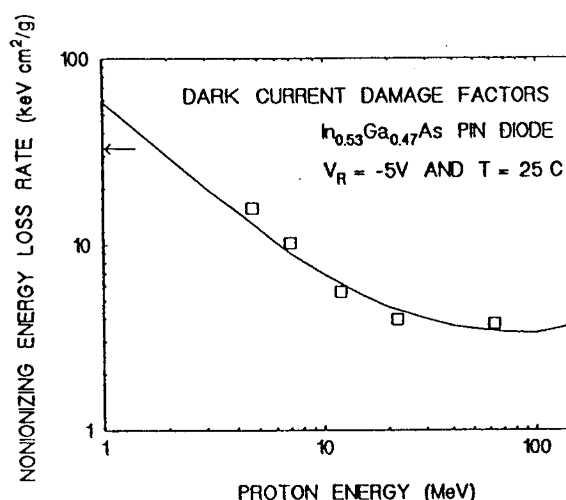

Fig.6.13. The calculated NIEL for InGaAs exhibits the same energy dependence as the measured generation lifetime damage factors. The two are scaled by a constant of 1.4×10^{-10} μA g/MeV which relates leakage to damage. (After Marshall et al. [6]).

6.2.2 Radiation Defects and Material Aspects in Ternary Compounds

When dealing with displacement damage in photonic devices, one should keep in mind that the active regions are generally not at the surface but may reside several μm (or more) below the exposed surface. In addition, for photodetector devices, the region where photo-generated carriers are collected may extend several tens of μm in the device, e.g. a few minority carrier diffusion lengths. For these reasons, one should correct for the energy loss of an impinging particle with a given energy before it reaches the active region, in order to calculate the correct "local" NIEL, as illustrated schematically in Fig. 6.14 [5].

There are a few additional material related aspects that need to be considered carefully for GaAs and related photonic ternary and quaternary compounds. For the deposition of QW layers, quite often, use is made of techniques like Metalorganic Vapor Phase Epitaxy (MO-VPE) or Molecular Beam Epitaxy (MBE), which differ from the commonly used Vapor Phase Epitaxial (VPE) growth, for HEMTs and MESFETs. One may wonder whether there is a dependence on the growth technique of the radiation response. Initial studies for electron irradiated material indeed suggest a different behavior [17]. Not only is an additional radiation induced trap observed for high background doping material, but on top of that the simple linear response of the radiation defect density with

electron fluence is not retrieved. Instead, a complex carrier removal rate, depicted in Fig. 6.15 is observed. This implies that the popular damage factor concept is not strictly valid for such material. More studies are required to identify the origin of this behavior and to establish an alternative displacement damage monitor.

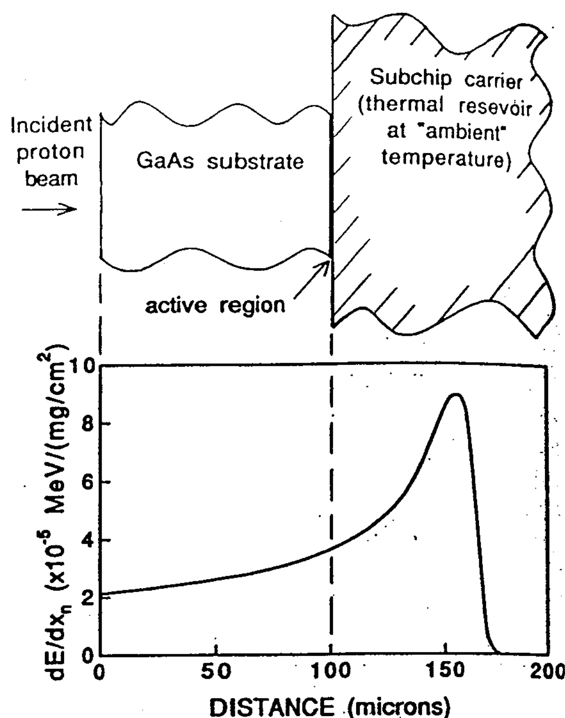

Fig. 6.14. Approximate non-ionizing energy deposition profile for 5.5-MeV protons incident on GaAs. Device substrate thickness and active layer position are depicted above. (After Evans et al. [5]).

Another issue is related to the nature of the fundamental displacement centers created in epitaxial compound layers like AlGaAs, InAlAs, InGaAsP, etc., which are often used in photonic devices. In the first instance, one expects simple Frenkel pairs, whereby, like in GaAs, the As vacancy (V_{As}) is one of the predominant stable radiation defects at room temperature [18-19]. In AlGaAs, a trap at 420 meV from the conduction band (25% Al), with largest introduction rate has been ascribed to V_{As}. It corresponds to the E2 level in GaAs (see Table 5.1 in previous chapter). The corresponding shallower state is expected to lie at approxiamtely E_C-320 meV [19]. Two additional unidentified, deeper levels have been observed recently in the 10^{18} cm^{-3} doped AlGaAs layer of neutron irradiated HEMTs [20].

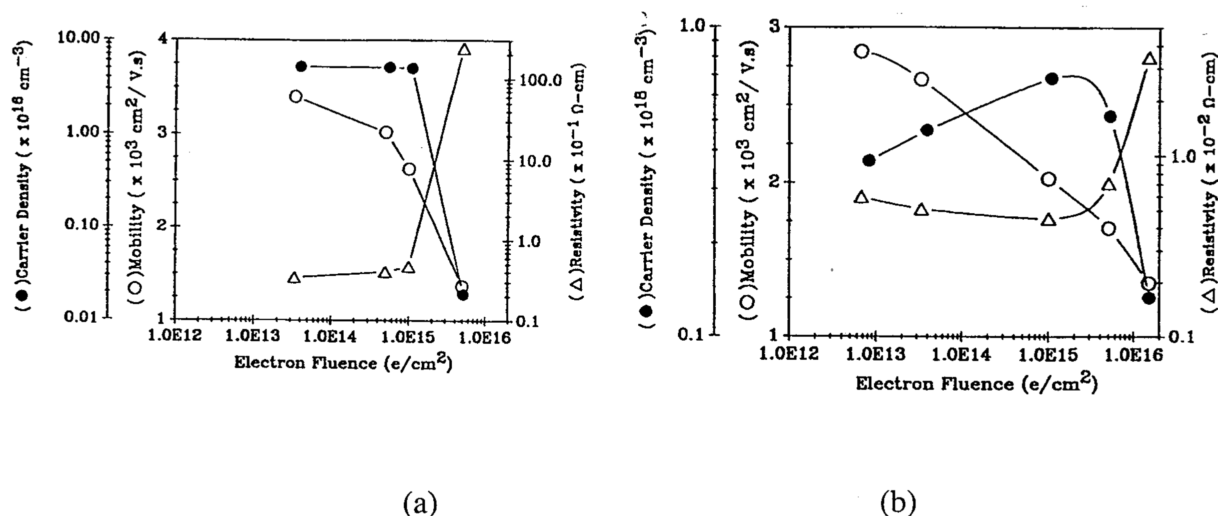

(a) (b)

Fig. 6.15. RT carrier density, mobility and resistivity of n≈10^{16} cm^{-3} (a) and ≈10^{17} cm^{-3} MO-VPE material as function of 7 MeV e^- fluence. (After Yousefi et al. [17]).

The impact of the Al fraction on the electron-irradiation induced deep levels has been studied recently by Zaidi et al. [19]. As shown in Fig. 6.16, the trap level position of the five radiation related defects in the DLTS spectrum and, hence, the corresponding activation energy, shifts with x. The DX center, present in un-irradiated material and giving rise to the peak at 140 K remains unaffected by the irradiation. It is believed that the EZ1 level corresponds to the E2 second V_{As} level in GaAs and is thus related to the arsenic vacancy. The four other levels are thought to correspond with the E3 level in electron irradiated GaAs, i.e. with an V_{As}-As_i pair. This level assignment and interpretation stands, however, in slight contrast with previous studies [21]. The reason for the splitting of a single level in GaAs in four levels in GaAlAs is related to the presence of the Al fraction, which changes the local atomic arrangement around the same basic Frenkel pair. It has furthermore been shown that some of the levels are pinned to the conduction band edge (donor nature), while other follow the valence band. No hole traps corresponding to H0 and H1 were detected in irradiated GaAlAs. It was finally observed that the trap introduction rates increase with increasing Al concentration. This is evidenced by the individual and total introduction rates for 1 MeV electron irradiation in Fig. 6.17a and b, respectively. From this, it is concluded that the presence of Al stabilises the Frenkel defects in the As sub-lattice. Calculations indicate that the variation of the introduction rates with x could be explained by 2 or 4 neighboring Al atoms [19].

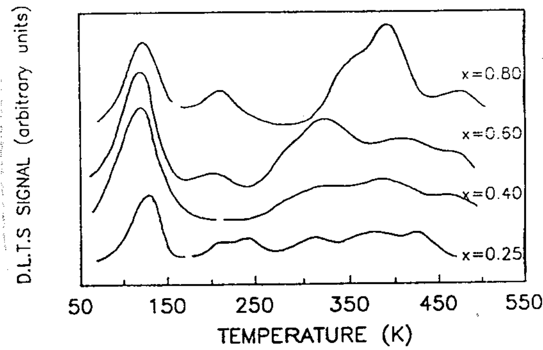

Fig. 6.16. DLTS spectra in 1 MeV electron-irradiated samples of various alloy compositions x. (After Zaidi et al. [18]).

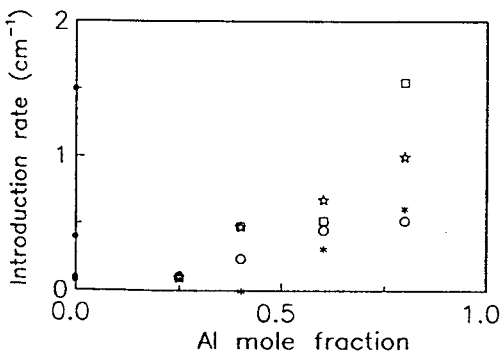

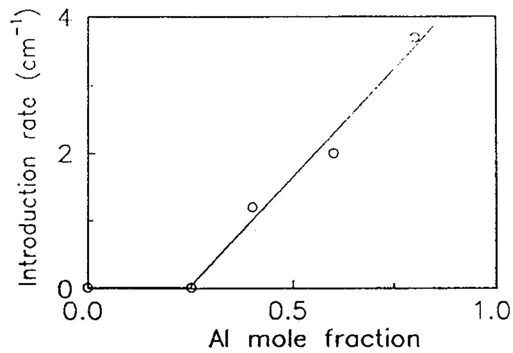

(a) (b)

Fig. 6.17. Variation of the introduction rates versus alloy composition for the various defects EZ2(*), EZ3 (stars), EZ4(squares) and EZ5 (o). The case of the radiation defects in n-type GaAs is indicated by the full circles (a). Variation of the total defect introduction rate vs alloy composition (b). (After Zaidi et al. [18]).

It is known for quite some time that low-temperature irradiated n-type GaAs shows three annealing stages, which can be discerned in Fig. 6.18, representing the carrier density in function of the isochronal annealing temperature, after 85 K 1 MeV proton irradiation [21]. Stage I occurs around 235 K, stage II at 280 K and stage III at 520 K. It is believed that the latter one is related to the annealing of Frenkel defects in the As sub-lattice, i.e. the annealing of the E1 to E5 levels, related to V_{As} and the V_{As}-As_i center. The earlier stages have been shown to require higher irradiation energies and thus corresponding to a higher threshold, suggesting that the stage I and II defects are produced by double displacements. It has furthermore been shown that in the 280 K stage three hole traps are removed in

proton irradiated n-type GaAs [22-23]. The same three annealing stages can be identified for low temperature irradiated AlGaAs in Fig. 6.18. One marked difference is the stage III annealing which is smeared out over a broader temperature range. This can be understood by considering the presence of the Al fraction, which causes local variations in the atomic configuration of the As related defects. Another important observation is that the stage II step is far less pronounced in $Al_{0.22}Ga_{0.78}Ga$ than in GaAs [21]. From the observations it is concluded that, first, the underlying defects are in the Ga sub-lattice and b, more than one Ga atom is involved in the defect centers. Possible candidates are Ga_{As}-V_{Ga} antisite-vacancy close pairs, with a nearby interstitial As_i, produced by the displacement of one Ga and an adjacent As atom. This also explains why most of the Ga sub-lattice defects are hardly observed in room temperature irradiated GaAs, since their formation/stability temperature lies well below 300 K.

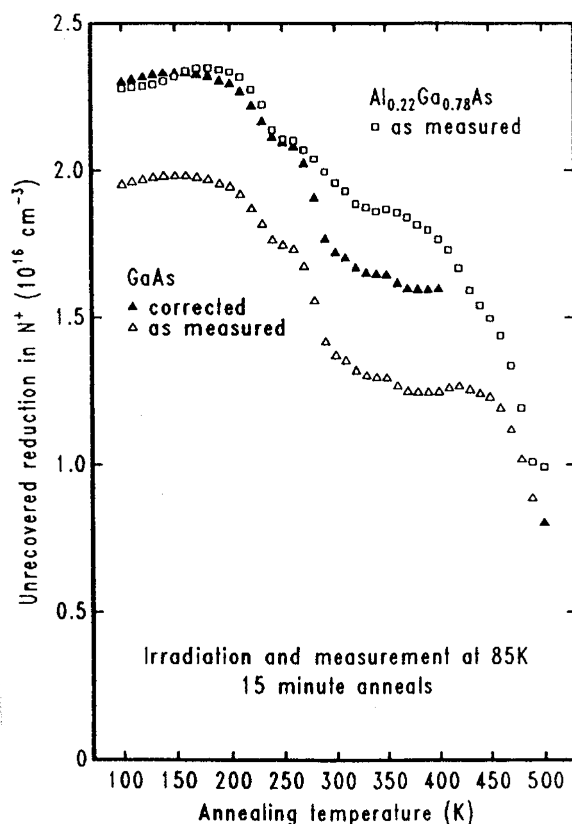

Fig. 6.18. Open triangles and squares: recoveries and postillumination 85-K values of the electron concentration, as a function of 15 min. isochronal annealing temperature after simultaneous irradiation of the two materials at 85 K to a dose of 4.6×10^{12} 1-MeV H^+/cm^2. Solid triangles: recovery of the post-illumination electron density in the GaAs after correction, to remove the influence of the E1 and E2 defects from the GaAs plot. (After Irvine and Palmer [21]).

Another important aspect for photonic devices is the current transport across AlGaAs/GaAs interfaces, which border the GaAs QW in many structures. It has been observed that the I-V characteristics of the AlGaAs/GaAs barriers at sufficiently high temperatures are dominated by trap assisted tunneling, whereby carriers tunnel to traps near the interface, which have been identified as DX centers [19]. They are subsequently emitted to the conduction band with an ionization energy E_i, which is determined by Poole-Frenkel lowering, i.e., showing a linear dependence of E_i on the square root of the electric field or on $\sqrt{V}$. This additional source of dark current is detrimental for the detectivity of QW photodetectors. In order to control the mechanism, one can deliberately introduce traps by high energy particle irradiation. It has been shown that exposure to high fluences (10^{17} cm^{-2}) 1 MeV electrons significantly alters the barrier height from 225 meV (prior to -) to ~300 meV (post irradiation) [19]. This yields a substantial reduction of the dark current (Fig. 6.19) and offers the possibility for defect control in such barriers. The responsible centers are thought to be mainly V_{As} [19].

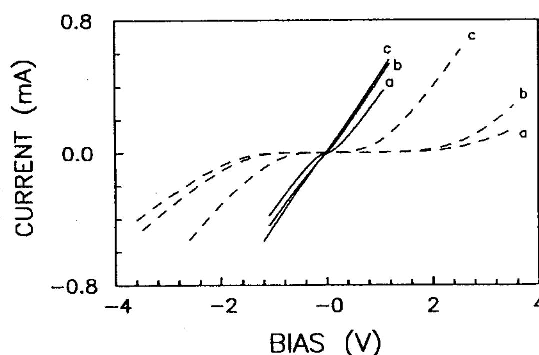

Fig. 6.19. Typical current-voltage characteristics monitored at various temperatures: 80 K (a); 180 K (b), and 300 K (c) before (full lines) and after (dashed lines) electron irradiation. (After Chaabane and Bourgoin [19]).

In 1 MeV electron irradiated $In_{0.53}Ga_{0.47}As$ p-i-n photodetectors irradiated by 1 MeV electrons, two electron traps have been identified by DLTS after exposure [24], at 0.1 and 0.29 eV below the conduction band (Fig. 6.20). The introduction rate of the deeper level is 0.07 cm^{-1} and shows a thermal annealing stage around 425 K. A similar deep level, at E_c-0.31 eV has been observed in 63 MeV proton irradiated InGaAs [6]. It is believed that this defect corresponds to the V_{As} defect. It is furthermore demonstrated that the annealing behaviour of the dark current of irradiated p-i-n diodes follows closely the annealing of the 0.29 eV center [24].

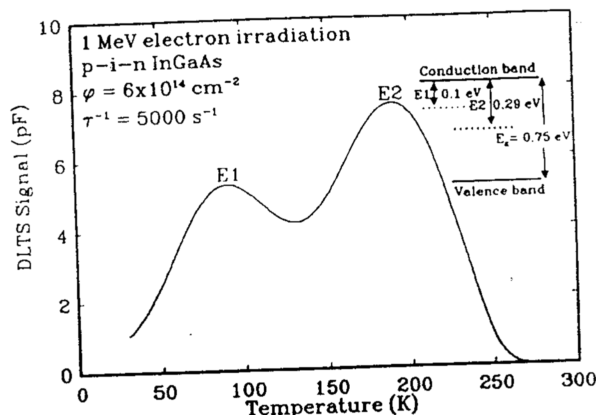

Fig. 6.20. Typical DLTS spectrum measured on the $Ga_{0.47}In_{0.53}As$ material after 1 MeV electron irradiation. (After Walters et al. [24]).

Probably similar energy levels exist in other alloys, whereby the distance of the E2 like level from the conduction band will increase for larger band gap alloys

Another application of radiation-defect engineering in III-V compounds is the use of proton or helium ion implantation (bombardment) to create highly resistive lateral isolation regions for laser diodes, for example (see e.g. Fig. 6.5). In the case of GaAs, high-resistivity regions (>10^7 Ω cm) can be produced by radiation damage in n- or p-type material, through carrier removal and compensation by induced defects. For InP, the resistivity can only be increased to the 10^3 - 10^4 Ω cm range. Using 33 keV He^+ implantations, an increase of the starting resistivity by a factor of up to 3×10^5 is possible for InGaAsP, a material useful for laser production in the 1.3-1.6 μm wavelength range [25].

6.3 Radiation Effects in Opto-Electronic Components

6.3.1 LEDs and LDs

The degradation of the light output L of an LED following irradiation is often expressed in terms of a damage factor [2-5], given by:

$$\frac{L}{L_o} - 1 = \tau_o K_\tau \Phi \quad (6.9a)$$

or alternatively:

$$\left(\frac{L}{L_o}\right)^{2/3} - 1 = \tau_o K_\tau \Phi \quad (6.9b)$$

Equation (6.9a) is valid if L is measured in function of the forward bias, Eq. (6.9b) in function of the forward current [3], whereby it is assumed that L is dominated by the diffusion component given by Eq. (6.3). Other expressions are available if the L-I (or J-V) characteristics are dominated by space charge recombination (see for example Table 2 in Ref. 4). The formula's (6.9) are in fact an alternative form of Eq. (6.8), but expressed in measurable quantities. As shown in Fig. 6.21, Eq. (6.9b) reasonably well describes the degradation of a QW LED, in function of the proton fluence [5]. A damage factor of $\approx 4\times10^{-14}$ cm^2/proton was found from the slope in Fig. 6.19. It has also been observed that not only the maximum spectral intensity (Fig. 6.1) but also the spectral width degrades upon irradiation (Fig.6.22).

As shown in Fig. 6.2, in addition, the LED forward I-V is modified by the irradiation. Often, an increase of the current is found, which indicates the creation of an additional space charge recombination current component. The latter is caused by non-radiative recombination centers, introduced by the irradiation and normally corresponds to an n=2 ideality factor of the forward diode characteristic, although n=1 could also occur if the levels form an overlapping band of shallow states [2]. Another important observation is that the characteristics improve under forward current annealing (Fig. 6.2 and Fig. 6.23) [2]. In other words, operating the irradiated device for a certain time at large forward current either *during or after* the exposure removes part of the damage. This defect annealing may be partially related to self-heating although it is believed that an athermal diffusion mechanism, to be discussed below, is operational.

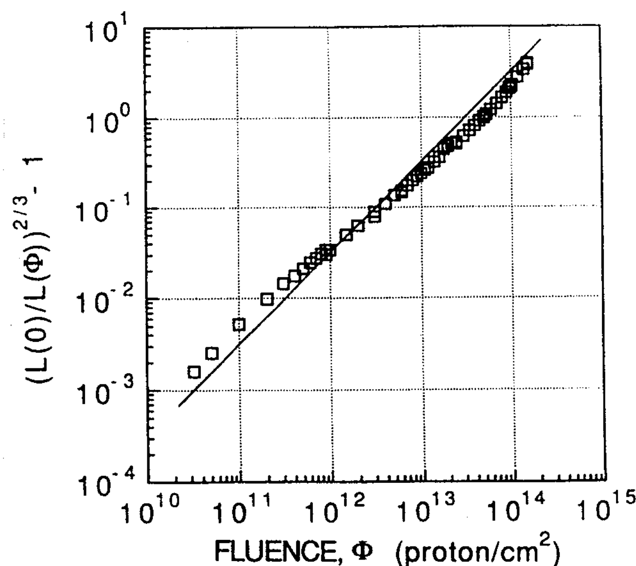

Fig. 6.21. Analysis of strained QW LED degradation while operated at 100 mA and 20 ^oC corresponding to a K_τ τ_0 product of 4.0×10^{-14} cm^2/5.5 MeV proton. (After Evans et al. [5]).

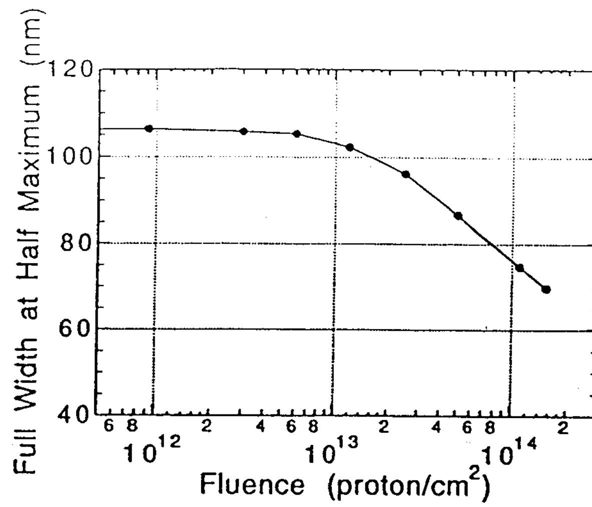

Fig. 6.22. QW LED spectral width versus proton fluence. (After Evans et al. [5]).

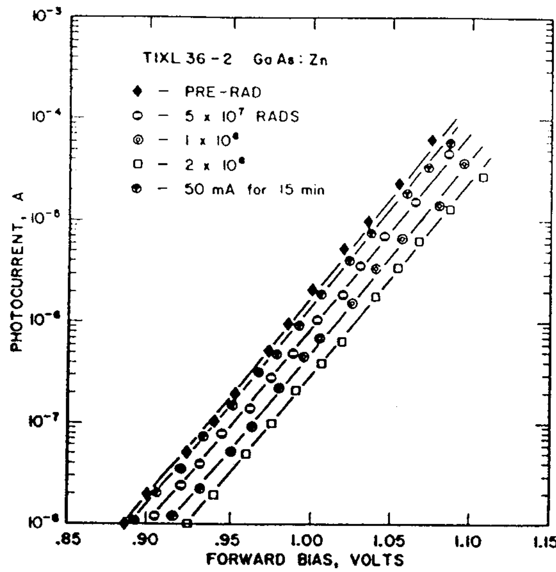

Fig. 6.23. Light intensity (phototransistor collector current) - voltage curve of a typical Zn-diffused LED prior to and following gamma irradiation and forward bias annealing. The true L-V characteristic is distorted by the nonlinear phototransistor response. As in the case of the I_{LED}-V data, forward bias recovery of the L-V characteristic is nearly complete. (After Barnes [2]).

From Eq. (6.9) readily follows that the larger the starting recombination lifetime, the more prone the LED will be to radiation damage. Its light output is thus a sensitive function of the starting material quality and explains why early amphoteric GaAs LEDs where less suitable for space applications than GaAlP or GaAsP counterparts. The damage factor also relies on the material composition, as shown in Fig. 6.24 [4], where a decade difference can be seen in $\tau_o x K_\tau$, as a function of the P fraction. Typical values for epitaxial GaAs are in the range of 1-2x10^{-13} cm^2 per 2 MeV electron [3], one decade higher. This also explains why in earlier studies, laser diodes turned out to be harder than LEDs. This may no longer be the case for state-of-the-art QW structures [5], where the opposite can be found.

As shown in Fig. 6.6, the major degradation of a laser diode is the increase in the current threshold I_{th}. A more or less linear variation of I_{th} with proton fluence is observed in Fig. 6.25 [8]. This radiation-induced change in I_{th} can be modeled by the threshold voltage damage factor [8]:

$$\frac{I_{th}}{I_{tho}} = \frac{\tau_o}{\tau} = 1 + K_\tau \tau_o \Phi = 1 + K_I \Phi \tag{6.10}$$

I_{tho} is the pre-rad current threshold. From Fig. 6.25 follows that the increase in I_{th} is larger for higher operation temperatures. The degradation is also higher for devices shorted during the exposure, than for those biased, with I_{bias}=35 mA. The latter is related to the occurrence of forward bias annealing during the irradiation. From Figs 6.26 and 6.27, one can derive that the degradation of the normalized optical power is smaller at lower operation temperature and high operation current, irrespective of the bias during exposure. Typical K_I values are in the range 1.5 to 4.6x10^{-15} cm^2/p (200 MeV energy) [8]. It is furthermore assumed to be proportional to the NIEL S, through: K_I=4.5x10^{-12}xS. It was also observed that K_I(horizontal) > K_I(parallel) > K_I(normal), whereby the direction of incidence of the proton beam has been defined in Fig. 6.4.

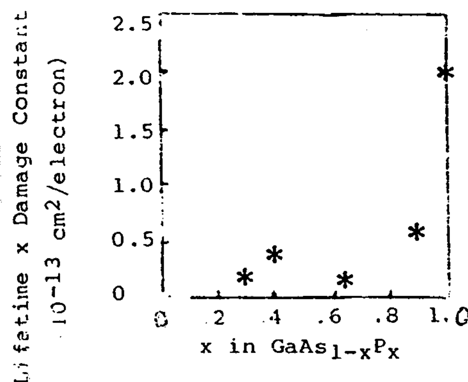

Fig. 6.24. Lifetime damage constant product versus composition. (After Dimiduk et al. [4]).

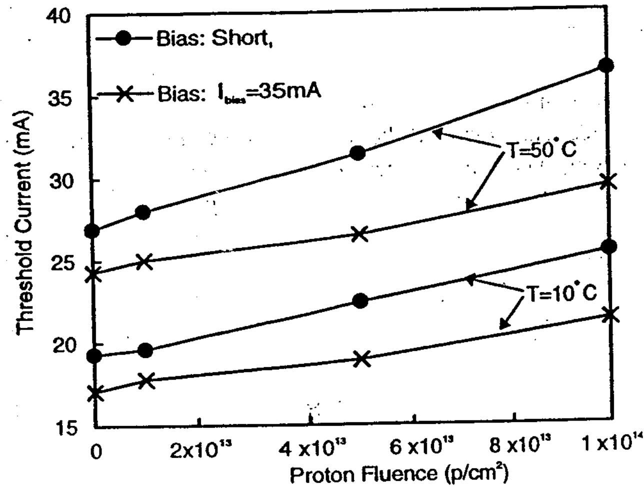

Fig. 6.25. Threshold current vs. proton fluence for devices with different biases during irradiation and measured at different temperatures. (After Zhao et al. [8]).

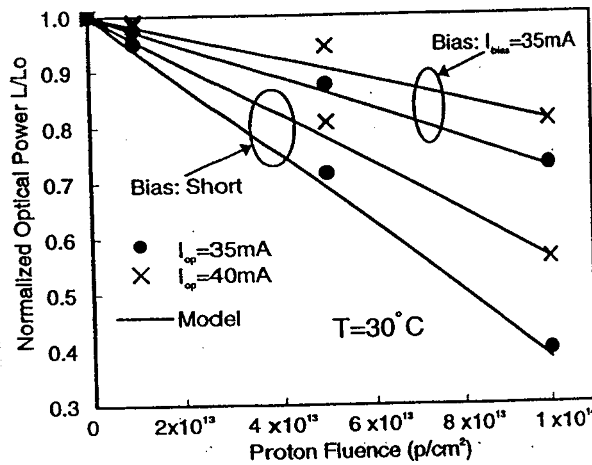

Fig. 6.26. Experimental and modeling L/L_O vs. proton fluence for devices with different biases during irradiation and measured at different operation currents. (After Zhao et al. [8]).

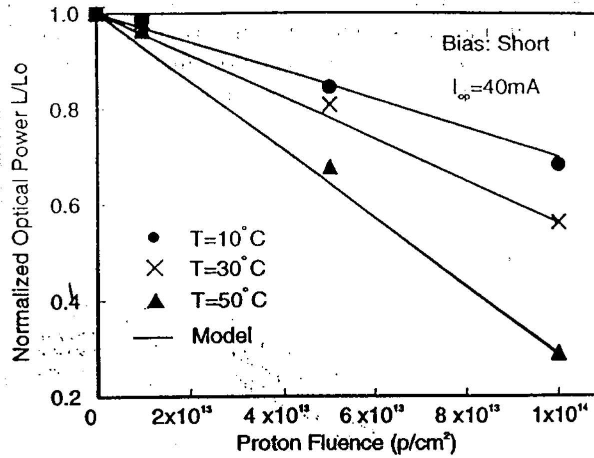

Fig. 6.27. Experimental and modeling L/L_O vs. proton fluence for devices shorted during irradiation and measured at different operation currents. (After Zhao et al. [8]).

In addition, the slope efficiency may change slightly after irradiation (Fig. 6.6) [8]. This is related to optical absorption and scattering from defects induced by the irradiation. At low proton fluences ($<10^{13}$ cm^{-2}), however, η increases slightly for the device of Fig. 6.6, which is interpreted as being due to the radiation induced order effect, for example by relaxation of the grown-in stress in the QW [8]. At low fluences, the energy deposited by the protons can reduce the stress, which overcomes the effect of the created Frenkel defects. At higher fluences, the balance goes the other way.

Finally, the radiation-induced change in optical power L can be expressed as follows [8]:

$$\frac{L}{L_O} = 1 - \frac{I_{tho}}{I_{op} - I_{tho}} K_I \Phi \qquad (6.11)$$

In writing Eq. (11), it is assumed that the slope efficiency remains constant, i.e. that $\eta/\eta_O \approx 1$.

From formula (6.11) follows a few simple guidelines for the hardness of LDs [8].

(1) First, the degradation will be lower for higher L_O. This means that higher operation bias is better for the radiation tolerance. It should also be remarked here that when comparing radiation results from different devices and sources, one should take into account the operation conditions during and after irradiation. In addition, a high

operation bias during exposure could produce sufficient annealing so that the correlation with NIEL may be violated.

(2) The lower I_{tho}, the less the degradation of optical power after irradiation. Thus, low I_{tho} is most suitable for radiation applications. This suggests that QW laser diodes may be more suitable for radiation applications, since they have lower I_{tho}.

(3) The higher η_o, the higher the degradation of optical power after irradiation. This suggests that LDs with lower η_o are more suitable for radiation applications, though they are not optimized lasers.

(4) When operation temperature increases, I_{tho} increases, so that the optical power degrades more for higher operation temperatures.

A more refined numerical modeling procedure of the current threshold increase of irradiated laser diodes has been proposed by Jolly and Vicrey [26] and takes into account the interaction between the optical and the electrical properties of the device. In more detail, the change in the internal quantum efficiency is coupled to the additional electrical field, caused by trapped holes. This model should extend the calculations to larger (neutron) damage ranges, where the forward bias drop over the diode changes by several hundred milivolts, instead of the usual milivolts. It was also observed that there was no radiation induced shift of the spectral line width or position of the GaAlAs QW laser studied (Fig. 6.28).

The annealing behavior of 780 nm MQW laser diodes after proton irradiations has been investigated recently by Zhao et al. [27]. A typical response is shown in Fig. 6.29. Three stages can be identified in Fig. 6.29: during stage I, the laser diode stabilises, whereby the junction temperature increases 20-25 ^{o}C, at an operation current of 35 mA. In stage II, the laser diode was irradiated by 68.5 MeV protons till a fluence of $6x10^{12}$ p/cm^2 was reached. In stage III, the device was allowed to anneal under forward bias, for 1800 s. The annealing effects are most significant during the first 100 s. It can be fitted by an exponential function:

$$L(t) = L_o + \Delta L\ [1-\exp(-t/\tau_A)] \qquad (6.12)$$

with ΔL the amplitude and τ_A the time constant of the annealing. The initial value is in the range of 50 s, followed by a slower recovery at τ_A=1000 s. Finally, the annealing proceeds even more slowly at time constants of $1.5x10^4$ to $2x10^4$ s. These three stages indicate the removal of different kinds of radiation induced defects. Simple Frenkel defects like a vacancy or a vacancy-interstitial pair will anneal easily, while the antisite defect will be very stable and hard to remove when created. The major mechanism of this forward bias annealing is not thermal dissociation and diffusion of defects, but rather related to the so-called Recombination Enhanced Defect Reaction (REDR) mechanism [27-28]. It means that when a non-radiative electronic transition occurs, the phonon energy deposited locally can enhance the temperature at the defect and activate it. Then the defect has more energy to move and the reaction (annihilation or dissociation) rate increases. This REDR mechanism typically finds place in the active device region.

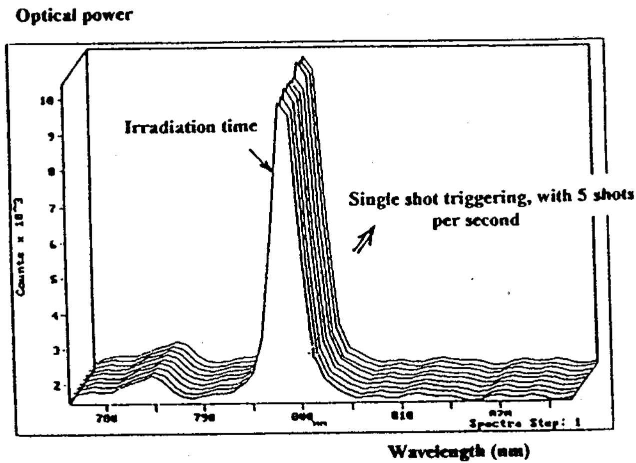

Fig. 6.28. Transient effects of pulsed 17 MeV electrons on the optical spectrum of the SDL 3230T laser bar. The laser bar is tested with I=80 A, the optical analyzer being triggered once every 5 seconds after the beginning of the electron burst. (After Jolly and Vicrey [26]).

From this bias annealing, it is furthermore concluded that at the lower fluxes typical for space, the degradation of LD may be less than in a laboratory experiment [27].

The recovery of irradiated laser diodes through isochronal thermal annealing following ^{60}Co gamma irradiation has been studied by Barnes in the early days [1]. He found an activation energy of about 1.7 eV and an annealing stage centered around 237 ^{o}C. This corresponds approximately with the removal of the E1-E5 electron traps, associated with the V_{As}-As_i defects.

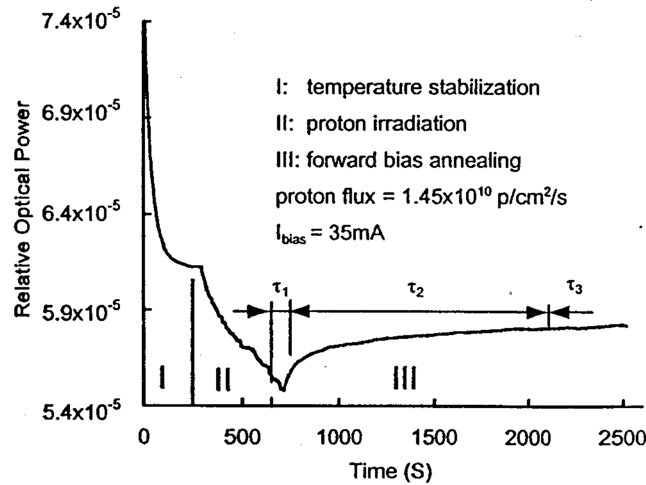

Fig. 6.29. The relative optical power vs. time, including temperature stabilization (I), proton irradiation (II), and forward bias annealing. (After Zhao et al. [27]).

Other damage mechanisms have also been reported for irradiated laser diodes. For example, facet damage (cracks) may develop during neutron exposure [7]. Also thermal effects (self-heating) play a role in the enhanced degradation [7,9], which may be particularly important for VCSELs.

Finally, the radiation characteristics of a number of commercially available LEDs and LDs has been studied by Lischka et al. [29-30], for neutron, gamma and X-ray exposure. One of their conclusions was that InGaAsP LEDs are more radiation tolerant than InGaAs, which on their turn behave better than GaAs LEDs [30].

6.3.2 Photodetectors

The degradation of irradiated InGaAs photodetectors has been studied by a number of groups [6,10,24]. One of the primary parameters investigated is the dark reverse current, which sets the detection limit and low-frequency noise of the PD. As shown in Fig. 6.30a [10], the reverse current increases significantly with 1 MeV neutron fluence. Consequently, the photo-response will be degraded (Fig. 6.30b). At the same time, the spectral response represented in Fig. 6.31 changes, whereby both the amplitude and the width of the spectral region reduce. The reduction in normalized response, following 63 MeV proton exposure is given in Fig. 6.32 [6]. Upon thermal annealing in the range 100 to 300 ^{o}C, a considerable recovery is found, both in the dark current (Fig. 6.33a) and in the optical response (Fig. 6.33b). A broad annealing stage in the range 400 to 500 K is found in fair agreement with other reports [24,31-32]. Above 550 K a second stage, related to the annealing of more stable radiation defects is observed. Such a deeper stage was also found by Walters et al. [24].

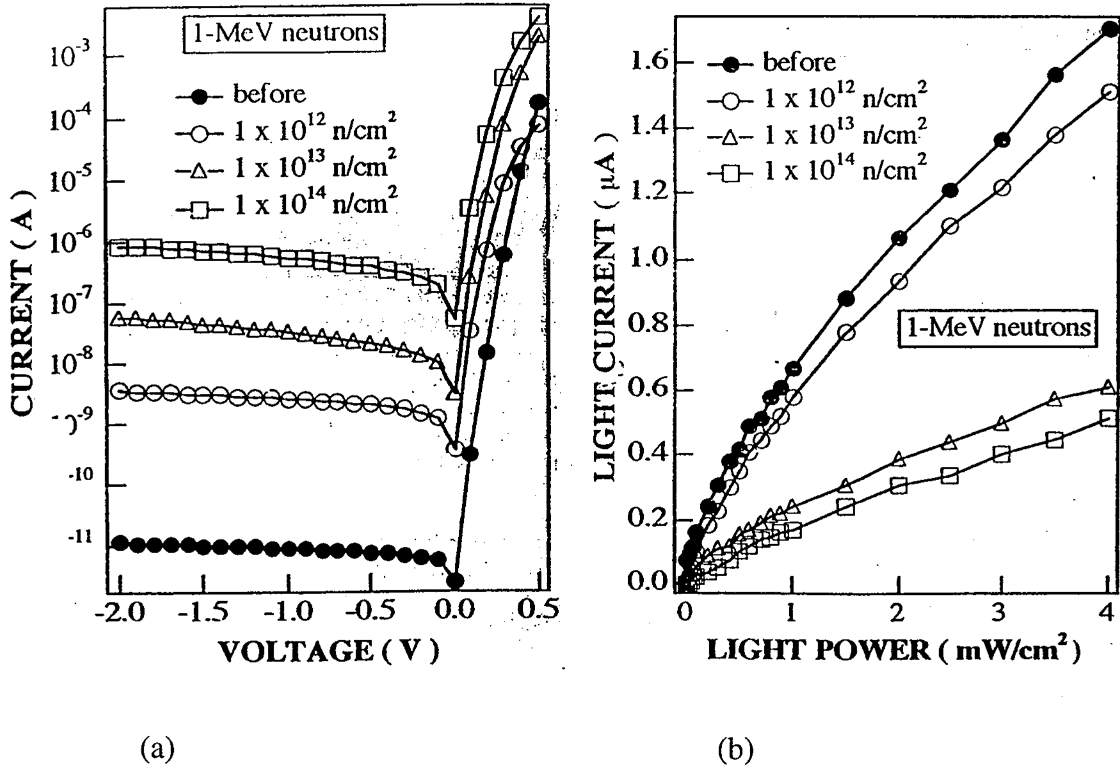

Fig. 6.30. Influence of 1 MeV neutron irradiation on the I-V (a) and I_L-P_L (b) curves of an InGaAs photodetector. (After Ohyama et al. [10]).

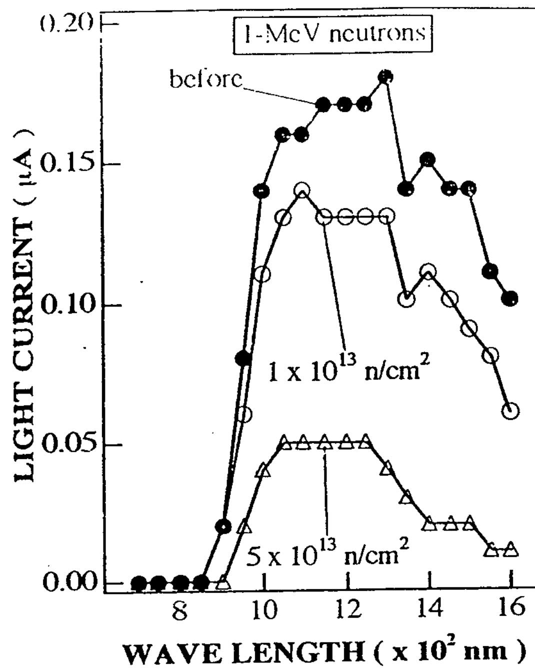

Fig. 6.31. Influence of 1 MeV neutron irradiation on I_L-λ characteristics of InGaAs photodetectors. (After Ohyama et al. [10]).

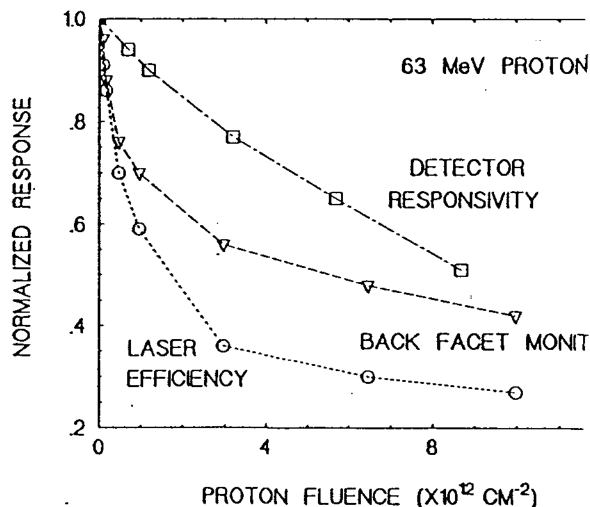

Fig. 6.32. More degradation is seen with fluence for the laser's optical and monitor outputs than for the separate InGaAs photodiode, and they vary differently with fluence. (After Marshall et al. [6]).

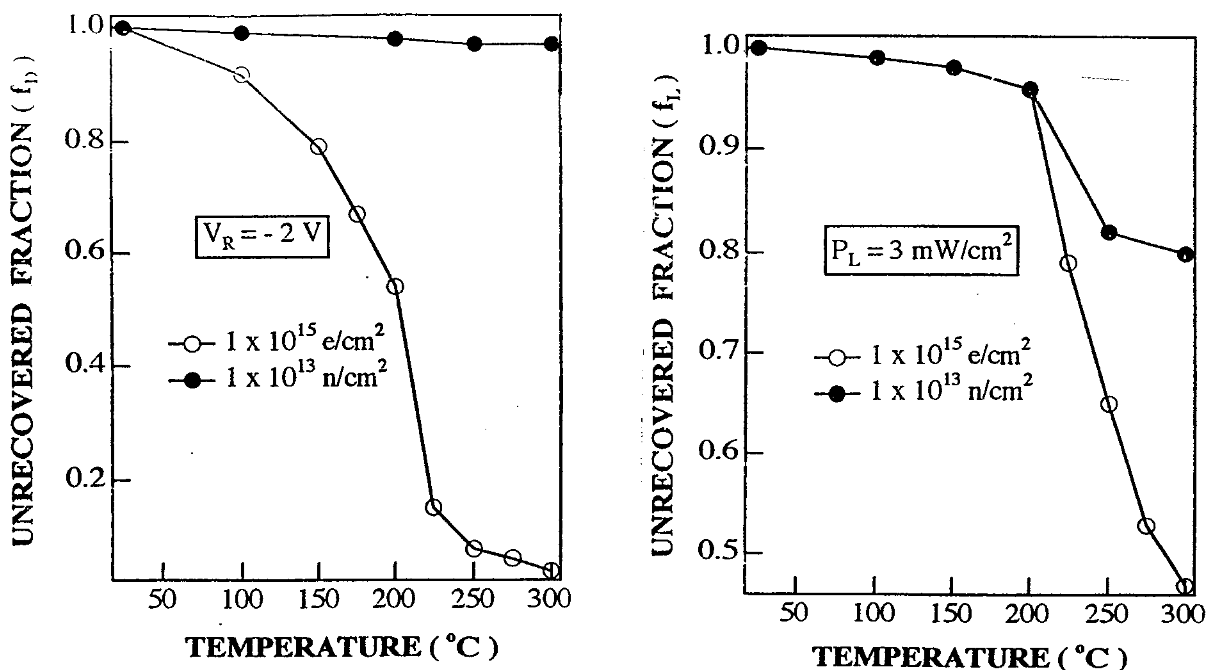

(a) (b)

Fig. 6.33. Unannealed fraction of dark current (a) and photocurrent (b) as a function of annealing temperature for a fluence of 10^{13} n/cm^2 and 10^{15} e/cm^2. (After Ohyama et al. [10]).

The annealing rate shows an activation energy in the range 0.38 eV (dark current) to 0.41 eV (photocurrent) (Fig. 6.34), which is significantly smaller than the 1.7 eV found from irradiated GaAs laser diodes [1], or the 0.9-1.1 eV activation energies found in [32] for InGaAs photodiodes. As shown in Fig. 6.35, there is a reasonable agreement between the annealing of the E_C-0.29 eV level and the dark reverse current, for 1 MeV electron irradiated PDs [24,31-32]. This is supported by the activation energy derived from the Arrhenius plot of the reverse current, shown in Fig. 6.36 [31]. It is believed that the corresponding defects are V_{As} or arsenic vacancy/impurity related defect complexes [24,31].

Ohyama and co-workers have studied in detail the radiation response of InGaAs PDs to 1 MeV neutron and electron [10,33], 20 MeV alpha's [34] and 220 MeV C [35] exposure. Assuming that the degradation of the reverse dark and photocurrent can be modeled in the same way, i.e., by:

$$I_{D,L}(\Phi) = I_{D,L}(0) + K_{D,L}\,\Phi \qquad (6.13)$$

with $I_{D,L}(0)$ the pre-radiation values, the damage factors $K_{D,L}$ for the dark (subscript D) and photocurrent (L) of Table 6.1 have been obtained. As can be seen, in first instance, there is a reasonable agreement with the calculated number of knock on atoms N_d (cm^{-3}), which scales with NIEL.

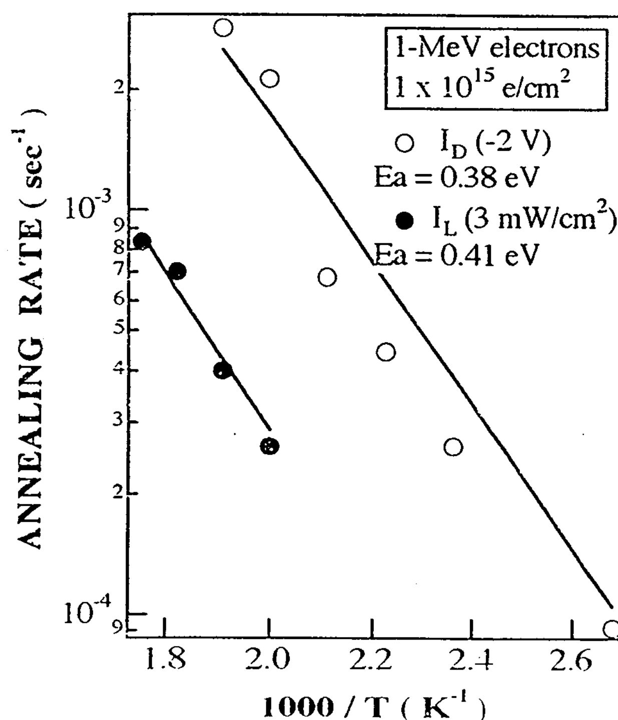

Fig. 6.34. Relationship between the annealing rate and the temperature, corresponding to 15 min isochronal annealing. (After Ohyama et al. [10]).

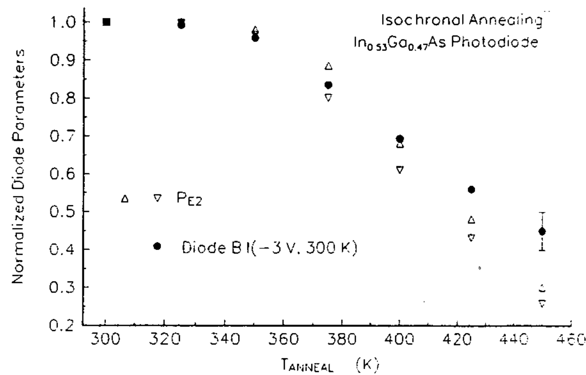

Fig. 6.35. Isochronal annealing behavior of the E2 DLTS peak height for two InGaAs photodetectors irradiated up to $6x10^{14}$ cm^{-2} 1 MeV electrons. Also shown is the annealing behavior of the reverse current of diode B as measured at -3 V and 300 K. The data are normalized to their pre-anneal values. (After Shaw et al. [31]).

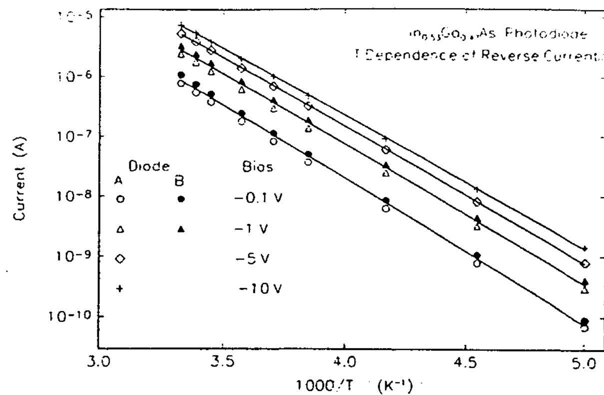

Fig. 6.36. Temperature dependence of reverse current at several voltages for diodes A and B. The solid lines are fits and E_A ranges from 0.44 to 0.4 eV as the reverse bias is increased from -0.1 to -10 V. (After Shaw et al. [31]).

A parameter, which certainly requires further study, is the low-frequency noise of the irradiated photodetectors.

The radiation response of IR QWIPs to high energy proton and alpha particles has been studied recently [11,36-37]. The impact on the dark current at 77 K of 0.8 MeV

protons is depicted in Fig. 6.37. A clear reduction of the dark current is observed, which may amount to two to three orders of magnitude for the maximum fluence studied (2.0×10^{13} p/cm^2). The corresponding spectral responsivity is shown in Fig. 6.38 [37], from which a clear drop in intensity at the central wavelength is noted. The change in operability, defined as the fractional change in responsivity D* for the same devices, under proton irradiation, is given in Fig. 6.39. Comparing the change in responsivity with the one in the dark current shows that the latter parameter is much more sensitive to irradiation. The reason is that the current across the QW is exponentially dependent on the density of electrons and, hence, the carrier removal rate in the 10^{18} cm^{-3} doped GaAs QWs, while the infrared absorption is proportional to n. The impact of the carrier removal on the current is thus much more pronounced: it generates an increase of the Schottky barrier height and a reduction of the electron mobility and lifetime. Similar results have been obtained for alpha particle and oxygen ion irradiations, whereby the degradation, as expected, increases with particle fluence and mass and with decreasing particle energy [37].

Table 6.1. Dark and photocurrent damage factors defined in Eq. (6.13) and derived for irradiated InGaAs photodetecors, exposed to different particles. In the 4th column, the calculated number of knock-on As atoms is indicated. No bias was applied during the irradiations.
*average number of In,Al and Ga atoms.

Particle	K_D (Acm^2)	K_L (Acm^2)	N_d (cm^{-3})
1 MeV e	3.8×10^{-23}	-3.5×10^{-22}	0.003
1 MeV n	8.2×10^{-21}	-8.1×10^{-20}	8.4
20 MeV α	4.5×10^{-18}	-5.5×10^{-19}	93*
220 MeV C	1.5×10^{-18}	-7.0×10^{-19}	252

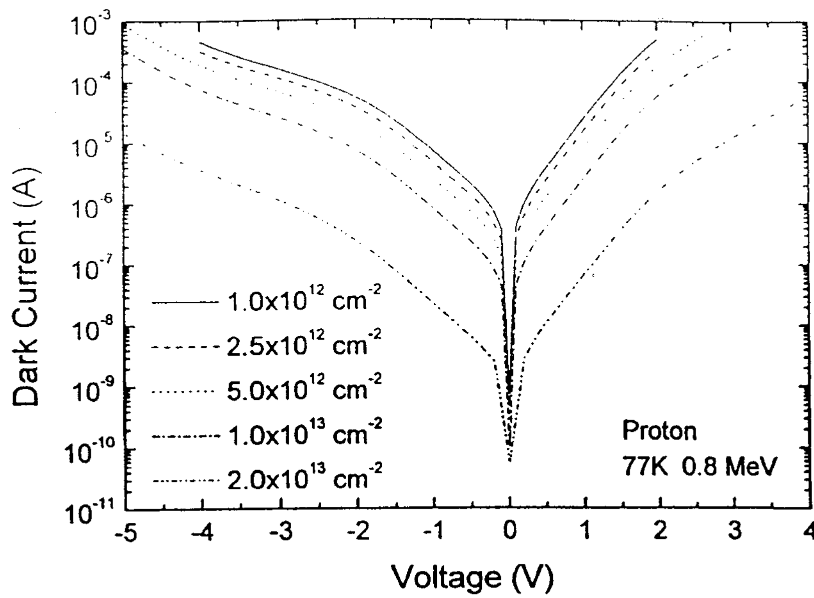

Fig. 6.37. Dark current versus bias voltage characteristics at 77 K for 0.8 MeV proton irradiated QWIPs at different fluences. (After Li et al. [37]).

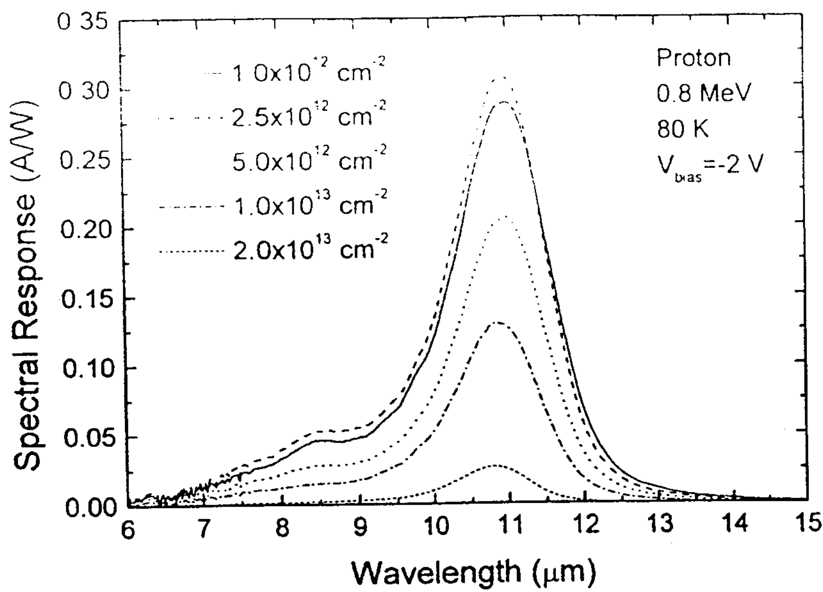

Fig. 6.38. Spectral responsivity versus wavelength characteristics at 80 K and -2 V for 0.8 MeV proton-irradiated QWIPs at different fluences. (after Li et al. [37]).

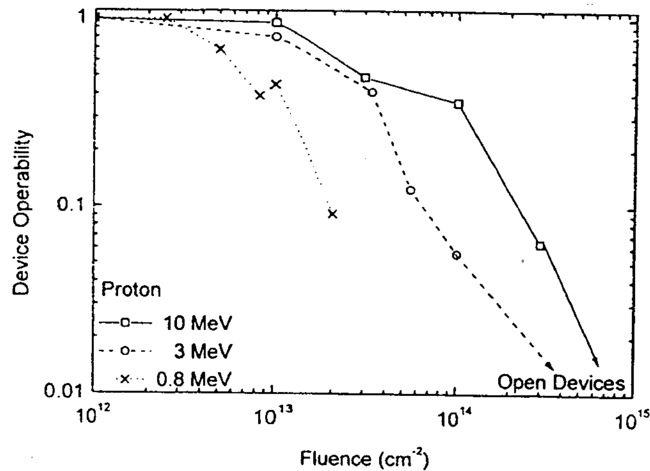

Fig. 6.39. Device operability (defined as the fractional reduction in responsivity) versus fluence for QWIPs irradiated with different high energy proton particles (After Li et al. [37]).

6.3.3 Optocouplers

The radiation response of an optocoupler is complex, since it is composed of the degradation of the LED/LD, the PD and possibly the coupling medium and optics (lenses, fibers,...). In addition, both displacements and ionization damage can play important roles depending of the type of light emitting and sensitive devices. Figure 6.40 illustrates the impact of the different parts of the optocoupler of Fig. 6.10b on the overall current transfer ratio [13], showing that for that particular type, displacement damage in the LED dominates the overall performance. In that case, a silicon bipolar phototransistor is used as photosensitive device, whereby both the current gain and the photo-response degradation should be considered. It turns out that the decrease in carrier recombination lifetime is the decisive factor for the phototransistor response, while ionization damage effects on the current gain only play a minor role in the performance degradation [13]. Using a shorter wavelength LED can substantially improve the photo-response after irradiation (e.g. 700 nm versus 850 nm), because of the smaller penetration depth of the light and the reduced sensitivity to the changes in the minority carrier diffusion length in the phototransistor [13]. Little effect of the coupling medium for the lateral structure has been found in this case.

The sandwich structure of Fig. 6.10a, on the other hand, hardly suffers from the LED degradation and, therefore, shows a better hardness (Fig. 6.41). This is partly related to the shorter wavelength of the LED, which reduces the sensitivity of the PD to the irradiations. It was also observed that the displacement damage produces more damage than the accompanying ionization by the high energy protons (Fig. 6.42) [13]. In another study,

it has been concluded that the CTR of optocouplers with an AlGaAs LED is limited by the light output degradation, while for GaAlP sources, it is the photo-response of the detector which is the major mechanism [12].

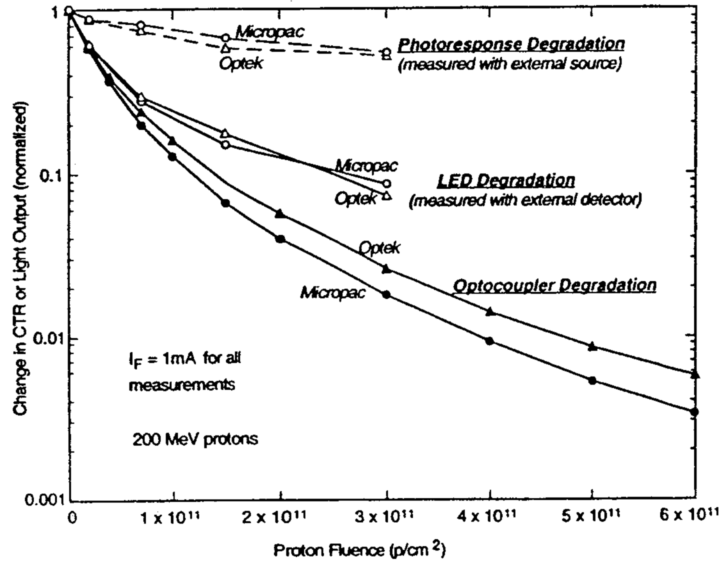

Fig. 6.40. Effects of proton degradation for photo-response, LED, and optocoupler. (After Rax et al. [13]).

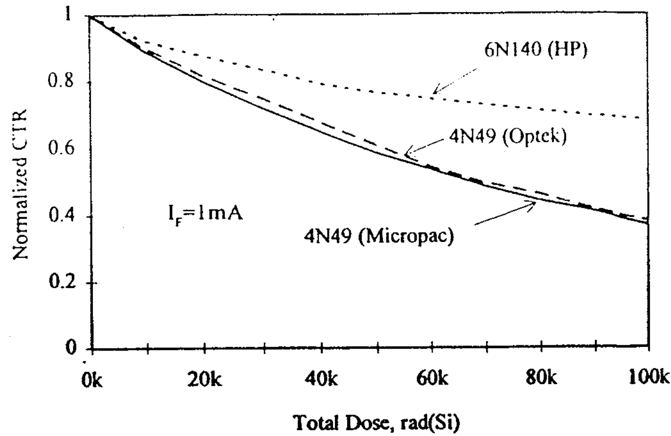

Fig. 6.41. Comparison of CTR degradation for two types of optocouplers after irradiation with cobalt-60 gamma rays. (After Rax et al. [13]).

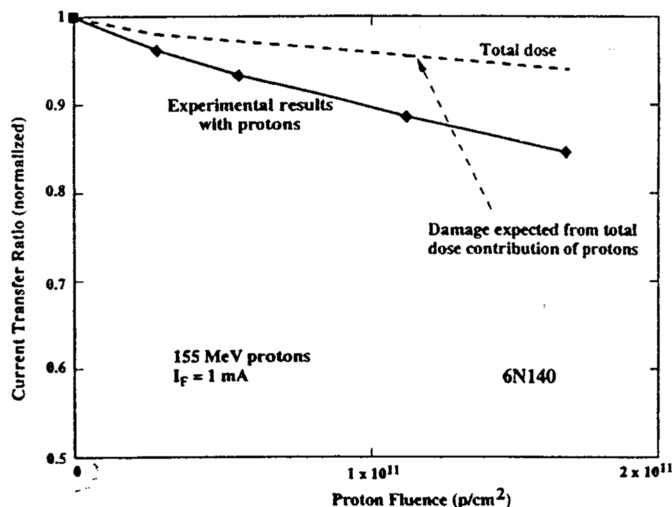

Fig. 6.42. Comparison of measured CTR degradation with calculated degradation from displacement damage of the phototransistor. The main reason for the difference is the shorter penetration depth of the 700 nm wavelength, which reduces the effect of changes in diffusion length (with displacement damage). (After Rax et al. [13]).

Another emerging issue for broad band systems is the occurrence of single event upsets and transients [12]. Finally, it has been demonstrated that state-of-the art devices can be used for CERN's Large Hadron Collider (LHC), even for the parts operating at liquid argon temperatures [38]. It is furthermore shown that the radiation induced increase of the LF noise of the LEDs and LDs is within acceptable ranges. Compared with more classical structures, QW LEDs show the largest radiation resistance (Fig. 6.43), in agreement with other reports [8].

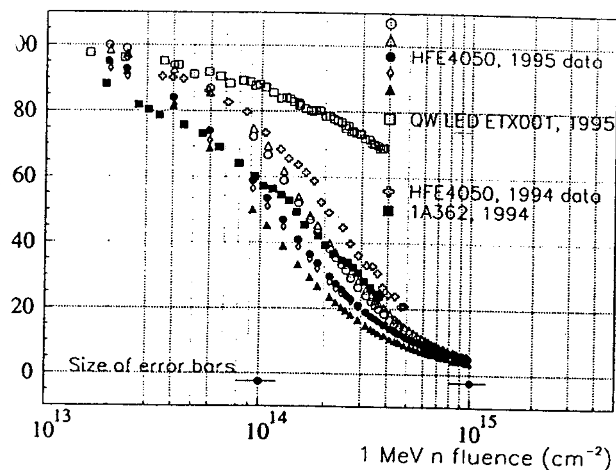

Fig. 6.43. LED output as a function of received neutron fluence. (After Söderqvist et al. [38]).

6.4 Conclusions

The new generation of III-V based light sources and detectors show great promise for space applications and in a radiation environment. However, since these technologies are under development, substantial radiation testing is necessary in order to verify their suitability for space photonics. There is also a lack of basic damage knowledge, compared with GaAs. While the latter material has been studied since the early 60ties, radiation defects in ternary compounds are still rather unexplored. Initial studies indicate that although there are definitely some links with the simple Frenkel defects in GaAs, the situation may become quite complex due to alloying. It is also clear that while for MESFET and HEMT devices carrier removal is the dominant effect, the opto-electronic components suffer mainly from a decrease of the carrier lifetime. Especially for the case of the photodetectors, LF noise studies would be welcome, in order to determine the impact on the detectivity. Additionally, they could provide fundamental information on the radiation defects. A final important observation is the fact that the operation bias of light sources during irradiation (and also during testing, although to a minor extent) dramatically changes the radiation response. Meaningful testing, therefore, should be performed as close as possible under realistic operation (biasing) conditions.

References

[1] C.E. Barnes, "Effects of Co^{60} gamma irradiation on epitaxial GaAs laser diodes", Phys. Rev B **1**, 4735 (1970).

[2] C.E. Barnes, "A comparison of gamma-irradiation-induced degradation in amphoterically Si-doped GaAs LED's and Zn-diffused GaAs LED's", IEEE Trans. Electron Devices **26**, 739 (1979).

[3] B.H. Rose and C.E. Barnes, "Proton damage effects on light emitting diodes", J. Appl. Phys. **53**, 1772 (1982).

[4] K.C. Dimiduk, C.Q. Ness and J.K. Foley, "Electron irradiation of GaAsP LEDs", IEEE Trans. Nucl. Sci. **32**, 4010 (1985).

[5] B.D. Evans, H.E. Hager and B.W. Hughlock, "5.5-MeV proton irradiation of a strained quamtum-well laser diode and a multiple quantum-well broad-band LED", IEEE Trans. Nucl. Sci. **40**, 1645 (1993).

[6] P.W. Marshall, C.J. Dale and E.A. Burke, "Space radiation effects on optoelectronic materials and components for a 1300 nm fiber optic data bus", IEEE Trans. Nucl. Sci. **39**, 1982 (1992).

[7] R.F. Carson and W.W. Chow, "Neutron effects in high-power GaAs laser diodes", IEEE Trans. Nucl. Sci. **36**, 2076 (1989).

[8] Y.F. Zhao, A.R. Patwary, R.D. Schrimpf, M.A. Neitfeld and K.F. Galloway, "200 MeV proton damage effects on multi-quantum well laser diodes", IEEE Trans. Nucl. Sci. **44**, 1898 (1997).

[9] A.H. Paxton, R.F. Carson, H. Schöne, E.W. Taylor, K.D. Choquette, H.Q. Hou, K.L. Lear and M.E. Warren, "Damage from proton irradiation of vertical-cavity surface-emitting lasers", IEEE Trans. Nucl. Sci. **44**, 1893 (1997).

[10] H. Ohyama, J. Vanhellemont, Y. Takami, K. Hayama, T. Kudou, T. Hakata, S. Kohiki and H. Sunaga, "Degradation and recovery of $In_{0.53}Ga_{0.47}As$ photodiodes by 1-MeV fast neutrons", IEEE Trans. Nucl. Sci. **43**, 3019 (1996).

[11] S.M. Khanna, H.C. Liu, P.H. Wilson, L. Li and M. Buchanan, "High energy proton and alpha radiation effects on GaAs/AlGaAs quantum well infrared photodetectors", IEEE Trans. Nucl. Sci. **43**, 3012 (1996).

[12] R.A. Reed, P.W. Marshall, A.H. Johnston, J.L. Barth, C.J. Marshall, K.A. LaBel, M. D'Ordine, H.S. Kim and M.A. Carts, "Emerging optocoupler issues with energetic particle-induced transients and permanent radiation damage", IEEE Trans. Nucl. Sci. **45**, 2833 (1998).

[13] B.G. Rax, C.I. Lee, A.H. Johnston and C.E. Barnes, "Total dose and proton damage in optocouplers", IEEE Trans. Nucl. Sci. **43**, 3167 (1996).

[14] A.L. Barry, A.J. Houdayer, P.F. Hinrichsen, W.G. Letourneau and J. Vincent, "The energy dependence of lifetime damage constants in GaAs LEDs for 1 - 500 MeV protons", IEEE Trans. Nucl. Sci. **42**, 2104 (1995).

[15] G.P. Summers, E.A. Burke, M.A. Xapsos, C.J. Dale, P.W. Marshall and E.L. Petersen, "Displacement damage in GaAs structures", IEEE Trans. Nucl. Sci. **35**, 1221 (1988).

[16] A.L. Barry, R. Wojcik and A.L. MacDiarmid, "Response of GaAs displacement damage monitors to protons, electrons and gamma irradiation", IEEE Trans. Nucl. Sci. **36**, 2400 (1989).

[17] G.H. Yousefi, J.B. Webb, R. Rousina and S.M. Khanna, "Electron irradiation induced defects and Schottky diode characteristics for Metalorganic Vapor Phase Epitaxy and Molecular Beam Epitaxial n-GaAs", J. Electron. Materials **24,** 15 (1995).

[18] M.A. Zaidi, H. Maaref, M. Zazoui and J.C. Bourgoin, "Defects in electron-irradiated GaAlAs alloys", J. Appl. Phys. **74** , 284 (1993).

[19] H. Chaabane and J.C. Bourgoin, "Irradiation effect in electron transport through GaAlAs barriers", Appl. Phys. Lett. **64**, 1006 (1994).

[20] M. Papastamatiou, N. Arpatzanis, G.J. Papaioannou, C. Papastergiou and A. Christou, "Neutron radiation effects in high electron mobility transistors", IEEE Trans. Electron Devices **44**, 364 (1997).

[21] A.C. Irvine and D.W. Palmer, "Demonstration of gallium-annealing at 280 K in irradiated GaAs and $Al_xGa_{1-x}As$", Phys. Rev. B **49**, 5695 (1994).

[22] W.O. Siyanbola and D.W. Palmer, "Low temperature annealing of deep electron traps produced by proton irradiation of n-GaAs", Semicond. Sci. Technol. **5**, 7 (1990).

[23] W.O. Siyanbola and D.W. Palmer, "Electronic energy levels of defects that anneal in the 280-K stage in irradiated n-type gallium arsenide", Phys. Rev. Lett. **66**, 56 (1991).

[24] R.J. Walters, G.J. Shaw, G.P. Summers, E.A. Burke and S.R. Messenger, "Radiation effects in $Ga_{0.47}In_{0.53}As$ devices", IEEE Trans. Nucl. Sci. **39**, 2257 (1992).

[25] D. Comedi, J. Zhao, K. Jankowska, D.A. Thompson and J. Simmons, "High-resistivity regions in n-type InGaAsP produced by $^4He^+$ ion bombardment at 80 and 300 K", Appl. Phys. Lett. **63**, 2126 (1993).

[26] A. Jolly and J. Vicrey, "Modelling threshold shift of power laser diodes under neutronic and photonic irradiation", In Proc. RADECS '93, The IEEE (New York), pp. 232-238 (1994).

[27] Y.F. Zhao, R.D. Schrimpf, A.R. Patwary, M.A. Neifeld, A.W. Al-Johani, R.A. Weller and K.F. Galloway, "Annealing effects on multi-quantum well laser diodes after proton irradiation", IEEE Trans. Nucl. Sci. **45**, 2826 (1998).

[28] L.C. Kimerling, "Recombination enhanced defect reactions", Solid-State Electron. **21**, 1391 (1978).

[29] H. Lischka, H. Henschel, W. Lennartz and H.U. Schmidt, "Radiation sensitivity of light emitting diodes (LED), Lased Diodes (LD) and Photodiodes (PD)", In Proc. RADECS 1991, The IEEE (New York), pp. 423-427 (1992).

[30] H. Lischka, H. Henschel, O. Köhn, W. Lennartz and H.U. Schmidt, "Radiation effects in light emitting diodes, laser diodes, photodiodes and optocouplers", In Proc. RADECS 1993, The IEEE (New York), pp. 226-231 (1994).

[31] G.J. Shaw, S.R. Messenger, R.J. Walters and G.P. Summers, "Radiation-induced reverse dark currents in $In_{0.53}Ga_{0.47}As$ photodiodes", J. Appl. Phys. **73**, 7244 (1993).

[32] G.J. Shaw, R.J. Walters, S.R. Messenger and G.P. Summers, "Time dependence of radiation-induced generation currents in irradiated InGaAs photodiodes", J. Appl. Phys. **74**, 1629 (1993).

[33] H. Ohyama, J. Vanhellemont, Y. Takami, K. Hayama, T. Kudou, S. Kohiki, H. Sunaga and T. Hakata, "Degradation of InGaAs pin photodiodes by neutron irradiation", Semicond. Sci. Technol. **11**, 1461 (1996).

[34] H. Ohyama, E. Simoen, C. Claeys, Y. Takami, T. Kudou and H. Sunaga, "Radiation source dependence of degradation and recovery of irradiated $In_{0.53}Ga_{0.47}As$ PIN photodiodes", In Proc. RADECS '97, Eds G. Barbottin and P. Dressendorfer, The IEEE (New York), pp. 108-113 (1998).

[35] T. Kudou, H. Ohyama, E. Simoen, C. Claeys, Y. Takami, K. Shigaki, A. Fujii and H. Sunaga, "Radiation damage of InGaAs photodiodes by high energy particles", Mat. Res. Soc. Proc. Vol. **487**, pp. 471-476 (1998).

[36] H.C. Liu, P.H. Wilson, M. Buchanan and S.M. Khanna, "Nulear radiation effects on GaAs/AlGaAs quantum well inrared photodetectors", In Proc. SPIE Vol **2746**, pp. 134-141 (1996).

[37] L. Li, H.C. Liu, P.H. Wilson, M. Buchanan and S.M. Khanna, "Influence of high energy particle radiation on GaAs/AlGaAs quantum well infrared photodetectors", Semicond. Sci. Technol. **12**, 947 (1997).

[38] J. Söderqvist, L.O. Eek, J. Collot, J.P. Coulon, B. Dinkespiler, J.Y. Hostachy, M. Jevaud, B. Lund-Jensen, B. Merkel, E. Monnier, C. Olivetto, P. de Saintignon and S. Tisserant, "Radiation hardness evaluation of an analogue optical link for operation at cryogenic temperatures", IEEE Trans. Nucl. Sci. **44**, 861 (1997).

7. FERROELECTRIC MATERIALS AND DEVICES FOR SPACE

The research activities on ferroelectric materials and devices, aiming at the development of ferroelectric memories started already in the middle of the 50ties. Considerable efforts have been undertaken by IBM, RCA and Bell laboratories and were in the first place oriented towards fundamental material research in order to obtain on an industrial scale ferroelectric layers with the desired properties. Presently a variety of techniques for depositing very thin, pinhole-free films are available; sputtering, sol-gel spin-on, laser ablation, MOCVD..... can be used for preparing optically uniform films over large areas up to 150 mm and capable of withstanding more than 4 MV/cm. Beside the memory field, another strong growing application field are the infrared sensors, used for remote sensing, biomedical thermography, gas detection and alarms [1]. In this case the pyroelectric properties of the material are important. These are expressed by a figure of Merit FM, given by

$$FM = p/\varepsilon c \qquad (7.1)$$

with p a pyroelectric coefficient, ε the dielectric constant and c the specific heat. High FMs can be correlated with the Curie temperature of the material. Interesting materials with a high Curie temperature are $PbTiO_3$ and $LiTaO_3$. The most promising ferroelectric materials are belonging to the PZT ($PbZr_xTi_{1-x}O_3$) group.

In order for the ferroelectric materials and devices to achieve a market breakthrough, work is needed on materials, i.e. optimization of the electrical characteristics and reliability, on device operation physics enabling the development of simulation models for the ferroelectric switching associated with circuits, and on process development for obtaining specific process steps and modules which are compatible with the standard IC processing. For the latter, issues such as contamination control and cleaning aspects are crucial. A good review of the ferroelectric thin films and devices can be found in ref. [2]. Also IMEC is very active in the field of ferroelectrics for non-volatile memories. As within the frame of a present ESA contract the radiation hardness of ferroelectric materials is under study, this chapter will be kept short and only highlight the present status.

7.1 IMECs Activities on Ferroelectrics

7.1.1 Material Aspects

IMEC has mainly been focussing on PZT material, whereby a new technique has been developed based on spin-coating of liquid metal-alkoxide sol-gel precursors. This approach allows very uniform PZT films of 200 nm thickness. The films have preferential (111) orientation, controlled by the bottom Pt-electrode structure [3] resulting in optimized hysteresis characteristics [4]. For implementation in electronic memories, the film thickness scaling is an essential parameter. Presently the thickness can be reduced below 50 nm,

without degradation of the remanent polarization and of hysteresis loop rectangularity. The 50 nm film retain a large polarization of 30 μC/cm^2 and show fully saturated switching at only 1.5 V [5].

To improve the endurance of ferroelectric capacitors, work on RuO_2 electrodes is performed. These layers are deposited by reactive sputtering, whereby a good control of the oxygen partial pressure, substrate heating and time delay between electrode deposition and PZT are important parameters. An illustration of the good hysteresis characteristics is given in Fig. 7.1.

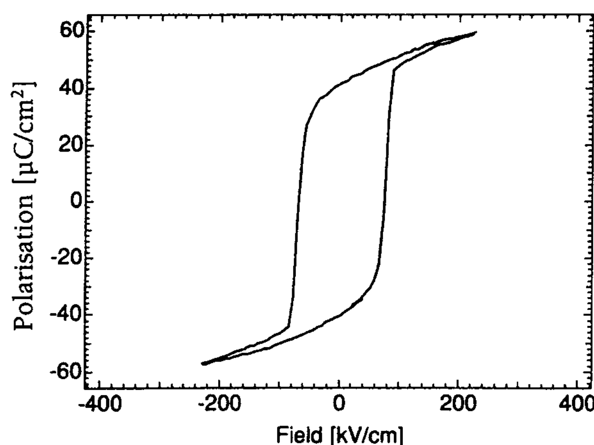

Fig. 7.1. Illustration of the hysteresis characteristics of a ferroelectric capacitor with a 200 nm PZT film on RuO_2, showing a good rectangularity and a polarization of 39 μC/cm^2. (After Wouters et al. [5]).

7.1.2 Device Research

The strong interest in ferroelectrics is related to digital memories, and more in specific the non-volatile memories. Figure 7.2 gives a schematic overview of the 14 different families of memories that are used in the microelectronic computer industry. The FRAM (Ferroelectric Random Access Memory) gives a good performance for a reduced cost. A special feature is the non-volatile aspect, whereby the memory information is not lost when the electric power is switched off.

Although the fundamental material research has been done on capacitors, IMEC is also fabricating non-volatile memories. In this case the main issue is the implementation of the ferroelectric layer in a CMOS technology, whereby special precautions have to be taken in order to avoid contamination. For the moment, the integration in a full 0.5 μm CMOS technology is on going. Special attention is given to the dry etching and the isolation aspects. A 1 Mb RAM is being processed as a demonstrator.

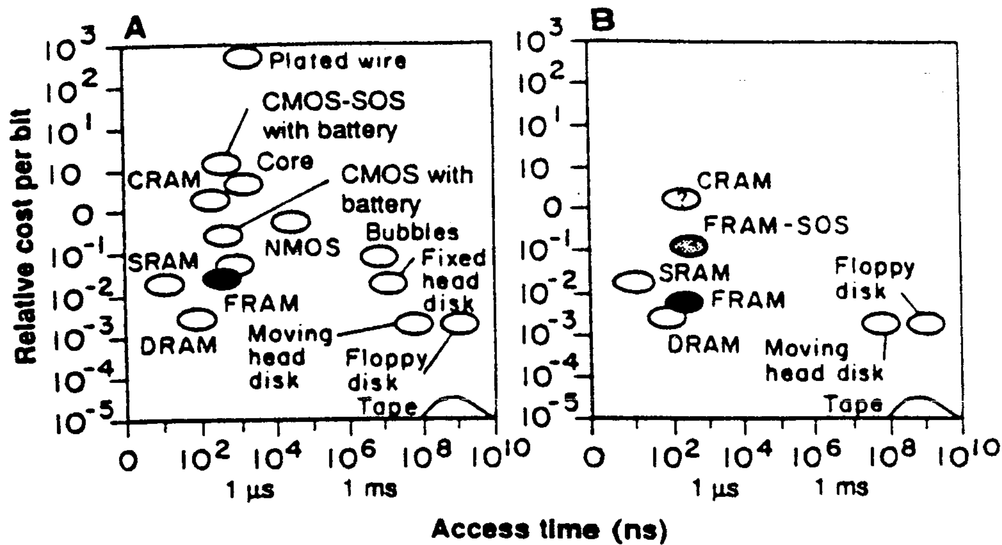

Fig. 7.2. Cost per bit versus access time for 14 generic digital memories (log-log plot): A) 1988, FRAM introduction; B) projections for 1998: SOS (Silicon-on-Sapphire), NMOS (Nitride Metal Oxide Semiconductor), CRAM (Crosstie permalloy RAM). The vertical scale is approximately 1 cent/bit. (After Scott et al. [2]).

7.2 Radiation Hardness of Ferroelectric Materials and Devices

For use in space applications, the radiation hardness of ferroelectric materials has been studied, although the available literature is limited. There are some conflicting data reported, whereby a severe degradation of PZT films occurred already at 1 Mrad, while other observed satisfactory behavior up to 100 Mrad, far exceeding military requirements for aircraft, space satellite or missile use [6]. Within the frame of a present ESA contract, IMEC has studied more in detail the radiation hardness of their technology. As the full report is available, only some highlights are reported here.

7.2.1 Purpose of the Testing

The purpose of the test was twofold:

a) to evaluate the radiation resistance of the IMEC ferroelectric PZT capacitors.

Ferroelectric capacitors, in particular PZT-based, are reported to have high radiation resistance, up to extremely large doses (> 5Mrad total dose and $2x10^{11}$ rad/s for gamma-irradiation [7]). However, reported results on radiation tests based on only hysteresis measurements should be interpreted with care, as effects can be induced that are important for memory operation but that are unrevealed by hysteresis measurements alone. For instance, irradiation of Pt-electroded PZT capacitors (with 10-keV Xrays at 17 krad/min) induced only very little changes in the ferroelectric P-E hysteresis loops up to 1.7 Mrad, while strong degradation of the ferroelectric switching charges in short-time pulse

measurements has been observed. Therefore, for a particular technology, one should carefully evaluate both the hysteresis and "memory" pulse measurements.

b) to evaluate the radiation resistance of the 0.5μm IMEC CMOS process

For making ferroelectric memories, ferroelectric capacitors have to be integrated with CMOS. The radiation tolerance of the memory hence will be limited also by the radiation resistance of the CMOS part. Previous tests have been performed on the IMEC non-volatile memory 1.25 μm CMOS process (see ESTEC/Contract No.: 8615/90/NL/PM(SC), Call-off order No.5, WO4 –Pleiades, Work Order "The development of a 1.25μm N-well CMOS DLM Non-Volatile Memory Process", Deliverable D8, Doc.No: P30270-IM-RP-0033, June 1992). Strong transistor degradation effects (in particular excessive field leakage) were observed from doses at or above 10 krad on NMOS transistors with positively biased gate. As the dimensions of all oxide layers (gate oxide and also field oxide thickness) are reduced for the 0.5 μm process compared to the 1.25 μm process, a better radiation tolerance can be expected for the 0.5 μm process. This has been discussed in detail in Chapter 4. This part of the test report is not further addressed here.

7.2.2 Experimental Test Conditions

Ferroelectric capacitors (FECAP's) with Pt top and bottom electrode, with PZT composition Zr/Ti=20/80 and film thickness of 200nm were tested by hysteresis and pulse measurements. FECAP's with top electrode area of 1000 μm^2 were used for the measurements. Four sample capacitors were then mounted on the boards containing also the MOSFET test samples. During irradiation, the capacitors were left in open circuit condition. This corresponds to information storage in a real memory, where the information-containing FECAP is also disconnected from the circuitry through the select transistor.

The irradiations were performed at the radiation facility of the Université Catholique de Louvain at Louvain-la-Neuve using a ^{60}Co source, which produces high energetic gamma rays. The placement of the samples was calculated to result in a radiation dose rate of 5 krad/hr. Four different total doses were applied: 5 krad, 10 krad, 15 krad and 20 krad. The MOSFET gates were biased to +3V during irradiation, while the FECAPs were unbiased (open circuit conditions).

7.2.3 Experimental Results on Ferroelectric Capacitors

Hysteresis measurements

Ferroelectric hysteresis loops were measured with a Modified Sawyer-Tower circuit, i.e. with an analog integrator with virtual ground input stage in parallel to the test ferroelectric capacitor (instead of a fixed measurement capacitor as in the standard Sawyer-Tower test circuit). Figures 7.3a (before irradiation) and 7.4a (after 20Krad irradiation) show a set of "nested" hysteresis loops, measured with a 1-10V amplitude 1kHz triangular drive signal (the horizontal axis was converted to electrical field assuming 200nm film thickness).

Figures 7.3b (before irradiation) and 7.4b (after 20Krad irradiation) show the remanent polarization (Pr) and maximum polarization (Pmax) (both positive and negative polarization) as function of amplitude, calculated from these sets of nested hysteresis loops

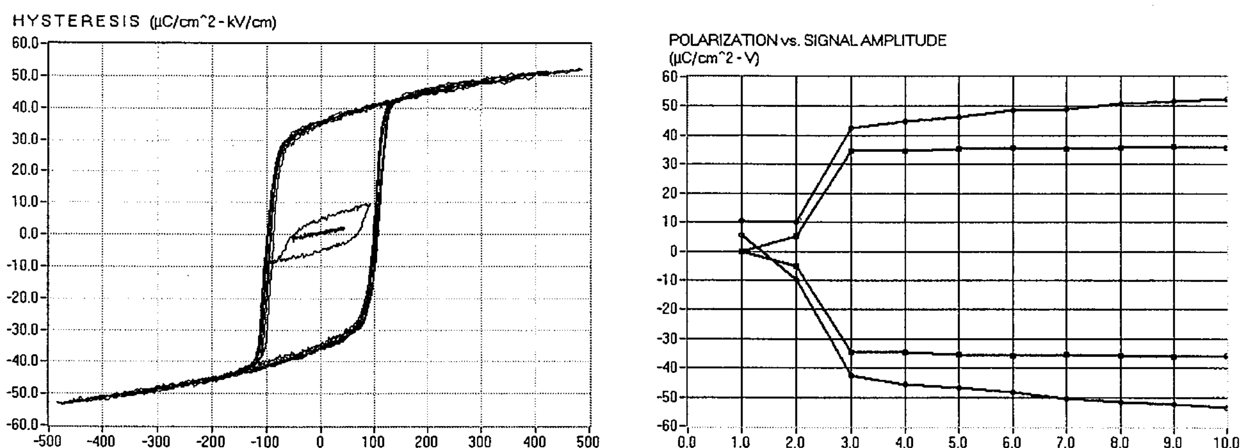

Fig. 7.3 Hysteresis measurement results for non-irradiated sample. A) P-E loops, 1kHz, 1-10V amplitude; b) remanent polarization (Pr) and maximum polarization (Pmax) as function of signal amplitude.

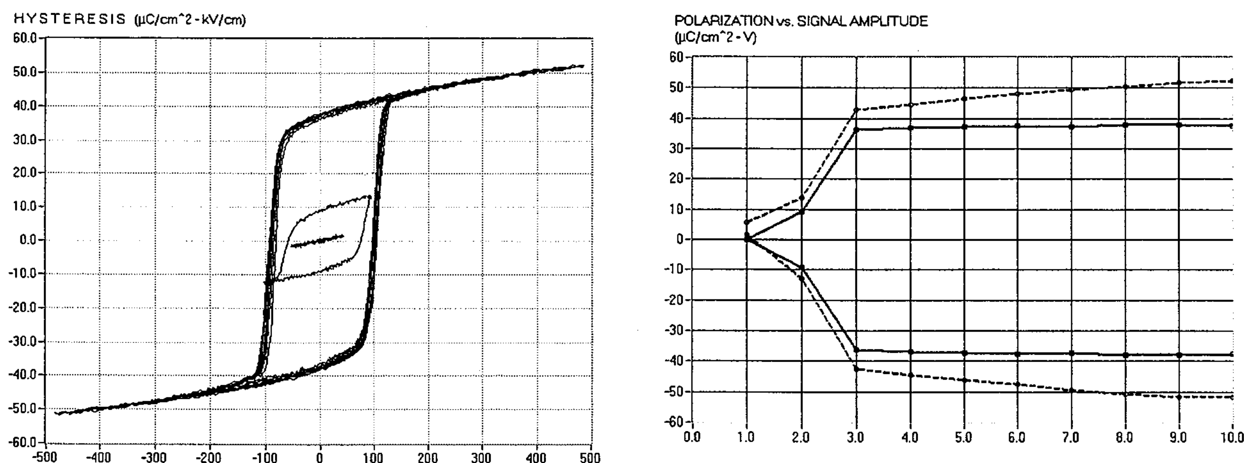

Fig. 7.4. Hysteresis measurements results for a 20 krad irradiated sample. a) P-E loops, 1 kHz, 1-10 V amplitude; b) remanent polarization (Pr) and maximum polarization (Pmax) as function of signal amplitude.

No degradation of the ferroelectric hysteresis loops could be observed. Very rectangular hysteresis loops are measured both before and after irradiation, with saturated remanent polarization Pr values > 35 $\mu C/cm^2$ from amplitudes equal or larger than 3 V (minimum switching voltage). Coercive fields are about 100kV/cm (corresponding to a coercive voltage of 2 V); at 2 V amplitude partial switching is obtained.

Pulse measurements

To check in more detail possible degradation of the ferroelectric switching behavior at short times (i.e., relevant for memory operation), pulse measurements were performed on 1000 $_{\mu}$m2 area FECAPs by voltage pulses with 5-10 nsec rise time and 150 nsec width. From the integrated current response, both (positive and negative) switched charge Q_S and (positive and negative) non-switched charge Q_{ns} were determined, resulting in the memory "window" Q_S-Q_{ns} that, for ideal behavior should be equal to 2xPr as determined by the hysteresis measurements.

In a first series of experiments, a set of pulse measurements with varying pulse amplitude was performed, revealing the dependencies on the charges Q_S, Q_{ns} and Q_S-Q_{ns} versus pulse amplitude, see Fig. 7.5 (before irradiation) and Fig. 7.6 (after 20 krad irradiation), to be compared with Figs. 7.3b and Fig. 7.4b, respectively

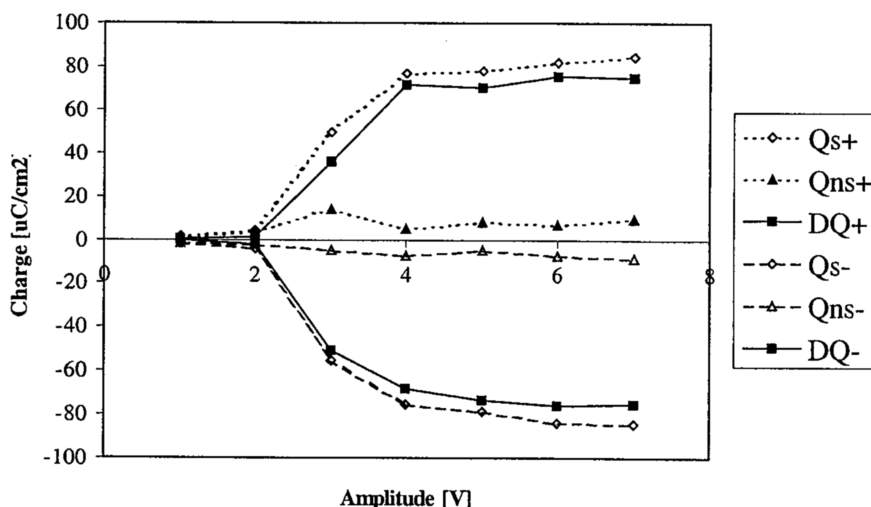

Fig. 7.5. Pulse charge measurements before irradiation.

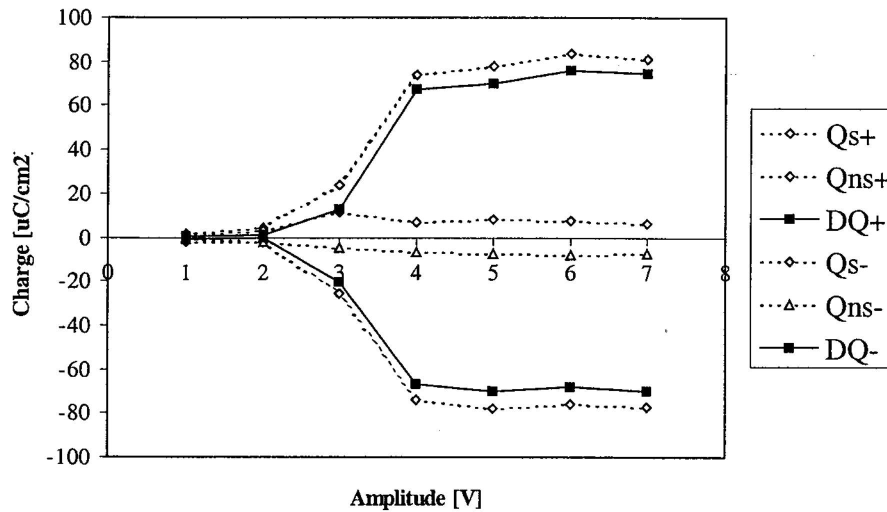

Fig. 7.6. Pulse charge measurements after 20 krad irradiation

Both for the non-irradiated and the 20 krad irradiated sample, Q_S-Q_{ns} values of 70 μC/cm^2, in excellent correspondence with 2xPr from the 1 kHz hysteresis measurements, are obtained for pulse amplitudes equal or larger than 4 V. It has to be remarked that many publications on PZT or SBT based ferroelectric capacitors report a deviation between the results of pulse and hysteresis measurements, that has been attributed to short-time relaxation. In general the term Pnv = "true" volatile polarization has been defined with Pnv<Pr as measured by continuous hysteresis loop. For our samples, such deviation is not observed, indicating absence of fast relaxation components of the polarization.

The discrepancy between the hysteresis results at 3 V amplitude (full saturation) and the pulse measurements at 3 V amplitude are due to slower switching speed at lower voltage, resulting in a switching time > than the 150 nsec pulse width. It has to be remarked here that this switching speed is extrinsic controlled and increases with the capacitor area. In real memory applications FECAP area and switching time will be much smaller than obtained here for 1000 μm^2 capacitors. The equal results obtained on samples with and without irradiation indicate that no degradation of the switching has taken place. To further examine in detail the switching characteristics, also pulse delay dependence and pulse width dependence measurements are performed.

Pulse delay dependence

In the pulse delay measurement, the dependence of the measured charges (Q_S and Q_{ns}) on the delay time between program and read pulses is measured. This test probes the short-time retention properties of the programmed polarization, and may reveal the existence of short-time relaxation effects. Figures 7.7 and 7.8 give the result before and after 20 kKrad irradiation.

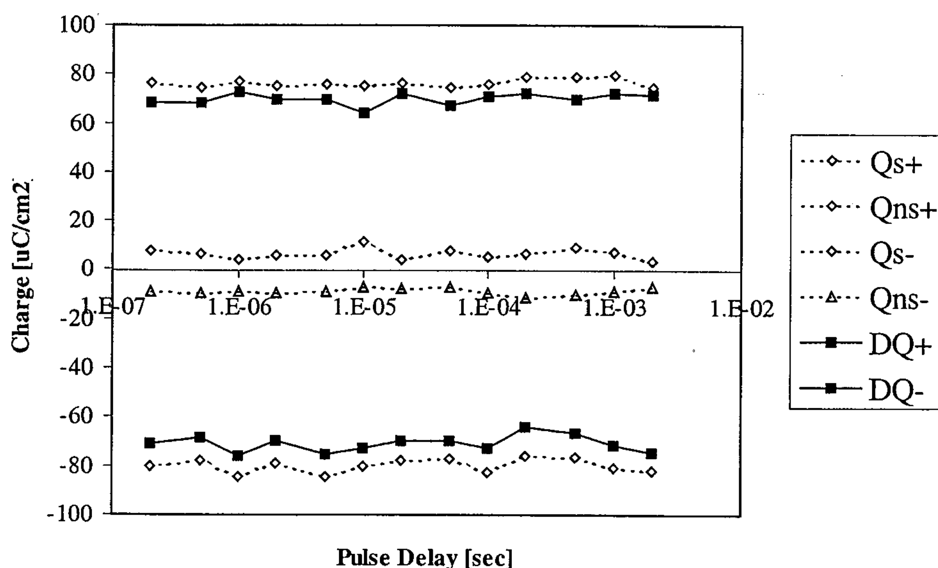

Fig. 7.7. Pulse delay dependence, sample before irradiation

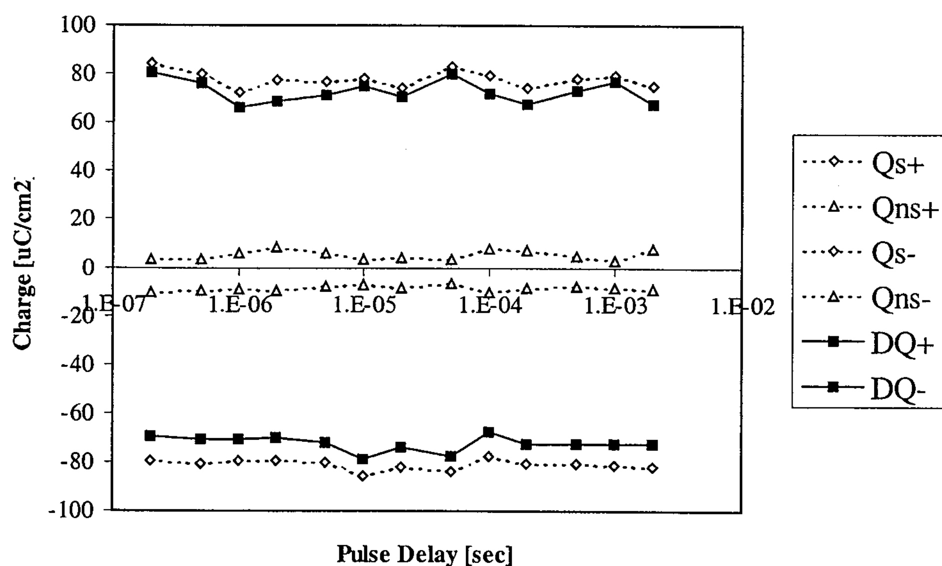

Fig. 7.8 Pulse delay dependence, sample after 20 krad irradiation

Pulse width dependence measurements

Pulse width dependence measurements probe the possible existence of slow programming effects. For poor samples, an increase of the switched charges with increasing programming pulse width has indeed been observed (although by constant measurement integration time). Experimental data are shown in Figs 7.9 and 7.10.

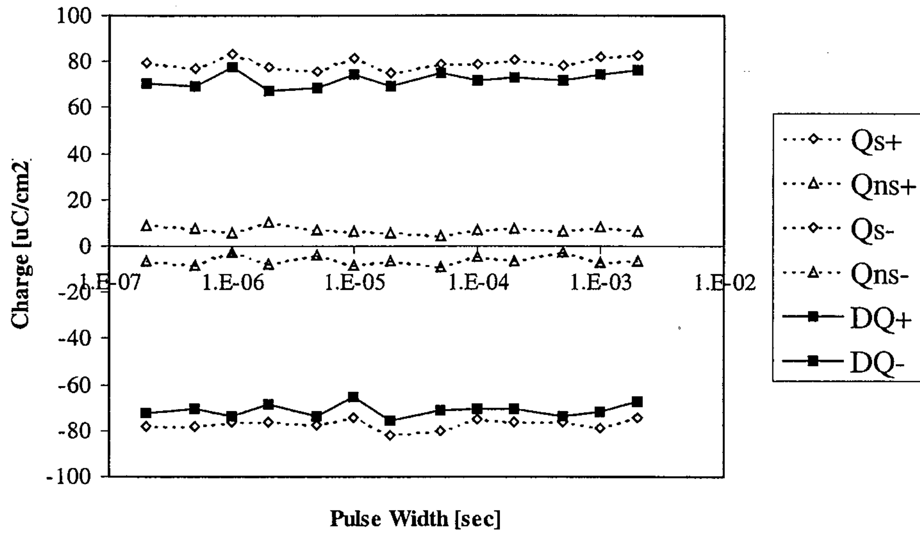

Fig. 7.9. Pulse width dependence of sample before irradiation

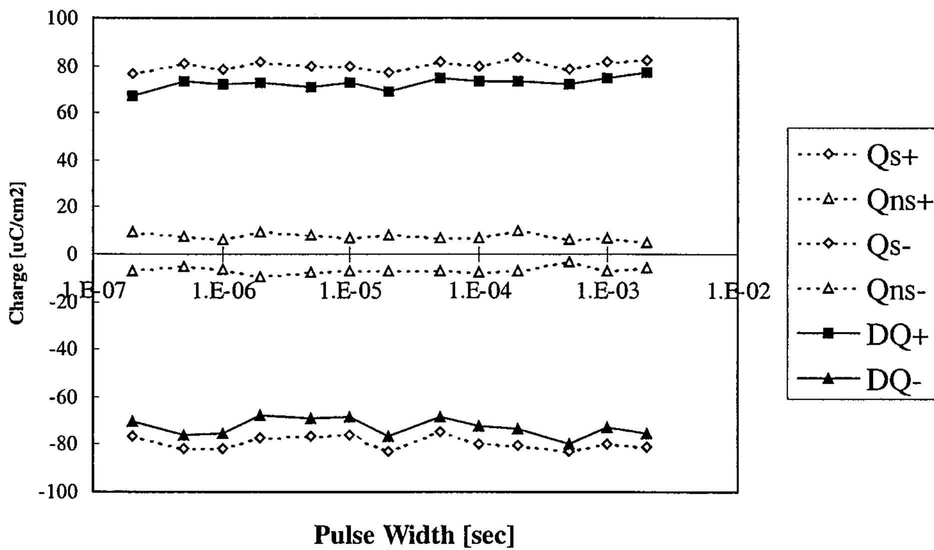

Fig. 7.10. Pulse width dependence of sample after 20 krad irradiation

From the pulse measurements, two important facts can be observed:

- there is an excellent correspondence between the results of hysteresis and pulse measurements. From the pulse delay and pulse with measurements, this is due to the absence of important rapid relaxation or slow programming effects. This property was already reported for our sol-gel PZT capacitors. It has to be remarked that for the capacitors of ref. [6], whereby a strong degradation of the pulse measurement characteristics was observed, even for the non-irradiated sample a strong deviation

between hysteresis and pulse measurements was observed, and also a strong short time relaxation effect (20% loss of Pr in 1 msec!).

- there is no degradation of the characteristics after 20 krad radiation dose. The measured radiation-induced damage in the samples in [7] hence may be due to the presence of defects (like oxygen vacancies) in these samples that are also causing the short-time relaxation effect.

7.3 Conclusions

This brief report points out that FZT ferroelectrics has a good potential for non-volatile memories to be used for space applications. Initial testing demonstrated that no degradation is observed after 20 krad. It should be kept in mind, however, that so far only gamma testing has been performed. Additional testing on other high-energy particles is required in the future in order to obtain a complete picture of the radiation performance of ferroelectric materials and devices.

References

[1] F.Y. Chen, Y.K. Fang, C.Y. Shu and J.-R. Chen, "Numerical analysis of $PbTiO_3$ ferroelectric thin-film infrared optical diode", IEEE Trans. Electron Devices **44**, 937 (1997)

[2] J.F. Scott, C. A. Araujo, and L.D. McMillan, "Ferroelectric thin films and thin film devices", in Ferroelectric Ceramics, Eds N. Setter and E.L. Colla, Birkhauser Verlag, Berlin, 185 (1993).

[3] G. Willems, D. Wouters, H.E. Maes and R. Nouwen, "Nucleation and orientation of sol-gel PZT films on Pt electronics", Integrated Ferroelectrics **15**, 19 (1997).

[4] D. Wouters, G. Willems, E. Lee and H.E. Maes, "Elucidation of the switching process in tetragonal PZT by hysteresis loop and impedance analysis", Integrated Ferroelectrics **15**, 79 (1997).

[5] D. Wouters, G. Norga, F. Beckers, L. Bogaerts and H.E. Maes, "Scaling of sol-gel PZT ferroelectric capacitors for low voltage operation", in Proc. 9th Int. Symp. on Integrated Ferroelectrics (ISIF).

[6] R.A. Moore, J. Benedetto and B.J. Rod, "Total dose efffects on ferroelectric PZT capacitors used as non-volatile storage elements", IEEE Trans. Nucl. Sci. **40**, 1591 (1993).

[7] J.F. Scott, C. A. Araujo, H. Bret Meadows, L.D. McMillan, S. Shawabkeh, "Radiation effects on ferroelectric thin film memories: Retention failure mechanisms", J. Appl. Phys. **66**, (1989) 1444.

8. CONCLUSIONS AND FUTURE ACTIVITIES

The most important conclusions resulting from this critical literature review are as follows summarized:

- The radiation-induced defects in Ge materials and devices are much less studied and characterized than those in silicon. To some extent this is due to the fact that the available analytical tools have mostly been optimized for silicon and are more difficult to use for Ge. Therefore, there are still a lot of questions to be answered such as the impact of the irradiation particle on the divacancy and the role of the substrate quality on the irradiation-induced defects. In view of the strong interest to use Ge-based solar cells for space applications, it would be interesting to study the impact of high energy proton irradiations.

- SiGe is a rather new technology, which is gaining more and more interest. Although the dominant radiation-induced defects are known, less clear information is available on the impact of the Ge concentration. Much activity has to be done related to modeling the impact of these defects on the electrical performance of the devices. The radiation response of SiGe diodes is rather well documented, no real data is available on the SiGe field effect devices. It is therefore too early to make any conclusions on their radiation hardness compared to silicon based devices.

- The radiation performance of bipolar devices has been studied for several decades. Also the radiation behavior of modern bipolar technologies is being studied and there is the general trend that downscaling will improve the radiation resistance. However, detailed information is lacking on the bulk damage effects after high-energy particles. Some of the advanced processing steps may also lead to plasma-induced damage, especially in the spacer oxides.

- Also for future submicron CMOS technologies, it is expected that downscaling of the geometries will have a positive impact on the radiation performance. The implementation of alternative gate dielectrics and advanced isolation schemes (e.g. shallow trench isolation) has surely to be monitored in order to avoid the occurrence of second-order effects which may become more pronounced and therefore can have a degrading impact on the device/circuit lifetime and reliability. In view of the general trend to use COTS for space applications, an investigation of the radiation hardness of sub 0.35 μm technologies is required.

- GaAs-based technologies are well known for their excellent radiation hardness, which is much better than for silicon-based technologies. There is also a good understanding of the fundamental aspects of the irradiation-induced defects and the correlation with microscopic parameters such as NIEL. There is, however, some discrepancy between the calculated NIEL and the experimentally observed variation of the device parameters in case that high energies are used. This requires some further attention.

- A totally new generation of optoelectronic III-V based devices are nowadays gaining more and more interest for a variety of applications. Before they can be used for space applications a more detailed radiation testing is needed. An important parameter to monitor is the low frequency noise performance. Even more pronounced than for some other components, it is essential to irradiate these devices while applying the standard operating conditions.

- Ferroelectric materials and devices are newcomers in the field and therefore only a limited amount of information on their radiation hardness is available. Initial irradiation testing is, however, showing very promising results. It is expected that ferroelectrics may become very important for both infrared and non-volatile memory applications.

This clearly points out that the future use of the present day state-of-the-art devices and materials requires some additional radiation testing, complemented in some cases by more fundamental studies. Within the Activities of the present Work Order, attention will be given to a radiation study of advanced devices fabricated by IMEC. Although further in-depth discussions with ESA will be done, the future radiation plan may include the following technologies:

- Advanced CMOS devices, processed in a 0. 25 μm and 0.18 μm, respectively. Devices coming from runs with different process splits (gate dielectric and trench isolation) will be selected.
- Bipolar components, fabricated in a 0.35 μm BICMOS technology making use of a SiGe base.
- SiGe structures with different Ge content.
- Exploratory 100 nm CMOS devices
- ....

No ferroelectric devices will be studied, as this is forming the content of another Work Order. The final selection of the devices for irradiation will also depend on the availability of the components. Only devices with a typical performance should be used for the irradiation studies.

Depending on the on time availability of the components, it may be envisaged to investigate also the irradiation performance of some GaAs-based HEMTs and photodiodes and some silicon based avalanche diodes. In first instance, depending on the availability of the irradiation facilities, high-energy proton and gamma irradiations will be executed.

ACKNOWLEDGMENT

The authors would like to thank M. Caymax, J. Poortmans, S. Decoutere, H. Ohyama, and D. Wouters for stimulating discussions and the use of some co-authored results.